DEVELOPMENT AND CHARACTERIZATION OF SEMICONDUCTING POLYMER DOTS FOR APPLICATIONS IN BIOANALYSIS

by

Kelsi Lix

B.Sc., McGill University, 2014

A THESIS SUBMITTED IN PARTIAL FULFILLMENT OF

THE REQUIREMENTS FOR THE DEGREE OF

DOCTOR OF PHILOSOPHY

in

THE FACULTY OF GRADUATE AND POSTDOCTORAL STUDIES

(Chemistry)

THE UNIVERSITY OF BRITISH COLUMBIA

(Vancouver)

December 2019

The following individuals certify that they have read, and recommend to the Faculty of Graduate and Postdoctoral Studies for acceptance, the dissertation entitled:

Development and Characterization of Semiconducting Polymer Dots for Applications in Bioanalysis

submitted by Kelsi Lix in partial fulfillment of the requirements for

the degree of Doctor of Philosophy

in Chemistry

Examining Committee:

W. Russ Algar, Chemistry
Supervisor

Dan Bizzotto, Chemistry
Supervisory Committee Member

Supervisory Committee Member

Sarah Burke, Chemistry and Physics
University Examiner

Urs Hafeli, Pharmaceutical Sciences
University Examiner

Additional Supervisory Committee Members:

Michael Wolf, Chemistry
Supervisory Committee Member

Keng-Chang Chou, Chemistry
Supervisory Committee Member

Abstract

Semiconducting polymer dots (Pdots) are rapidly gaining popularity as fluorescent probes in bioanalysis and imaging. These materials have several remarkable and highly advantageous properties, including their extremely high per particle brightness, large one- and two-photon absorption cross sections, biocompatibility, and ease of preparation. However, being a new material, Pdots suffer from several key limitations that must be addressed before they may find widespread use in bioanalysis. Pdots are typically synthesized by the manual nanoprecipitation method which suffers from poor control and reproducibility. Although energy transfer-based chemical and biological sensors have been developed using Pdots, their photophysics and mechanisms of energy transfer are poorly understood, limiting the rational design of such sensors. Being held together by relatively weak entropic forces, Pdots are only moderately stable and are often prone to non-specific binding due to their surface chemistries. To date, relatively few surface and bioconjugate chemistries have been reported.

This thesis presents the development of a novel, flow-based synthetic method for Pdots yielding improved reproducibility, tuneable particle sizes, and the ability to synthesize Pdots on small (1 mL) and large (100 mL) scales. A comprehensive study of energy transfer between Pdot donors and organic dye acceptors is also presented, and considers the frameworks of Förster Resonance Energy Transfer (FRET), Dexter energy transfer, and photoinduced electron transfer (PET). The results suggest that FRET alone is not sufficient to describe energy transfer in such systems, and that Dexter ET and PET likely also contribute. Thirdly, a surface coating material based on dextran, a biosynthetic glucan, was used to functionalize the Pdot surface and enabled preparation of

immunoconjugates using tetrameric antibody complexes (TACs), resulting in improved performance in proof-of-concept immunoassay and cellular imaging applications. Overall, this thesis presents key contributions to the development of Pdots for applications in bioanalysis, including their synthesis, a deeper understanding of their photophysics, and enhanced performance in biosensing and imaging.

Lay Summary

Fluorescence, or the emission of light stimulated by other light, is a powerful tool for studying biological processes. Although many types of fluorescent materials exist, each material has certain limitations and drawbacks. This thesis aims to further develop and better understand a new class of super-bright emissive materials made of polymers, called “polymer dots” (Pdots). These materials have many desirable properties, including high brightness and biocompatibility, but are difficult to synthesize reproducibly, poorly stable, and have complex interactions with other fluorescent materials. Presented here are a novel and improved synthetic method for Pdots, the development of surface coating materials that enhance their stability and performance in bioanalytical applications, and a study of energy transfer between Pdots and other fluorescent materials, which together lay the groundwork for better design of bioanalysis and imaging methods.

Preface

Kelsi Lix and Russ Algar conceived the research in Chapter 4. KL designed and performed the experiments and analyzed the data. Saeid Kamal assisted with measurements of fluorescence lifetimes. AFM images were acquired by Ethan Sauvé (under the supervision of Zachary Hudson). KL and ES analyzed the AFM results.

Chapter 5 is based on unpublished work. The research in Chapter 5 was conceived by RA, Jason Hein, and KL. KL and Ryan Chung designed the syringe pump system and performed initial testing and troubleshooting experiments. Further experiments were done by KL and undergraduate research assistants under her supervision: Jamie Dearnley, Chelsea Cayayab, Valentin Saibi, and Gilles Poitau. KL designed the general experimental protocols and also specific experiments with the research assistants. The continuous flow pump system was designed by JH, Henry Situ, and Sebastian Steiner. HS and SS wrote the operational code for this system. KL designed the scaleup experiments and performed them with GP and HS. KL performed a global analysis of all data presented in this chapter.

Chapter 6 is based on a manuscript currently in preparation, co-written by KL and RA. The research was conceived by KL and RA. KL designed and performed all experiments and analyzed the data with assistance from RA. SK assisted with fluorescence lifetime and transient absorption measurements. Valerie Chiykowski and Yang Cao (under the supervision of Curtis Berlinguette), Kaylyn Leung and Dan Bizzotto assisted with cyclic voltammetry measurements.

Chapter 7 is based on a published manuscript, "Dextran-Functionalization of Semiconducting Polymer Dots and Conjugation with Tetrameric Antibody Complexes for Bioanalysis and Imaging," ACS Applied Bio Materials, DOI: 10.1021/acsabm.9b00899. This manuscript was written by KL with editing from RA and minor contributions from coauthors. RA and KL conceived the research in Chapter 7. KL synthesized the materials, performed the experiments, and analyzed the data with the following exceptions: AFM images were provided by ES, cell labelling and imaging experiments were done by Michael Tran who analyzed the data with KL, NMR analysis was done by Kelly Rees, and immunoassay development and data analysis were done by Melissa Massey.

Table of Contents

List of Tables

List of Figures

List of Schemes

List of Abbreviations

2PA	Two photon absorption
Abs.	Absorption
AcOH	Acetic acid
AFM	Atomic force microscopy
AIE	Aggregation induced emission
AP	Amphiphilic polymer
ATR-FTIR	Attenuated total reflection Fourier-transform infrared
BEHP-PPV	Poly([2-[2′,5′-bis(2″-ethylhexyloxy)phenyl]-1,4-phenylenevinylene]-co-[2-methoxy-5-(2′-ethylhexyloxy)-1,4-phenylenevinylene])
BHT	Butylated hydroxytoluene
BP	Band pass
CB	Conduction band
CCD	Charge-coupled device
CEA	Carcinoembryonic antigen
cFRET	Concentric Förster resonance energy transfer
$CHCl_3$	Chloroform
CNMEHPPV	Poly[2-methoxy-5-(2-ethylhexyloxy)-1,4-(1-cyanovinylene-1,4-phenylene)]
ConA	Concanavalin A
CV	Cyclic voltammetry
Cy	Cyanine
Dex	Dextran
Dex-Pdots	Dextran-Pdots
DIPEA	*N*,*N*-Diisopropylethylamine
DLS	Dynamic light scattering
DMF	Dimethylformamide
DMSO	Dimethyl Sulfoxide
EDC	1-ethyl-3-(3 dimethylaminopropyl)carbodiimide hydrochloride
EEO	Electroendosmosis
ELISA	Enzyme-linked immunosorbent assay
Em.	Emission
EPO	Erythropoietin

ET	Energy transfer
EtOH	Ethanol
Ex.	Excitation
F8BT	Poly(9,9-dioctylfluorene-alt-benzothiadiazole)
FLIM	Fluorescence lifetime imaging microscopy
FLISA	Fluorescence linked immunosorbent assay
Fluor.	Fluorescence mode
FP	Fluorescent protein
fps	Frames per second
FRET	Förster resonance energy transfer
FT-IR	Fourier transform infrared
FWHM	Full width at half maximum
HEPES	4-(2-hydroxyethyl)-1-piperazineethanesulfonic acid
HER2	Human epidermal growth factor receptor 2
HMDA	Hexamethylene diamine
HMTU	*N*,*N*,*N*′,*N*′-Tetramethyl-O-(N-succinimidyl)uranium hexafluorophosphate
HOMO	Highest occupied molecular orbital
HRP	Horseradish peroxidase
ID	Internal diameter
IR	Infrared
LP	Long pass
LRET	Luminescence resonance energy transfer
LUMO	Lowest unoccupied molecular orbital
MEHPPV	Poly[2-methoxy-5-((2-ethylhexyl)oxy)-p-phenylenevinylene]
MeOH	Methanol
MES	2-(N-morpholino)ethanesulfonic acid
MW	Molecular weight
MWCO	Molecular weight cut off
NA	Numerical aperture
NAv	NeutrAvidin
nb	Non-bonding molecular orbital
NHS	*N*-hydroxysuccinimide
NIR	Near infrared

NMR	Nuclear magnetic resonance
NP	Nanoparticle
NTA	Nanoparticle tracking analysis
PAGE	Polyacrylamide gel electrophoresis
PAI	Photoacoustic imaging
PBS	Phosphate buffered saline
PCDTBT	Poly[N-9'-heptadecanyl-2,7-carbazole-alt-5,5-(4',7'-di-2-thienyl-2',1',3'-benzothiadiazole)]
PDI	Polydispersity index
Pdot	Polymer Dot
PDT	Photodynamic therapy
PE-b-PEG	Polyethylene-block-polyethylene glycol
PEG	Polyethylene glycol
PET	Photoinduced electron transfer
PFMEHPPV	Poly[(9,9-dioctyl-2,7-divinylenefluorenylene)-alt-co-(2-methoxy-5-(2-ethylhexyloxy)-1,4-phenylene)]
PFO	Polydioctylfluorene
PFVA	Poly[(9,9-dioctyl-2,7-divinylenefluorenylene)-alt-co-(9,10-anthracene)]
PL	Photoluminescence
PMAO	Poly(maleic anhydride-alt-1-octadecene)
p-NH_2-Dex	Pendant amine dextran
POC	Point-of-care
PPE	Polyphenyl ether
ppm	Parts per million
PS	Polystyrene
PSA	Prostate specific antigen
PS-b-PAA	Polystyrene-block-polyacrylic acid
PS-b-PEG	Polystyrene-block-polyethylene glycol
PSMA	Poly(styrene-co-maleic anhydride)
PSPEGCOOH	Polystyrene-graft-polyethylene glycol end functionalized with carboxy
PTFE	Polytetrafluoroethylene
PTT	Photothermal therapy
PVK	Poly(9-vinylcarbazole)
QD	Quantum Dot

rcf	Relative centrifugal force
Rh	Rhodamine
rhEPO	Human recombinant erythropoietin
ROS	Reactive oxygen species
rpm	Rotations per minute
Scatter.	Scattering mode
sCMOS	Scientific complementary metal–oxide–semiconductor
SD	Standard deviation
SDS	Sodium dodecyl sulfate
SEM/EDX	Scanning electron microscopy with energy dispersive X-ray spectroscopy
SOFI	Super-resolution optical fluctuation imaging
SP	Semiconducting polymer
SPN	Semiconducting polymer nanoparticle
SSR	Sum of squared residuals
STED	Stimulated emission depletion
Sulfo-NHS	*N*-hydroxysulfosuccinimide
TA	Transient absorption
TAC	Tetrameric antibody complex
TBE	Tris borate EDTA buffer
TCSPC	Time correlated single photon counting
TEM	Transmission electron microscopy
THF	Tetrahydrofuran
TLC	Thin layer chromatography
UCNP	Upconverting nanoparticle
UV	Ultraviolet
VB	Valence band
vis	Visible
w/v	Weight per volume

Acknowledgements

Completing this thesis was one of the most daunting things I've ever done, and I owe an enormous debt of gratitude to the many people who helped me get to the finish line.

A colleague once told me I think "exactly like" my supervisor, Russ Algar, which was an immense compliment, but also a sign it was time to start thinking about writing up this thesis. Russ, thank you for patiently guiding me through what ended up being a more difficult than anticipated project, and teaching me (amongst many, many other things) how to think like a scientist.

My supervisory committee, Michael Wolf, Dan Bizzotto, and Keng Chou, are thanked for their guidance throughout my time at UBC. I'd also like to thank Dan for his feedback on this thesis and instructing me in the art of electrochemistry. José Rodríguez Núñez is also thanked for his mentorship. Working with him has made me a better, more compassionate teacher (though I may never live down the desiccator incident).

I am grateful to the members of staff within and outside of the chemistry department for training and assistance with instrumentation: Saeid Kamal from the LASIR facility for assistance with lifetime imaging and transient absorption; Emily Seo and Ben Herring from the Shared Instrument Facility for training on the various instruments therein; and to Garnet Martens, Brad Ross and Derrick Horne from the UBC Bioimaging Facility for training and assistance with TEM.

It's been a privilege to work amongst colleagues who are generous with their time and expertise in exchange for nothing more than a "thank you". Valerie Chiykowski, Yang Cao, Kaylyn Leung and Dan Bizzotto are thanked for many hours of assistance with electrochemistry. Andy Tran and Mark MacLachlan are thanked for assistance with and frequent access to the DLS. I was lucky to have Zac Hudson and his group so close by—thank you to Ethan Sauvé for assistance with AFM imaging, Alex Polgar for assistance with the use of the integrating sphere, Zac and Nathan Paisley for their valuable insights into the world of DFT, and Wesley Hudson for being a constant source of moral support.

It's been a joy to work in a group with such talented, hardworking, and kind co-workers. Thank you to my past and present colleagues in the Algar lab for your constant support and friendship throughout the years. I'm grateful to my collaborators, both within and outside of the group, for their contributions. I'd also like to thank the undergraduate students and visiting researchers I had the pleasure to supervise for their hard work, curiosity, and research contributions: Jamie Dearnley, Valentin Saibi, Chelsea Cayayab, Gilles Poitau, and Jennifer Whetter. The members of the Withers group have provided a second home for me within the department; thank you for your friendship, hospitality, and the frequent lending of chemicals.

My experience at UBC was enriched by the graduate students I had the pleasure to work with on the CGSS. I'm grateful to them for constantly striving to make the department a better place and for teaching me how to be an effective leader.

I may not have made it out of undergrad, at least in one piece, without the 'Krieble Krew'. Thank you to Alex, Brian, and Seb for perfectly balancing your steadfast support and friendship with constant, biting mockery.

Much of this thesis was written sitting across from Elesha Hoffarth, whose enduring friendship was a rare constant over the past five years. Thank you for spending countless hours in the library with me, and for hosting 'The Batches' every week.

Finally, I don't have the words to express the depths of my gratitude towards Phillip Danby, whose support and unwavering belief that I could tackle any challenge I thought insurmountable were instrumental to the completion of this thesis. Thank you for everything.

Chapter 1: Introduction

Bioanalysis is a field of research concerned with the identification, quantification and characterization of molecules in biological systems, and the development of novel measurement techniques to achieve these aims [1]. Bioanalysis is a far-reaching field; many analyses are directly or indirectly related to biology, with their motivation spanning fundamental research, clinical medicine, the production of consumer products, the design of industrial processes, and beyond [2]. Advances in bioanalysis often arise from enhancements in instrumentation, novel computational techniques, and developments in materials science. The field of bioanalysis encompasses many different experimental techniques, including but not limited to mass spectrometry (*e.g.*, the 'omics' fields), electrochemistry, and optical spectroscopy. Of particular interest in bioanalysis is the application of fluorescence spectroscopy and microscopy to solve analytical problems.

1.1 Fluorescence in bioanalysis

Fluorescence is a powerful tool for studying biological species and processes, especially at subcellular length scales. Fluorescence measurements have many advantages over other modes of detection. They are typically fast, highly sensitive (at best single molecule detection), and non-destructive to the sample. Convenient multiplexing is achieved using fluorophores with well-resolved emission colours. Multiple properties of fluorescence may be measured: intensity, wavelength, lifetime, and polarization. Altogether these properties make fluorescence a very versatile tool across many disciplines, particularly when analysis on microscopic scales is required.

Fluorescence methods are most frequently enabled by the use of exogenous labels. Although some intrinsic probes exist (*e.g.*, tryptophan in proteins), such examples are rare and are typically not

brightly emissive. Addition of an exogenous label can sometimes perturb the system being studied, but potential perturbations may be minimized by careful selection of the fluorescent label, considering the system under study, and the size and brightness of the label.

1.1.1 Fluorescent probes

The parameters and limitations of a given fluorescence experiment largely depend upon the physicochemical and optical properties of the fluorophore used. Important physicochemical considerations include the chemical nature and size of the fluorophore, its biocompatibility, and the interactions the fluorophore may have with the analyte or its environment. Salient optical properties include the spectral position, width and shape of the fluorophore's absorption and emission bands, its molar extinction coefficient, and its quantum yield. The Stokes shift is a measure of the spectral overlap between a fluorophore's absorption and emission bands and therefore determines how easily the excitation signal may be separated from the measured emission [3]. With these considerations in mind, an ideal and highly utile fluorophore has the following characteristics:

(1) Convenient excitation wavelengths that avoid excitation of the background or surrounding biological matrix;
(2) Detection possible with conventional instrumentation;
(3) High emission brightness, defined as the product of the molar extinction coefficient at the excitation wavelength and the quantum yield of the fluorophore;
(4) High solubility in aqueous and biologically relevant media;
(5) Good chemical and photostability in relevant conditions;
(6) Contains functional groups appropriate for site-specific labelling of biological targets;

(7) Well-known photophysics;

(8) Available in a highly reproducible format (*e.g.,* consistent physical and optical properties).

Depending upon the requirements of a specific application, further considerations may include steric or size effects of the fluorophore, delivery of the fluorophore into cells, biocompatibility and cytotoxicity, and multiplexing capabilities [3].

In response to the broad utility and popularity of fluorescence methods, many classes of fluorophores have been developed that meet many of the above requirements. Fluorophores may be broadly categorized as follows:

(1) Molecular fluorophores with well-defined chemical structures including organic dyes, transition metal-ligand complexes (*e.g.,* $Ru(bby)_3^{2+}$), and lanthanide chelates;

(2) Fluorophores of biological origin such as genetically encoded fluorescent proteins (FPs);

(3) Nanocrystals with size-dependent optical properties such as quantum dots (QDs), carbon-based QDs, and silicon NPs;

(4) Nano- or micro-sized particles with size-independent optical properties, such as dye-loaded silica NPs and semiconducting polymer dots (Pdots) [3].

Currently, molecular fluorophores and FPs are most commonly used. FPs are large (*ca.* 25 kDa) fluorophores that may be genetically encoded into cells to avoid the need for an additional labeling step, although their large size may cause non-trivial perturbations to the system under study. Mutants of the original green fluorescent protein have been developed with varying optical properties, including a rainbow of emission colours, although green-, yellow- and red-emitting FPs

are most common. Wild-type FPs suffer from several drawbacks including low folding efficiency at physiological temperatures, low fluorescence intensity and low levels of expression in certain types of mammalian cells [4]. Molecular dyes are small (*ca.* 1 kDa) but must be introduced to the system under study. The optical properties of molecular dyes depend on the chemical and electronic structure of the molecule. Emission of visible photons is enabled when the molecule features extended π-orbital overlap along its structure (*i.e.,* delocalization of electrons) or due to intramolecular charge transfer [3]. Dependent upon the chemical structure of the probe, it may or may not be sensitive to its local environment (*e.g.,* pH or solvent polarity), a property which may be matched to the intended application. Although molecular fluorophores are used extensively, they are often limited by their relatively low brightness and fast rates of photobleaching. Over the past several decades, luminescent nanomaterials have emerged as an alternative to molecular dyes, overcoming some of these limitations.

1.1.1.1 Luminescent nanomaterials

Luminescent nanomaterials represent a broad class of emissive materials larger than single molecules but having at least one dimension less than 100 nm [5]. Most luminescent nanomaterials are inorganic or contain metals, but several types of organic nanomaterials have been developed in recent decades. Although luminescent nanomaterials encompass a broad range of materials, many share several key advantages over molecular fluorophores and FPs. Luminescent nanomaterials typically have high brightness, good resistivity to photodamage, tuneable optical properties, functionalizable surfaces and for some soft materials, a useable volume (*e.g.,* for carrying a payload). Luminescent nanomaterials also suffer from limitations not applicable to molecular dyes and FPs, namely their poorly defined structures, synthetic variability, and non-

uniform size distributions. Luminescent nanomaterials have non-trivial sizes and may induce greater perturbations in the system under study than molecular dyes.

The following sections briefly introduce the main classes of luminescent materials currently used in the field of bioanalysis and highlight some of their key applications in biosensing and imaging. Selected physical and optical properties of these materials are summarized in Table 1.1.

Table 1.1. Selected physical and optical properties of luminescent nanomaterials. Adapted from ref. [6].

NP	Size (nm)	$\lambda_{Ex.}$ (nm)[a]	$\lambda_{Em.}$ (nm)[b]	Brightness	Photostability	Toxicity
QDs	4-10	330-450	420-700	High	High	Low (if properly passivated)
Carbon dots	2-20	350-500	450-700	Good	High	Low
UCNPs	8-100	780-980	350-NIR[c]	Poor	High	Low
Dye doped NPs	15-100	UV to NIR[c]	UV to NIR[c]	High	Fair	Low

[a] Range of excitation wavelengths [b] Range of emission wavelengths [c] Near Infrared (800-2500 nm)

1.1.1.1.1 Semiconductor quantum dots

Semiconductor quantum dots (QDs) are one of the most utilized types of luminescent nanomaterial in bioanalysis. Owing to their ubiquity, broad scope of demonstrated applications and many desirable optical properties, QDs are the 'gold standard' luminescent nanomaterial and make a natural point of comparison for other materials. QDs are small (4-10 nm) inorganic nanocrystals composed of semiconducting materials such as CdSe or silicon. The physical stability and optical properties of QDs can be enhanced by overcoating the semiconducting core with a shell material such as ZnS. QDs exhibit many advantageous optical properties including bright, spectrally narrow and size-tuneable emission, high quantum yields, broad absorption bands and high resistance to

photobleaching. QDs are often synthesized with heavy metals and their degradation products are generally considered toxic. Potential toxicity is mitigated by high quality surface coatings which prevent the leaching of heavy metals from the QD core and the low concentrations required for exceptional signal contrast because of their high brightness [7].

QDs are ideal fluorophores for multiplexing applications because of their spectrally narrow (and therefore resolvable) emission bands, broad absorption bands allowing excitation of multiple QDs at a single wavelength, and finely size-tuneable emission colour. Their high brightness is also ideal for technologically demanding applications such as the development of point-of-care (POC) theranostic assays with fluorescent readout [8].

Taking advantage of the multiplexing capabilities of QDs, Chen and coworkers designed a paper-based fluorescence sandwich-style immunoassay for the simultaneous detection of carcinoembryonic antigen (CEA) and prostate specific antigen (PSA) using CdTe QDs as fluorescent labels [9]. This sensor design leveraged the characteristic narrow emission bands of QDs to enable multiplexed detection of two cancer biomarkers within a single spot on a paper strip. QDs emitting at 525 nm (green) and 605 nm (orange) were used to label detection antibodies for CEA and PSA, respectively. Capture antibodies for CEA and PSA were localized on the same spot of the paper strip, and the corresponding labelled detection antibody were bound only in the presence of the specific analyte. Both QDs were excited at the same wavelength owing to the characteristic broad absorption bands of these materials. This assay design is only possible because of the narrow and well-resolved QD emission peaks allowing simultaneous detection [9].

Novel QD materials maintaining the desirable optical properties of existing QDs are currently under development. Bruns and coworkers developed a new class of indium arsenide QDs with shortwave IR (1000-2000 nm) emission, exhibiting many of the same desirable optical properties as conventional QDs including narrow and size-tuneable emission bands and good quantum yields [10]. InAs QDs were incorporated into higher order structures including phospholipid micelles, nanosomes (lipoprotein micelles) and composite particles. The authors demonstrated the utility of these probes in a wide variety of *in vivo* imaging applications including real-time imaging of lipoproteins to monitor metabolic processes, quantitation of heart rate and respiration in mice, and the visualization of the brain vasculature of mice [10].

1.1.1.1.2 Carbon nanomaterials

The term carbon nanomaterial is used to describe several distinct types of organic nanoparticles that are composed of mostly carbon, hydrogen, and in some cases oxygen atoms. Both carbon and graphene quantum dots exhibit size tuneable emission but are differentiated by the arrangement of the carbon atoms in their cores. Whereas carbon quantum dots consist of sp^2 or sp^3 hybridized carbon atoms in a crystalline geometry, graphene quantum dots consist of individual sheets of graphene (sp^2 hybridized carbon atoms) less than 20 nm in length. Carbon dots represent a third class of carbon nanomaterial and are amorphous, quasi-spherical particles consisting of disordered sp^3 hybridized carbon atoms in their cores. These materials exhibit size independent emission arising from an assembly of individual emitters within the core [11]. Because they contain only benign organic materials, carbon nanomaterials are generally considered biocompatible and surface-functionalized carbon nanomaterials have been used to non-specifically label and image cells and for photothermal therapy [12]. The emission intensity and wavelength of carbon

nanomaterials may be sensitive to several parameters including changes in environment (*e.g.*, solvent, pH) or analyte concentration (*e.g.*, metal ions) which is useful for sensing applications [13].

Carbon dots may contain several inherent functional groups that are responsive to certain environmental factors such as pH. Xia and coworkers leveraged intrinsic dual-emission from carbon dots for ratiometric pH sensing [14]. Nitrogen-containing carbon dots having resolved emission peaks at 393 nm and 580 nm under 365 nm excitation were synthesized using *o*-phenylenediamine, polyethylene glycol (PEG) and oxalic acid. Both emission peaks exhibited pH-dependence albeit with opposite trends. The 580 nm peak decreased in intensity with decreasing pH whereas the intensity of the 393 nm peak increased with decreasing pH. The ratio of the two intensities was used as the sensing parameter. The pH responsive properties are inherent to these carbon dots; intrinsic nitrile, amine and carboxylic acid functionalities are protonated at low pH, changing the π-conjugation of the carbon cores and tuning the emission wavelength. Carbon dots uniquely enable ratiometric sensing using a single probe without the incorporation of pH-sensitive organic dyes [14].

The intrinsic functional groups found in carbon dots can also be leveraged for *in vitro* imaging of analytes. Liu and coworkers developed formaldehyde-sensitive carbon dots containing carbonyl and amino groups [15]. Intramolecular charge transfer occurred from the amino groups to the carbonyl groups resulting in strong emission at 580 nm. Formaldehyde selectively reacted with the amino groups, suppressing charge transfer and quenching emission at 580 nm. In response to increasing formaldehyde concentrations, a second blue-shifted peak at 500 nm emerged. These carbon dots were observed to target lysosomes natively, an effect postulated to arise from the

acidotropic effect of their intrinsic amino groups, and were used to ratiometrically image formaldehyde in living HeLa cells [15].

1.1.1.1.3 Upconverting nanoparticles

Upconverting nanoparticles (UCNPs) are a class of nanomaterial that emit due to the upconversion effect, where emitted light is of a shorter wavelength (higher energy) than the excitation light. Upconversion is most commonly observed in materials containing rare earth metals such as trivalent lanthanide or actinide ions, which are doped into a non-emissive host matrix to form nanoparticles. Absorption in these materials occurs sequentially, first to the metastable and long lived first excited state, then subsequently to a higher energy excited state from which emission occurs. As a result, UCNPs are excited in the near-IR where most biological samples are transparent, minimizing autofluorescence and allowing efficient excitation at low incident power.

UCNPs have many desirable optical properties including spectrally narrow emission bands, large Stokes shifts, long emission lifetimes (up to milliseconds), high chemical stability, and good biocompatibility [16]. The visible emission colour can be tuned by the choice of the luminophore (*i.e.,* rare earth metal species), although multiple emission bands contribute to the observed colour, usually at several distinct wavelengths. UCNPs dot not photobleach or exhibit blinking, but are less bright than QDs used in similar applications [17].

UCNPs are useful for multiplexing applications as multiple spectrally resolvable luminophores may be excited at a single excitation wavelength. Because of their long emission lifetimes, time-gating can be used to eliminate background scattering or autofluorescence from biological samples

[17]. UCNPs may be used as fluorescent labels in chemical and biological assays, or their emission may be modulated via luminescence resonance energy transfer (LRET) when paired with an appropriate acceptor (*e.g.*, oxygen sensitive dyes or heavy metals) in a sensing configuration [16-17].

Zhang and coworkers developed a hypochlorous acid (HOCl) sensor using ytterbium-containing UCNPs coupled to a ruthenium(II) complex which is responsive to HOCl. Upon excitation at 980 nm, the UCNPs emitted blue light (450 and 475 nm), which overlapped with the absorption spectrum of the Ru(II) complex, efficiently quenching UNCP emission via LRET [18]. HOCl reacted with the Ru(II) complex, forming a product with a suppressed a blue-shifted absorption band that did not have suitable spectral overlap for LRET, causing the UCNP emission to 'turn-on' to an extent dependent upon the HOCl concentration. UCNP emission at 800 nm was not affected by LRET and was used as an internal reference. The ratio of intensities at 450 or 475 and 800 nm was used as the analytical signal to determine HOCl concentration. Sensing was performed in solution as well as using a paper-based assay. Sensing and imaging of HOCl were also performed *in vitro* and *in vivo*, leveraging the near-infrared (NIR) excitation of UCNPs to minimize autofluorescence and interference from background signal [18].

Zhao and coworkers leveraged NIR excitation capabilities of UCNPs to design a photoactivatable nanodevice for the detection of microRNAs *in vitro* and *in vivo* [19]. In this study, a DNA beacon structure containing a UV-cleavable bond in its hairpin loop was functionalized onto the surface of UCNPs. Upon NIR irradiation, the UCNPs emitted UV light, cleaving this bond, and allowing the displacement of the quencher-labelled strand by the microRNA analyte. Fluorescence of the dye-labelled complementary strand was then restored, acting as a 'turn-on' sensor for microRNA.

The nanodevice was deployed in living HeLa cells and HeLa tumor bearing living mice, and was demonstrated to enable spatially and temporally controlled imaging of microRNA [19].

1.1.1.1.4 Dye-doped nanoparticles

Some of the inherent limitations of molecular dyes may be circumvented by doping a large number of dyes (≥10 000) inside of an inert non-emissive matrix such as silica or latex, yielding brightly emissive nanoparticles. These particles are orders of magnitude brighter than an individual dye as thousands of emitters are superimposed within the particle core. Doped dyes are shielded from the surrounding environment and are therefore less prone to photobleaching than individual dye molecules. Dye doped nanoparticles are often favoured for applications involving high signal intensity and long measurement times such as single particle tracking (if the application suits the particle size). Many surface chemistries are accessible via the silica and silane reagents used in NP synthesis (*e.g.,* carboxylic acid, amine, thiol) enabling many possible bioconjugation pathways, and the use of dye doped nanoparticles as fluorescent labels in biosensing applications and specific cellular labelling. Multiplexed sensing may be achieved by doping with dyes of multiple emission colours, creating two or three colour barcodes embedded within a single NP [20].

Dye-doped nanoparticles may be prepared using a variety of dopants responsive to multiple analytes of interest, enabling convenient multiplexing. Wang and coworkers developed multiplexed sensors for the simultaneous detection of temperature, oxygen and pH using silica-coated dye-doped polystyrene (PS) nanoparticles [21]. PS NPs were doped with a NIR emissive chromium(III) complex that is sensitive to both oxygen and temperature. Fluorescein, a pH responsive dye, was conjugated to the particle surface. A dye with constant emission was also doped into the particle core to act as a reference. All three

emissive species were excited at the same wavelength but had resolvable emission bands, allowing for the sensing of three different analytes simultaneously [21].

The beneficial optical and physical properties of luminescent NPs may be combined for theranostic applications. Kim and coworkers developed Cy5-doped ultrasmall (<10 nm) silica NPs for *in vitro* and *in vivo* fluorescence imaging and cancer cell targeting [22]. The dye doped silica NPs were surface functionalized with melanoma-targeting peptides, allowing localization of the NPs in cancer cells. These NPs were observed to induce cell death (ferroptosis) in various cancer cell lines and were observed to inhibit tumor growth in xenograft mouse models. Both *in vitro* and *in vivo* fluorescence imaging were used to locate the therapeutic NPs and monitor cell death and tumor growth [22].

The highlighted sensing applications of QDs, Carbon Dots, UCNPs and dye-doped nanoparticles are summarized in Table 1.2.

Table 1.2. Biosensor and assay properties for selected examples using different types of luminescent nanomaterials

Nanomaterial	Analyte	Fluorescence signal readout	Detection Limit	Dynamic range	$\lambda_{Em.}$ (nm)	$\lambda_{Ex.}$ (nm)	Recognition element	Ref.
CdTe QDs	Protein cancer biomarkers	Multiplexed fluorescence	0.3 ng/mL (CEA), 0.4 ng/mL (PSA)	1.0-40 ng/mL	525/605	272	Detection antibody	[9]
Dual-emissive Carbon Dots	pH	Ratiometric fluorescence	N/A	2.2-8.0	393/580	365	(De)protonation of intrinsic functional groups	[14]
UCNPs	HOCl	Ratiometric LRET	166 nM (450 nm), 136 nM (475 nm)	0.60 µM-2.0 µM	450/475 (modulated), 800 (reference)	980	$Ru(bpy)_2$ complex	[18]
Dye-doped nanoparticles (silica-coated polystyrene)	Temperature, O_2, pH	Ratiometric fluorescence	N/A	3.8-8.7 (pH), 282-343 K (temperature), 0.3 hPa-214.5 hPa (oxygen)	740/778 (Cr(III) complex), 520 (fluorescein), 633 (reference)	440	Cr(III) complex (temperature, O_2), fluorescein (pH)	[21]

Overall, luminescent nanomaterials display broad applicability across many bioanalytical applications, and offer unique flexibility in their properties, design, and surface functionalization. Although QDs, carbon dots, UCNPs and dye-doped particles are well-developed and widely used, each material faces certain inherent drawbacks and limitations. The continued development of novel fluorescent probes with complementary properties will allow for innovation in fluorescence biosensing and imaging. Important considerations for the development of new luminescent materials include biocompatibility for downstream regulatory approval and high brightness to meet the increasingly high technical demands of emerging techniques such as single particle spectroscopy and point-of-care diagnostics. Semiconducting polymer dots (Pdots) are an emergent luminescent nanomaterial that may prove invaluable to the development of novel fluorescence techniques.

1.2 Semiconducting Polymer Dots (Pdots)

The focus of this thesis is the development and optimization of Pdots as a fluorescent probe in bioanalytical sensing and imaging. The group of Jason McNeill first reported the formation of aqueously dispersed nanoparticles of single molecules of the semiconducting polymer poly[2-methoxy-5-((2-ethylhexyl)oxy)-p-phenylenevinylene] (MEHPPV) in 2005 [23]. The first biological application of Pdots followed soon after in 2008, where the McNeill group non-specifically labelled cells with Pdots of varying composition and emission colour [24].

Since these early reports, Pdots have exploded in popularity as a fluorescent probe in a variety of bioanalytical applications due to their many advantageous properties, including their extremely high per particle brightness, biocompatibility, permeable cores suitable for loading with cargo, and

relative ease of synthesis. As of 2019, over 500 original research articles[1] have been published on Pdots since they were first reported in 2005. Although they have seen rapid growth, Pdots are still in their infancy and, like other luminescent nanoparticles, require optimization and the overcoming of several key limitations before they may find more widespread use.

1.2.1 What is a Pdot?

Pdots can be considered as a subclass of polymer nanoparticle. A polymer nanoparticle is defined as "a submicrometer-sized entity which represents a separate discontinuous phase surrounded by a continuous free-flowing medium", usually a low molecular weight solvent and most often water [25]. This classification consists of particulate colloids and excludes macromolecules in the solution phase (*i.e.*, unaggregated polymers fully soluble in their solvent) and nanophase-separated solid bulk materials [25]. The group of Daniel Chiu defines Pdots as polymer nanoparticles consisting of semiconducting polymers (SPs) at a volume fraction or weight concentration of at least 50% (ideally > 80%) and having particle sizes comparable to those of QDs, typically less than 30 nm [26]. The limitation on size is somewhat ambiguous as the diameter may be given as either the hydrodynamic or dehydrated diameter, and the average or median diameter is not representative of the broad size distribution usually obtained. The volume fraction or weight concentration of a semiconducting polymer nanoparticle (SPN) is correlated to its desirable optical properties, namely its extremely high per particle fluorescence brightness. A nanoparticle with a higher fraction of the emissive component is expected to have greater per particle brightness. The composition requirement therefore differentiates Pdots from other nanomaterials containing only

[1] Web of Science results for original research articles containing "Polymer Dots" or "Pdots" in all fields since 2005

a small fraction of SPs, such as dye loaded silica or latex NPs. Nanoparticles with sufficiently high volume fractions of SPs but greater particle sizes are typically classified more generally as semiconducting polymer nanoparticles (SPNs) [26]. Pdots should also contain a hydrophobic polymer core. The inclusion of a significant fraction of hydrophilic species within the core may swell the particles, reduce the overall colloidal stability of the particles, cause increased non-specific binding through electrostatic interactions, and affect the packing density of the SP chains in the interior which may affect the fluorescence brightness or other optical properties [27].

Although there exists a proposed definition, the term *Pdo*t is applied more generally in the literature. There are many examples where the term *Pdot* is used to describe nanoparticles that do not meet the proposed conditions of size, composition, or in some cases, either [28-29]. The most common case is SPNs that fulfill the proposed composition requirement but exhibit particle sizes above 30 nm [28, 30-32].

The term *Pdot* is also frequently used to describe polymer NPs that do not meet the proposed condition of composition [33-34]. In some cases, SPNs that contain less than 50% SP by weight or volume are classified as Pdots [35]. There are also examples where the term Pdot is used to describe NPs composed of other, non-semiconducting polymer materials, such as 'non-conjugated' Pdots [36-45] which are usually emissive by crosslink enhanced emission, or aggregation-induced emission (AIE) Pdots [46-47]. Non-emissive polymers with pendant fluorophores have also been referred to as 'Pdots' [48].

Because of the broad use of the term *Pdot* in the literature, a more general definition is emerging. Pdots are generally considered to be SPNs with sub-100 nm average (hydrodynamic) diameters with > 50% SP by mass having (assumed) hydrophobic cores [49]. Thusly the term *Pdot* is used to describe all SPN materials used in this thesis, regardless of their size, as almost all materials used here meet the conditions of this emergent definition. Particle sizes obtained by nanoprecipitation methods are often difficult to control, and consequently, Pdots of sizes ranging from ~30–100 nm were used throughout this thesis.

1.2.2 Pdot synthesis

There exist two general methods for the preparation of polymer nanoparticles. The direct polymerization method involves the polymerization of low molecular weight monomers directly into nanoparticles, without first forming free solution phase polymer. Optical properties of the resulting nanoparticles can be easily tuned by adjusting the monomers used in synthesis. It is possible to obtain SPNs with small (< 100 nm) diameters via direct polymerization [50]. However, this method suffers from several key difficulties, namely that the polymerization reactions used typically require a transition metal catalyst and are often inherently incompatible with water or other dispersion solvents. Aqueous NPs are preferred for down stream biological applications. Contaminants present in reagents or side reactions may also affect the resultant nanoparticles [51]. The direct polymerization method is thus rarely used to synthesize Pdots or SPNs intended for biological applications.

The post-polymerization method uses high molecular weight polymers to form nanoparticles. The polymer is first dissolved in an organic solvent and nanoparticles are produced when the dissolved

polymer is introduced to water or another dispersion solvent. The exact mechanism of nanoparticle formation depends on the miscibility of the particular organic solvent with the dispersion solvent. When the SP is dissolved in a water-immiscible solvent such as chloroform ($CHCl_3$), NPs are formed by the mini-emulsion process. When a water-miscible solvent like tetrahydrofuran (THF) is used, NPs are formed by the nanoprecipitation process, the most common route for synthesizing small polymeric NPs such as Pdots. The post-polymerization method is considerably easier than the direct polymerization method. Many high-quality and pure semiconducting polymers are commercially available so this method is accessible without expertise in organic synthesis or access to specialized equipment [26].

1.2.2.1 Mini-emulsion

The mini-emulsion method is used when the semiconducting polymer is dissolved in a water-immiscible solvent. This method typically produces larger NPs with diameters above 100 nm. A mini-emulsion is a system where highly stable small droplets are created in a bulk continuous phase using high shear, such as ultrasonication [52]. Droplet growth occurs via collisional exchange and Ostwald ripening (mass exchange). To obtain small, uniform droplets, an emulsifier or surfactant such as sodium dodecyl sulfate (SDS) is used to prevent collisional exchange, and a highly hydrophobic species (hydrophobe) may be used to minimize mass exchange. After mixing of the immiscible and dispersion solvents (*i.e.*, droplet formation), the immiscible solvent is removed (*e.g.*, by evaporation) to produce stable nanoparticles. Depending on the precise conditions and which surfactant(s) are used, droplet sizes can range from 30 nm to 800 nm [53]. Mini-emulsion was first used to prepare semiconducting polymer nanospheres in 2002. Landfester and co-workers showed that various classes of SPs could form single polymer or polymer blend

NPs (diameters > 70 nm) when emulsified from $CHCl_3$ or xylene using SDS as a surfactant [54-55]. There have since been several other examples of mini-emulsion synthesis of Pdots using PEG [56] or SDS [57] as an emulsifier, although this pathway remains far less common than nanoprecipitation. Mini-emulsion can also be used to produce NPs by the direct polymerization method [52], although this is not a common pathway for the synthesis of Pdots or SPNs. In this method, monomers are first confined to the droplet phase followed by the initiation of polymerization.

1.2.2.2 Nanoprecipitation

The most common synthetic route to small (< 100 nm) polymeric nanoparticles is nanoprecipitation, sometimes called reprecipitation. A dilute solution of SP in water-miscible solvent, often THF, is rapidly introduced to and mixed with water. The sudden change in solvent polarity (*i.e.,* decrease in solubility of the SP) and hydrophobic interactions between polymer chains or within individual polymer chains results in the formation of spherical nanoscale aggregates. The organic solvent is then removed by evaporation [51]. This method does not require the use of small molecule surfactants, although an amphiphilic co-polymer is often co-precipitated with the SP to stabilize the NPs.

Nanoprecipitation was first employed to make polythiophene SPNs (40–140 nm) by the group of Hiroshi Masuhara in 2004 [58]. Soon thereafter the McNeill group used nanoprecipitation to make Pdots, differentiated by their small diameters, in 2005. In this work, the conjugated polymer MEHPPV was dissolved in THF and rapidly mixed with water. Resultant NPs were small (< 10

nm) which is much smaller than particles synthesized by other methods such as mini-emulsion [23].

Particle formation via nanoprecipitation depends upon competition between aggregation (*i.e.*, multiple polymer chains coming together) and chain collapse (*i.e.*, a single polymer chain folding on itself). Some tuning of particle size should therefore be possible by variation of the precursor concentration [24]. Some groups have shown that lower precursor concentrations result in Pdots of smaller diameter [59], although this trend is not widely reported and has not been studied systematically. Particle size has also been reported to increase with the volume of the organic phase [60]. There is some evidence that suggests the conformation of the polymer before precipitation occurs can influence how the polymer chains are packed in the Pdot core and can therefore alter Pdot photophysics [61].

1.2.3 Composition

Formation of SPNs by nanoprecipitation is a generalizable method that works with a wide variety of polymers having variable but hydrophobic structures. Single types of SP in the absence of stabilizers have been shown to form Pdots via nanoprecipitation. Although the polymer structure itself is hydrophobic due to the extended π-conjugation along its backbone, these particles remain stable in water. It is thought that the oxidation of surface sites creates charged species which act to stabilize the particles [62]. More commonly, SPs are co-condensed with another, non-fluorescent polymer species. These can be amphiphilic (*i.e.*, containing both hydrophobic and hydrophilic moieties or regions) small-molecule or polymeric surfactants and may be ionic (charged) or neutral. The hydrophobic portion is believed to co-condense with the hydrophobic SP

in the NP core. The hydrophilic portion is thought to remain on the surface of the particle, forming a shell-like structure around the hydrophobic core [63]. The true core/shell structure of Pdots in not known, including the thickness and surface coverage of the hydrophilic shell and the degree to which the SP and amphiphile intermix.

1.2.3.1 Semiconducting polymers

Semiconducting polymers typically contain alternating single and double bonds along the length of their backbones, an arrangement known as π-conjugation. This specific arrangement of molecular orbitals allows valence electrons to delocalize along a conjugated structure instead of being closely associated with a single atom or bond. Alternating single and double bonds also prevent rotation around an individual bond, conferring structural rigidity and a mostly planar structure. As the length of a conjugated segment increases, neighbouring π–bonding or π–antibonding orbitals become closer in energy. In a semiconducting polymer, the energy levels become close enough to form a continuum of states, known as a band, instead of discrete energy levels. The occupied π–bonding orbitals form the valence band which is occupied by valence electrons. The unoccupied π–antibonding orbitals form the conduction band, which lies at a higher energy than the valence band. The difference in energy between the highest occupied molecular orbital (*i.e.*, the top of the valence band) and the lowest unoccupied molecular orbital (*i.e.*, the bottom of the conduction band) is known as the band gap (E_g) and corresponds to the absorption onset of the polymer (Figure 1.1). Organic semiconductors typically have band gaps between 1.5 and 3.5 eV (*ca.* 350-850 nm) [64].

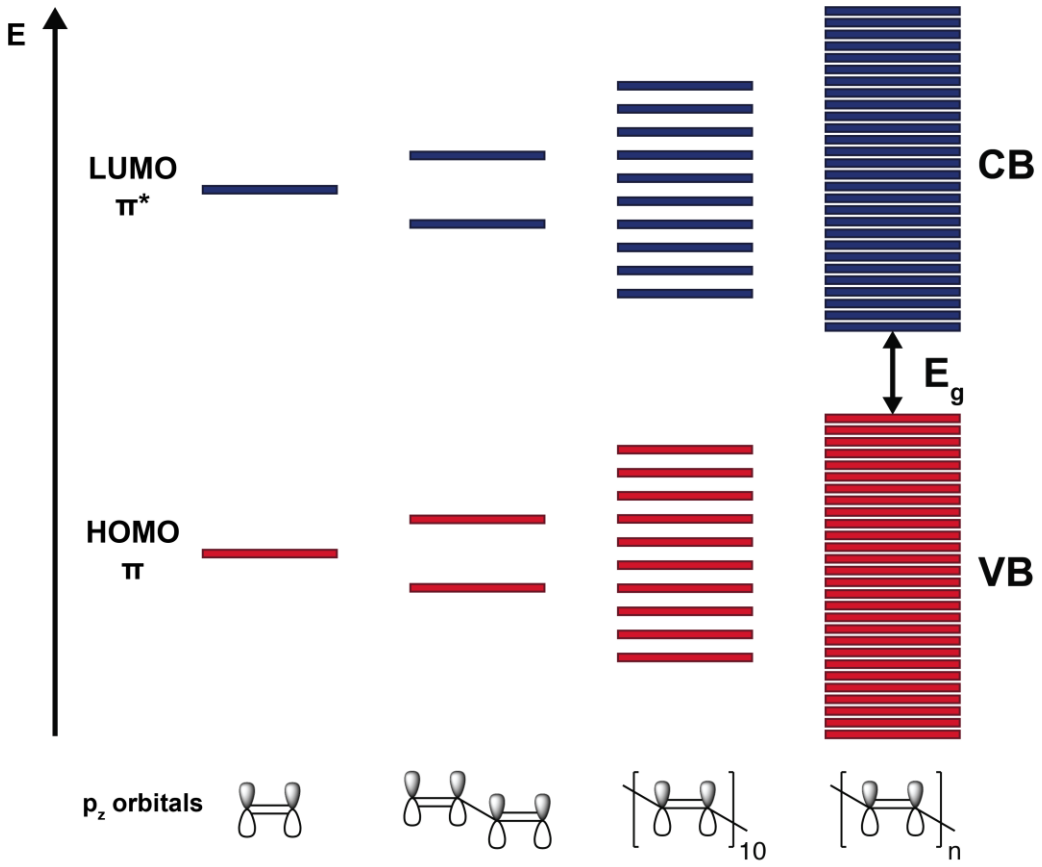

Figure 1.1 Band structure of a simplified semiconducting polymer (polyacetylene). A single carbon-carbon double bond is illustrated on the left. The lowest energy optical transition occurs from the HOMO (red), a π-bonding orbital, to the LUMO (blue), a π-antibonding orbital. As the extent of conjugation increases (*i.e.,* more alternating single and double bonds), more π and π* orbitals occur at similar energies. For a semiconducting polymer, the orbitals become close enough in energy to form a quasi-continuum of states, forming a band structure. The lower energy occupied orbitals become the valence band (VB) and the higher energy unoccupied orbitals become the conduction band (CB). The gap between the top of the VB and the bottom of the CB is known as the bandgap energy (E_g).

In reality, π-conjugation does not persist across the entire length of a single polymer chain. Local changes in conformation, such as bending or kinking of the backbone, can prevent strong π-orbital overlap at the site of the conformation change. Electrons are delocalized over shorter lengths of

the backbone bordered by areas of poor overlap. These shorter conjugated segments are referred to as the *effective conjugation length* of the polymer.

The energy levels and bandgap of a SP are dependent upon its chemical structure. The inclusion of different aromatic rings in the repeat unit or functionalization with electron donating or withdrawing groups can be used to tune the energy levels. Further tuning can be achieved using donor-acceptor polymers whose monomers consist of alternating electron rich (donor) and electron poor (acceptor) co-monomers. Smaller bandgaps can be achieved by orbital mixing of the two co-monomers (Figure 1.2), resulting in desirable red or near-IR emission for biological applications. Alternating donor and acceptor monomers also increases the overall double bond character along the polymer backbone, increasing planarity and electron delocalization [65].

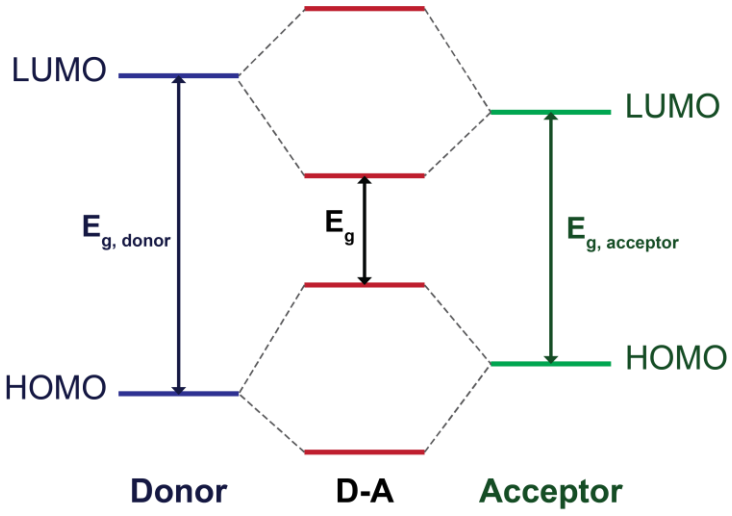

Figure 1.2 Orbital mixing in donor-acceptor semiconducting polymers leading to decreased bandgap energies.

Dozens of SPs with emission colours spanning the visible spectrum are commercially available and many have been shown to form Pdots or SPNs. Figure 1.3 shows the chemical structures of common commercial SP monomer units. MEHPPV, an orange-red emitter based on the methoxy-phenylenevinylene monomer, is often used as a model system in the study of SPs and its thin films have been studied extensively [66]. MEHPPV [24, 67] and its derivatives such as poly[2-methoxy-5-(2-ethylhexyloxy)-1,4-(1-cyanovinylene-1,4-phenylene)] (CNMEHPPV) [60-61, 68] and poly([2-[2′,5′-bis(2″-ethylhexyloxy)phenyl]-1,4-phenylenevinylene]-co-[2-methoxy-5-(2′-ethylhexyloxy)-1,4-phenylenevinylene]) (BEHP-PPV) [56] have been widely used for Pdot synthesis. Many SPs are based upon the fluorene monomer, the simplest of which are polydioctylfluorene (PFO) and its derivatives. PFO emits blue light, but its emission colour may be tuned by the inclusion of other co-monomers. PFO [24, 69-72] or similar SPs differing only by the length of their pendant alkyl chains [73-76] are often used to synthesize Pdots. Poly(9,9-dioctylfluorene-alt-benzothiadiazole) (F8BT) is a popular donor-acceptor PFO derivative for Pdot synthesis, differing by the inclusion of a benzothiadiazole co-monomer rendering its emission green [24, 28, 31, 59, 77-82]. Poly[(9,9-dioctyl-2,7-divinylenefluorenylene)-alt-co-(2-methoxy-5-(2-ethylhexyloxy)-1,4-phenylene)] (PFMEHPPV), a green emitter, contains both the fluorene and methoxy-phenylenevinylene monomers and has been used for Pdot synthesis [24, 31, 74]. Other commonly used commercial SPs include poly[N-9'-heptadecanyl-2,7-carbazole-alt-5,5-(4',7'-di-2-thienyl-2',1',3'-benzothiadiazole)] (PCDTBT) [57], poly(9-vinylcarbazole (PVK) [33, 83], polyphenyl ether (PPE) [24], and polymers based on thiophene [32, 84]. Blends of multiple polymers may be used to synthesize Pdots where efficient energy transfer between the two species is desired [85].

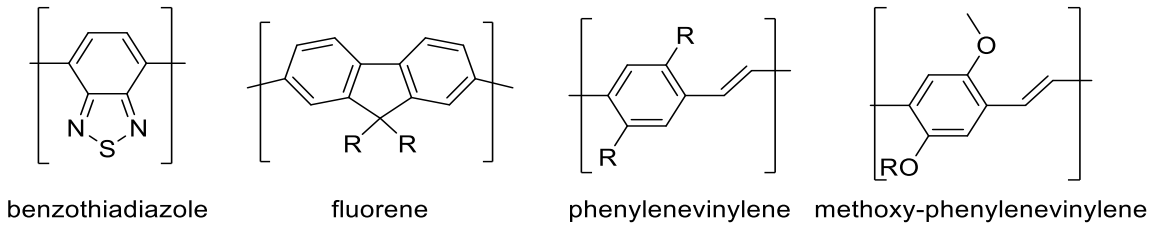

Figure 1.3 Chemical structures of common monomer units incorporated into SPs

Custom synthesized SPs are also used in Pdot synthesis as they offer more flexibility in design. 'In-house' synthesized SPs may be designed to tune optical properties, confer specific functionalities, or integrate conjugation chemistries without the use of a non-fluorescent additive. Additional chromophores such as porphyrins may be directly added to the polymer backbone to change the observed emission colour due to energy transfer [86]. Emission colour, Stokes shift, and even photoblinking behaviour can be tuned by selection of co-monomers and their ratios (*e.g.*, fluorene and benzothiadiazole as in F8BT) [50, 87-88]. Fluorine-substitution of a benzothiadiazole-based polymer was shown to improve the quantum yield and emission brightness of the resultant Pdots, but also changed their morphology [89]. Monomers responsive to an analyte of interest can be incorporated directly into the SP backbone for sensing applications [30, 90-91]. Reactive functionalities (*e.g.*, carboxylic acids [92-94], azides for click reactions [95]) can be installed directly on the SP backbone to facilitate conjugation, or amphiphilic SPs can be used to form Pdots directly [96]. Functionalized π-conjugated oligomers have also been shown to form emissive NPs [97]. Photocrosslinkable functionalities may be added to the polymer backbone to improve Pdot stability or confer desired nanoscale structure [98-99]. However, use of custom designed SPs requires expertise in organic synthesis and is therefore not accessible to many

researchers. Synthesis of SPs usually requires an expensive and air-sensitive palladium catalyst. An alternate route to custom polymers is the chemical modification of commercial SPs to confer desired properties, such as the additional of a radical scavenger to prevent photobleaching [72].

1.2.3.2 Non-fluorescent polymers and surface chemistries

Although Pdots can be made without amphiphiles or other additives [24, 30, 76, 82], such materials are often poorly stable, prone to non-specific binding to the hydrophobic Pdot surface, and are of limited use in bioanalytical applications due to the lack of surface functional groups available for conjugation. The most common solution to these problems is the co-precipitation of an amphiphilic polymer during Pdot synthesis. These additives may be classified as ionizable (*i.e.,* charged) or neutral. Two ionizable amphiphiles are commonly used for Pdot synthesis. Poly(styrene-co-maleic anhydride) (PSMA) is a random co-polymer containing hydrophobic styrene residues and hydrolyzable anhydride residues that produce carboxylate groups when introduced to water. PSMA is often used in Pdots [32-33, 61, 69-71, 73, 75, 77-81, 88]. Polystyrene-graft-polyethylene glycol end functionalized with carboxy (PSPEGCOOH) is another common amphiphile for Pdot synthesis because of its unique structure [28, 59, 68, 72, 83-86, 89, 92]. PSPEGCOOH is a graft co-polymer containing a hydrophobic styrene backbone, grafted with hydrophilic carboxy-end functionalized PEG. The hydrophobic nature of the styrene block promotes precipitation with the SP in the Pdot core, while the hydrophilic PEG groups remain on the surface and prevent non-specific binding. Each PEG chain is end-functionalized with a carboxylate group, providing additional steric and electrostatic stabilization and a chemical handle for conjugation chemistry. Small molecule surfactant such as SDS and nonionic surfactants such as PEG and triblock PEG-containing polymers have also been used in Pdot synthesis [56, 67, 100], although some evidence

suggests that nonionic surfactants are easily displaced from the SPN surface by other species such as serum proteins [101].

Other strategies for altering the surface chemistry of Pdots have been reported but not widely explored, such as silica shelling [102-104]. In a similar fashion to dye-doped nanoparticles, individual Pdots have been encapsulated in a silica matrix [105]. Pdots have also been used to seed the formation of a non-emissive polymer shell [106].

1.2.3.3 Dopants

A unique property of Pdots compared to other luminescent nanomaterials is their soft structure and permeable cores. Pdots and SPNs can serve as a host matrix for hydrophobic species and have been demonstrated to release cargo under certain conditions. Modified doxorubicin was shown to release from Pdots in cell nuclei via the acid-catalyzed cleavage of hydrazone bonds [107]. Most frequently, optically active species are non-specifically doped into the Pdot core that may participate in energy transfer. Pdots are excellent energy donors because they absorb excitation light efficiently. Doped acceptors are suitably close by to receive energy at high efficiencies, significantly quenching Pdot emission. This strategy has been used to narrow and red-shift Pdot emission [63], or to load photosensitizers for other applications such as photothermal therapy [79, 108]. Analyte sensitive dyes may be non-specifically doped into the Pdot core for sensing applications [75]. Examples of optically active dopants include singlet oxygen sensitizers enabling afterglow emission (*i.e.*, long lived emission after the cessation of excitation) [100], photoswitchable energy acceptors enabling controllable on/off Pdot emission [68], and

luminescent europium complexes enabling high excitation efficiency with long luminescence lifetimes [83].

1.2.4 Physical properties

Although Pdots may be composed of a variety of emissive and non-emissive materials, they typically share some commonalities in terms of their physical properties. Table 1.3 lists selected physical properties of Pdots and how they compare to QDs and organic dyes.

Table 1.3. Selected physical properties of Pdots, QDs and fluorescent dyes. Adapted from ref. [109].

	Pdots	QDs	Fluorescent dyes
Composition	π-conjugated polymers	Inorganic semiconducting nanocrystal	Small organic molecule
Doping[a]	Molecules, other NPs	Ions	-
Surface passivation	-	Inorganic shell(s)	-
Diameter[b]	5-100 nm	4-10 nm (core/shell)	~1 nm
Size polydispersity	Moderate to high	Low	-
Aqueous dispersion[c]	Amphiphilic polymers, direct functionalization of polymer	Ligands, amphiphiles	-

[a] Discrete entities within the NP
[b] Geometric diameter of species (core/shell diameter for QDs), exclusive of surface functionalization
[c] Methods for stabilization in aqueous environments

1.2.4.1 Structure

Pdots are composed of soft, weakly bound materials, and therefore have a poorly defined structure. Some evidence suggests that the constituent polymer chains adopt a disordered glassy phase when Pdots are suspended in water [110]. Pdots are assumed to be spherical in water due to entropic

effects (*i.e.*, exclusion of water molecules from the hydrophobic core) and enthalpic effects (*e.g.*, hydrophobic interactions, pi-pi stacking). Surface tension between the hydrophobic core and surrounding aqueous environment may also play a role in the spherical particle morphology. It is not possible to directly ascertain the particle geometry in solution, so measurements of morphology are usually performed on samples dried on a substrate, which is not truly indicative of the aqueous structure when the particles are surrounded by and partially swollen with water. Nevertheless, transmission electron microscopy (TEM) and atomic force microscopy (AFM) images show Pdots to be spherical or quasi-spherical with sub-100 nm diameters.

Unlike metallic or crystalline NPs, Pdots are porous and permeable to other species, which may partition into the Pdot core without disrupting the molecular-level structure. Permeability may be advantageous, for example, in allowing access of analytes to the Pdot core, or may be disadvantageous, for example in allowing dissolved oxygen or other quenchers to access chromophores located in the core.

Pdots synthesized with an amphiphile are thought to adopt a core/shell-like structure, where the hydrophobic SP and the hydrophobic segment of the amphiphile condense into the core and the amphiphilic segment of the amphiphile forms a shell around this core. This core/shell structure has not been definitively shown, and the coverage of the SP by the amphiphile, the thickness of the shell, and the degree of intermixing between the SP and the amphiphile are not known. The hydrophilic portion of the amphiphile determines the surface chemistry of the Pdot. Pdots are typically synthesized with negatively charged or neutral amphiphiles. Many amphiphiles contain reactive functionalities like carboxylic acids that can be used for conjugation reactions. The

identity of the amphiphile also determines the surface charge and therefore the zeta potential of the particles, which has been shown to have little dependence on the particle size [61]. Although evidence suggests that, on average, charged groups are on the Pdot surface (*e.g.*, zeta potential measurements, gel electrophoresis), some of these groups may also be located within the particle core, particularly with a random copolymer such as PSMA.

Single chain Pdots have been reported [23, 111-112], but typically Pdots are estimated to have between 10-1000 polymer chains per particle, depending upon the molecular weight of the polymer (where polymers of lower molecular weight will yield more chains per particle), the size of the Pdots (the number of chains should roughly scale with the cube of the particle radius), and the density of chain packing in their core. McNeill and co-workers have estimated a 20-30 nm Pdot contains 100-200 chains of F8BT (M_W ~10 kDa) [113]. Pdots composed of MEHPPV having a higher molecular weight (~200 kDa) of ~20 nm diameter were estimated to have 10-20 molecules per particle [74]. It is non-trivial to estimate the number of chains per Pdot as the polymer density and nature of chain packing in the core are unknown. It is possible to estimate the number of chains per particle assuming that all the polymer added is incorporated into nanoparticles during synthesis, but usually some proportion of materials form large aggregates or precipitate out of solution, limiting the accuracy of such estimates.

Another potential complication in characterization of the Pdot structure, although not yet addressed in the literature, is the possibility of a dynamic structure, where for example individual Pdots may collide or break apart, exchange material with other Pdots, or form large aggregates over time. The effects of such processes would be difficult to observe on an ensemble level but may impact the

downstream use of Pdots. Liposomal systems are known to undergo fission, fusion, and the dynamic exchange of materials, which may occur analogously with Pdots [114].

1.2.4.2 Size and size distributions

Pdots and SPNs have been synthesized over a wide size range, from < 10 nm to 100s of nm or microns. To be considered a Pdot, SPNs must have an average diameter less than 100 nm, although NPs above this size cut-off retain many of the same physical and optical properties. Pdot size is influenced by a number of factors including the structural rigidity of the SP, the precursor concentration used in synthesis, and the relative volumes of the organic and aqueous phases during nanoprecipitation [24, 61, 74]. Hydrodynamic sizes are usually determined by dynamic light scattering (DLS) and dehydrated particle sizes are determined by TEM and AFM.

Pdots made by nanoprecipitation typically have broad size distributions (standard deviations) ranging from 15–30 nm, although some groups have reported much narrower distributions (< 5 nm) for some materials [24]. Broad size distributions likely arise from the polydispersity of the starting materials and the poor control observed with nanoprecipitation. Size distributions are best described by a lognormal function, because there are significant contributions above the average diameter from larger aggregates.

1.2.5 Optical properties

The optical properties of a Pdot are largely conferred by its constituent SP. Unlike QDs, the optical properties are not directly dependent on particle size but instead are influenced by the arrangement and packing of the SP chains in the particle core, which are somewhat related to particle size,

among other factors such as backbone rigidity [24, 61]. Changes in the optical properties due to particle size or chain packing are often subtle and obscured by the wide size distributions across an ensemble of particles. Selected optical properties of Pdots, QDs, and dyes are listed in Table 1.4.

Table 1.4. Selected optical properties of Pdots, QDs and fluorescent dyes. Adapted from ref. [109].

	Pdots	QDs	Fluorescent dyes
Electronic transition[a]	π-π*	VB-CB	π-π*, nb-π*
Number of chromophore units[b]	10^2-10^5	1	1
Absorption coefficient[c]	10^7-10^8 $M^{-1}cm^{-1}$	10^5-10^7 $M^{-1}cm^{-1}$	10^4-10^5 $M^{-1}cm^{-1}$
Absorption FWHM	50-200 nm	150-300 nm	30-80 nm
Two-photon cross-section[c]	10^3-10^7 GM	10^3-10^4 GM	10^1-10^2 GM
Quantum yield	0.1-0.6	0.1-0.9	0.05-0.9
Emission lifetime[d]	100 ps to 1 ns	10-50 ns	1-10 ns
Emission FWHM[e]	50-100 nm	25-40 nm	30-80 nm
Blinking[f]	Size dependent	Typical	Some
Number of photons emitted[g]	10^8-10^9	10^7-10^8	10^4-10^6

[a] Electronic transition associated with photon absorption and emission
[b] Number of chromophore units per NP or molecule
[c] Values increase with NP size
[d] Pdots and QDs often have multiexponential lifetimes whereas dyes have single exponential lifetimes
[e] Pdots and dyes have asymmetric red-tailed emission that is under-represented by the FWHM
[f] Only small Pdots (<10 nm diameter) exhibit emission blinking
[g] Total number of photons emitted by a single NP or molecule before irreversible photobleaching

1.2.5.1 Absorbance

Pdots typically have very broad absorption bands, ranging from the UV into the visible and usually containing multiple electronic transitions. The particle size has a negligible effect on the peak shape, but larger particles, containing more chromophores, have larger absorption cross sections. For example, the peak absorption cross section of 15 nm Pdots was reported to be ~10^{-13} cm^2,

orders of magnitude greater than QDs or organic dyes [24]. Many groups do not report absorption cross sections or molar extinction coefficients for Pdots because of the difficulty and significant uncertainty involved in determining their concentrations, but estimated molar extinction coefficients range from 10^7-10^9 $M^{-1}cm^{-1}$ depending on the nature of the material [109].

An unaggregated polymer chain dissolved in a good solvent primarily exists in a straight or open conformation, although it will still experience some amount of bending or kinking along its backbone where π-conjugation is broken due to poor orbital overlap. Polymer segments bounded by these conformational changes act as linked but independent chromophores having different extents of π-conjugation. As approximated by the 1D particle in a box model, longer segments will have lower π-π* energy gaps. As the solvent quality decreases (*i.e.*, polarity increases), the polymer chain will begin to coil on itself or form chain-chain aggregates. The formation of coils decreases the effective conjugation length, increasing the energy of the π-π* energy gap and blue-shifting the absorption spectrum. The absorption spectrum of the resultant Pdot is the superposition of absorption from the individual segments having different effective conjugation lengths. Resultingly, Pdot absorption bands are typically broad (> 50 FWHM) [61].

Pdots are promising materials for use in multiphoton spectroscopy. Conventional fluorophores have two photon absorption (2PA) cross sections less than 100 GM [115]. Pdots have high two- and three-photon absorption cross sections, allowing for excitation in the NIR-I (700-950 nm) or NIR-II (1000-1700 nm) transparency windows. Pdots approximately 20 nm in diameter having varying composition were reported to have 2PA absorption cross sections between 10^4-10^5 GM [74]. Pdots containing two types of SPs were reported to have 2PA cross sections of 10^6 GM [116].

2PA applications have been reported using Pdots, where NIR excitation and emission overcomes some limitations of traditional fluorescence imaging. The high tissue penetration of NIR light has allowed Pdots to find use as 2PA fluorescence probes for in vivo imaging of vasculature in mice brains [117]. More recently, NIR-I emitting Pdots with a 2PA cross section of *ca.* 10^3 GM were used to image brain vasculature through the skulls of living mice [35].

1.2.5.2 Steady state emission

Pdot fluorescence arises solely from the constituent semiconducting polymer. SPs are inherently emissive due to their molecular structure (see section 1.2.3.1). SPs feature extended π-conjugation along their backbones, and as a result a large number of molecular orbitals with similar energies exist forming band-like electronic structures, giving rise to their semiconducting character. SP and Pdot emission arise from π-π* transitions from the LUMO (*i.e.*, bottom of the conduction band) to the HOMO (*i.e.*, top of the valence band). The emission colour of the Pdot solely depends on the identity of the SP and unlike QDs is not directly dependent on the particle size (*i.e.*, not quantum confinement).

When SP chains collapse into a Pdot, many competing photophysical processes occur simultaneously, namely electronic energy transfer from high to low energy states, triplet-triplet annihilation, exciton quenching by triplets, and singlet exciton quenching polarons [66]. Emission typically redshifts compared to the unaggregated polymer in solution because of increased interchain interactions. Some fraction of the chromophores within the Pdot form aggregate species of lower energy. Chromophores of relatively high π-π* gaps may absorb simultaneously within the Pdot, but, due to the tight chain packing and short donor-acceptor distances, efficient energy

transfer occurs driving energy towards the lower energy aggregate chromophores. This energy transfer process is very rapid and emission only occurs from the low energy states, of which there are 1-3 per polymer chain [24].

Unmodified Pdots typically have broad, asymmetric emission peaks (FWHM 50-100 nm), arising from the range of effective conjugation lengths of the chromophores, the differing local environments of the chromophores (*i.e.,* in the hydrophobic core or contacting polar water molecules at the surface) and rapid energy transfer processes to low energy states [26]. The peak width may be a disadvantage for applications requiring spectral purity such as multiplexing, but various strategies have been deployed to narrow the emission band, usually doping in a sufficiently high number of organic dyes to act as energy acceptors and cause near complete quenching of the SP [118].

1.2.5.3 Time-resolved emission

The excited state dynamics of SPs and Pdots are complex as a large number of photophysical processes may occur simultaneously [119]. Fluorescence lifetimes of SPs are typically studied using thin films for applications in organic electronics, which are seen to have short (< 5 ns) lifetimes whose values are dependent upon the phase of the polymer and interactions with neighbouring species (*e.g.,* energy transfer decreasing measured lifetimes) [120-121]. Solution-phase SPs also typically have fluorescence lifetimes on the order of a few nanoseconds [122]. Pdots typically display short fluorescence lifetimes (< 1 ns) [24, 123]. Some high-speed applications benefit from such a fast radiative rate such as flow cytometry, high-speed imaging and single particle tracking [26].

1.2.5.4 Quantum yield and per particle brightness

The quantum yield of Pdots can vary dramatically depending upon the identity of the SP or simply from batch-to-batch variation. Typical Pdot quantum yields range from a few to 40% [24]. Pdots containing multiple types of SPs have been reported to have quantum yields up to 57% [117]. There are conflicting reports on the relationship between particle size and quantum yield. Some groups have reported that there is little effect of particle size on quantum yield [59], while other studies have shown that smaller Pdots have higher quantum yields owing to the higher efficiency of energy transfer to various quenchers in larger particles [24].

The brightness of a fluorophore is usually quantified as the product of its quantum yield and molar extinction coefficient at the excitation wavelength, Eqn. 1.1, where B is the brightness, Φ is the quantum yield and ε is the molar extinction coefficient.

$$B \propto \Phi\varepsilon \tag{1.1}$$

As a multichromophoric system, Pdots have very high per-particle brightness, orders of magnitude brighter than QDs, which are themselves heralded as an ultrabright fluorophore and are orders of magnitude brighter than organic dyes [124]. For example, F8BT/PSPEGCOOH Pdots were reported to be 30 times brighter than QDs (Qdot 565 from Invitrogen) or the molecular dye Alexa 488 when excited at 488 nm [59]. Pdot brightness scales with particle size, as larger particles contain more chromophores and active fluorophores (*i.e.,* low energy emissive states).

Sun *et al.* performed a systematic study of the effect of Pdot size and brightness using single particle fluorescence imaging [61]. CNMEHPPV/PSMA Pdots were synthesized having average

diameters of 16 nm, 33 nm and 59 nm. The quantum yields of all batches were comparable (between 40-50%), indicating that any changes in particle brightness must arise from changes in the molar extinction coefficient or absorption cross section. The volume of a spherical particle, or in the case of a Pdot the number of chromophores per particle, scales with the cube of its radius and therefore particle brightness was also expected to have a cubic dependence on particle diameter. However, a quadratic dependence between particle diameter and brightness was observed. Although the authors suggest several experimental rationales that may account for this deviation, changes in the photophysical behaviour of Pdots as a function of size likely affect the efficiency of absorption and the observed fluorescence brightness.

1.2.5.5 Photostability

Pdots are typically reported to have excellent photostability and have been reported to emit between 10^6 and 10^9 photons before irreversibly photobleaching (*i.e.,* the death number), corresponding to a photobleaching quantum yield of 10^{-10} to 10^{-8} [24, 74]. They typically do not photobleach over short times (at low excitation power) and their resistance to photobleaching is better than organic dyes and comparable to QDs [56, 67, 124].

Efforts have been made to characterize the photobleaching behaviour of Pdots. At sufficiently low excitation powers, organic dyes exhibit monoexponential photobleaching kinetics. SPs and Pdots exhibit much more complex behaviour due to interactions between a large number of species within and around the polymer(s) including excitons, polarons, molecular oxygen, and partially oxidized polymeric species whose structures are unknown [76]. Photobleaching of Pdots has been hypothesized to occur largely by photoinduced radicals that may be quenched by radical

scavengers (*e.g.*, HEPES and MES buffer) to reduce photobleaching [72]. In some cases, observed emission can increase upon prolonged photoexcitation, for example, if emissive species are formed from the oxidation of the SP backbone [76].

1.2.5.6 Fluorescence intermittency (blinking)

Fluorescence intermittency or blinking refers to the phenomenon of a fluorophore switching between an 'on' (emissive) and 'off' (non-emissive) state under continuous excitation. Blinking is a commonly observed phenomenon in single particle measurements of QDs, where typical blinking time scales range from milliseconds to seconds [125].

Large Pdots (> 10 nm diameters) do not exhibit blinking, but smaller Pdots sometimes do [59, 74]. Smaller (and dimmer) Pdots contain fewer chromophore units. On/off dynamics occurring within a single Pdot cause fluctuations in the number of fluorophores that are in the on state versus the off state. When the number of chromophores is sufficiently high, there is always an appreciable fraction of fluorophores in the on (emissive) state leading to constant fluorescence. Single chain NPs may blink when single photooxidation events generate polarons (positive charges) that quench excitons within a radius larger than the radius of the NP [66]. Tuneable blinking has been demonstrated with Pdots, where the ratio of the donor and acceptor monomers of the SP is varied to change the proportion of time a single Pdot spends in the on or off state, which is desirable for some super-resolution imaging techniques [88].

1.2.6 Biocompatibility

The physical and chemical properties of a nanoparticle, specifically its size, shape and surface chemistry, largely determine its biocompatibility [126]. Biocompatibility is generally defined as "the quality of not having toxic or injurious effects on biological systems" or more specifically "the ability of a material to perform with an appropriate host response in a specific application" [127]. Pdots are typically considered to be one of the most biocompatible fluorescent nanomaterials because of their benign chemical composition. Pdots are usually composed of only organic materials and contain no metals or metalloids that may induce toxicity (unless such materials are doped into the Pdot core to achieve a specific function). This is a key advantage over heavy metal-containing QDs which may have deleterious effects if poorly passivated (*i.e.,* if heavy metal atoms leach from the core). Being brighter, lower concentrations of Pdots are required to achieve similar signal levels as QDs, further decreasing the likelihood of negative effects on the biological matrix [128].

For *in vitro* experiments, biocompatibility is considered in terms of cytotoxicity, defined as the "effect or range of effects, microscopic and/or visual ranging from impairment in growth to complete cell lysis or dissolution, caused by the presence of test materials, in cultures, relative to control cultures" [127]. Such effects include "decreased plating efficiency, lysis, inhibition of macro-molecular synthesis and cell growth, and detachment of cells from the substrate" [127]. Pdots have been observed to be taken up into cells non-specifically by an endocytic mechanism [24, 67, 82], although the specific endocytic mechanism and the kinetics of uptake depend on the cell line under study [129]. Numerous studies have shown that Pdots of varying compositions have no measurable cytotoxic effects on a variety of cell lines [33, 67, 82, 128], and in some cases Pdots

induce cell proliferation [73]. However, surface chemistry is an important factor for determining cytotoxicity. For example, SDS is known to cause damage to the cell membrane, so SDS-coated SPNs may be toxic, particularly in the presence of excess SDS (*i.e.*, inefficient purification) [67]. Conversely, PEG-capped SPNs were shown to cause no damage to the cell membrane upon 2 h incubation [56].

Biocompatibility of Pdots or SPNs may be further increased by custom design of constituent SPs to make them metabolizable *in vivo*. SPs containing vinyl bonds that may be enzymatically cleaved or oxidized were used to synthesize SPNs for photoacoustic imaging and photothermal therapy. These materials were used to perform *in vivo* imaging in a mouse model, and resulting metabolites were small (~1 nm) and were cleared from the body by the hepatobiliary and renal systems [130-131].

1.2.7 Applications of Pdots

Although Pdots are still in their infancy, many bioanalytical applications have been reported using Pdots. Their unique physical structure and other characteristics are favourable for a variety of applications in chemical and biochemical sensing and *in vitro* and *in vivo* imaging. Pdots have become increasingly popular materials for photodynamic and photothermal therapy due to their efficient absorption of excitation light and the relative ease of doping in energy acceptors.

1.2.7.1 Sensing

Fluorescence sensors using Pdots have been developed for a wide range of biologically relevant analytes. Pdots may be used as a fluorescent label, for example, in a sandwich style immunoassay

[60] or a multiplexed lateral flow assay [132]. Binding of surface carboxylate groups of F8BT/PSMA Pdots to Cu(II) or Fe(II) ions was used to design an aggregation-induced quenching assay [77]. When deposited onto an electrode, Pdots have been used as an electrochemiluminescent probe for amino acids [79], protein biomarkers for disease [80], microRNA [81] and metal ions [133]. Pdots have also been paired with other fluorophores, such as luminescent lanthanide complexes, for ratiometric fluorescence sensing [71].

1.2.7.1.1 Energy transfer-based sensing

Pdots are promising materials as energy donors in energy transfer-based sensing applications. They efficiently absorb excitation light and transfer that energy with high efficiency to nearby acceptors either within the Pdot core or at the Pdot surface. Hydrophobic dyes are often non-specifically doped into Pdots to facilitate energy transfer and redshift the emission signal. Porphyrin-doped Pdots have been used as sensors for oxygen with both conventional and smartphone camera detection for point-of-care diagnostics [75, 108]. Target-sensitive and target-insensitive fluorophores may be jointly included in the SP backbone for ET sensing, for example of reactive oxygen species (ROS) *in vitro* and *in vivo* [90]. Pdots have also been incorporated into sensors as the energy acceptor, for example, in a thermochemiluminescent sensor system with enhanced fluorescence brightness [60].

Pdots may also be paired with non-emissive quenchers such as gold nanoparticles to facilitate 'turn-on' sensing where upon binding of a target, the linkage between the Pdot and the quencher is broken, preventing energy transfer and restoring emission from the Pdot [69]. A positive readout lateral flow assay for a small molecule analyte was also reported combining Pdot and AuNPs for

generating the analytical signal [134]. Similarly, Pdots were conjugated to a metal organic framework quencher by a peptide offering turn-on fluorescence sensing of enzymatic cleavage [70].

ET-based sensors are often advantageous in that the analytical signal can be taken as a ratio of the donor and acceptor emission, minimizing effects of the local environment or fluctuations of the excitation beam or detection method. Rhodamine B, an inherently temperature sensitive dye, was end functionalized onto hydrophobic polystyrene for doping into Pdots and was used for ratiometric temperature sensing [31]. Pdots may also be paired with sensitizers known to participate in photoinduced electron transfer (PET). Liao *et al.* reported an *in vivo* NO^{2-} sensor using a Pdot where Rhodamine B was incorporated into the SP backbone. Bonding of the analyte to the polymer prevented PET from occurring between the modulator polymer segment and Rhodamine B, the transducer element [91].

1.2.7.2 Imaging

1.2.7.2.1 *In vitro*

Pdots make a near-ideal fluorescence imaging probe due to their brightness and high absorption cross section, allowing efficient absorption of excitation light and therefore bright emission at low incident power. Pdots were first used for *in vitro* imaging in 2008, where Pdots of different emission colours (*i.e.*, composed of different SPs) were used to non-specifically label cells [24]. Non-specific cellular labelling has since been demonstrated by a number of research groups [56, 67, 89], and some specific immunolabeling applications have also been reported [59, 61]. Pdots

have also been used as labels for flow cytometry [59, 89]. Analyte-sensitive Pdots have also been used for imaging, for example oxygen-sensitive Pdots were used for hypoxia imaging [135].

The energy transfer capabilities of Pdots have also been used in imaging applications. Europium-grafted Pdots have been used for live cell imaging leveraging the efficient absorption of Pdots with the long-lived emission from luminescent lanthanide complexes to achieve time-gated imaging [33, 83]. Photoswitchable molecular quenchers have also been incorporated into the Pdot to allow for selective cellular imaging dubbed 'optical painting' [68], flow cytometry applications, and the specific labelling of sub-cellular structures [94].

Owing to their extreme brightness, Pdots have also found use in super-resolution imaging techniques such as super-resolution optical fluctuation imaging (SOFI) [88, 136], and stimulated emission depletion (STED) microscopy [137]. 2D and 3D single particle tracking has also been demonstrated with F8BT Pdots, where their fast emission rates (10^9 photons per second) resulted in good (*i.e.*, less than 2 nm) lateral and spatial resolution [138].

1.2.7.2.2 *In vivo*

Pdots have found use in a wide variety of *in vivo* imaging applications. For these applications, emission (and excitation) in the NIR region of the spectrum is favoured as tissue is typically transparent at these wavelengths, reducing the effects of autofluorescence and scattering from the sample. Pdot emission is easily tuned to the red or NIR via the use of doped dyes (*e.g.*, porphyrins) or by utilizing blends of multiple SPs.

Pdots have been used for the specific and non-specific imaging of tumors in mouse models. Via carbodiimide chemistry, tumor targeting peptides such as chlorotoxin can be conjugated to the Pdot surface to enable specific imaging [124]. NIR-emitting self-luminescing Pdot probes were reported by Xiong *et al.*, where an energy cascade involving both bioluminescence resonance energy transfer and FRET enabled *in vivo* imaging of lymph nodes and tumors in a mouse model without external excitation [139]. Miao *et al.* designed NIR-emitting Pdot probes capable of super-bright 'afterglow' emission where emission continues after the cessation of excitation to eliminate interference from autofluorescence. These probes were used to non-specifically image both lymph nodes and tumors in a mouse model [100].

Pdots have also been developed for the detection of analytes *in vivo*. By incorporation of an oxygen sensitive porphyrin into the SP backbone, oxygen sensitive Pdots were prepared and used to detect hypoxia (low oxygen concentrations) *in vitro* and *in vivo* [135]. Oxygen-sensitive Pdots containing long-lifetime phosphorescent dyes were conjugated to glucose oxidase for *in vivo* monitoring of euglycemia (normal blood glucose levels) and hyperglycemia (high blood glucose levels) in live mice. The consumption of glucose by glucose oxidase consumed oxygen, restoring emission from the dye and changing the emission colour of the sensor. The Pdot-enzyme complex was implanted into live mice and used to monitor blood glucose levels, and was sufficiently bright to enable detection via a smartphone camera in lieu of traditional fluorescence instrumentation [75].

More recently, Pdots have been developed for multiphoton fluorescence applications. Pdots, having 2PA cross sections orders of magnitude higher than other fluorophores, are well suited for 2PA and multiphoton bioimaging. Of particular interest are fluorescent probes that can both absorb

and emit in the NIR region of optical transparency. Both two- and three-photon fluorescence techniques have been demonstrated using NIR-emitting Pdots with varying composition for the imaging of vasculature and tumors in mouse models [140-141].

1.2.7.3 Photothermal and photodynamic therapy

Due to their highly efficient absorption of excitation light and the ease of doping energy acceptors into their cores, Pdots have become popular sensitizers for photothermal therapy (PTT) and photodynamic therapy (PDT) [49]. In PTT, incident light energy is transformed by a sensitizer into heat to treat certain medical conditions such as cancer. In PDT, light energy is absorbed by a photosensitizer that acts to produce cytotoxic singlet oxygen or other reactive oxygen species. Both methods are favoured for being non-invasive and localized only to the area of irradiation (*i.e.*, minimal toxicity to healthy tissue). When used with Pdots these methods are often paired with photoacoustic imaging (PAI), a technique where optical excitation of a probe leads to heating and thermal expansion, causing the probe to emit ultrasonic waves that can be detected by ultrasonic transducers to produce images. PAI is sometimes favoured over fluorescence as it has deep tissue penetration and good spatial resolution.

Photoacoustic imaging with SPNs was first investigated in 2014 where they were doped with ROS-sensitive dyes to achieve ROS sensing and whole body lymph node mapping of mice [142]. PAI was also used to monitor embryonic stem cell-derived cardiomyocytes using SPs encapsulated in a non-emissive matrix [143].

In vitro PDT was first demonstrated with Pdots in 2014 [144]. Energy transfer from the fluorene units to phosphorescent iridium units both in the polymer backbone produced singlet oxygen for PDT. Some semiconducting polymers are inherently photothermal (*i.e.*, convert light to heat) and have been used to synthesize photothermally active Pdots without the need for a secondary sensitizer. NPs containing a photothermally active SP encapsulated in a non-emissive polymer matrix were seen to ablate tumor cells by PTT in 2015 [145]. *In vitro* and *in vivo* PTT with Pdots was first reported in 2016, where Pdots demonstrated high (65%) photothermal conversion efficiency [32]. Similar systems were used to achieve concurrent PTT and photoacoustic imaging with maximum photothermal conversion efficiencies above 40% and 50% respectively [84, 146]. Biodegradable PTT and PAI active SPNs were reported in 2018 [130] and enzyme-cleavable SPNs soon followed in 2019 [131].

Multimodal PTT and PDT has also been reported with Pdots. Jiang *et al.* designed Pdots with inherent PTT and PDT activity, with 40% photothermal conversion efficiency and 3% photodynamic conversion efficiency. A therapeutic agent was coupled to the particle surface via a linker that was cleaved by singlet oxygen. Upon irradiation, singlet oxygen was produced by the Pdot core and the therapeutic agent was released, improving its delivery to the tumor site [95]. PTT, PAI and nitric oxide therapy have similarly been combined using an SPN platform [147].

1.2.7.4 Multimodal Pdots

Pdots may be combined with species of other functionalities to create fluorescent multimodal materials for a variety of applications, beyond combinations of PTT, PDT and PAI.

Pdot nanocomposites have been reported where a distinct inorganic nanoparticle is doped into the Pdot core. Magnetic iron oxide NP-doped Pdots may be used for concomitant cellular separation and fluorescence imaging, or gold NP-doped Pdots may be used to provide contrast in brightfield and fluorescence imaging using a single probe [148]. Pdot-coated gold nanorods have been reported for dual-modal colourimetric and plasmon-enhanced fluorescence readout of a lateral flow assay for PSA as a model analyte [149]. SPs have also been used to form Janus structures embedded with magnetic iron oxide NPs used for magnetic particle imaging, magnetic resonance imaging, photoacoustic imaging and fluorescence imaging *in vivo* [150]. Gold NP-doped Pdots have also been reported for concomitant *in vivo* X-ray computed tomography and fluorescence imaging [85]. Lanthanide-coordinated Pdots were reported to provide signals for both flow cytometry (*i.e.,* fluorescence-labeling) and mass cytometry [92]. QDs have been doped into the Pdot core via covalent conjugation to the SP backbone to combine the desirable optical properties of both species [151]. Pdots may be localized along with therapeutic agents such as doxorubicin in the hydrophobic cores of micelles or liposomes for theranostic applications [152-153].

1.2.8 Bioconjugation strategies

Many bioanalytical applications of fluorescence require the fluorophore to be specifically conjugated to the analyte of interest or another species to enable specific targeting (*e.g.,* streptavidin, specific antibodies, *etc.*). The fluorophore therefore must contain reactive functional groups to enable the formation of covalent bonds between itself and the desired target. The ideal conjugation reaction is highly efficient, specific and selective, both chemically and with regards to the site of conjugation. Non-covalent conjugation may be achieved via non-specific binding (*i.e.,* adsorption), but this strategy is disfavoured as it offers limited control.

1.2.8.1 Carbodiimide crosslinking

Carbodiimide crosslinking involves the reaction between a carboxylic acid group and a primary amine, forming a stable amide bond. This reaction is extremely common due to its ease, rapidity, and the ubiquity of carboxylic acid and amine groups in biological species. The following section describes the mechanism of carbodiimide crosslinking, possible side reactions, and its use for bioconjugation to the Pdot surface.

1.2.8.1.1 Mechanism and side reactions

Carbodiimides directly couple an amine and a carboxylic acid without the insertion of other atoms. The most common water soluble carbodiimide reagent is 1-ethyl-3-(3 dimethylaminopropyl) carbodiimide hydrochloride (EDC). EDC reacts with carboxylic acids to form an *O*-acylisourea intermediate that is highly reactive towards nucleophiles such as primary amines (Scheme 1.1). Reaction with a primary amine forms the desired product by way of amide bond formation [154].

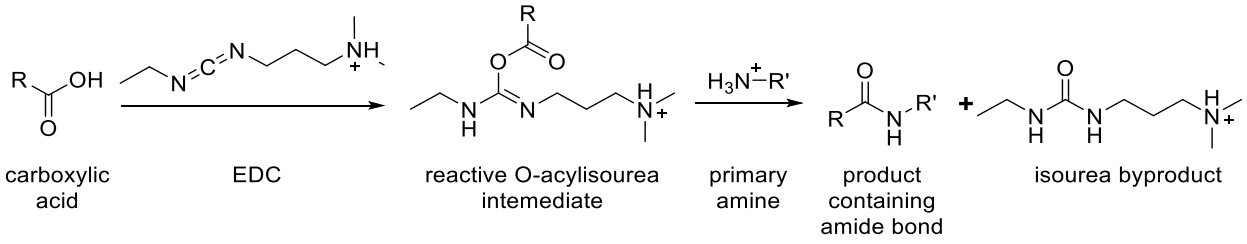

Scheme 1.1 EDC mediated reaction of a carboxylic acid with a primary amine.

However, several side reactions are possible that do not result in the desired bond formation. EDC may hydrolyze and form a non-reactive isourea side product, either directly or by first forming the reactive O-acylisorea intermediate (Scheme 1.2). A non-reactive N-acylisourea derivative may also be formed between two neighbouring EDC molecules. For species containing both an amine and carboxylic acid functionality, self-polymerization may also occur [154].

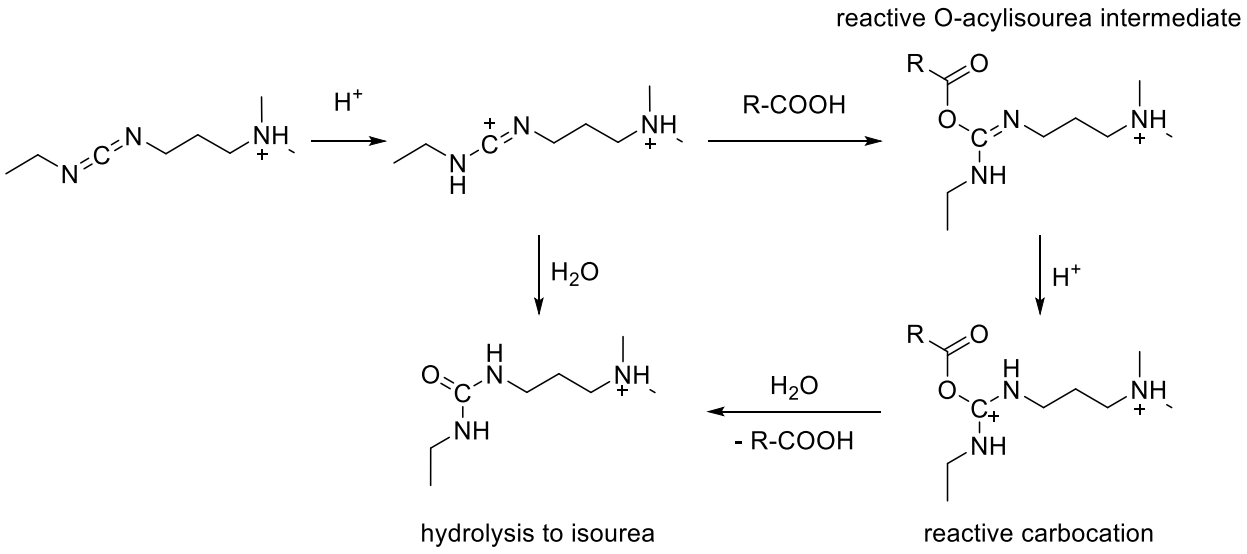

Scheme 1.2 Hydrolysis of EDC to the isourea byproduct.

Although carbodiimide crosslinking is ubiquitous, the use of this reaction has several key drawbacks. The reaction suffers from a lack of selectivity and site specificity. EDC will link any carboxylic acid to any primary amine, both of which are common functionalities in biomolecules.

The lack of specificity is especially problematic when carbodiimide crosslinking is used with proteins which contain many amine and carboxylate groups. Conjugation may occur within the active site, or conjugation to a large body such as a nanoparticle may block the active site. The reaction also suffers from poor efficiency. Even using optimized reaction conditions, it is difficult to control the extent of the reaction and only a subset of available groups will participate in the reaction.

1.2.8.1.2 Carbodiimide crosslinking with Pdots

Pdots are commonly synthesized to have surface carboxylate groups, suitable for carbodiimide crosslinking with primary amines. Carbodiimide crosslinking is the dominant method for Pdot conjugation. Most commonly, EDC is used to couple streptavidin to the Pdot surface to enable further conjugation to biotin-labelled species such as antibodies for cellular labelling [28, 60-61, 68, 83, 89, 92, 94]. Antibodies may also be directly conjugated to the Pdot surface via carbodiimide crosslinking albeit with no of control of orientation [132]. Carbodiimide crosslinking has been used to conjugate other recognition elements to the Pdot surface such as tumor-targeting peptides and DNA, and is generalizable so long as the species contains at least one primary amine [80, 124]. Functional enzymes such as glucose oxidase have also been conjugated to the Pdot surface via EDC coupling [155]. Organic dyes have been conjugated to the Pdot surface by EDC to participate in energy transfer [156].

Carbodiimide crosslinking as also been used to introduce other functional groups to the Pdot surface that are useful for other types of bioconjugation reactions. For example, the Chiu group

coupled small alkyne- and azide-terminated amine molecules to the Pdot surface to facilitate biorthogonal click reactions [78].

1.2.8.2 Other strategies

To date, few alternative bioconjugation strategies have been reported with Pdots. Amphiphilic polymers containing reactive groups other than carboxylic acids have been used to enable new bioconjugation pathways, such as the thiol-containing polystyrene reactive against isothiocyanates and maleimides [157]. Reactive functionalities may be directly added to the backbones of custom-synthesized SPs. In such cases reactive groups are usually appended to the long alkyl substituents of the fluorene monomer to minimize disruptions to the overall electronic structure of the polymers. In the absence of carboxy-containing amphiphile, carboxylic acid may be incorporated into the SP backbone although such a structure still requires carbodiimide crosslinking for bioconjugation [93]. Other reactive groups, such as azides for use in click chemistry reactions, may also be introduced to the SP during synthesis [95]. Silica-coated Pdots have a wider variety of bioconjugate chemistries accessible via the diversity of silanization reagents available for their preparation [102].

1.2.9 Current limitations

Pdots have many of the characteristics of an ideal fluorophore as outlined in Section 1.1.1. They have a broad excitation band, have extremely high per particle brightness, have good aqueous stability over the time course of a typical fluorescence experiment, and contain some surface functional groups for bioconjugation. However, Pdots are highly deficient in some areas and require continued development and optimization. Because of their brightness and apparent

biocompatibility, these materials are extremely promising as a fluorescent probe in a wide variety of applications across not only bioanalysis but also in fields such as organic electronics. For Pdots to go beyond their current niche these limitations must be addressed.

1.2.9.1 Pdot synthesis

Current synthetic methods for Pdots suffer from many limitations. Nanoprecipitation is poorly controlled and poorly reproducible. Although some variables have been identified that affect the particle sizes obtained, the effects of mixing efficiency, injection rate, and the volume of mixing have not been quantified. Consequently, synthetic methods are difficult to reproduce between research groups who are likely using different equipment for synthesis. Studies on the effect of particle size are difficult to perform due to difficulties producing multiple batches of the same size and the broad size distributions obtained. As nanoprecipitation is usually performed manually, it suffers from inherent limitations in scale. Pdot research would greatly benefit from an improved and more precisely defined synthetic method allowing greater control over particle size. Additionally, commercial adoption of Pdots will require synthetic methods more amenable to larger volume scales.

1.2.9.2 Poor aqueous stability

Pdots are typically reported to have good aqueous stability over the time course of several months. However, such statements are rarely supported by quantitative data regarding the particle size, concentration, or fluorescence brightness over time. Although their aqueous stability is suitable for the time course of a typical fluorescence experiment (*i.e.*, hours to days), in our hands Pdots tend to form large aggregates, sometimes visible to the naked eye, or destabilize on longer time

scales. Destabilization (*i.e.*, the loss of colloidal stability) is typically marked by the deposition of fluorescent material on the walls of the storage vessel and is thought to occur from surface-induced unfolding.

Additionally, Pdots display poor stability in acidic, neutral, and basic buffers and solutions of high ionic strength. Most bioanalytical sensing and imaging methodologies must be performed in an environment of controlled pH and thusly poor Pdot stability in such conditions presents a serious limitation. Possible solutions include covalent crosslinking of the Pdot to itself [99, 158] or the engineering of the Pdot surface to enhance stability.

1.2.9.3 Dearth of bioconjugation chemistries

Bioconjugation to the Pdot surface is almost always performed using carbodiimide crosslinking, whose limitations are discussed in Section 1.2.8.1.1. There currently exists a significant dearth of site specific or biorthogonal conjugation chemistries demonstrated with Pdots, arising from the limited number of unique surface chemistries that have been investigated with Pdots. Carbodiimide crosslinking is not optimal for methods where the orientation or number of species on the Pdot surface matters for the downstream applications. For example, the binding site of an antibody may be inaccessible to its antigen if bound in a non-productive orientation or the active site of an enzyme may be blocked if too near the particle surface. It is non-trivial to control the number of energy acceptors bound to the Pdot surface for energy transfer-based sensing applications when they are conjugated via EDC. The investigation of alternative surface chemistries and coatings is necessary to expand the scope of possible conjugation chemistries and improve the utility of Pdots in bioanalysis.

1.2.9.4 Poorly understood photophysics

An individual Pdot comprises hundreds or thousands of closely packed chromophores. The internal structure of Pdots including the chain packing density, crystallinity, and extent of intermixing between the SP and amphiphile is not well known and is difficult to control via current synthetic methods. The photophysical processes within the Pdot core and on the Pdot surface are likely highly dependent on these factors. Additionally, multiple short-lived species such as excitons and polarons are likely involved in Pdot photophysics.

There are many examples of energy transfer-based Pdot sensors in the literature. In most cases, FRET is assumed to be the mechanism of action. There is limited evidence that FRET is the dominant mechanism either when the energy acceptor is doped with the Pdot core or located at the surface. The location of energy acceptors is poorly defined due to the permeable and ill-defined structure of the Pdot itself. Although FRET is a probable mechanism because of its long range of action compared to other ET mechanisms, it is not the only possibility. Dexter energy transfer and photoinduced electron transfer (PET) are alternate mechanisms that act at shorter donor-acceptor distances. Energy acceptors doped within the Pdot core or adsorbed onto its surface may be close enough to the Pdot chromophores for Dexter ET and/or PET to occur with good efficiency. This ambiguity leads to difficulty in rational sensor design, where the number and location of energy acceptors and the mechanism of ET affect how the fluorescence signal is modulated. Pdot photophysics must be investigated more thoroughly for the development of improved, ultrabright fluorescence sensors relying on these materials.

1.3 Contributions of this thesis

Pdots are a very promising emergent fluorescent probe for a variety of applications in bioanalysis. However, development beyond proof-of-concept applications will require fundamental research into and optimization of their synthesis, photophysics, surface chemistry, and bioconjugation chemistries. As highlighted in Section 1.2.9, Pdots have several major deficiencies currently precluding their widespread adoption in bioanalysis. This thesis describes efforts towards the optimization of Pdots in overcoming some of these limitations. Namely, improvements were made towards Pdot synthesis, the understanding of Pdot photophysics, and the stability and surface chemistry of Pdots. Additionally, Pdots with improved surface chemistry were used in proof-of-concept immunoassay and cellular imaging applications, demonstrating their utility as a bright fluorescent probe.

To date there have been limited attempts to systematically study Pdot synthesis by nanoprecipitation. Pdots are typically synthesized manually, that is with limited control over how the precursor and aqueous solutions are introduced and mixed, with poor reproducibility as the result. Additionally, the nature of SP and amphiphilic polymer (AP) materials that will reliably form small, colloidally stable Pdots has not been studied systematically. Chapter 5 of this thesis addresses these problems using a flow-based manufacturing methodology for Pdot synthesis. The use of a semi-automated system allowed for the systematic study of the variables impacting particle sizes and size distributions. A variety of SPs and amphiphilic polymers having different properties were surveyed to test whether small, colloidally stable particles could be produced. Finally, as a first step to the commercial production of Pdots, the flow-based method allowed for the scale-up of Pdot synthesis to volumes not achievable using the manual injection method.

Because Pdots are multichromophoric, their photophysics are complicated and they do not have a direct analogue in other luminescent nanomaterials. Although it is possible to design energy transfer-based sensors without full knowledge of the system's photophysics, such sensors must be designed empirically. The ability to predict the system's response to an analyte would allow for the rational design of chemical and biological sensors and would enable a higher degree of sophistication. Some studies on the nature of energy transfer in Pdot systems have been performed, but a full picture of the photophysical processes occurring therein has yet to emerge. Chapter 6 presents an in-depth photophysical study of Pdots in an energy transfer configuration with a variety of organic dyes to elucidate the mechanism of ET in such systems. Although FRET has been postulated to be the dominant ET mechanism with Pdots, Chapter 6 considers Dexter energy transfer and photoinduced electron transfer as alternate and concurrent mechanisms.

Surface chemistry is an important consideration for any system to be deployed in a biological context. The surface chemistry of a material governs its interactions with its environment and controls what chemical modifications are possible. Pdots are most often synthesized having a negatively charged (above pH 5) carboxylated surface and are therefore prone to non-specific binding with many species that may be present in a biological matrix. Pdot surface chemistry is usually controlled by the identity of the co-precipitated amphiphile forming the putative shell structure. Additional surface coating materials are a potential strategy for easy modification of surface chemistry but have not been widely explored beyond a limited number of examples with silica. Chapter 7 presents the development of a dextran-based surface coating material for Pdots that was shown to improve colloidal stability in physiologically relevant conditions and to reduce

non-specific binding for *in vitro* bioanalytical applications. The dextran surface coating also enabled novel bioconjugation pathways for fluorescent labeling with Pdots.

The research presented in this thesis has made several key contributions to the development of Pdots as a fluorescent probe in bioanalysis. In addition to the practical improvements to Pdot synthesis and physiochemical properties presented in Chapters 5 and 7, Chapters 5 and 6 present experimental results that further the conceptual understanding of Pdot synthesis and photophysics, respectively.

1.4 Thesis organization

This thesis is divided into eight chapters, including this introductory chapter. Additional data and data analysis are included as appendices.

Chapter 2 introduces the theory of fluorescence and energy transfer. Various techniques for measuring fluorescence (and absorbance) are also discussed. This chapter is meant to provide the reader with the background to understand the methods and research results presented in Chapters 3-7.

Several experimental methods and characterization techniques were used repeatedly throughout this thesis. The experimental details for these methods are described in Chapter 3. Chapters 5-7 contain additional experimental details specific to those chapters.

Chapter 4 presents an overview of the various Pdot materials used in this thesis, their constituent polymer species and the various methods used to characterize them. The operational theory of each technique is also discussed. Of particular importance to the results in Chapters 5 and 6 is the discussion of Nanoparticle Tracking Analysis (NTA), a method that allows for the simultaneous determination of particle sizes and concentrations. NTA is the most widely used particle characterization technique in this thesis because of its rapidity, good sizing accuracy, and its unique ability to determine particle concentrations. However, the technique suffers from some limitations that may ultimately limit the accuracy of some numerical results, as discussed in Chapter 4.

A flow-based manufacturing system for Pdots is presented in Chapter 5. Syringe pumps were used to control the flow and mixing of the organic and aqueous phases for nanoprecipitation, resulting in semi-automated Pdot synthesis. The reproducibility of this method allowed for a systematic study of the affect of both the identity of the semiconducting polymer species and the amphiphilic polymer species on particle size and optical properties. The use of positive displacement pumps in lieu of syringe pumps allowed for proof-of-concept scale up of flow synthesis.

FRET [76, 113, 159], possibly concurrent with PET [119], are postulated to be the dominant mechanisms of ET in Pdots. Chapter 6 describes an investigation into the nature of energy transfer between Pdot donors and organic dye acceptors, considering three dynamic ET mechanisms, FRET, Dexter ET and PET. By using several series of acceptor dyes, the analysis takes into account effects of donor-acceptor distance, spectral overlap, and batch-to-batch variations in Pdot properties.

The utility and widespread adoption of Pdots is current limited by their poor colloidal stability and propensity towards non-specific binding. Currently, there is a dearth of suitable surface and bioconjugate chemistries in use with these materials. To address these problems simultaneously, Chapter 7 presents the development of a dextran-based surface coating material for Pdots, and demonstrates the use of dextran-coated Pdots in proof-of-concept fluorescence immunoassay and cellular immunolabelling applications.

Chapter 8 summarizes the key conclusions from the preceding chapters and outlines future directions for the continuation of this research.

In summary, this thesis presents unique and important contributions to nanotechnology, materials chemistry, and bioanalytical chemistry. Several key improvements were made to improve the utility of Pdots in bioanalysis in terms of their synthesis, stability, bioconjugate chemistry, and our understanding of their energy transfer-related photophysics. With continued optimization, Pdots will find extended use as fluorescent probes for a wide variety of applications.

Chapter 2: Theory and measurements of fluorescence

This chapter presents a basic description of fluorescence theory, fluorescence measurements and energy transfer processes. An understanding of fluorescence theory will enable the reader to understand many aspects of the research presented in this thesis including experimental design, the techniques used, the data presented, and the analysis and interpretation of the results.

2.1 Fluorescence theory

Luminescence is defined as the spontaneous emission of a UV, visible or infrared photon from an electronically excited species [115]. Several excitation processes may lead to luminescence, including photon absorption (photoluminescence), chemical processes (chemiluminescence), biological processes (bioluminescence) or applied electric potential (electroluminescence). Luminescence is different than *incandescence*, which refers to excitation via an input of heat. *Fluorescence* is a specific type of luminescence that results from electronic relaxation from an excited singlet state to the singlet ground state. *Phosphorescence* describes the emission of a photon via electron relaxation from a triplet to a singlet state. The following sections outline the fundamental theory of fluorescence and describes the methods used for measuring fluorescence.

2.1.1 Jablonski diagram

The emission of a photon via fluorescence represents one of a multitude of possible vibronic transitions (*i.e.*, simultaneous changes in the electronic and vibrational state of a molecule) in a molecular fluorophore. Photophysical processes occurring within a molecular fluorophore are conventionally shown on a Jablonski diagram (Figure 2.1). On a Jablonski diagram, singlet (S_n) or triplet (T_n) electronic states are represented by potential wells, each containing vibrational states

(ν_n), which themselves contain rotational states (which are not shown for clarity). Electronic states are separated by energies on the order of 1–10 eV (~8000 cm^{-1}–80 000 cm^{-1}), and vibrational states within a given electronic state are separated by energies on the order of 0.25 eV (~2000 cm^{-1}) [160]. A vibronic transition from the ground electronic state to an excited electronic state may be brought on by the absorption of a UV-visible photon of wavelength 200-800 nm.

The simplest pathway resulting in fluorescence is shown in Figure 2.1A. Upon absorption of a UV-visible photon of appropriate energy (*i.e.*, resonant to the energy difference between the initial and final states) by the fluorophore, an electron is excited from the ground state, $S_0\nu_0$ to a vibrational state within the first electronic excited state, $S_1\nu_n$. The absorption process occurs rapidly, on a scale on femtoseconds. Through vibrational relaxation (*i.e.*, the loss of energy to the solvent as heat), the fluorophore decays to the lowest vibrational state of the first electronic state, $S_1\nu_{0,}$ on a picosecond time scale. The fluorophore remains in the S_1 state for picoseconds to nanoseconds, corresponding to its fluorescence lifetime. Fluorescence occurs from $S_1\nu_0$ to a vibrational state of the ground electronic state, $S_0\nu_n$, a phenomenon known as Kasha's rule, resulting from the relative time scales of vibrational relaxation and fluorescence. Because emission usually occurs from the lowest energy vibrational state of the first excited electronic state, molecular emission spectra are independent of the excitation wavelength. The emission of a photon occurs on a similar time scale to the absorption of a photon (femtoseconds). The fluorophore decays further to $S_0\nu_0$ by vibrational relaxation returning the fluorophore to its ground state [115].

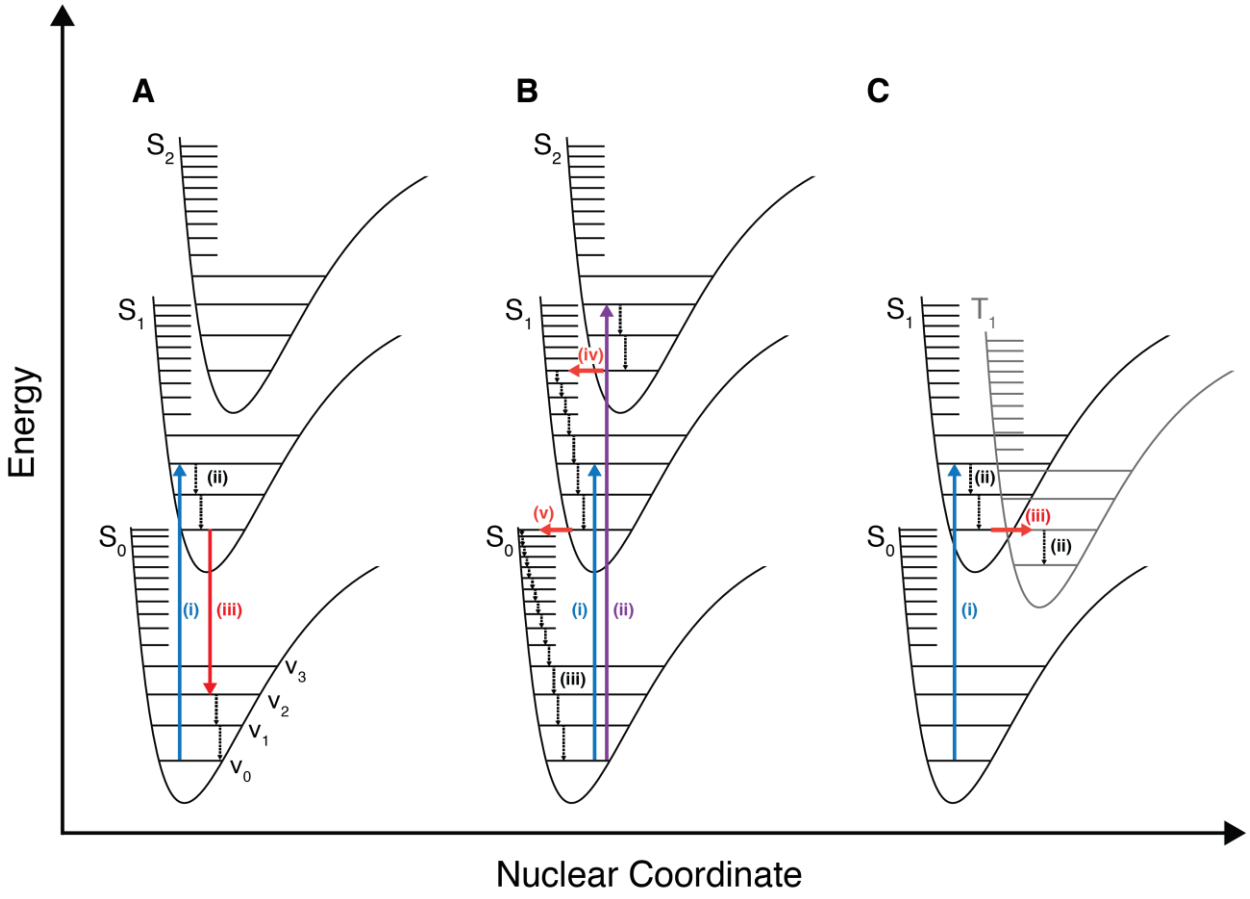

Figure 2.1 Jablonski diagrams illustrating the processes involved in photoluminescence, including absorption and competing non-radiative pathways. Electronic states are shown as potential wells where S_n corresponds to a singlet state and T_n corresponds to a triplet state. Vibrational states, v_n, are shown within each electronic state. Rotational states are not shown for clarity. **(A)** Pathways involved in fluorescence. Upon absorption of a photon (i), an electron is excited from S_0v_0 to S_1v_2. Non-radiative decay occurs via vibrational relaxation to S_1v_1 then S_1v_0 (ii). Radiative decay (*i.e.,* fluorescence) occurs (iii) and the electron returns to the ground electronic state. **(B)** Non-radiative decay pathways. Upon absorption of a photon, the electron may be excited to S_1 (i) or S_2 (ii). Vibrational relaxation occurs to S_2v_0 (iii), followed by internal conversion to S_1 (iv). Vibrational relaxation occurs to S_1v_0 followed by either fluorescence (see panel A) or internal conversion to S_0 (v). The system returns to S_0v_0 via vibrational relaxation (iii). **(C)** Intersystem crossing. Upon excitation to S_1v_2 (i), vibrational relaxation occurs to S_1v_0 (ii). The system then undergoes intersystem crossing to T_1v_1 (iii), followed by vibrational relaxation to T_1v_0 (iv). From this state the system will return to the ground state non-radiatively, or radiatively via phosphorescence or delayed fluorescence (process not shown in diagram).

Fluorescence competes with other de-excitation pathways whose probabilities depend on their relative rates. These processes include internal conversion, where the excited fluorophore returns to the ground electronic state via transition to a resonant vibrational state within S_0, intersystem crossing involving a spin forbidden transition to a triplet state, intramolecular charge transfer and conformational change within the fluorophore. The excited triplet state populated by intersystem crossing may decay non-radiatively to $T_1\nu_n$ by vibrational relaxation, then may decay to the ground state non-radiatively or radiatively in a process called phosphorescence. Phosphorescence is spin forbidden and is therefore slow (10^{-4}–10^{2} s) and occurs with low or negligible intensity for most fluorophores. De-excitation processes are discussed in detail in Section 2.1.3. Other excited state interactions also compete if they occur on a comparable time scale including electron transfer, proton transfer, energy transfer, and the formation of excited state species (excimers or exiplexes) [115].

2.1.2 Absorbance

There are three possible physical effects when matter interacts with light: elastic (Rayleigh) scattering, inelastic (Raman) scattering, or absorption. In a polyatomic molecule, absorption describes the electronic transition of an electron in a ground state orbital to an unoccupied orbital of higher energy via photon absorption. Absorption of a UV-visible photon usually results in a transition from the highest occupied molecular orbital (HOMO) to the lowest unoccupied molecular orbital (LUMO), corresponding to a transition from a pi bonding (π) or non-bonding (n) orbital to a pi antibonding orbital (π^*). In conjugated systems, where there are extended sections of alternating single and double carbon-carbon bonds, electrons are delocalized over the conjugated segment due to extensive overlap of pi orbitals, known as the resonance effect. Such

segments are typically responsible for these transitions, where the energy associated with the transition decreases as the length of the segment increases [115]. The segment of a molecule where absorption occurs is known as a *chromophore*.

Absorption events are governed by two quantum mechanical selection rules. Transitions involving a change of spin multiplicity are forbidden (*i.e.*, transitions from a singlet state to a triplet state or *vice versa*). This rule is relaxed where spin-orbit coupling causes weak interactions in the wavefunctions of the singlet and triplet states, allowing a small number of spin-forbidden transitions to occur. The Laporte selection rule states that for a centrosymmetric molecule (*i.e.*, a molecule containing an inversion centre of symmetry) transitions conserving parity (either symmetry or antisymmetry about the inversion centre) are forbidden. Transitions within a set of p or d orbitals, in which electrons are redistributed within the subshell, are forbidden. Vibrations of the molecule can momentarily distort the symmetry, allowing symmetry-forbidden transitions to occur [115].

The efficiency of light absorption at a wavelength λ is given by the absorbance, A, or the transmittance, T, described by Eqn. 2.1, where I_0 and I are the intensities of the light beam entering and exiting the sample respectively.

$$A(\lambda) = \log \frac{I_0}{I} = -\log T(\lambda) \tag{2.1}$$

For many molecular chromophores, absorbance follows the Beer-Lambert law, Eqn. 2.2, where ε is the molar absorption coefficient, *b* is the absorption path length and *c* is the concentration of the absorbing species.

$$A(\lambda) = \log \frac{I_0}{I} = \varepsilon(\lambda) bc \tag{2.2}$$

The molar absorption coefficient describes the ability of a molecule to absorb light of a wavelength λ in a given solvent and is also used to describe the probability of the corresponding vibronic transition. For n → π* transitions, typical ε values are on the order of 10^2 or less, and for π → π* transitions, ε values are on the order of 10^4 or higher for relatively large chromophores [115].

The strength of a transition can also be described by the oscillator strength (*f*), Eqn. 2.3, where ε_0 is the vacuum permittivity, *m* and *e* are the mass and elementary charge of an electron respectively, *c* is the speed of light, λ is the wavelength, and λ_{av} is the average transition wavelength. Oscillator strength is descriptive of the entire transition, as in its determination the molar absorption coefficient is integrated over the range of wavelengths associated with the transition. Classically, the absorption of light by a chromophore is described considering the molecule as an oscillating dipole. The oscillator strength is expressed as a ratio of the strength of the transition and the strength of the dipole of a bound electron behaving as a harmonic oscillator [115].

$$f = \frac{4\ln 10\varepsilon_0 mc}{N_a e^2}\int \varepsilon(\upsilon)d\upsilon = \frac{4\ln 10\varepsilon_0 mc^2}{N_a e^2 \lambda_{av}^2}\int \varepsilon(\lambda)d\lambda \qquad (2.3)$$

Absorption may also be characterized by the molecular absorption cross-section ($\sigma(\lambda)$), Eqn. 2.4, where N is the number of absorbers contained in a unit volume of the absorbing medium along the light path, and b is the path length. The molecular absorption cross-section corresponds to the photon-capture area associated with an individual molecule [115].

$$\sigma(\lambda) = \frac{1}{Nb}\ln\frac{I_0}{I} \qquad (2.4)$$

2.1.2.1 Franck-Condon principle

The Franck-Condon principle states that over the time course of an electronic transition, the atomic nuclei are stationary, and the molecule does not vibrate because the motions of electrons are much faster than the motions of nuclei. Consequently, the motions of the electrons and the nuclei can be treated separately. The promotion of an electron from the ground electronic state to an excited electronic state takes about 10^{-15} s, whereas molecular vibrations typically occur on time scales of 10^{-10}–10^{-12} s [115]. In a Jablonski diagram (Figure 2.2), transitions occur vertically; the energy of the electron changes but the nuclear position remains stationary. The quantum mechanical description of the Franck-Condon principle states that the intensity of a vibrational transition is proportional to the square of the overlap integral between the vibrational wavefunctions (Ψ) of the initial and final states, Eqn. 2.5. This overlap integral is known as the Franck-Condon factor (FCF).

$$FCF = \left[\Psi^*_{final} \cdot \Psi_{initial} d\tau \right]^2 \quad (2.5)$$

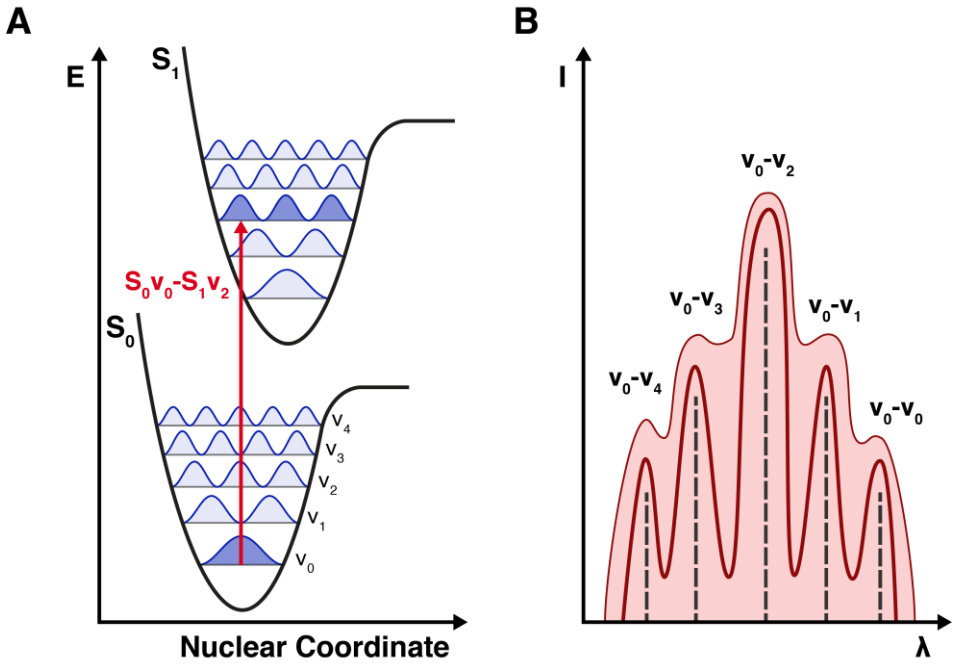

Figure 2.2 (A) The probability of an electronic transition depends on the overlap of the probability densities of the initial and final vibrational states. **(B)** Shape of absorption spectrum. The intensity of each band depends on the probability of the transition described by the Franck-Condon factor. In the gas phase, several bands may be observed corresponding to individual vibronic transitions. In solution, these bands are obscured by band broadening effects.

The extent of vibrational overlap depends on the offset between the equilibrium bond lengths for the ground and excited state potential wells. Because there is no nuclear movement over the course of an excitation event (10^{-15} s), the final vibrational energy level must be instantaneously compatible with the nuclear position of the initial state. The non-equilibrium state achieved instantaneously upon excitation is known as a Franck-Condon state. After the excitation event the

electronic configuration of the molecule has changed, and the nuclei must reorient to the new electronic configuration resulting in molecular vibration. Decay to thermal equilibrium occurs rapidly (~1 ps) as the chromophore undergoes many (10^{12}) collisions per second with neighbouring solvent molecules [161].

At room temperature, absorption occurs from the $S_0\nu_0$ state. The population of vibrational states in a molecule is described by the Boltzmann distribution, Eqn. 2.6, where N is the number of molecules in the 1st or 0th vibrational state having energy levels of E_1 or E_0 respectively, k is the Boltzmann constant ($k = 1.3807\times10^{-23}$ J K^{-1}) and T is the absolute temperature [115].

$$\frac{N_1}{N_0} = e^{\frac{-(E_1-E_0)}{kT}} \tag{2.6}$$

At room temperature, the thermal energy (kT) is much less than the energy difference between neighbouring vibrational states (~200 cm^{-1} and 1000–3000 cm^{-1} respectively). The population of vibrational levels above the ground state is negligible [161].

The shape of the absorption spectra therefore arises from the relative probabilities of transitions from $S_0\nu_0$ to $S_1\nu_n$. The most intense peak corresponds to the transition with the highest extent of vibrational wavefunction overlap. For some fluorophores, distinct peaks corresponding to each vibronic transition may be resolved at low temperature. However, at room temperature, significant band broadening occurs. Many normal vibrations of the molecule are coupled to the electronic transition (*i.e.*, arising from the change in electron density). Within each vibrational level are

rotational states that are significantly broadened from solvent collisions that hinder rotation. Collisions and electrostatic interactions with surrounding solvent molecules contribute to peak broadening. As a result of these effects, a quasicontinuum of states is superimposed on every electronic level, and broad absorption bands are observed in practice [161].

2.1.2.2 Multiphoton absorbance

Conventionally, a single photon is absorbed whose energy is resonant to the energy difference between $S_0\nu_0$ and $S_1\nu_n$. Excitation to the excited state is also possible by the simultaneous absorption of multiple photons whose cumulative energies are resonant with the energy of the overall transition (Figure 2.3). In this way, incident light of lower energy (higher wavelength) can be used to incite an electronic transition in a chromophore typically requiring higher energy input. Multiphoton absorbance occurs via short lived virtual states whose energies lie between S_0 and S_1. The probability of a multiphoton absorption event depends on both the spatial and temporal overlap of the incident photons as all photons must reach the absorption cross section of the chromophore within 10^{-18} s. Multiphoton absorption depends non-linearly on the intensity of the excitation light (quadratic for two-photon, cubic for three-photon, *etc.*). Although the most common configuration for multiphoton excitation involves a coherent, high-intensity laser, the photons do not need to be resonant. Two-photon absorption cross-sections, σ_2, are usually given in units of 10^{-50} cm^4 s, known as Goeppert-Mayer units (GM). Two-photon cross-sections for typical fluorophores range from 1–100 GM, corresponding to low absorbance. Thus, high intensity incident radiation, usually from a high-power laser, is required for multiphoton excitation [115].

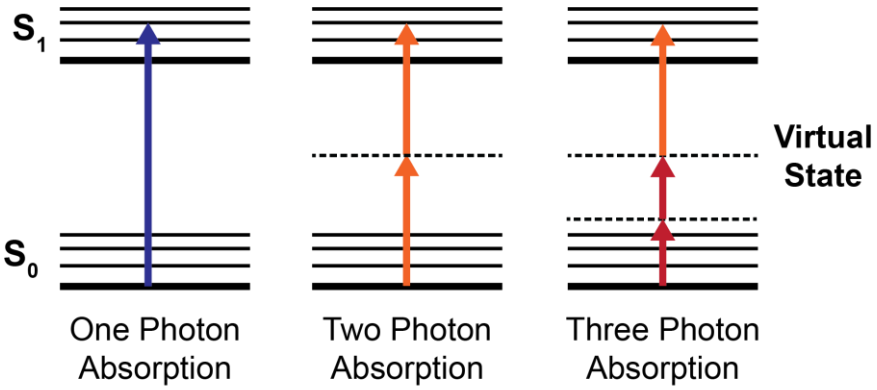

Figure 2.3 Schematic of one, two and three photon absorption. Multiphoton absorbance occurs via a short-lived virtual state, demarcated by a dashed line. Although resonant photons from a laser source are often used for multiphoton excitation, multiphoton absorbance is also possible with non-resonant photons as demonstrated here for three photon absorption.

2.1.3 De-excitation pathways

A chromophore in the excited state will undergo several processes as it relaxes back to the ground state ($S_0\nu_n$). These processes are demonstrated on the Jablonski diagram in Figure 2.1 (*vide supra*). Relaxation may occur non-radiatively (vibrational relaxation, internal conversion, intersystem crossing) or radiatively (fluorescence, phosphorescence). De-excitation pathways are summarized in Table 2.1.

A chromophore in a higher excited singlet state ($S_{n>1}$) will rapidly relax to S_1 via internal conversion (*vide infra*) within 10^{-11}–10^{-14} s. Chromophores in the first excited state ($S_1\nu_{n>0}$) relax to the lowest vibrational state of S_1 by losing energy to other molecules (*e.g.*, solvent) as heat through collisions in a process called *vibrational relaxation*. Vibrational relaxation occurs on time

scales of 10^{-10}–10^{-12} s, faster than the other processes that depopulate S_1, and thusly the chromophore will relax to S_1v_0 before any subsequent relaxation process will occur [161].

Table 2.1. Overview of de-excitation pathways of excited electronic states of molecular dyes. Adapted from ref. [161].

Process	Electronic Transition	Time Scale (s)	Rate Constant
Internal Conversion	S_n–S_1, T_n–T_1	10^{-11}–10^{-14}	k_{ic}
Internal Conversion	S_1–S_0	10^{-7}–10^{-6}	k_{ic}
Vibrational Relaxation	$S_1v_{n>1}$–S_1v_0	10^{-10}–10^{-12}	k_{vr}
Fluorescence	S_1–S_0	10^{-11}–10^{-7}	k_f
Intersystem Crossing	S_1–T_1, T_1–S_1	10^{-7}–10^{-9}	k_{isc}
Phosphorescence	T_1–S_0	10^{-3}–10^{2}	k_p

Internal conversion is a non-radiative transition that occurs between two resonant (or near-resonant) electronic states of the same spin multiplicity (*i.e.,* S_n-S_m or T_n-T_m). Internal conversion occurs very rapidly from S_2-S_1, but the efficiency of internal conversion from S_1-S_0 is much lower because of the large energy gap between these states. As an important consequence, fluorescence (and intersystem crossing leading to phosphorescence) can compete with internal conversion and the emission of photons can possibly be observed [115].

Intersystem crossing is a non-radiative transition between two resonant vibrational levels within electronic states of different spin multiplicity (*i.e.,* S_n-T_n or T_n-S_n). Transition involving a change in spin multiplicity are spin forbidden but can occur when spin-orbit coupling is significant (*i.e.*, coupling between the orbital magnetic moment and the spin magnetic moment). The presence of

heavy atoms increases the spin-orbit coupling and favours intersystem crossing. Typically, a chromophore excited to S_1 will first relax to the lowest vibrational state of this level by vibrational relaxation before undergoing intersystem crossing [115]. The triplet state is of lower energy than the singlet state because of the exchange energy between two electrons having the same spin. Intersystem crossing will occur to $T_1\nu_{n>0}$ followed by vibrational relaxation to $T_1\nu_0$ before subsequent radiative (phosphorescence) or non-radiative (intersystem crossing and vibrational relaxation) relaxation to S_0. Transitions between triplet and singlet states are spin forbidden and therefore the excited triplet state may be long lived. It is possible for internal conversion to happen from T_1 to S_1, resulting in an emissive process known as *delayed fluorescence* [161]. Non-radiative relaxation of T_1 is favoured due to its long lifetime; many collisions of the chromophore with solvent molecules favour intersystem crossing to a high vibrational state of S_0 followed by vibrational relaxation. Radiative relaxation from T_1 to S_0 (phosphorescence) becomes competitive with non-radiative processes at low temperature or in rigid (viscous) media where collisions with solvent are reduced. The phosphorescence spectrum of a fluorophore is red-shifted compared to its fluorescence spectrum as T_1 is of lower energy than S_1.

Fluorescence is the spontaneous emission of a photon arising from relaxation from S_1 to S_0. The time scale of fluorescence is 10^{-11}–10^{-7} s, corresponding to the amount of time the fluorophore remains in the $S_1\nu_0$ state before relaxation. The actual emission of a photon occurs on the same time scale as an absorption event (10^{-15} s) and is considered instantaneous. Because the transition is rapid, like absorption, fluorescence is governed by the Franck-Condon principle, where transitions involving greater orbital wavefunction overlap will have greater intensity. The fluorescence spectrum is an approximate mirror image of the absorption spectrum and is red

shifted (lower energy) than the absorption spectrum due to the loss of energy associated with vibrational relaxation to $S_1\nu_0$ (*i.e.,* Kasha's rule). The difference between the wavelength of maximum absorbance and maximum fluorescence is known as the *Stokes shift*.

2.1.4 Quantum yield and fluorescence lifetime

The observed intensity and fluorescence lifetime of a species depends on the relative rates of all de-excitation processes that may occur. The fluorescence lifetime describes the average amount of time a fluorophore remains in the excited state before it decays to the ground state. The fluorescence lifetime, τ, is given by Eqn. 2.7, where k_r is the radiative rate constant and Σk_{nr} is the sum of the rate constants for all non-radiative decay processes.

$$\tau = \frac{1}{k_r + \Sigma k_{nr}} \tag{2.7}$$

For an arbitrary species *A*, an instantaneous light pulse of suitable energy at time 0 will excite a proportion of molecules to the excited state, *A**. The rate of relaxation of *A** from S_1 to S_0 is given by Eqn. 2.8, accounting for contributions from radiative and non-radiative processes [115].

$$-\frac{d[A^*]}{dt} = (k_r + k_{nr})[A^*] \tag{2.8}$$

The intensity of emission at an arbitrary time, *I(t)*, after the excitation pulse follows an exponential decay (Eqn. 2.9) where I_0 is the intensity at t=0. The fluorescence lifetime is a statistical average

and corresponds to the time when ~63% of excited fluorophores have decayed to ground state, or, equivalently, when the intensity has reached 37% (e^{-1}) of its initial value [162].

$$I(t) = I_0 e^{\frac{-t}{\tau}} \tag{2.9}$$

The fluorescence lifetime is related mathematically to the quantum yield (Φ) by Eqn. 2.10. Qualitatively, the quantum yield of a fluorophore is the ratio of the number of photons emitted to the number of photons absorbed, or equivalently, as the fraction of molecules in the excited state that decay to the ground state via emission of a photon. Quantitatively, the quantum yield can be described by the radiative rate constant, k_r, and the sum of all non-radiative rate constants, Σk_{nr}, which encompasses all non-radiative decay pathways including internal conversion, intersystem crossing, or other intra- and inter-molecular quenching mechanisms (Eqn. 2.11), where k_q is the rate constant of all quenching processes (excluding energy transfer) and k_{et} is the rate constant of energy transfer [161].

$$\Phi = \frac{k_r}{k_r + \Sigma k_{nr}} = k_r \tau \tag{2.10}$$

$$\sum k_{nr} = k_{ic} + k_{isc} + k_q + k_{et} + \ldots \tag{2.11}$$

2.1.5 Quenching processes

Any process that leads to a decrease in the fluorescence intensity may be described as *fluorescence quenching*, although processes that permanently change the molecular structure of the fluorophore are typically excluded. Photochemical reactions or photobleaching (*vide infra*) are not typically

considered quenching process as they cause permanent changes to the molecular structure of the fluorophore. Many substances are potential quenchers; for example, molecular oxygen is of particular note as it quenches most known fluorophores [162]. Dynamic quenching acts on the excited state of the fluorophore. As the result of a dynamic quenching process, the fluorophore returns to the ground state without emission of a photon, therefore decreasing the fluorescence lifetime of the fluorophore. Collisional quenching is an example of dynamic quenching, where quenching results from collisions between the fluorophore and the quencher while the fluorophore is in the excited state. Dynamic quenching processes include collisions with heavy atoms and energy transfer processes (*vide infra*) such as electron or charge transfer or FRET (a through-space quenching mechanism) [115].

The Stern-Volmer equation, Eqn. 2.12, describes collisional quenching, where I_0 and I are the fluorescence intensities of the fluorophore in the absence and presence of quencher, respectively, k_q is the bimolecular quenching constant, τ_0 is the lifetime of the fluorophore in the absence of the quencher and Q is the concentration of the quencher. K_{SV} is the Stern-Volmer constant for purely dynamic quenching.

$$\frac{I_0}{I} = 1 + k_q \tau_0 [Q] = 1 + K_{SV} [Q] \qquad (2.12)$$

For a single type of fluorophore uniformly accessible to the quencher, a plot of I_0/I vs. $[Q]$ is linear with slope K_{SV}.

Static quenching processes inhibit the formation of the excited state and do not affect the observed fluorescence lifetime. Static quenching occurs either due to the existence of a sphere of effective quenching or the formation of a non-emissive ground state complex of the fluorophore and quencher [115]. In the case of complex formation, static quenching is described by Eqn. 2.13 where K_s is the association constant for complex formation.

$$\frac{I_0}{I} = 1 + K_s[Q] \tag{2.13}$$

Both dynamic and static quenching depend upon the concentration of the quencher and are not easily resolved by steady state intensity measurements. Lifetime measurements are used to differentiate static and dynamic quenching. For dynamic quenching, changes in intensity and lifetime are concomitant (*i.e.*, $I_0/I = \tau_0/\tau$). For static quenching, the complexed fluorophores are not emissive, whereas uncomplexed fluorophores are unperturbed and their lifetimes are unmodified (*i.e.*, $\tau_0/\tau = 1$) [162].

Dynamic and static quenching can occur concurrently by the same type of quencher. This process is described as combined quenching, and results in non-linear deviations from the Stern-Volmer relationship.

2.1.6 Photobleaching

Photobleaching refers to the irreversible photochemical modification of a fluorophore in its excited state resulting in the loss of its ability to fluorescence (or absorb). Photobleaching is distinct from

fluorescence intermittency (blinking) because fluorescence is not restored after time spent in the 'dark' state. The particular mechanism responsible for photobleaching and the photobleaching rate are dependent upon the molecular environment of the fluorophore and the intensity of the incident radiation. The underlying mechanisms of photobleaching are poorly understood and the process itself is thought to be very complex. Of the prevailing theories, the most common is reaction with ground state triplet oxygen ($^3O_2$). For a fluorophore with high propensity for the excited triplet state (*i.e.*, a high quantum yield of intersystem crossing), a considerable fraction of the fluorophores will be in the long-lived excited triplet state at any given time. The lifetime of this state is relatively long (10^{-6}–10^{-3} s) which permits a longer time scale for potential photoreactions to occur. Interactions between fluorophores in the triplet state and molecular oxygen produce singlet oxygen, which itself produces reactive radical species upon its decomposition. Fluorophores in the excited triplet state are also highly reactive to other organic molecules, potentially leading to photodegradation [163].

The resistivity of photobleaching varies from fluorophore to fluorophore. Some dyes emit only a few hundred photons before photobleaching whereas others may emit tens of millions [163]. The rate of photobleaching depends both on the fluorophore's environment as well as excitation intensity. Observed rates of photobleaching decrease when the fluorophore is protected from molecular oxygen. Photobleaching is also a concern in multiphoton absorbance experiments, as a higher incident power is required for excitation [163].

2.1.7 Fluorescence measurements

Steady state and time resolved fluorescence measurements are a widely used analytical tool in bioanalysis. Many properties of fluorescence can be measured to gain information about the system under study including intensity, emission wavelength, excited state lifetime and anisotropy (polarization).

2.1.7.1 Steady state measurements

Steady state fluorescence measurements are typically recorded using a spectrofluorometer, where the sample is continuously irradiated by a source with constant photon fluence (constant number of photons per unit time). The time scale of steady state measurements is much greater than the time scale of relaxation of the fluorophore, so steady state is effectively achieved immediately upon first exposure to the excitation beam. The concentration of excited fluorophores remains constant over the course of the measurement (*i.e.,* the sample is in equilibrium between the ground and excited states) [115].

Steady state fluorescence may be recorded as a function of wavelength with a constant excitation wavelength (selected by a monochromator of non-zero bandwidth) called an *emission spectrum,* or as a function of excitation wavelength with a constant emission wavelength called an *excitation spectrum*. The excitation spectrum typically has similar peak shape and spectral position as the absorbance spectrum.

For a dilute solution, the steady state fluorescence intensity measured at a given wavelength is approximated by Eqn. 2.14, where $I_F(\lambda_E)$ is the fluorescence intensity measured at wavelength *E*,

K is an experimental proportionality factor, Φ_F is the quantum yield of the fluorophore, $\varepsilon(\lambda_E)$ is the molar absorption coefficient at wavelength *E*, *b* is the path length and *c* is the concentration of the fluorophore. The brightness of a fluorophore, Eqn. 1.1, follows from this relationship.

$$I_F(\lambda_E) \cong 2.3K\Phi_F I_0(\lambda_E)[\varepsilon(\lambda_E)bc] \tag{2.14}$$

For fluorescence measurements performed using the same experimental setup (*i.e.*, with equivalent *K* values), the total intensity depends on both the quantum yield of the fluorophore, its molar extinction coefficient and the intensity of the excitation light [115].

2.1.7.2 Fluorescence lifetime measurements

The decay of emission intensity over time is measured in time-resolved fluorescence measurements. For time-domain measurements, intensity is recorded as a function of time after the excitation pulse and this information is used to determine the fluorescence lifetime.

Lifetime measurements are most commonly performed using time correlated single photon counting (TCSPC). In this method, the sample is excited with a short light pulse that also sends a signal to a constant function discriminator that measures the arrival time of the pulse. The electronic signal is passed to a time-to-amplitude converter that increases a voltage linearly with time on the nano- or picosecond scale. Conditions are adjusted so only *ca*. 1 in 100 excitation pulses leads to the emission of a photon such that only a single photon arrives at the detector and the time-to-amplitude convertor can be restored to its initial voltage before the arrival of a subsequent photon. The arrival of the first emitted photon is recorded, and the timing of the arrival

is determined by the constant function discriminator, which sends an electronic signal to stop the voltage ramp. The magnitude of the voltage is proportional to the delay time between the excitation pulse and the emitted photon. The voltage is converted to a digital value that is stored with its corresponding time delay. The excitation and emission process is repeated hundreds of thousands of times and a histogram of number of photons vs. delay time is generated. The histogram corresponds to the decay profile of the sample [162].

Fluorescence lifetime measurements may also be recorded in two dimensions by fluorescence lifetime imaging microscopy (FLIM) (or three dimensions if confocal or multiphoton microscopy are used). FLIM is favoured for some imaging applications because fluorescence lifetimes are independent of concentration (unlike intensity) but are often affected by the local environment of the fluorophore. In FLIM, the excitation source is rastered across the sample in two dimensions and the lifetimes are recorded for each pixel using a microscope and a TCSPC system. The pixels are combined to create an image that contains spatial information about the fluorescence lifetime in various regions of the image [162].

2.1.7.3 Transient absorption spectroscopy

Transient absorption (TA) spectroscopy measures dynamic processes affecting the excited state of chromophores on ultrafast time scales. Measurements of absorbance rather than fluorescence are advantageous because non-emissive states may be probed. An excitation pulse, called the pump pulse, is passed through the sample promoting a small fraction (*ca*. 0.1–10%) of chromophores to an electronic excited state. After a variable delay time, a second weak pulse is passed through the sample. The probe pulse has sufficiently low intensity to avoid multiphoton absorption events. The

difference in the absorption spectra of the excited sample and the ground state sample, ΔA, is recorded for each delay time (Eqn. 2.15).

$$\Delta A = -\frac{\log I(\lambda)_{pumped}}{\log I(\lambda)_{unpumped}} \tag{2.15}$$

As the delay time is modulated ΔA is recorded as a function of delay time and wavelength, and this function contains information about dynamic processes occurring on ultrafast time scales. Such processes include pathways that populate or de-populate the excited state such as excited-state energy migration and charge transfer [164].

Plots of ΔA usually contain multiple features corresponding to different dynamic processes. The ground-state bleach peak occurs at roughly the same spectral position as in the steady state absorption spectrum. Upon application of the pump pulse, the number of chromophores in the ground state is reduced. The ground state absorption of the excited sample (*i.e.*, investigated by the probe pulse) is less than that of the non-excited sample. The result is a negative signal in the ΔA spectrum. Stimulated emission of the excited sample may occur upon application of the probe pulse (*i.e.*, a photon of the probe pulse inducing emission from an excited state chromophore), increasing the light intensity striking the detector and therefore resulting in a negative ΔA signal. Stimulated emission occurs only for optically allowed transitions and will have a peak position similar to the steady state fluorescence peak of the fluorophore. Excited-state absorption, that is absorption from the first excited state to higher excited states, may be brought upon by the probe pulse. Since the probe pulse is being absorbed, the result is a decrease of light striking the detector

and a positive ΔA signal. Absorption events arising from the products of photochemical reactions may also contribute to the observed ΔA traces [164].

2.1.7.4 Fluorescence microscopy

Fluorescence microscopy is used to obtain spatial and intensity (or in the case of FLIM, lifetime) information about a sample. The sample is illuminated with a light source whose wavelength and associated bandwidth are selected by optical filters or by choice of a specific laser. The detected light originates from the sample itself and scattered excitation light is filtered out by a dichroic mirror and an emission filter [115]. The optical image formed by the microscope is recorded by a digital camera such as a charge-coupled device (CCD) camera or a scientific complementary metal–oxide–semiconductor (sCMOS) camera. The digital image is a two-dimensional array of pixels, each of which represents a specific location within the sample. The number of photons detected at an individual pixel is recorded and converted to an intensity value, correlated to the number of fluorophores within that area (and their brightness) [165]. The resolution of an optical microscope is limited by the diffraction limit (*ca.* one half the wavelength of light imaged, 200–400 nm) and is therefore useful for imaging whole cells but not small subcellular structures [115].

2.2 Energy transfer

Many fluorescence sensing applications rely on energy transfer (ET) as their mechanism of action. Transfer of the excitation energy of a donor species to a nearby acceptor species may occur under certain conditions and when there is sufficient overlap between the emission spectrum of the donor and the absorbance spectrum of the acceptor (for some mechanisms). When the donor and acceptor chromophores are different species energy transfer is called described as *heterotransfer*. In the

case where the donor and acceptor are identical species, energy transfer is referred to as *homotransfer*. If the homotransfer process repeats and the energy transfers between several chromophores, the process is called excitation transport or energy migration. Energy transfer may occur radiatively, where a photon emitted by the donor is absorbed by the acceptor, or non-radiatively where the energy is transferred without donor emission. Non-radiative energy transfer involves short or long-range interactions between the donor and the acceptor [115].

2.2.1 Förster Resonance Energy Transfer (FRET)

Förster Resonance Energy Transfer (FRET) is a long range (*i.e.,* nanometre scale), non-radiative ET mechanism where energy is transferred from a donor species in its excited state to a nearby acceptor in its ground state through dipole-dipole (Coulombic) interactions. The FRET process is illustrated on the Jablonski diagram in Figure 2.4. The rate of FRET, k_T, depends on a number of factors: the extent of overlap between the donor emission and acceptor absorbance spectra (*i.e.,* the resonance condition where transitions must have the same energy), the quantum yield of the donor, the relative orientation of the transition dipoles of both species, and the donor-acceptor distance. The distance dependence of FRET allows it to be used as a 'molecular ruler' for the determination of relative distances on the nanometre scale [162].

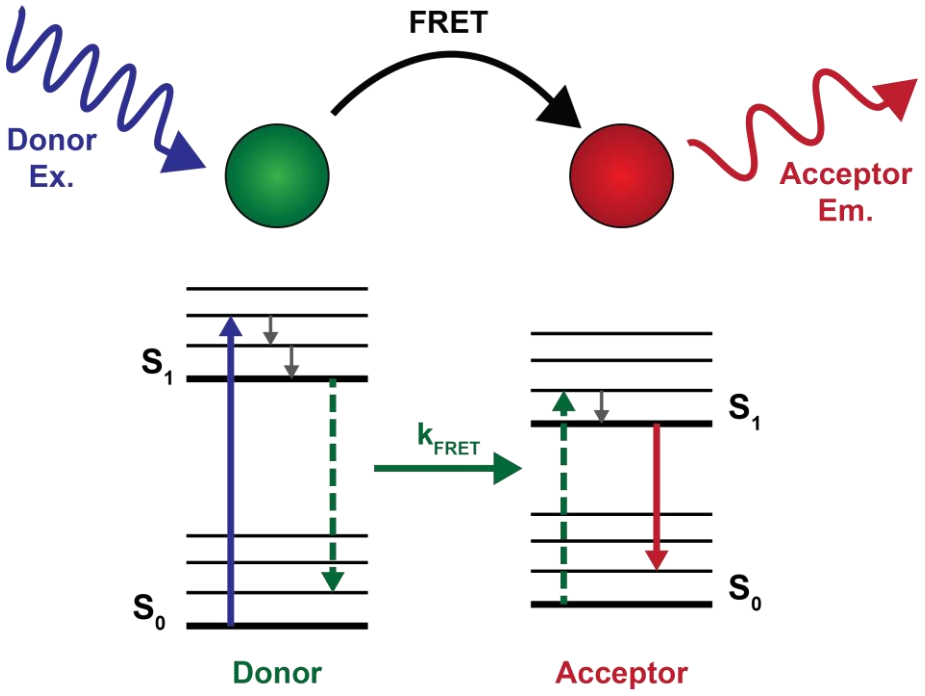

Figure 2.4 Jablonski diagram illustrating the process of FRET. The donor is excited to S_1 by a high energy photon. It undergoes vibrational relaxation to the lowest vibrational state of S_1 then transfers its energy to a nearby acceptor, relaxing to S_0 and promoting the acceptor to S_1. The acceptor then undergoes vibrational relaxation and then relaxes to S_0 via emission of a lower energy photon (if it is a fluorophore) or via a non-radiative pathway.

The classical FRET formalism treats the donor and acceptor molecules as oscillating dipoles which may interact through space if they have similar resonant frequencies. The rate of FRET (k_T) between a single donor and single acceptor at a distance r is given by Eqn. 2.16, where Φ_D is the quantum yield of the donor in the absence of the acceptor, κ^2 is an orientation factor describing the relative orientations of the donor and acceptor transition dipoles normally assumed to be 2/3 for randomly oriented dipoles, τ_D is the fluorescence lifetime of the donor in the absence of the acceptor, N is Avogadro's number, n is the refractive index of the medium, and $J(\lambda)$ is the spectral overlap integral given by Eqn. 2.17 [162].

$$k_T(r) = \frac{\Phi_D \kappa^2}{\tau_D r^6}\left(\frac{9000(\ln 10)}{128\pi^5 N n^4}\right) J(\lambda) \tag{2.16}$$

$$J(\lambda) = \int_0^\infty F_D(\lambda)\varepsilon_A(\lambda)\lambda^4 d\lambda \tag{2.17}$$

$$J(\lambda) = \frac{\int_0^\infty F_D(\lambda)\varepsilon_A(\lambda)\lambda^4 d\lambda}{\int_0^\infty F_D(\lambda) d\lambda} \tag{2.18}$$

In Eqn. 2.17, $F_D(\lambda)$ is the fluorescence intensity of the donor between λ and $\lambda + d\lambda$ where the total intensity of the fluorescence spectrum has been normalized to a peak area of 1. Eqn. 2.18 is an equivalent expression showing the mathematical normalization of the emission peak. $\varepsilon_A(\lambda)$ is the molar absorption coefficient of the acceptor at wavelength λ. J is represented graphically in Figure 2.5, albeit qualitatively as the illustration does not account for the λ^4 dependence.

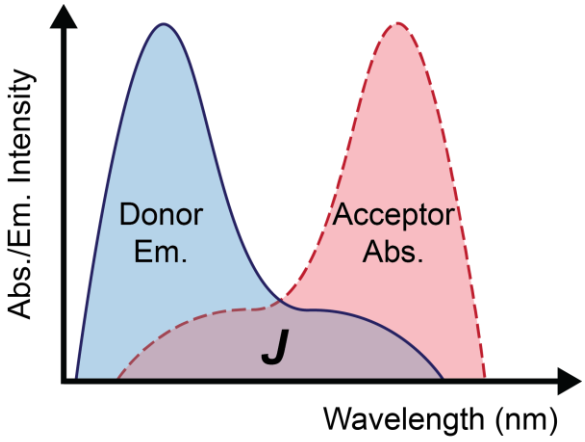

Figure 2.5 Graphical representation of the spectral over integral (purple) of the donor emission spectrum (blue) and the acceptor absorption spectrum (red).

It is often more convenient to describe FRET using distances rather than transfer rates. The donor-acceptor distance at which the FRET efficiency is 50% for a particular donor-acceptor pair is denoted the Förster distance, R_0, given by Eqn. 2.19.

$$R_0^6 = \frac{9000(\ln 10)\kappa^2 \Phi_D}{128\pi^5 N n^4} J(\lambda) \tag{2.19}$$

R_0 can be determined from the spectral properties of the donor-acceptor pair and the quantum yield of the donor. Typical R_0 values range from 2–6 nm. At R_0, half of the excited donors decay by FRET and half decay by the usual radiative and non-radiative pathways. The rate of FRET for a single donor and single acceptor can be determined by Eqn. 2.20 [162].

$$k_T(r) = \frac{1}{\tau_D}\left(\frac{R_0}{r}\right)^6 \tag{2.20}$$

FRET efficiency for a single donor-acceptor pair, E, is the fraction of photons absorbed by the donor whose energies are transferred to the acceptor and is given by Eqn. 2.21.

$$E = \frac{k_T(r)}{\tau_D^{-1} + k_T(r)} = \frac{R_0^6}{R_0^6 + r^6} \tag{2.21}$$

The FRET efficiency has a strong dependence on the donor-acceptor distance (Figure 2.6). When r is much less than R_0, FRET efficiency is near 100% and results in near complete quenching of the donor. When r is much greater than R_0, the FRET efficiency is near 0%. Thusly the practical range for FRET measurements ranges from $r = 0.5R_0$ (E = 95.5%) to $r = 2R_0$ (E = 1.54%) [162].

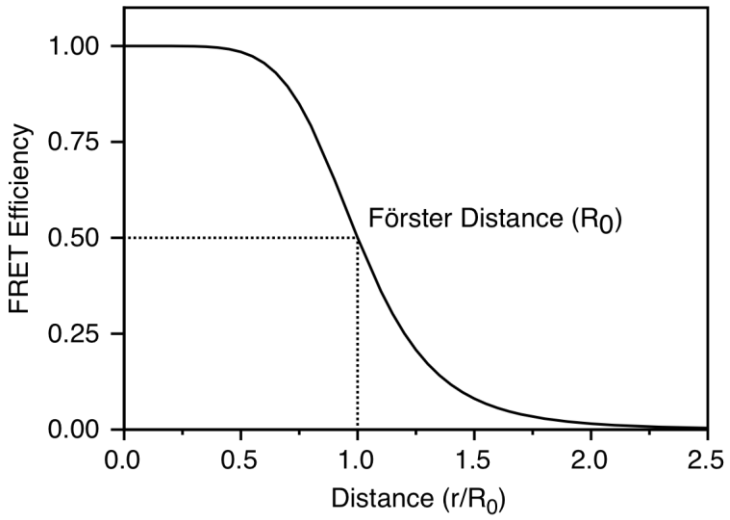

Figure 2.6 FRET efficiency as a function of the donor-acceptor distance, r, over the Förster distance, R_0.

When multiple equivalent acceptors (*i.e.*, dyes having the same identity and same donor-acceptor distance) are within close proximity of a single donor, Eqn. 2.21 becomes Eqn. 2.22 where a is the number of acceptors per donor. The probability and therefore efficiency of FRET increases in the presence of multiple donors as there are more energy transfer pathways available [166].

$$E = \frac{ak_T(r)}{\tau_D^{-1} + ak_T(r)} = \frac{aR_0^6}{aR_0^6 + r^6} \tag{2.22}$$

FRET efficiency can be tabulated directly from measurements of donor intensity or lifetime in the presence and absence of the acceptor, Eqn. 2.23, where *D* refers to the donor alone and *DA* refers to the donor in the presence of the acceptor [162].

$$E = 1 - \frac{F_{DA}}{F_D} = 1 - \frac{\tau_{DA}}{\tau_D} \tag{2.23}$$

2.2.2 Dexter energy transfer

Dexter energy transfer, also known as electron exchange, involves the transfer of an electron from a donor in the excited state to an acceptor in the ground state. Electron transfer requires overlap of the donor and acceptor molecular orbitals and thus Dexter ET only occurs appreciably for donor acceptor distances less than 5 Å [167]. The process of Dexter ET is illustrated in Figure 2.7.

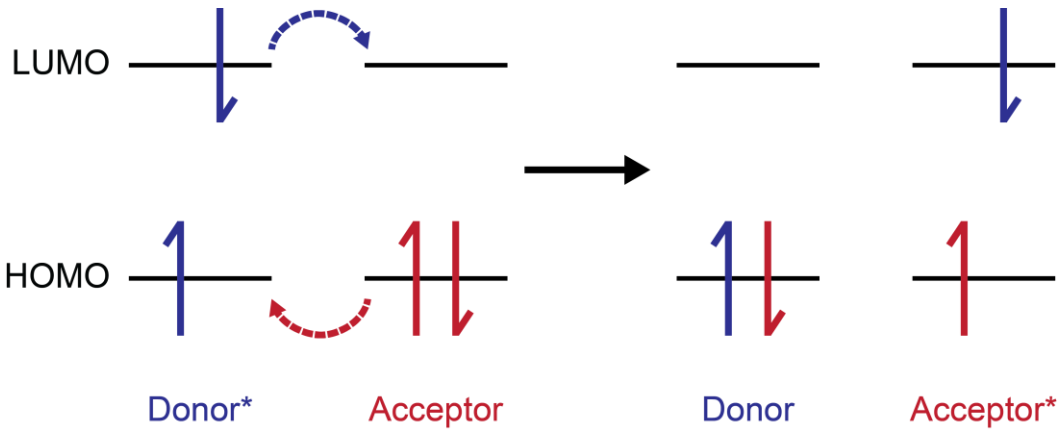

Figure 2.7 Schematic representation of Dexter energy transfer. A donor in its excited state (denoted by an asterisk) transfers an electron from its LUMO to the vacant LUMO of the acceptor. Concurrently, the acceptor transfers an electron from its HOMO to the singly occupied HOMO of the donor, leaving the acceptor in its excited state.

A donor in its excited state contains an electron in its LUMO. When in close contact (*i.e.*, within van der Waals contact distance) of a ground state acceptor, the electron in the excited state may be transferred to the acceptor. The acceptor simultaneously transfers an electron from its HOMO back to the donor. As a result the donor is in the ground state and the acceptor is in the excited state [162]. Although the result of Dexter ET is similar to that of FRET, the underlying mechanisms of ET, their rates and their dependences on the donor-acceptor distance are quite different.

The rate of Dexter ET, k'_T, is given by Eqn. 2.24, where h is the Planck constant (6.6×10^{-34} J s), K is an experimental constant not related to the spectral properties of the donor and acceptor, J' is the Dexter spectral overlap (Eqn. 2.25), r is the donor-acceptor distance, L is the average Bohr radius of the donor and acceptor, and R_c is the distance of closest approach, F($\bar{\nu}$) is the donor fluorescence intensity as a function of wavenumber, and ε($\bar{\nu}$) is the acceptor molar extinction coefficient as a function of wavenumber [115].

$$k_T^{'} = \frac{2\pi}{h} KJ' e^{\frac{-2r}{L}} = k_0^{'} e^{\frac{-2(r-R_C)}{L}} \tag{2.24}$$

$$J' = \frac{\int F(\bar{\nu})\varepsilon(\bar{\nu})d\bar{\nu}}{\int F(\bar{\nu})d\bar{\nu}\int \varepsilon d\bar{\nu}} \tag{2.25}$$

Unlike the r^{-6} dependence of FRET, the rate of Dexter ET decays exponentially as a function of the donor-acceptor distance. The steep decay in rate is responsible for the short-range nature of

Dexter interactions. Observations of Dexter ET are often challenging as FRET may occur between the donor and acceptor at longer separation distances before Dexter ET is able to occur (*i.e.*, before near-contact between the donor and acceptor for sufficient wavefunction overlap for Dexter ET) [162].

2.2.3 Photoinduced electron transfer

Photoinduced electron transfer (PET) is an additional energy transfer mechanism requiring van der Waals contact between a fluorophore and a quencher, and thus occurs at sub-nanometre length scales. PET can arise from molecular collisions or from the formation of excited state complexes that persist for multiple excitation-emission cycles [168].

Upon absorption of light and promotion to the excited state, the redox activity of a chromophore can change and favour PET. Depending upon the relative oxidation and reduction potentials of the fluorophore and the quencher, electron transfer can occur from the fluorophore to the quencher or *vice versa*. In descriptions of PET, the terms *donor* and *acceptor* refer to the species that donates or accepts the electron respectively and may be either the fluorophore or the quencher. The oxidative and reductive transfer processes are illustrated by Eqns. 2.26 (oxidative PET) and 2.27 (reductive PET) where *D* refers to the electron donor (either the fluorophore or the quencher), *A* refers to the electron acceptor and ● denotes a radical species. These processes are illustrated schematically in Figure 2.8.

$$^1D^* + A \rightarrow D^{\bullet+} + A^{\bullet-} \quad (2.26)$$

$$^1A^* + D \rightarrow D^{\bullet+} + A^{\bullet-} \quad (2.27)$$

Typically, PET forms a charge transfer complex (*e.g.*, D^+A^-) that returns to the ground state non-radiatively. In some cases, the formation of an excited state complex (exciplex) can lead to emission. As a final step, the electron is returned to the electron donor and the complex dissociates.

The standard Gibbs energy for either of the above reactions is given by Eqn. 2.28, where F is the Faraday constant (96 485 C mol^{-1}), E^0 is the reduction potential for the donor or acceptor, N is Avogadro's number, $h\nu_{00}$ is the excitation energy corresponding to the energy difference from $S_0\nu_0$ to $S_1\nu_0$ for the fluorophore, e is the electron charge, ε is the permittivity of the solvent, and R is the distance between the two species. The final term represents the Coulombic energy of the formed ion pair.

$$\Delta G^0 = F(E^0_{D^{\bullet+}/D} - E^0_{A/A^{\bullet-}}) - Nh\upsilon_{00} - \frac{Ne^2}{4\pi\varepsilon R} \quad (2.28)$$

For a given donor/acceptor pair in a given solvent, Eqn. 2.28 can be used to determine the feasibility of PET. Thermodynamic feasibility alone is not sufficient to predict PET; the rate of PET, which depends on the strength of the interaction between the donor and acceptor and the donor-acceptor distance, must also be competitive with other decay processes [115].

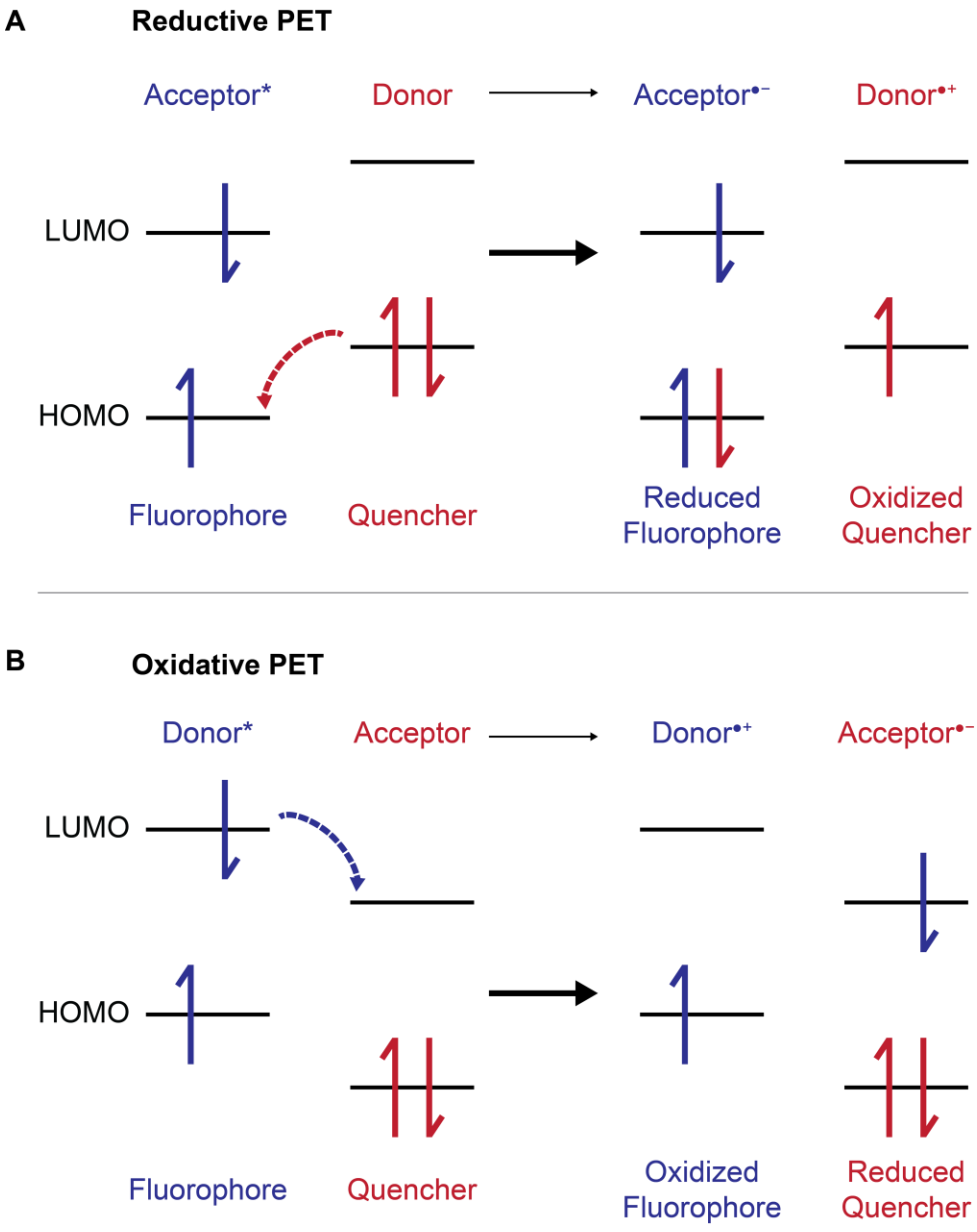

Figure 2.8 Schematic representation of **(A)** reductive PET and **(B)** oxidative PET. Reductive PET occurs when the HOMO of the fluorophore is lower in energy than the HOMO of the quencher. Promotion of an electron to the fluorophore's LUMO leaves a vacancy in its HOMO into which the quencher transfers an electron. Oxidative PET occurs when the quencher's LUMO is of lower energy than the LUMO of the fluorophore. Upon excitation, the electron in the fluorophore's LUMO is transferred to the vacant LUMO of the quencher. The terminology donor and acceptor here refer which species is donating/accepting the electron.

Chapter 3: General experimental methods

This chapter includes the experimental methods that are common between the subsequent research chapters. Chapters 5–7 will contain additional experimental methods specific to that chapter. Kelsi Lix designed and/or executed the experimental methods in this chapter, except for the AFM imaging experiments, which were done by Ethan Sauvé.

3.1 Polymer materials

Poly(9,9-dioctylfluorene-*alt*-benzothiadiazole) (F8BT, M_n 17–23 kDa), poly(styrene-*co*-maleic anhydride) (PSMA, M_n 1.7 kDa), poly(maleic anhydride-*alt*-1-octadecene) (PMAO), Jeffamine ED-600, IGEPAL CO-520, polyethylene-block-poly(ethylene glycol) (PE-b-PEG), Brij L23 and Pluronic F-127 were from Sigma-Aldrich (Oakville, ON, Canada). Poly[(9,9-dioctyl-2,7-divinylenefluorenylene)-*alt*-*co*-(9,10-anthracene)] (PFVA), poly[(9,9-dioctyl-2,7-divinylenefluorenylene)-*alt*-*co*-(2-methoxy5-(2-ethylhexyloxy)-1,4-phenylene)] (PFMEHPPV), poly[2-methoxy-5-(2-ethylhexyloxy)-1,4-phenylene-vinylene] (MEHPPV), and poly[2-methoxy-5-(2-ethylhexyloxy)-1,4-(1-cyanovinylene-1,4-phenylene)] (CNMEHPPV) were from American Dye Source, Inc. (Baie D'Urfé, PQ, Canada). Poly(styrene-*block*-acrylic acid) (PS-b-PAA), poly(styrene-*block*-ethylene oxide) (PS-b-PEG), and polystyrene-*graft*-ethylene oxide functionalized with carboxy (PSPEGCOOH) were from Polymer Source Inc. (Dorval, PQ, Canada).

3.2 Other materials

Water (>18.2 MΩ cm) was from a Milli-Q Synthesis Water Purification System from Millipore (Burlington, MA). 4-(2-hydroxyethyl)-1-piperazineethanesulfonic acid (HEPES) buffer and 1-

ethyl-3-(-3-dimethylaminopropyl) carbodiimide (EDC) were from Sigma-Aldrich (Oakville, ON, Canada). Agarose (low EEO) was from Fisher Scientific (Waltham, MA).

3.3 Pdot synthesis

Pdots were synthesized by the nanoprecipitation method [59]. In a typical synthesis, 100 μL of F8BT solution (1 mg/mL in THF) and 20 μL of PSMA solution (1 mg/mL in THF) were diluted to 5 mL with THF for final concentrations of 20 μg/mL and 4 μg/mL, respectively. The precursor solution was sonicated for 30 s to ensure complete mixing. A syringe was used to rapidly inject precursor solution into 10 mL of ultrapure water under sonication. Sonication was continued for an additional 2 min. The Pdot solution was concentrated by partial rotary evaporation or by heating to 90 °C under N_2 flow. Any large aggregates were removed by passing the concentrated solution through a 0.22 μm syringe filter.

3.4 Pdot characterization

Nanoparticle sizes and concentrations were determined by nanoparticle tracking analysis (NTA) using a NanoSight NS300 (Malvern Panalytical, Malvern, UK). Measurements were recorded in scattering and fluorescence modes (500 nm long pass filter) using a scattering/excitation laser wavelength of 488 nm. Pdots were diluted 500–5000× in 0.22 μm-filtered ultrapure water. Raw data were fit with a lognormal function, Eqn. 3.1 (where A, x_c and w are the parameters used for fitting), to determine particle sizes. Concentrations were usually determined by averaging the results from the scattering and fluorescence modes.

$$f(x) = \frac{A}{\sqrt{2\pi}wx} e^{-\frac{\left(\ln\frac{x}{x_c}\right)^2}{2w^2}} \quad (3.1)$$

Dynamic light scattering (DLS) and zeta potential measurements were performed using a NanoBrook Omni particle size analyzer (Brookhaven Instruments Corporation, Holtsville, NY) equipped with a 659 nm laser.

Transmission electron microscopy (TEM) images were recorded on a Hitachi H7600 TEM with an accelerating voltage of 80 kV. Undiluted aqueous Pdots (5 µL) were drop cast onto carbon coated copper grids (Ted Pella, Inc., Redding, CA) and dried at room temperature.

Atomic force microscopy (AFM) images were obtained (by Ethan Sauvé) using an Asylum Instruments Cypher S AFM system in tapping mode at scan rates of 0.1 Hz. Samples were prepared by spin-coating solutions of Pdots dispersed in water onto freshly cleaved mica at 2500 rpm for 1.5 min at concentrations of ~500 pM. Samples were placed under vacuum for at least 2 h before images were obtained using Mikromasch HQ:NSC14/No Al or HQ:NSC19/No Al probes, with typical resonance frequencies *f* and spring constants *k* of (*f* = 160 kHz, *k* = 5 N/m) and (*f* = 65 kHz, *k* = 0.5 N/m), respectively.

Pdots were analyzed by agarose gel electrophoresis. Samples were prepared by mixing 10 µL of aqueous Pdot solution (~500 pM-1 nM) with 4 µL of aqueous glycerol (20% v/v). Samples were loaded onto a 0.5% w/v agarose gel and run at 100 V (~6.5 V cm^{-1}) for 30 min in 1X TBE buffer

(pH 8.3, 89 mM Tris-borate, 2 mM EDTA). Gels were imaged under UV illumination (302 nm) using a Bio-Rad Gel Doc™ XR.

Photobleaching measurements were performed using an Olympus IX83 inverted fluorescence microscope. Aqueous samples (5.0 µL) with approximately equal initial fluorescence intensities were continuously irradiated with blue light (450/50 BP excitation filter) for 1.5 h. Images were captured every 60 s (500 LP emission filter and T510 dichroic mirror) and intensity values were determined using the Time Series Analyzer V3 plugin in ImageJ software (National Institutes of Health, Bethesda, MD).

3.5 Spectroscopic measurements

Absorbance spectra and fluorescence emission and excitation spectra of aqueous samples were measured using an M1000 multifunction fluorescence plate reader using 5 nm excitation and emission bandwidths (Tecan, Morrisville, NC).

Absorbance spectra of solution phase SPs were recorded using an Agilent Cary 5000 UV-Vis-NIR spectrophotometer. Fluorescence emission and excitation spectra of solution-phase SPs were recorded using an Agilent Cary Eclipse fluorescence spectrophotometer.

Fluorescence lifetime measurements were made on a Zeiss LSM510 two photon scanning confocal microscope equipped with a fluorescence lifetime imaging module (Becker & Hickl GmbH, Berlin, Germany). Two-photon excitation (720–800 nm) was from a tunable Coherent Chameleon XR femtosecond laser with a repetition rate of 80 MHz and a pulse width of 140 fs. Data

acquisition was done over 16 wavelength channels with an *xy*-resolution of 128 × 128 pixels and 256 time-channels with data collection for 30–60 min.

Quantum yields were determined a FS5 Spectrofluorometer (Edinburgh Instruments, Livingston, UK) fitted with an integrating sphere sample cassette, or by comparison with a standard. For the relative determination of quantum yield, fluorescein was used as a standard, either in ethanol (Φ = 0.79) or 0.1 M NaOH (Φ = 0.95). Five standard solutions of Pdots or fluorescein were prepared with maximum absorbances between 0.01–0.1, and the absorbance and emission spectra recorded. Linear plots of the absorbance (at 460 nm for F8BT Pdots) versus the integrated fluorescence intensity were obtained. The quantum yield was determined by Eqn. 3.2, where Φ is the quantum yield, m is the slope of the linear region of the plot, and η is the solvent refractive index of the sample or the fluorescein reference standard (std).

$$\Phi_{sample} = \Phi_{std}\left(\frac{m_{sample}}{m_{std}}\right)\left(\frac{\eta^2_{sample}}{\eta^2_{std}}\right) \tag{3.2}$$

Chapter 4: Physical and optical characterization of Pdots

4.1 Introduction

The term *Pdot* refers to a broad class of materials that have similar compositions and similar physical and optical properties. Virtually any hydrophobic semiconducting polymer (SP) is a likely candidate for the formation of aqueously dispersed nanoparticles (NPs), typically with the inclusion of an amphiphilic species to confer colloidal stability. Despite the wide range of materials that can be used to make Pdots, their overall physical properties are often similar. Any significant change in physical properties is often caused by the choice of amphiphilic component, whereas the optical properties of Pdots are largely determined by which SP is used in their synthesis. Unaggregated SPs exhibit many of the same optical signatures as Pdots: broad absorbance and emission peaks, short fluorescence lifetimes, and high quantum yields. Some optical properties change between the unaggregated polymer and the NP because of changes in effective conjugation length and local environment upon chain collapse, but the overall optical properties of the unaggregated SP are largely retained. The emission colour or other desired optical properties can therefore be tuned by appropriate selection of the SP.

This chapter presents an overview of the materials used for Pdot synthesis in this thesis, as well as the methods used for physical and optical characterization. Pdots were synthesized using commercially available SPs and amphiphilic copolymers. Typical results for each characterization method are described alongside representative data. Chapters 5–7 will also report characterization of the specific materials used therein.

Although the Pdot materials used throughout this thesis share similar physical and optical properties, their structures are poorly defined and challenging to characterize. Batch-to-batch variation arising from the synthetic method was observed to be significant, highlighting the importance of thorough characterization before use in downstream experiments. Owing to their good reproducibility and favourable optical properties, F8BT/PSMA Pdots were used most commonly throughout this work, although other types of materials are surveyed in Chapter 5, some of which presented additional characterization challenges. Despite these challenges, Pdots have found use in a wide variety of analytical applications and continue to be a promising emergent ultrabright fluorescent probe.

4.2 Materials

Dozens of SPs with emission colours spanning the visible spectrum are commercially available. We selected a series of polymers with emission colours ranging from green to red as these colours are best suited for our characterization methods and downstream bioanalytical applications. The molecular structures of these materials are shown in Figure 4.1. The SPs contain either the fluorene monomer or the methoxy-phenylene vinylene monomer. Emission stemming from these core functional groups is tuned by the inclusion of other functional groups along the polymer backbone (*i.e.*, that cause a change in bandgap energy) [65]. These polymers contain extended pi-conjugation throughout their backbones which leads to suitable energy level overlap for the formation of quasi-continuous valence and conduction bands, giving rise to their semiconducting properties. They also contain extended alkyl chains to confer solubility in organic solvents (*i.e.*, solution processability).

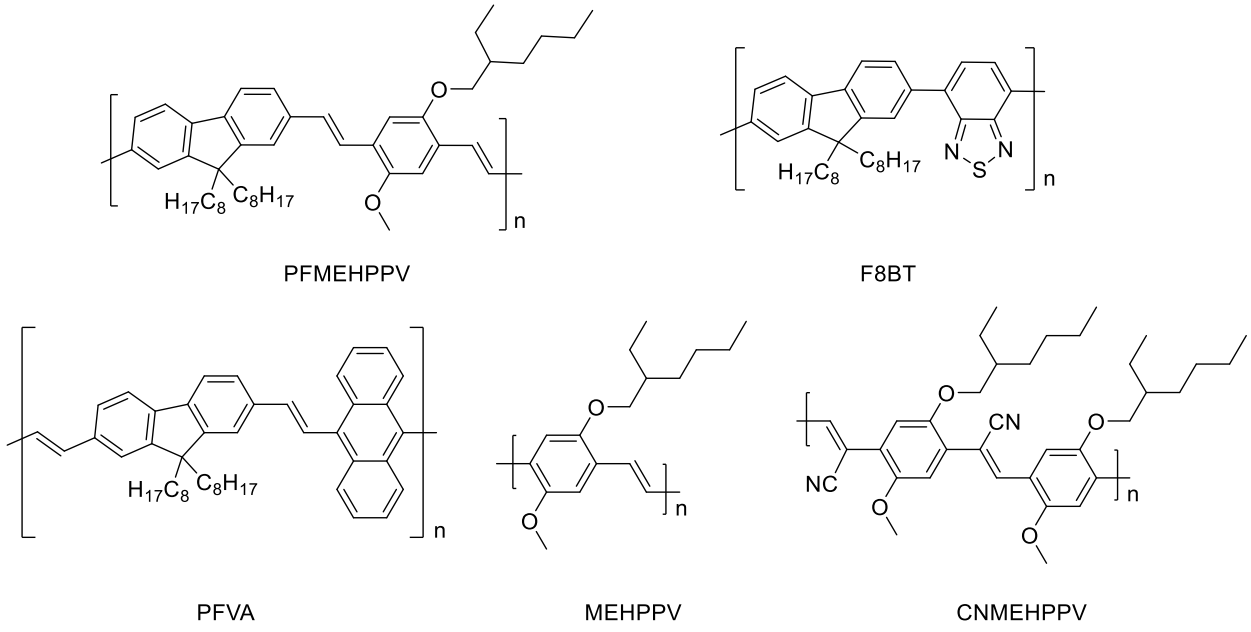

Figure 4.1 Chemical structures of SPs used to make Pdots in this thesis.

The co-condensation of an amphiphilic species with a SP increases the colloidal stability of the Pdots and provides reactive groups for conjugation reactions. In this work, Pdots were most often synthesized with PSMA as the amphiphilic component, as this amphiphile provided reliable stability against buffer or other chemical reagents. PSMA is a random copolymer of styrene and maleic anhydride monomers. It is thought that the hydrophobic styrene residues interact with the hydrophobic SP during Pdot synthesis, anchoring the amphiphile to the Pdot core [26]. The maleic anhydride groups hydrolyze when introduced to water, resulting in two carboxylic acid groups that, on average, are thought to remain at the particle surface due to their negative charge above pH 5 (Scheme 4.1). These functional groups impart additional colloidal stability and provide chemical handles for bioconjugation reactions that are not natively found in commercial SPs.

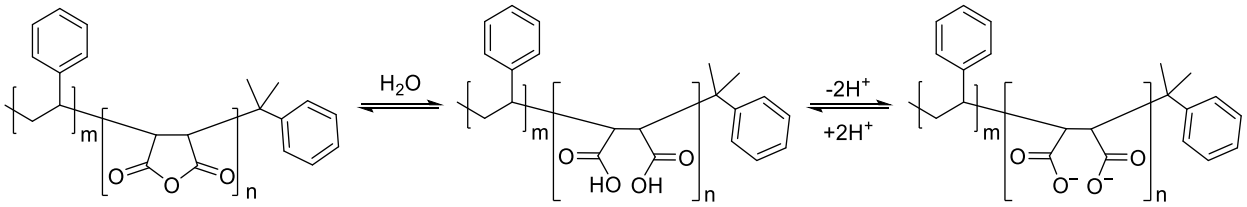

Scheme 4.1. Hydrolysis of PSMA in the presence of water.

Other amphiphilic polymers (APs) were used in this thesis to a lesser extent than PSMA. These polymers may be generally classified as co-polymers with ionizable functional groups (*e.g.*, carboxylic acids, amines) or surfactants with at least one polyethylene glycol segment in the polymer chain. The structures of the amphiphilic copolymers used for Pdot synthesis are shown in Figure 4.2.

Pdots were synthesized from one SP and from either one AP or occasionally without an amphiphile. It is possible to compose a Pdot with multiple SPs; however, highly efficient energy transfer is likely to take place because the chromophores are in close proximity, resulting in emission only from the species with the lowest energy emission band [85, 113]. Hydrophobic dopants such as organic dyes may be introduced during Pdot synthesis or may be added post-synthetically via non-specific partitioning.

4.3 Physical characterization

Several characterization methods were used to measure the physical properties of Pdots, most importantly the size and size distribution, the electrophoretic mobility, and the concentration. This section introduces each technique and gives a general summary of its results.

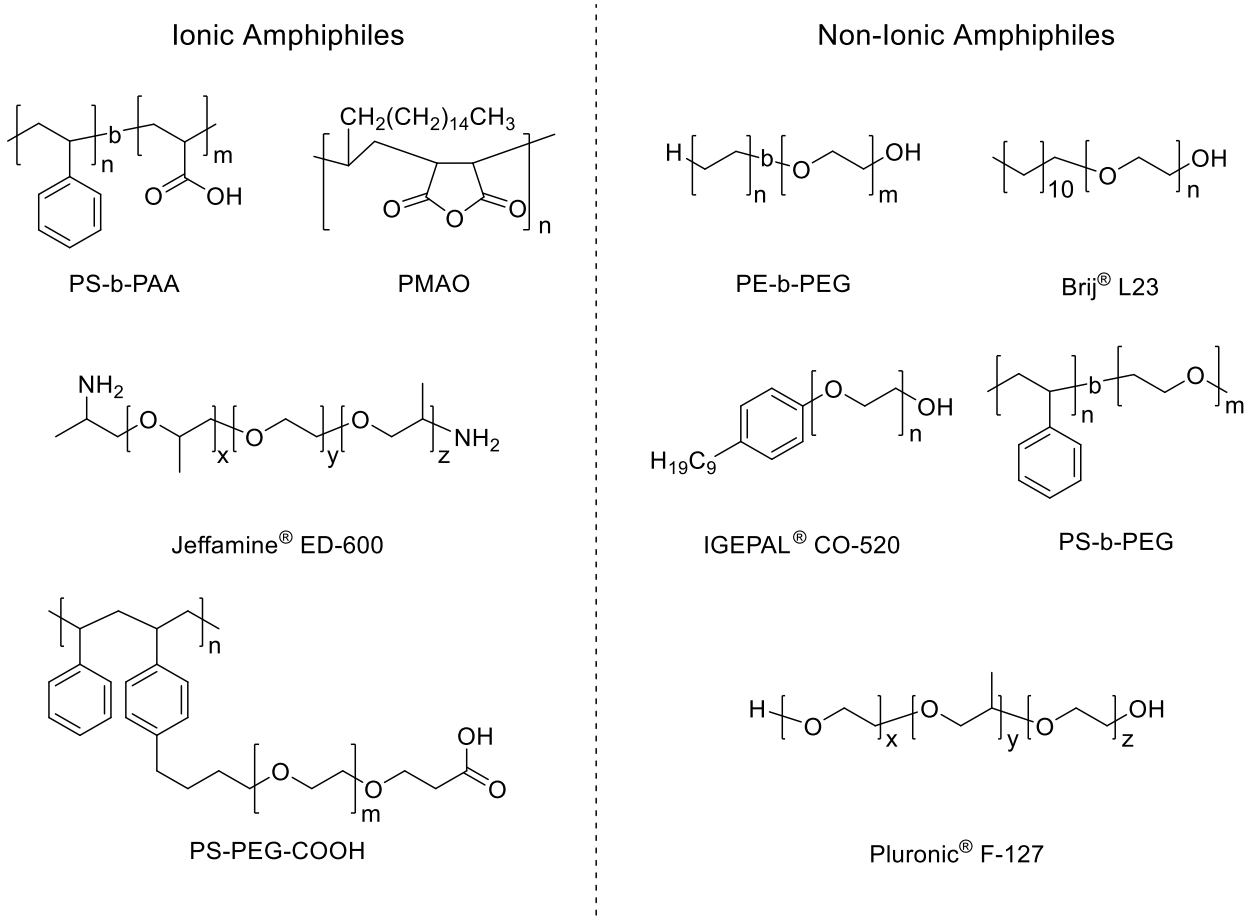

Figure 4.2 Chemical structures of ionic and non-ionic polymeric amphiphiles used to synthesize Pdots.

4.3.1 Hydrodynamic diameter

The hydrodynamic or Stokes radius of a particle represents "the radius of a hard sphere that diffuses at the same rate as that solute," or, equivalently, the "effective hydrated radius in solution" [169]. This value incorporates the effect of any ions and water molecules solvating and therefore diffusing with the NP. There is likely a strong solvation effect on the Pdot surface, as the negatively charged carboxyl groups strongly attract polar water (or solvent) molecules or dissolved ions. The extent of the solvation effect is determined by the strength of the electric field created by the particle. As Pdots are a soft, permeable material, it is also likely that the particles are somewhat swollen with water molecules, dissolved ions, or other small molecule species that escape the core (de-swell) when measurements are performed under vacuum or when samples are otherwise dried. The hydrodynamic radius is measured in the solution phase and therefore best represents the effective size of NPs as utilized in aqueous or solution phase experiments.

Hydrodynamic diameters were measured by two complementary techniques: nanoparticle tracking analysis (NTA) and dynamic light scattering (DLS). NTA is a single particle technique in which a dilute solution of NPs is irradiated with a laser. The NPs are sufficiently dilute so that the scattering and/or fluorescence from single NPs can be detected by a 20X objective lens in line with a camera (*e.g.*, sCMOS) (Figure 4.3A), and that the particles collide with one another infrequently. A video is recorded at 30 fps and the Brownian motion of the particles across the viewing window is tracked in two dimensions. The hydrodynamic radius, R_H, is calculated using the Stokes-Einstein (Eqn. 4.1), where $\overline{(x,y)^2}$ is the mean-squared speed of an individual particle, k_B is the Boltzmann constant (1.38×10^{-23} J K^{-1}), T is the temperature, and η is the viscosity of the medium [170].

Several hundred individual particles are tracked, and a distribution of particle sizes is determined. The raw distributions were fit with a lognormal function, Eqn. 4.2, where A, x_c, and s are the parameters used for fitting. Mean and mode particle diameters and standard deviations are determined from the lognormal distribution (Figure 4.3B). In practice, particles are flowed across the viewing window in order to obtain sufficiently high particle counts and the models are adapted to account for particle velocity from solution flow [171-172].

$$\overline{(x,y)^2} = \frac{2k_bT}{3R_H\pi\eta} \tag{4.1}$$

$$y = \frac{A}{\sqrt{2\pi}wx} e^{\frac{-\left(\ln\frac{x}{x_c}\right)^2}{2w^2}} \tag{4.2}$$

Pdot samples typically yielded mean and mode diameters between 30–100 nm by NTA, with large standard deviations of 20–40 nm. Measurements in scattering mode or fluorescence mode (*i.e.*, with a long pass filter to block scattered laser light from reaching the detector) often yielded slightly different particle sizes. Size differences not withstanding, the NTA scattering mode cannot discern nanoparticles from any dust or other particulate matter in the sample that scatters the laser light, which may influence the obtained size and size distribution. Although fluorescence mode excludes any non-fluorescent material in the sample, the NTA fluorescence mode may exclude smaller, less bright particles from the size distributions. In most cases, the reported mean or mode diameter from NTA was taken as the average of the corresponding values from scattering and fluorescence mode measurements, which typically agreed within ±10% for a well-behaved sample.

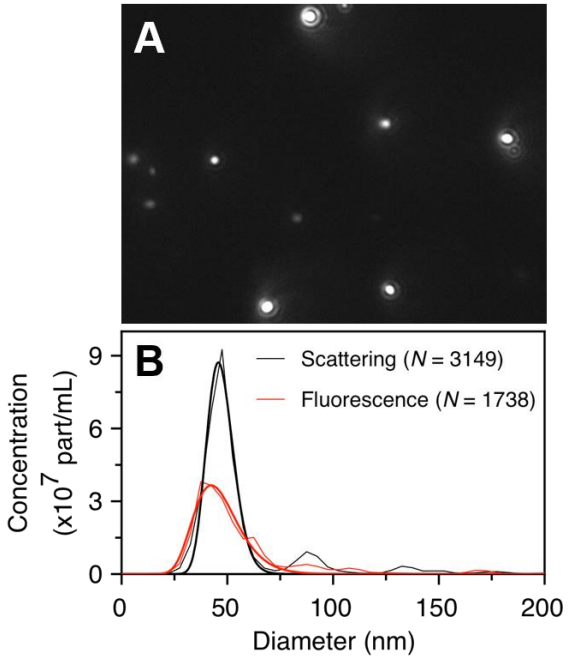

Figure 4.3 Nanoparticle tracking analysis. **(A)** Still frame from an NTA video of F8BT/PSMA Pdots recorded in fluorescence mode. **(B)** Raw data and lognormal fit curves for a representative sample of F8BT/PSMA Pdots in scattering (47 (46) ± 6 nm) and fluorescence modes (46 (43) ± 11 nm). The notation is mean (mode) ± standard deviation of the lognormal distribution.

DLS is an ensemble technique that measures many particles simultaneously. A relatively concentrated NP sample is irradiated with a monochromatic light source, usually a laser. Because the NPs sizes are significantly smaller than the wavelength of the incident beam, the NPs scatter the incident light in all directions (*i.e.*, Rayleigh scattering). The measured scattering intensity fluctuates with time due to the Brownian motion of the individual particles in solution. The scattered light will interfere constructively and destructively depending upon the motion of the particles, producing a two-dimensional 'speckle pattern' of bright and dim spots. Smaller, more rapidly diffusing particles cause the intensity signal to fluctuate rapidly compared to larger, more slowly diffusing particles. The intensity at a given spot over time is analyzed using an

autocorrelation function, Eqn. 4.3, where $g^2(\tau)$ is the normalized autocorrelation function, and the scattered intensities at an arbitrary time, t, and after a delay time, τ, are $I(t)$ and $I(t + \tau)$ respectively.

$$g^2(\tau) = \frac{\langle I(t)I(t+\tau)\rangle}{\langle I(t)\rangle^2} \tag{4.3}$$

At short delay times, the particles have not diffused much from their initial positions and the scattered intensity has not changed significantly, leading to high correlation. At longer delay times, the correlation decays exponentially as the particles diffuse away from their initial positions. The autocorrelation function decays more rapidly for smaller particles. Analysis of the autocorrelation function yields information about the time scale of translational diffusion of the particles, and therefore their hydrodynamic radius can be determined by the Stokes-Einstein equation (Eqn. 4.4) [173-174].

$$R_H = \frac{k_B T}{6\pi\eta D} \tag{4.4}$$

The size distributions of Pdots measured by DLS are best described by a lognormal distribution. Because larger particles have a greater contribution to the observed scattering, DLS is biased towards larger particle sizes and is not an ideal method for sizing polydisperse samples such as Pdots. However, DLS is useful for measuring samples that are not suited for measurement by NTA, such as samples that are small (< 30 nm in diameter), not brightly emissive, or weakly scattering.

A representative intensity-weighted and number-weighted size distribution measured by DLS is shown in Figure 4.4. DLS measurements of Pdots typically result in broad lognormal size distributions with mean and mode diameters less than 100 nm. The intensity distribution is weighted by the scattering intensity of each particle, which is a function of the particle's size and refractive index. The scattering intensity is therefore biased towards larger sizes by aggregation or a small population of larger particles. The intensity-weighted distribution can be converted to a number-weighted distribution when the refractive index of the material is known. The number-weighted distribution represents the number of particles in each bin of a given histogram [175]. For intensity-weighted distributions, the mean and mode diameters are usually greater than those determined by NTA, due to the increased influence of larger sized particles. DLS was used as a secondary technique either to validate NTA results or to measure Pdot samples that were unsuitable for analysis by NTA.

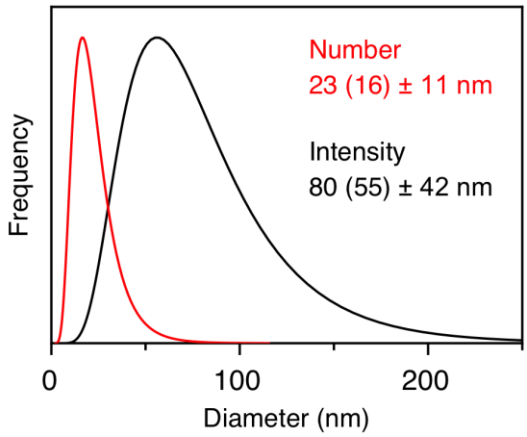

Figure 4.4 Representative intensity-weighted and number-weighted lognormal size distributions of F8BT/PSMA Pdots measured by DLS. Sizes are denoted as (mean (mode) ± 1 standard deviation).

4.3.2 Dehydrated sizes and particle morphology

TEM and AFM were used to determine the sizes of dehydrated Pdots. These methods require samples to be deposited on a surface and dried. Therefore, images are obtained of de-swelled particles. Although these methods are not truly representative of a Pdot in the solution phase, they can give direct information about particle size and morphology of the sample. As both methods analyze individual particles, raw measurements are not biased by the overall size distribution of the sample.

In TEM, a beam of electrons is accelerated through an ultra-thin sample. Contrast is achieved where the sample and the background have different electron densities. TEM showed that Pdots formed spherical or near-spherical particles (Figure 4.5). Typical dehydrated Pdot diameters were less than 100 nm with broad size distributions (standard deviation 30–40 nm). Although TEM is a robust characterization method, it is non-trivial to image the amphiphilic species or any non-conductive additives (*e.g.*, soft surface materials, small molecule cargo) because they will not interact strongly with the electron beam.

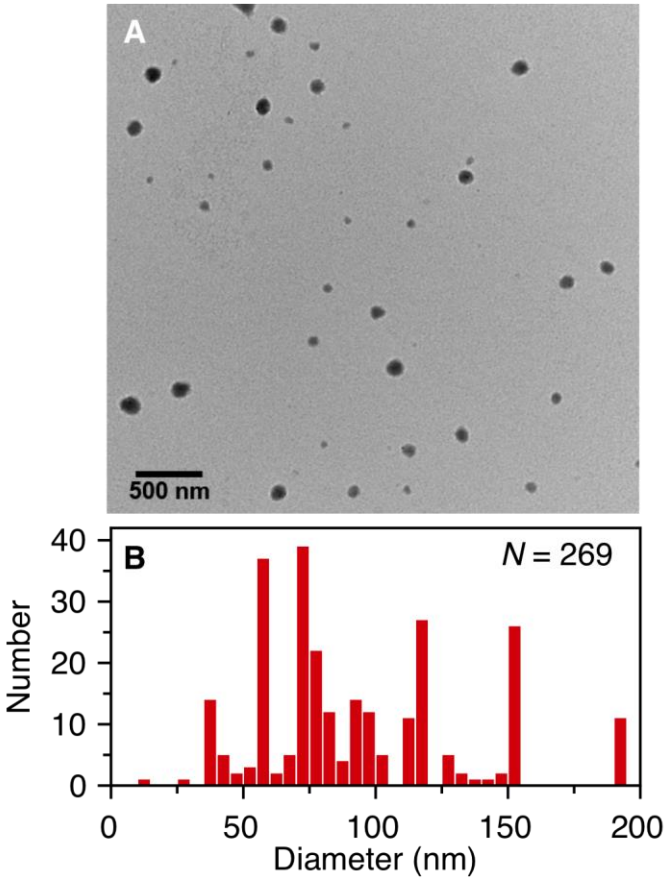

Figure 4.5 TEM characterization **(A)** TEM image of F8BT/PS-PEG-COOH Pdots. Average diameter 95 ± 43 nm (*N* = 269). 30000X magnification. **(B)** Size histogram for F8BT/PS-PEG-COOH Pdots.

In AFM, a nanometre-sized tip is rastered across a sample deposited on a flat substrate. The tip is affixed to a cantilever whose position is modulated by interactions between the tip and the sample. The extent of this modulation is recorded for each measured pixel and used to construct an image [176]. The AFM images shown in Figure 4.6 were recorded in tapping mode, where the AFM tip was oscillated at its resonant frequency. The amplitude of the oscillation is modulated by the surface topography of the sample and this information is used to generate the topography image. Tapping mode is preferred for fragile samples that may be disrupted by the higher lateral forces of

contact mode AFM [177]. The AFM image shows the morphology of dehydrated particles including any contribution from the amphiphilic component. The x/y resolution of the technique is limited by the size of the AFM tip, which is usually comparable to the size of the features being measured for the analysis of nanoparticles. The deflection of the AFM tip gives information about the height of measured features. Height measurements correspond to the dehydrated particle diameter, although this value is not fully reliable due to the soft nature of the materials. The observed height may decrease if there are significant interactions between the Pdot and the substrate as it dries, such that the Pdot loses its solution-phase morphology.

A typical AFM image of F8BT/PSMA Pdots is shown in Figure 4.6. Pdots whose structures are not further stabilized tend to form large aggregates as they dry on the hydrophilic substrate. Aggregates can be identified by analysis of height traces which tend to have multiple peaks implying multiple spherical particles have come together to form one mass. Non-aggregated particles tend to maintain a near-spherical morphology with similar dehydrated diameters as measured by TEM.

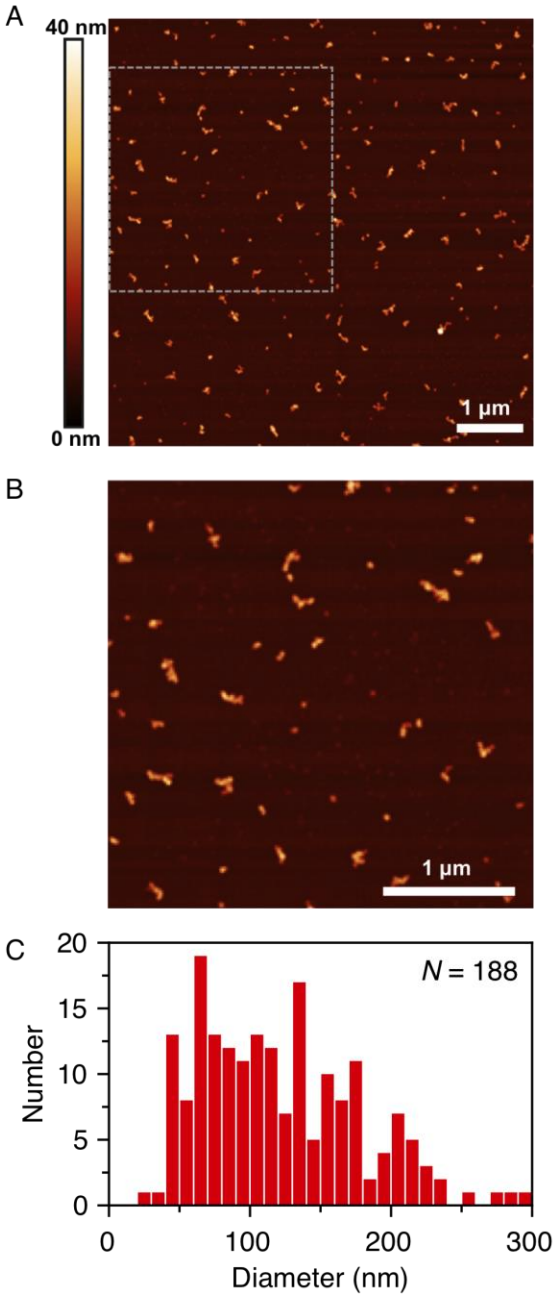

Figure 4.6 AFM characterization. **(A)** AFM topography image of F8BT/PSMA Pdots. Panel **(B)** corresponds to the region in the gray box in panel A. **(C)** Size histogram from AFM image.

4.3.3 Electrophoretic mobility and zeta potential

The electrophoretic mobility and zeta potential of a sample are related to its surface charge. Surface charge is an important parameter for a number of reasons. For example, surface charge can be correlated to the electrostatic colloidal stability of a particle, as modelled by DLVO theory [178]. The polarity and magnitude of the surface charge can also be used to infer the chemical nature of the particle surface and predict its behaviour, namely how it may interact with other species present in solution. It is non-trivial to directly measure the surface charge of a nanoparticle, so indirect techniques such as gel electrophoresis and zeta potential measurements are often used to indirectly probe the characteristics of the surface.

In gel electrophoresis, aqueous samples are loaded into hollow wells in a porous gel material. An electric field is applied across the gel, and samples migrate through the pores towards the opposite potential of their surface charge. The extent of migration through the gel depends on both the size and surface charge of the sample. Smaller species will migrate more easily through the porous structure of the gel and will therefore migrate further. Species with a higher surface charge-to-volume ratio experience a greater potential difference and will therefore be more strongly attracted to the opposite pole, resulting in increased migration. Gel electrophoresis can be used qualitatively and quantitatively (*e.g.*, Ferguson analysis) to infer information about both the size and surface charge of the species. Quantitative analysis generally requires well-defined bands. When qualitative, gel electrophoresis is most often used comparatively. For example, it is often used to test for chemical modification of the particle surface, or for the successful attachment of another

species to the particle surface, as these modifications may affect both the hydrodynamic size and surface charge of the particles.

Monodisperse, well-behaved samples will form narrow bands during migration through the gel. Materials such as QDs or gold nanoparticles typically exhibit narrow bands due to their good monodispersity and hard character. Pdots rarely exhibit this behaviour, and typically form non-uniform streaks originating from the well. Streaking may be a result of the large size distribution typical of Pdots, or, potentially, nonspecific interactions between Pdots and the agarose gel. It is also possible that Pdots unfold under the conditions in which the gel is run, and individual hydrophobic polymer chains bind non-specifically to the agarose gel. The electric field acts primarily on charged species (*e.g.*, the amphiphile and any charged species resulting from oxidation of the SP), and it may be possible that the pull of the electric field overcomes the weak hydrophobic interactions between the amphiphile and SP, resulting in unfolding.

The migration of Pdots in gel electrophoresis largely depends upon the choice of amphiphile. A fluorescence image of an agarose gel run with F8BT Pdots made with various amphiphiles is shown in Figure 4.7. Lane (i) shows F8BT Pdots with no amphiphile. Without the additional stabilization associated with the amphiphile, Pdots tend to form large (> 100 nm) aggregates and have low surface charge. Pdots synthesized without amphiphiles may be stabilized by the formation of negatively charged surface defects resulting from oxidation of the polymer chain [62]. Lanes (ii), (iii) and (iv) show Pdots made with ionic amphiphiles. These materials behave similarly, migrating towards the anode and forming streaks due to the negative surface charge

conferred by amphiphile carboxylate groups. Lanes (v), (vi) and (vii) correspond to Pdots synthesized with various non-ionic amphiphiles. Owing to their charge neutrality, these Pdots do not migrate strongly towards the anode. For neutral Pdots, some proportion of the sample may migrate towards the cathode because of electroendosmosis within the gel, as observed in lane (vii). In all lanes, some fluorescence is visible within the wells, arising from a population of aggregates or nanoparticles too large to enter the pores of the gel.

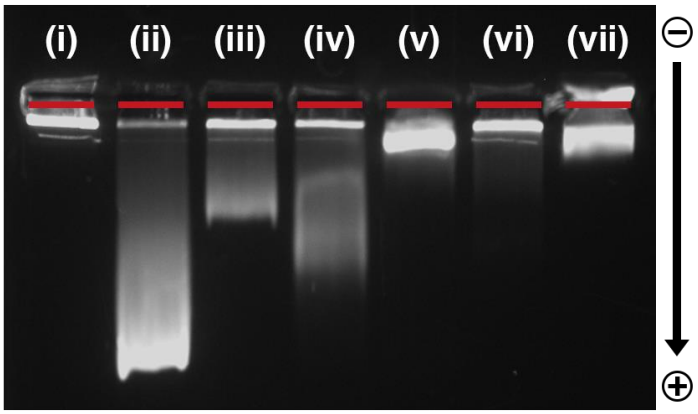

Figure 4.7 Fluorescence image of an agarose gel (0.5% w/v) of F8BT Pdots with (i) no amphiphile, (ii) PSMA, (iii) PSPEGCOOH, (iv) PMAO, (v) Pluronic F127, (vi) PE-b-PEG, and (vii) PS-b-PEG. The field strength was ~6.5 V cm^{-1} and the gel was run for 30 min.

Agarose gel electrophoresis was used over polyacrylamide gel electrophoresis (PAGE) because agarose gels have larger poor sizes better suited to the analysis of nanoparticles. PAGE is most commonly used for the separation of biological macromolecules. Attempts to characterize Pdots by capillary electrophoresis were not successful as the Pdots never eluted from the capillary.

A charged colloidal particle such as a Pdot is immediately surrounded by a somewhat immobile layer of counterions that strongly adhere to the particle surface, known as the Stern layer (Figure 4.8). Beyond this layer is a second, more diffuse layer of ions whose electrostatic interactions with the colloid are partially screened by the Stern layer. Both of these layers together are known as the electric double layer, and the ions contained therein diffuse with the particle through space. The boundary between the electric double layer and bulk solvent molecules is known as the slipping plane. The zeta potential is a measurement of the electric potential difference at the slipping plane and the bulk solution (*i.e.*, randomly oriented solvent molecules distant from the particle). The zeta potential is often used as a measure of the electrostatic stability of colloids. Particles with a high surface charge, positive or negative, will strongly repel one another, preventing aggregation or coagulation [169, 179].

The specific surface chemistry of a colloid determines its zeta potential. Pdots synthesized to have carboxylate surface chemistries display strongly negative zeta potentials (−10 mV or more in magnitude) as expected for a material with a negatively charged surface. Considerable batch-to-batch variation in the value for the zeta potential was observed, even for samples composed of the same materials and synthesized in the same way. The measured zeta potential represents the average across an ensemble, and Pdots are highly polydisperse, such that the measured zeta potential value may not truly encompass the variety of surface charges and electrostatic behaviour across an ensemble of Pdots.

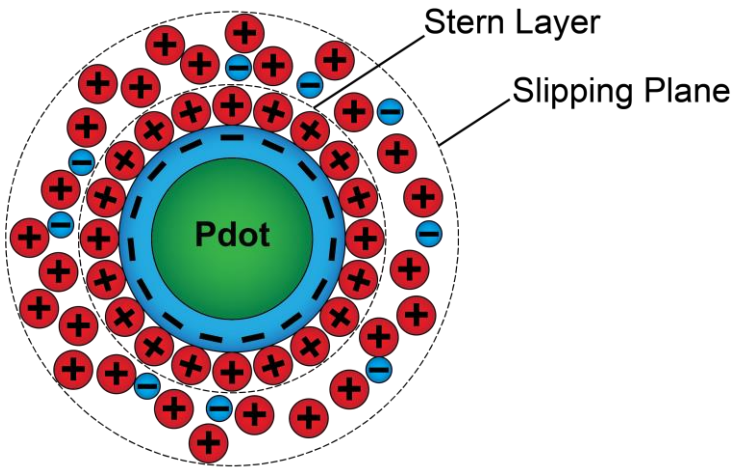

Figure 4.8 A negatively charged shell (amphiphile; blue) surrounds a hydrophobic Pdot core (SP; green) and attracts a layer of positively charged ions that diffuse with the particle and are known as the Stern layer. A second, more diffuse layer of counterions is also attracted to the Pdot, albeit that these interactions are partially screened by the Stern layer. The two layers of counterions are collectively known as the electric double layer.

4.3.4 Concentration

Pdot concentrations are often reported in units of μg/mL or ppm. These values reflect the total amount of material added in solution, but do not account for any losses from aggregation or precipitation and do not reflect the concentration of discrete NPs. For other types of NPs where the molar extinction coefficient is known, concentrations are usually determined by UV-vis absorption measurements. It is nontrivial to estimate the molar extinction coefficient of Pdots, as each NP contains many individual chromophores, and these chromophores exist in different local environments. It is not possible to determine the exact number of chromophores or their precise arrangement within the NP core. There is also considerable variation in particle size across and between ensembles, and it is not necessarily accurate to make estimations based solely on mean or mode sizes. Other techniques must therefore be used to determine Pdot concentration. Once the

concentration of a particular batch is known, it is then possible to calculate an estimated extinction coefficient for the rapid determination of concentration for samples from that batch. Due to batch-to-batch variation in Pdot synthesis, the molar extinction of a single batch of Pdots cannot be generalized to other batches made the same way using the same materials.

Given the limitations above, NTA was used to determine Pdot concentrations. NTA detects and counts single particles, extrapolating a concentration value as particles per unit volume. Although this method provides a straightforward and simple way to estimate Pdot concentrations, it has several key limitations. Concentration estimates depend on the sensitivity of the instrument, which is inherently limited by the scattering and fluorescence intensity of the sample. To obtain an accurate concentration value, the instrument must be able to discern every particle present from background noise. Camera sensitivity is also an important parameter. The quantum efficiency of the NTA sCMOS camera drops below 50% above 600 nm, making measurements of orange/red-emitting MEHPPV and CNMEHPPV Pdots more difficult. As particle brightness is correlated to particle size, it may be difficult to image smaller, less bright Pdots, such that larger particles may be overrepresented in the size distribution. Continuous irradiation with the laser source may also lead to photobleaching of the samples during the measurement. Operator error can also result in an appreciable fraction of the imaged particles being outside the focal plane of the objective lens, where these particles may not be counted appropriately. For these reasons, it is likely that NTA-derived concentrations are an underestimate of the true sample concentration. Despite these limitations, NTA remains the only robust, rapid and accessible method for determining Pdot concentrations. At best, the uncertainty may be estimated from the difference in concentration

between scattering and fluorescence modes, which typically agree within 50%. At worst, in the case where a significant fraction of particles is not counted, concentrations may be accurate only to the observed order of magnitude.

NTA results suggest that typical concentrations of as-synthesized Pdot range from 200 pM–1 nM, although the precise value depends on the details of the synthesis. Other groups report Pdot concentrations in the range of 1–5 nM, but do not state how they arrive at these values. It is likely that these values are derived from assumptions about the density and packing of SPs in the Pdot core, the molar extinction coefficient of the unaggregated SP, and the Pdot size.

4.3.5 Colloidal stability

Stored in water, Pdots generally remain colloidally stable for weeks or months. Over time, large aggregates that are visible to the naked eye begin to form but are easily removed from solution via filtration. Other signs of destabilization include the formation of dense precipitates or the irreversible deposition of fluorescent material on the walls of the storage vessel. If stored at too high a concentration, the rate of precipitation is increased. Pdots do not maintain their structure upon freezing, but may be lyophilized under certain conditions [180].

As Pdots are held together by relatively weak hydrophobic interactions, they are easily destabilized by changes in environment, particularly changes in pH and ionic strength. Simply storing Pdots in a buffer solution in lieu of water can cause dramatic loss of colloidal integrity. As an initial test for suitable storage conditions, F8BT/PSMA Pdots were stored in water or 25 mM HEPES buffer

at 4 °C over a period of 7 weeks. Absorption and emission spectra were recorded at regular intervals (Figure 4.9). The maximum absorbance at 460 nm remained relatively consistent for both solutions over the time scale of the experiment. However, the peak emission intensity at 540 nm for both samples decreased rapidly over the first week, achieved a minimum, and slowly began to rise over the course of the next 6 weeks. This result suggests that the total amount of material in solution remains constant, but the Pdots are a potentially dynamic material whose internal structure and photophysics change over time. The measured average diameter of the Pdots stored in water decreased over the first 10 days of storage where the diameter of the Pdots stored in buffer remained constant. Although both samples of Pdots came from the same batch, the Pdots stored in water initially had a larger average diameter than those stored in buffer. The cause of this effect is unknown but may be related to the relative ionic strengths of the two solutions. This result further suggests that the Pdot structure may be dynamic, possibly by the exchange of materials between particles, or that particles may break apart into smaller particles. Hydrophobic SPs are less soluble in environments of high ionic strength, preventing this behaviour for Pdots in buffer. Within the error associated with NTA concentration measurements, the concentrations of both solutions were constant over the course of the experiment. Chemical changes to the SP, such as oxidation, may also play a role in changing particle characteristics.

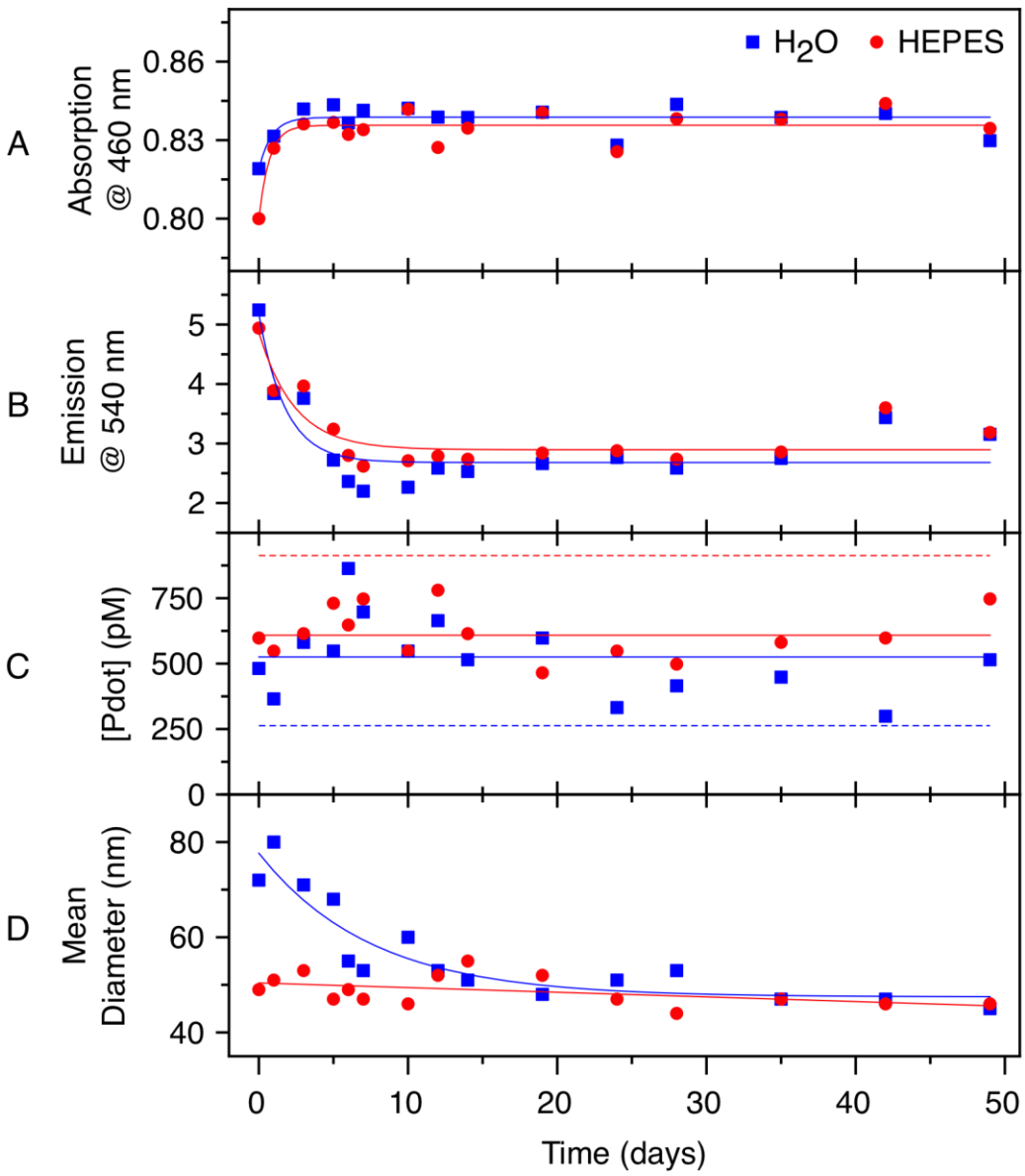

Figure 4.9 Colloidal stability test of F8BT/PSMA Pdots stored in water (blue) or ~25 mM HEPES buffer (red) over a period of 7 weeks. **(A)** Peak absorption. **(B)** Peak emission intensity. **(C)** Pdot concentration (average of NTA scattering and fluorescence modes). The solid lines represent the average concentration over the course of the experiment, and the dashed lines represent -50% error (blue, water) and +50% error (red, HEPES). **(D)** Mean diameter (average of NTA scattering and fluorescence modes).

4.4 Optical characterization

The optical properties of Pdots largely depend on the identity of the SP used in their synthesis. The selection of SP is often motivated by the emission colour of the SP and, accordingly, the desired emission colour of the resulting Pdots. Figure 4.10 shows a photograph of Pdots composed of the different SPs used in this thesis and PSMA under ambient lighting and under UV illumination.

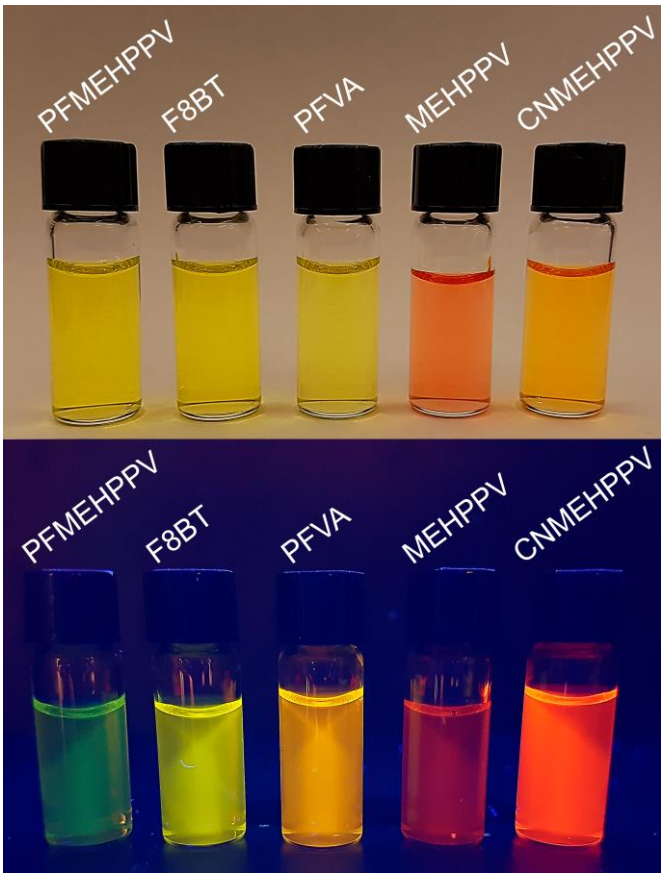

Figure 4.10 Photograph of Pdots composed of the indicated SP and PSMA amphiphile under ambient light (top) and 365 nm UV illumination (bottom).

4.4.1 Absorption and emission spectra of Pdots

The absorption, emission and excitation spectra of the unaggregated (*i.e.*, dissolved in THF) SPs used in this thesis are shown in Figure 4.11. Selected optical properties for the SPs are listed in Table 4.1. The SPs exhibit broad, asymmetric absorption spectra ranging from the UV to the blue or green regions of the visible spectrum. They also have a secondary peak in the UV region, likely arising from a higher order electronic transition analogous to the S_0-S_2 transition of the monomer species. The polymers exhibit relatively broad and asymmetric emission peaks, ranging from the green to red regions of the visible spectrum. Except for PFVA, the emission peaks are more spectrally narrow than the absorption peaks. The SPs exhibit varying Stokes shifts, which range from similar to those of organic dyes (~20 nm) to greatly exceeding those of organic dyes (> 100 nm). The practical importance of the Stokes shift for SPs is less than organic dyes because SP have broad absorption and emission bands, such that efficient excitation and emission can occur over a broad range of wavelengths.

Table 4.1. Spectral properties of unaggregated SPs in THF

SP	$\lambda_{max,Abs.}$ (nm)[a]	Abs. FWHM (nm)	$\lambda_{max,Em.}$ (nm)[b]	Em. FWHM (nm)	Stokes shift (nm)
PFMEHPPV	481	70	504	22	23
F8BT	453	79	540	80	87
PFVA	443	82	552	104	109
MEHPPV	502	91	555	37	53
CNMEHPPV	453	106	552	71	99

[a] Wavelength of maximum absorption [b] Wavelength of maximum emission

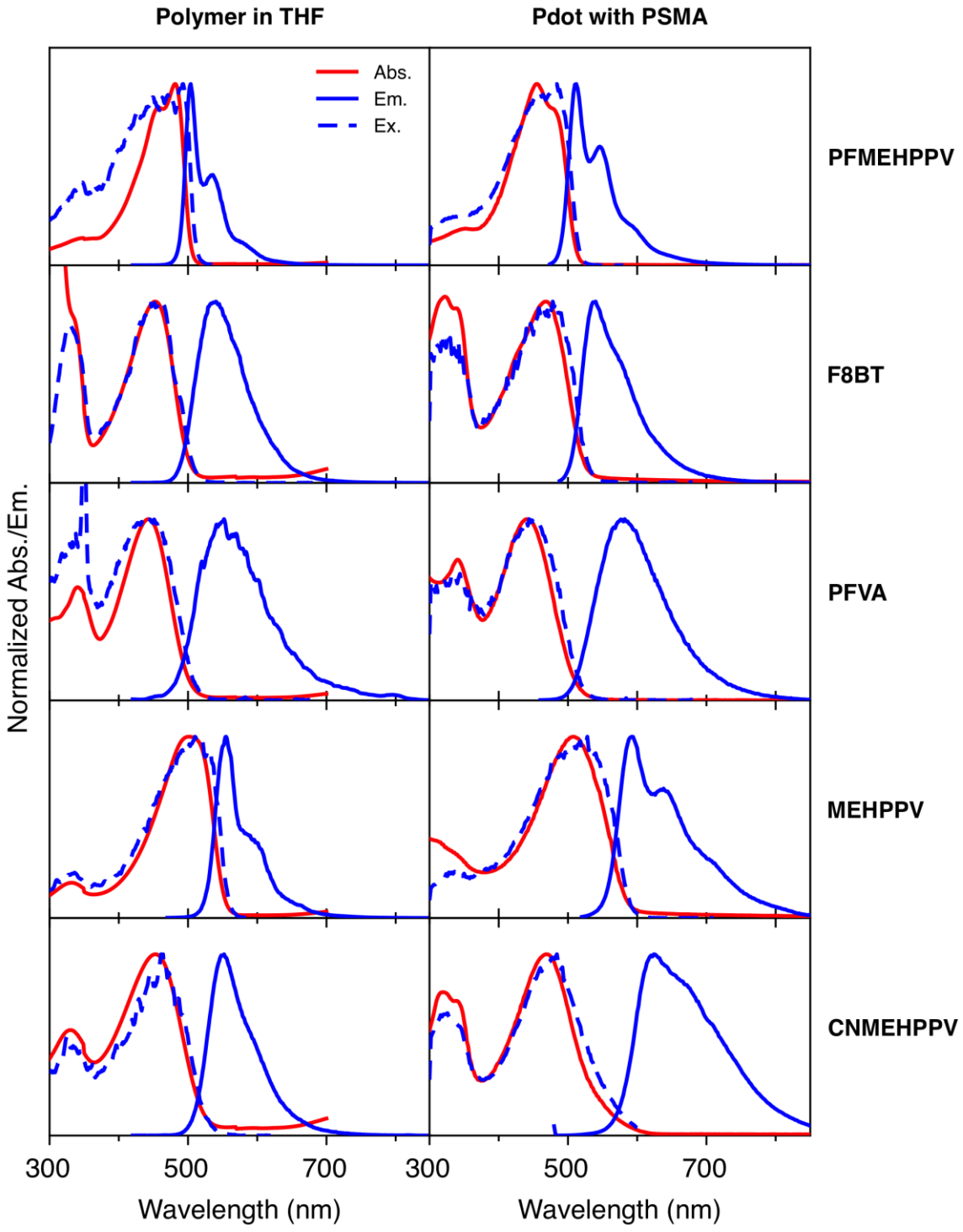

Figure 4.11 Normalized absorption, emission and excitation spectra for the unaggregated semiconducting polymers in THF (left column) and Pdots (right column) composed of the indicated SP and PSMA amphiphile.

SPs containing the MEHPPV monomer are known to contain high energy blue states and low energy red states. Blue states correspond to regions where the polymer is in an extended conformation, and red states corresponds to regions where the polymer undergoes local packing with adjacent monomers. The unaggregated, solution-phase polymer has majority blue states, although efficient energy transfer can occur to lower energy red states [66]. The presence of both states in the polymer is manifested as two distinct emission peaks in the spectra of PFMEHPPV and MEHPPV. CNMEHPPV also contains the MEHPPV monomer and may contain both red and blue states; however, only one broad emission peak is observed. Red-state emission likely contributes to the broad, red-tailed shoulder in the CNMEHPPV emission spectrum. Peak broadening may also be caused by high PDI of CNMEHPPV (*i.e.*, individual chains will have variable conjugation lengths and will emit at slightly different wavelengths).

The amphiphilic component of the Pdots is non-emissive and generally has no substantial impact on the optical properties of the NP. Many amphiphiles contain a styrene-like monomer as part of the hydrophobic element, which has absorption in the UV usually around 260 nm [181]. The molar extinction coefficients of polystyrene polymers are many orders of magnitude less than those of Pdots, although the specific value depends on the solvent, the number of styrene monomers in the chain and their specific arrangement. The amphiphilic component usually comprises no more than 20% by mass of the Pdots. Therefore, these species will have minimal contributions to the measured absorbance spectra of the Pdots.

The absorption, emission and excitation spectra of SP/PSMA Pdots are shown in Figure 4.11 (*vide supra*). Selected optical properties are listed in Table 4.2. Although the spectra were recorded for SP/PSMA Pdots, generally none of the amphiphiles tested here had a significant effect on the observed optical properties.

Table 4.2 Selected measured optical properties of Pdots composed of the indicated SP and PSMA.

SP	$\lambda_{max,Abs.}$ (nm)[a]	Abs. FWHM (nm)	$\lambda_{max,Em.}$ (nm)[b]	Em. FWHM (nm)	Stokes shift (nm)
PFMEHPPV	454	86	512	74	58
F8BT	468	94	540	78	72
PFVA	440	92	582	110	142
MEHPPV	508	114	592	96	84
CNMEHPPV	468	100	624	134	156

[a] Wavelength of maximum absorption [b] Wavelength of maximum emission

Pdots have absorption and emission peaks that are similar to those of the unaggregated SPs, although both peaks are typically broadened. The spectral positions of the absorption and emission peaks are affected by the polarity of the solvent surrounding a chromophore and changes in chain conformation [182]. Individual chromophores comprising a Pdot experience different local environments. Whereas a chromophore in the particle core is completely surrounded by other hydrophobic species, a chromophore on the particle surface may be partially solvated by the hydrophilic portion of the amphiphile or may be in direct contact with the polar solvent.

Interactions between the chromophore and solvating species change the energy of the molecular orbitals, therefore changing the amount of energy required for absorption or the amount of energy given off via emission, contributing to peak broadening. Additionally, the effective conjugation length of a SP decreases from the unaggregated polymer in solution to condensed polymer within a Pdot, as the chains will bend or kink at the particle boundary. Decreasing the effective conjugation length will increase (blue-shift) the band gap energy [183]. Individual polymer chains or segments will have different effective conjugation lengths depending on their specific arrangement within the Pdot, therefore also contributing to band broadening [66].

MEHPPV polymers exhibit significant emission peak broadening when condensed into Pdots. The number of low energy red states increases when polymers condense into particles. Red states correspond to areas where chains are well packed, such as within the Pdot core. These regions exhibit increased chain-chain electronic interactions and have an increased effective conjugation length because of the tight packing of the chains, both of which contribute to the lower energy nature of these states. Absorption will occur to a higher energy blue state, but energy is efficiently transferred to the lower energy red state where excitons become trapped and from which emission originates [66].

4.4.2 Fluorescence lifetime measurements

Fluorescence lifetime is a measurement of the amount of time a species remains in the excited state before decaying to the ground state via fluorescence. Fluorescence lifetime is an important

parameter for studying photophysical processes that act on the excited state, such as energy transfer or other dynamic quenching mechanisms.

Fluorescence lifetimes of Pdots were measured by time-correlated single-photon counting (TCSPC). This method measures the time delay between an excitation pulse and the emission of a single photon by the sample. This time delay corresponds to the amount of time the fluorophore remains in the excited state before decaying to the ground state via emission. Hundreds of thousands of emission events are recorded to construct a fluorescence decay curve. The fluorescence lifetime, τ, is given as Eqn. 2.7 (Chapter 2). More qualitatively, the fluorescence lifetime is the time after excitation at which the measured intensity has decreased to $1/e$ (~36.8%) of its maximum (*i.e.*, initial intensity).

For the materials used in this thesis, typical lifetimes ranged from hundreds of picoseconds to a few nanoseconds, although there was considerable batch-to-batch variation for materials with the same composition. The fluorescence lifetimes of seven different batches of F8BT/PSMA Pdots are shown in Figure 4.12. Although these materials were synthesized from the same starting materials and by the same procedure, measured amplitude-weighted average lifetimes varied from 480 up to 774 ps. Consequently, accurate comparisons of lifetime decays can only be made for experiments performed using the same batch of Pdots.

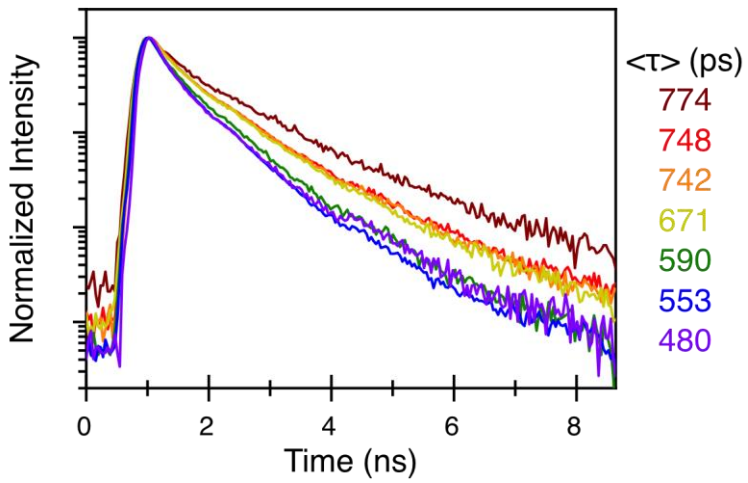

Figure 4.12 Fluorescence lifetime decay curves of various batches of F8BT/PSMA Pdots. The data were modeled as biexponential decays. The legend shows the amplitude-weighted average fluorescence lifetimes corresponding to each decay curve.

4.4.3 Quantum yield

Quantum yield is a measure of the relative rates of radiative and non-radiative decay pathways and can also be thought of as a measure of the efficiency with which a fluorophore emits the absorbed excitation light. Quantum yield is determined by comparison with a standard fluorophore or absolutely by use of an integrating sphere. Representative data for the determination of quantum yields for two separate batches of F8BT/PSMA Pdots is shown in Figure 4.13. The quantum yield of a species is directly related to its brightness by Eqn. 1.1 (Chapter 1) and is an important parameter for FRET (Eqn. 2.16, Chapter 2). Pdots typically have moderate-to-high quantum yields ranging from about 0.2–0.8. However, as with many of their physical and optical properties, batch-to-batch variation is significant, even for materials of the same composition. The extreme per-particle brightness of Pdots is a result of their high molar extinction coefficients more so than their quantum yields.

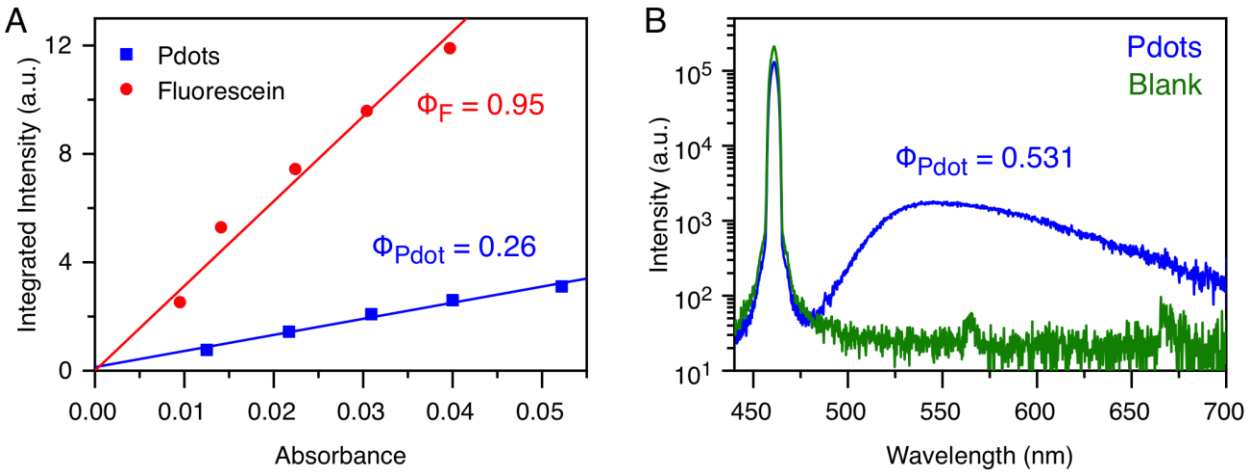

Figure 4.13 Representative data for the determination of quantum yield of two separate batches of F8BT/PSMA Pdots. **(A)** Quantum yield determination of F8BT/PSMA Pdots via comparison with fluorescein. **(B)** Quantum yield determination of F8BT/PSMA Pdots using an integrating sphere.

4.4.4 Photobleaching measurements

Photobleaching of F8BT/PSPEGCOOH and CNMEHPPV/PSPEGCOOH Pdots were measured on a fluorescence microscope and compared to green-emitting QDs (CdSeS/ZnS QD540 from Cytodiagnostics, Burlington, ON) and fluorescein (Figure 4.14). Samples were continuously irradiated with blue light suitable for excitation of all samples. Continuous, high intensity irradiation leads to irreversible photobleaching, upon which the species is no longer able to absorb or emit light, leading to a decrease in the observed PL intensity. Photobleaching curves were fit with a monoexponential function (fluorescein) or biexponential function (Pdots). Fitting parameters are listed in Table 4.3. The initial rate of photobleaching was comparable for both types of Pdots and fluorescein. After approximately 20 min, the Pdot emission intensity for both samples began to plateau at approximately 25% of the initial fluorescence intensity, whereas the fluorescein sample almost completely photobleached (near zero intensity). The plateau may be the result of photobleaching of chromophores near the particle surface whereas those in the core remain

photoactive. The QDs initially photobrightened (*i.e.*, an observed increase in the PL intensity upon continuous illumination), which is a known effect [184]. After about 20 min, the QD PL began to decay below its initial level, although at a slower rate than the dye and Pdots. Although Pdots have been reported to have good resistivity to photobleaching compared to organic dyes [56, 67, 124], these results suggest that on short time scales (~minutes), Pdots photobleach comparably to organic dyes and perform significantly worse than QDs. We hypothesize that Pdots of varying composition and size will exhibit different photobleaching rates due to their differing chemical structures and differing proportion of 'protected' chromophores in the particle core. Unlike fluorescein, Pdot intensity does not decay to zero; one possible rationale for this result is the gradual photobleaching of the outermost layer of chromophores forming a protective layer around the inner core.

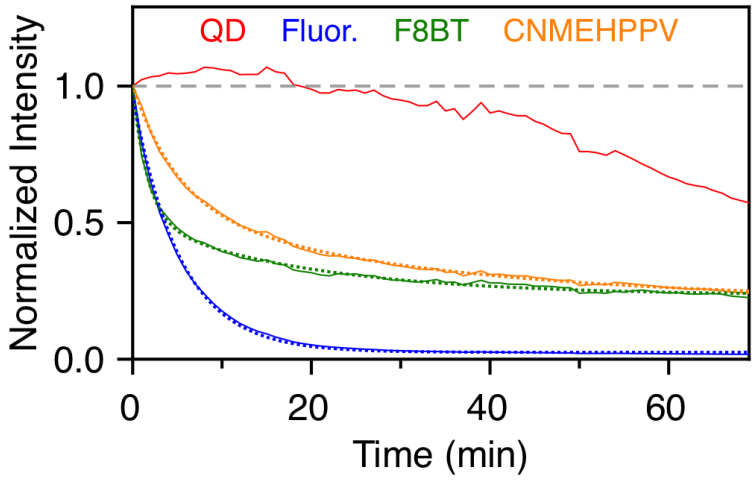

Figure 4.14 Photobleaching curves for QDs (red), fluorescein (blue), F8BT/PSPEGCOOH Pdots (green) and CNMEHPPV/PSPEGCOOH Pdots (orange). Data are shown as solid lines and fit curves are shown as dotted lines.

Ta**ble 4.3**. Fitting parameters for photobleaching rate

Material	k_1 (min^{-1})	a_1	k_2 (min^{-1})	a_2	half-life (min)
F8BT/PSMA	0.0527	0.37	0.595	0.63	5
CNMEHPPV/PSMA	0.0333	0.44	0.200	0.56	12
Fluorescein	0.189	1.0			4

4.5 Conclusions

The physical structure of Pdots is poorly defined and Pdots have complex and heavily environment-dependent photophysics. Despite the inherent challenges associated with characterising such materials, we have used a suite of different methods to develop a robust picture of the physical and photophysical properties of Pdots. Commonalities between materials include their sub-100 nm diameters, large size distributions, approximately spherical morphologies, picomolar to nanomolar concentrations post-synthesis, broad absorption and emission bands, moderate to high quantum yields, and sub-nanosecond fluorescence lifetimes. Despite the extent of characterization techniques used, it is not possible to get a complete picture of the physical structure of Pdots. The assumed core/shell structure of the SP and amphiphile is not readily observed, and it is difficult to ascertain the nature of chain packing, swelling within the hydrophobic core, and any effects arising from the possible oxidation of the SP. These unknowns

may play a significant role in the physicochemical behaviours of Pdots and pose a significant challenge to the further development of Pdots in bioanalysis.

A key conclusion from this research is that it is critical to characterize each batch of Pdots as much as possible before downstream use. Given the large impact of batch-to-batch variation on both the physical and optical properties, it is not prudent to make assumptions about a batch based on other batches that came before it. Pdots can also change their characteristics over time, so it is important to perform characterization shortly before any other experiments that will rely on the measured parameters. Batch-to-batch variation is particularly important considering the poor reproducibility and broad size distributions resulting from the typical nanoprecipitation method for Pdot synthesis.

Most experiments in this thesis used F8BT/PSMA Pdots, as this combination produced colloidally stable and reproducible Pdots (*i.e.,* clear solutions with sub-100 nm sizes). F8BT in Pdot form was shown to have favourable optical properties. Its absorption and emission bands match well with the requirements of NTA and DLS analysis, and the spectral position of its emission band allows it to act as an energy donor to many possible acceptors for the photophysical studies presented in Chapter 6. Other combinations of materials result in Pdots of similar physical and optical properties. The physical properties are mostly tuned by selection of the amphiphile, although the backbone rigidity of a given SP can affect the obtained particle sizes and presumably the chain

packing in the particle core. Emission colour can be tuned by choice of the SP, although other optical properties show minimal variance between materials.

Although a complete understanding of the physical and optical properties of Pdots has yet to be developed, Pdots have found use in many applications, particularly in optoelectronics and bioanalysis. There are many difficulties inherent in their characterization, but Pdots are still a rapidly emergent fluorophore due to their advantageous optical properties, particularly their extreme per particle brightness and biocompatibility (Section 1.2.6). As promising as the materials may be, it is unlikely that Pdots will reach their full potential as an analytical tool until they are characterized more completely, and their properties are better understood and better controlled.

Chapter 5: Flow-based synthesis and manufacturing of semiconducting Polymer Dots

The results presented in this chapter are currently unpublished. This research was conceived by Kelsi Lix, Russ Algar, and Jason Hein. KL designed the experimental protocols, data analysis methods, and performed some experiments using the syringe pump and continuous flow pump systems. KL supervised undergraduate researchers who performed experiments using protocols and data analysis methods designed by KL: Jamie Dearnley, Valentin Saibi, Chelsea Cayabyab, and Gilles Poitau. KL and Ryan Chung designed the syringe pump system and performed initial testing and troubleshooting. Henry Situ, Sebastian Steiner, and JH designed the continuous flow pump system. HS and SS wrote the operational code. Scale up experiments were performed by KL, HS, and GP. Global analysis of the data presented in this chapter was performed by KL.

5.1 Introduction

Semiconducting polymer dots (Pdots) are rapidly emerging as a fluorescent probe for bioanalysis and bioimaging. Pdots are a type of semiconducting polymer nanoparticle (SPN) demarcated from other SPN materials by their small sizes, high semiconducting polymer (SP) content and hydrophobic cores [26, 118]. Pdots and SPNs have many advantageous properties compared to other classes of fluorophores, including extremely high per-particle brightness, high absorption cross sections, good biocompatibility, and permeable hydrophobic cores [109]. To date, Pdots have found use in chemical and biological sensing [77, 157, 185], *in vitro* and *in vivo* imaging [139, 186], and photothermal and photodynamic therapy [144, 187-188].

Pdots are typically synthesized via nanoprecipitation, a process wherein a solution of an SP in a water-miscible solvent such as THF is rapidly injected into water under thorough mixing, usually via sonication [26]. Due to the sudden change in local solvent polarity, the hydrophobic polymer chains spontaneously collapse into spherical nanoparticles (NPs) with typical diameters less than 100 nm. This injection is usually done manually; for example, a syringe or pipette may be used to inject the polymer precursor solution into water. Manual nanoprecipitation is a very general method that has been applied to produce Pdots and other polymer nanoparticles of varying compositions, inclusive of both commercially available and custom synthesized semiconducting polymers. Nanoprecipitation requires only that the polymers are sufficiently hydrophobic to undergo chain collapse [24, 93]. This method can be tuned to produce particles of different sizes by changing the concentration of the polymer in the precursor solution [59], adjusting the relative volumes of solvent and water [60], and by adding water to the precursor solution incrementally to seed particle formation [61]. Depending upon the specific conditions and materials used, the resulting nanoparticles may have diameters from a few nanometres up to hundreds of nanometres, and may have relatively narrow or broad size distributions. Some size control is achievable by manual nanoprecipitation, but the extent of control is vastly limited by the method's poor reproducibility.

Controlled synthesis of inorganic and non-semiconducting polymer nanoparticles has been demonstrated using continuous-flow microfluidic methods [189-195], where mixing between solvents is controlled by the fluid dynamics that occur in confined microscale environments. Flow in these microfluidic devices tends to be laminar, where individual streams flow side-by-side and only mix via diffusion at the interface [196]. Although this method offers improved control, it is

limited in terms of scale and solvent compatibility of the microfluidic flow cells. SPs are typically soluble only in harsh solvents such as THF or chlorinated solvents, which are incompatible with many flow cell devices. Microfluidic synthesis of Pdots or SPNs is less common, although methods have been reported for polyaniline nanofibers [197] and thiophene-based SPs using supercritical fluids as a solvent [198]. Microfluidic syntheses of SPNs have been reported using both commercial and custom-synthesized SPs, but for NPs that contain low fractions of SP compared to the non-emissive polymer component [199-201]. Millifluidic nanoparticle synthesis, where channel diameters are between 0.5–10 mm, is a method that circumvents the need for intensive and sophisticated reactor production, as required microfluidic synthesis, while retaining many of its advantages and allowing for more convenient scale-up. Continuous flow millifluidics has been used to synthesize a variety of nanomaterials such as metal NPs [202-204], QDs [205-206], polysaccharide NPs [207-208], and non-emissive polymer NPs [209].

Here, we demonstrate the use of controlled, flow-based methods for Pdot synthesis in the millifluidic regime. Proof-of-concept was demonstrated using benchtop syringe pumps to control the flow and mixing of the organic and aqueous phases, producing a variety of Pdot materials. The flow-based method was shown to have improved reproducibility compared to the manual injection method. By variation of precursor concentration and flow rates, some tuning of particle sizes was achieved between 50–120 nm. Optically active small molecule dopants were efficiently incorporated into the Pdot core by flow synthesis. To demonstrate manufacturing of Pdots on a commercially relevant scale, flow-based synthesis was also performed using continuous flow positive displacement pumps to control flow and mixing of the two phases, reproducibly producing Pdots up to a 100 mL scale. Trends in size tuneability and synthetic reproducibility were similar

to those achieved using the syringe pump system. We have shown that the flow-based method has several benefits over the manual injection method, and with further optimization, will be a robust and reliable alternative to current synthetic methods like manual nanoprecipitation.

5.2 Results

5.2.1 Flow synthesis

Flow synthesis and manual injection are represented schematically in Figure 5.1. Briefly, a precursor solution containing SP and amphiphilic polymer (AP) was prepared in THF. Syringe pumps were used to pump the organic precursor solution and water together at a controlled flow rate through polytetrafluoroethylene (PTFE) tubing and through a mixing element (*e.g.,* T- or Y-mixer). The two solutions collided and mixed in the mixer, producing Pdots, which were collected at the mixer outlet. After removal of THF by evaporation, the resulting Pdots were characterized. Initial experiments were performed using F8BT and PSMA as this combination yielded good reproducibility and high signal-to-noise for NTA analysis. Optical spectra were also recorded. NTA and DLS characterization data for a representative sample of F8BT/PSMA Pdots are shown in Figure 5.2. Representative TEM images of F8BT/PSMA Pdots synthesized by manual injection and flow synthesis are shown in Figure 5.3.

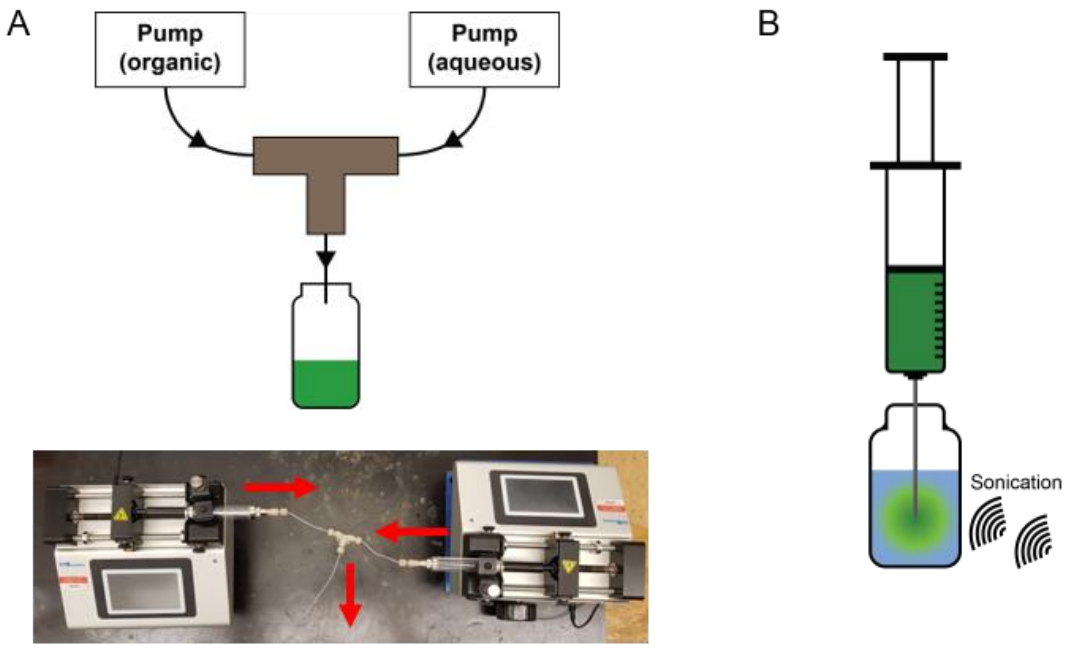

Figure 5.1 (A) Schematic of flow synthesis. The organic precursor and aqueous solutions are pumped together at a controlled flow rate then collide and mix within the mixer element (*e.g.,* T-mixer). Pdots are collected at the outlet. The photograph shows the syringe pump hardware, tubing and mixer element used for flow synthesis and the red arrows represent the direction of flow. **(B)** Schematic of manual injection synthesis. The organic precursor solution is injected into water under sonication, producing Pdots.

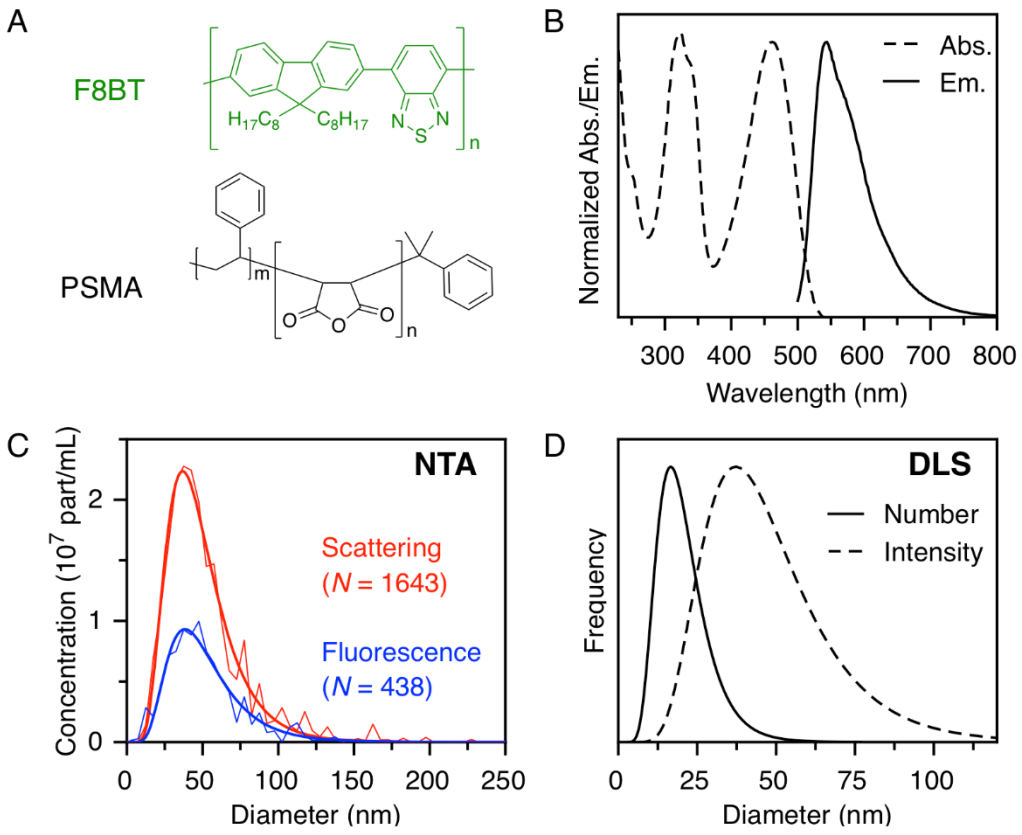

Figure 5.2 Representative characterization data for F8BT/PSMA Pdots produced by flow synthesis. **(A)** Chemical structures of F8BT and PSMA. **(B)** Normalized absorption and emission spectra ($\lambda_{ex.}$ = 460 nm). **(C)** Scattering mode (red, average particle size 49 (37) ± 22 nm) and fluorescence mode (blue, average particle size 52 (39) ± 25 nm) NTA sizing data. The number of particles counted, *N*, is noted in the figure. **(D)** Number-weighted (21 (17) ± 8 nm) and intensity-weighted (48 (37) ± 20 nm) DLS lognormal curve. The notations are mean (mode) ± standard deviation of the lognormal distribution.

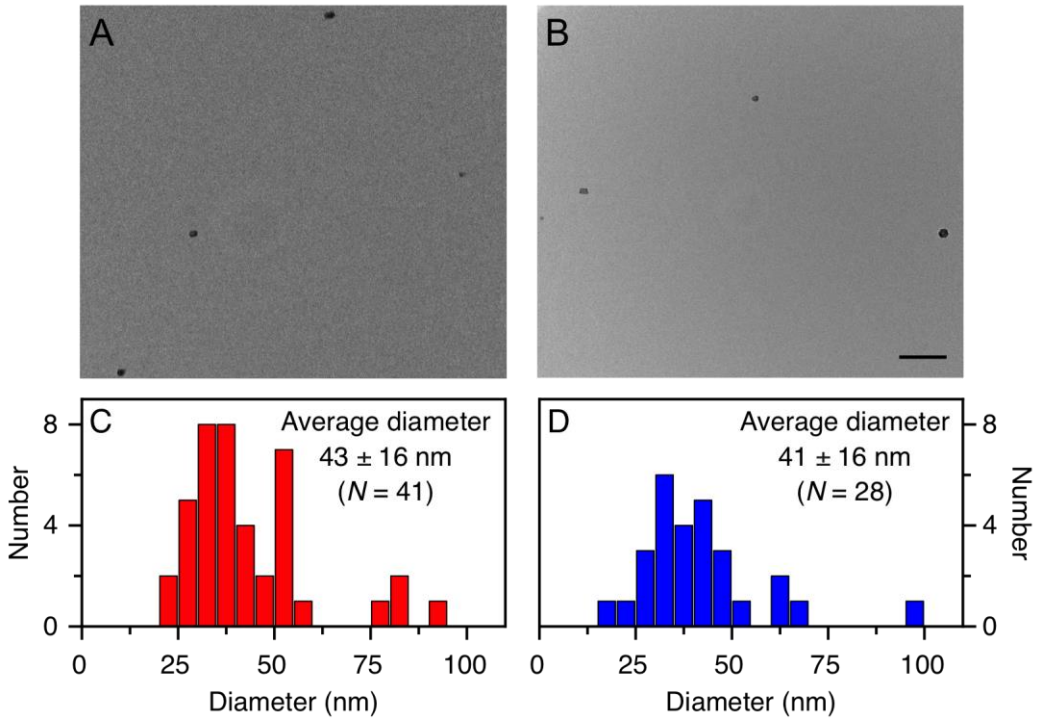

Figure 5.3 TEM images of F8BT/PSMA Pdots synthesized by **(A)** flow synthesis and **(B)** manual injection. Scale bar = 200 nm. Size distributions for **(C)** flow synthesis and **(D)** manual injection. The number of particles analyzed, *N*, is noted in the figure.

We performed a side-by-side comparison of flow and manual synthesis to measure the reproducibility of both methods. A precursor solution (5 mL) of F8BT (14 µg/mL) and PSMA (2.9 µg/mL) were injected into 5 mL of water either via syringe pump at 18 mL/min or manually at the fastest rate possible via syringe under sonication. The mean and mode diameters and standard deviations derived from lognormal fitting of NTA data for 12 replicates are shown in Figure 5.4A. Flow synthesis produced Pdots of smaller mean and mode diameters with considerably less variation in size than manual injection. The average mean and mode diameters of the manual injection method were skewed higher by a small number of data points with sizes significantly above the average. The width of the size distributions from both methods were similar and likely

represented a fundamental limit arising from the polydispersity of the constituent polymers and the imperfect mixing of the two solutions. Swapping the T-mixer for a Y-mixer of similar internal diameter (ID) did not appreciably change the size or size distribution of the resultant Pdots (Figure 5.4B).

Colliding the aqueous and organic solutions in a confined environment (*i.e.*, within a mixing element) was expected to improve mixing efficiency and generate smaller Pdots. Flow synthesis was done without a mixer, where the outlet tubes for both the organic and aqueous solutions were instead placed directly in the collection vial (Figure 5.5). The solutions mixed only upon delivery into the vial. Synthesis with no mixer was also performed with and without stirring, where the extent of mixing in the latter largely controlled by the velocity of the solutions exiting the tubing. Pdots were formed in both cases, although smaller diameters and less variation in size were observed when the solutions were stirred together at 340 rpm due to improved mixing of the solutions (Figure 5.4C). The sizes obtained were larger than those obtained using the T-mixer and Y-mixers (Figure 5.4A and B), indicating that efficient mixing was required to minimize particle size.

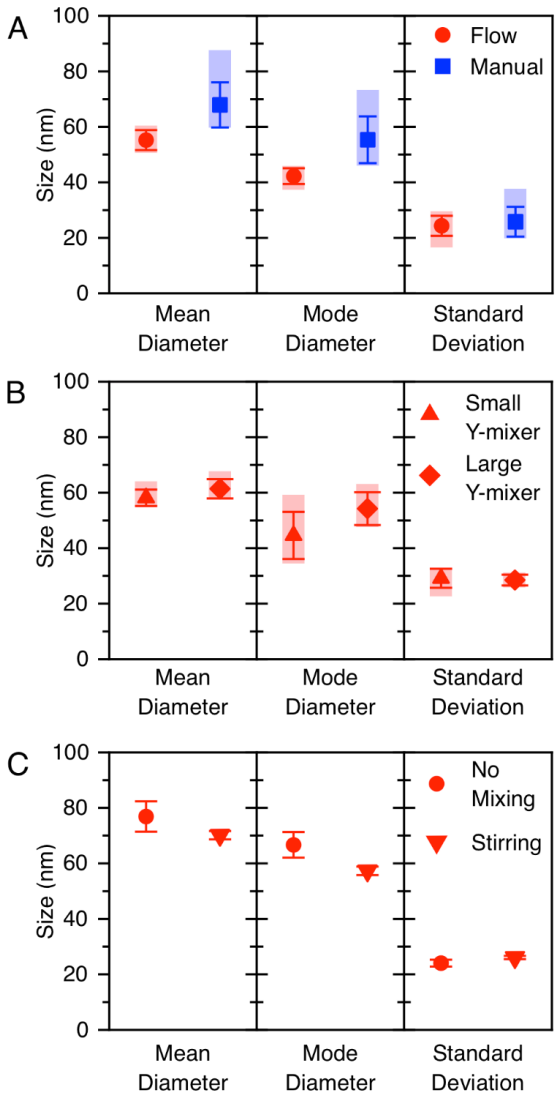

Figure 5.4 (A) Mean and mode diameters and standard deviation for F8BT/PSMA Pdots synthesized by flow synthesis (red) and manual injection (blue). Sizes were obtained from lognormal fitting NTA data (*N* = 12, average of scattering and fluorescence modes). **(B)** Mean and mode diameters and standard deviations for F8BT/PSMA Pdots synthesized by flow synthesis using a small Y-mixer (*N* = 6) and large Y-mixer (*N* = 5) obtained from lognormal fitting fluorescence mode NTA data. **(C)** Mean and mode diameters and standard deviations for F8BT/PSMA Pdots synthesized by flow synthesis with no mixing and with stirring at 340 rpm, obtained from lognormal fitting of fluorescence mode NTA data (*N* = 3). Error bars represent ±1 standard deviation and the coloured boxes represent the range of the data points.

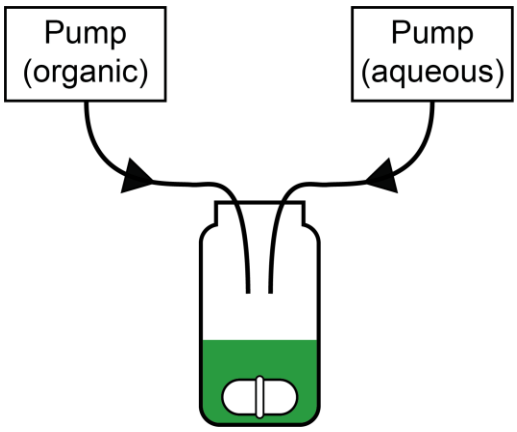

Figure 5.5 Schematic of flow synthesis without a mixer element (*i.e.,* Y- or T-mixer). Pdot solutions were either stirred at 340 rpm or not mixed.

5.2.2 Optimization of flow synthesis

Upon demonstration that flow synthesis reproducibly produced Pdots, we endeavoured to characterize and optimize the system with the aim of achieving reproducible size control. Variables such as the concentrations and compositions of the precursor organic and aqueous solutions, total and relative flow rates, and scale of synthesis were investigated.

The concentration of the SP in the precursor solution has been reported to affect particle size in nanoprecipitation [59]. Flow synthesis of F8BT/PSMA Pdots was performed using varying concentrations of F8BT and PSMA, maintaining a 5:1 mass ratio. Experiments were performed by three different operators using three different polymer stock solutions. The resultant Pdots were analyzed by NTA (Figure 5.6). Average particle diameters between *ca*. 50–100 nm were obtained by varying precursor concentration, where ~50 nm was the minimum size. A general trend between

polymer concentration and size was observed, where larger particles were produced at lower concentrations. Excepting the two outliers noted in Figure 5.6, which are attributed to operator error, average particles sizes ranged from ~50–70 nm. The disparity between experimenters may be caused by chemical changes occurring to the polymers when stored in THF (*vide infra*). For nanoprecipitation, it has been reported that smaller particles are obtained at lower precursor concentrations. Although growth is favoured over nucleation when there is less supersaturation, growth is limited by the diffusion of solubilized polymer chains toward the generated nuclei which is less probable when the concentration is low [210]. Particle sizes may also trend smaller because of the reduced viscosity of low concentration polymer solutions [211]. Our results suggest the opposite trend, where an increase in size is observed at lower concentrations, possibly due to the formation of larger Pdots from collisions between unstable Pdot nuclei (although fewer collisions are expected at low polymer concentrations). Any effects of solution viscosity are likely minimized by the low polymer concentrations used (*i.e.*, $\leq$ 200 μg/mL).

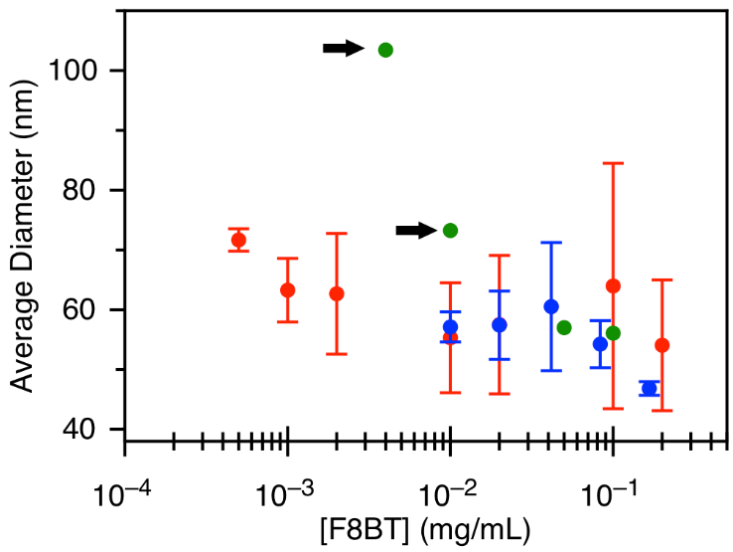

Figure 5.6 Average diameters (average of NTA scattering and fluorescence modes obtained from lognormal fitting of raw data) for syringe pump synthesis of F8BT/PSMA Pdots by three different operators using three different stock solutions over the span of 16 months. Outliers are denoted by arrows. These outliers were very infrequent, and their origin in unknown, but suggest that further optimization of the synthesis process is possible.

The efficiency of mixing was influenced by the flow rates of both pumps, and the internal diameter of the mixer. F8BT Pdots were synthesized with either PSMA or PSPEGCOOH using T-mixers of different internal diameters (Figure 5.7). Flow rates ranging from 1 to 18 mL/min were tested, where inefficient mixing was observed below 1 mL/min and 18 mL/min was the upper limit accessible with the syringe pumps and the 10 mL syringes. Preliminary results showed similar trends for both amphiphiles and both T-mixers. At flow rates less than 5 mL/min, partitioning was often observed (*i.e.*, the elution of separate layers, only one of which contained coloured material). In some cases, when a homogenous solution was eluted, visible Schlieren lines occurred in the eluent, implying poor and incomplete mixing in the mixer element at low flow rates but turbulent mixing in the eluted solution. In this regime, Pdots with diameters above 60 nm were obtained.

Above 5 mL/min, homogenous solutions were eluted with no visible Schlieren lines, implying complete mixing in the mixer element. In this regime, there was some correlation between flow rate and particle size, where smaller Pdots were obtained at higher flow rates, but average diameters quickly plateaued around 40–50 nm, implying the rate of mixing exceeded the rate of polymer aggregation. The nature of flow and mixing in the mixer (*i.e.*, laminar or turbulent flow) was not apparent, and warrants further study. Nevertheless, the transition from a flow regime with unmixed eluent versus well-mixed eluent is strongly suggestive of a transition from laminar to turbulent flow. Additionally, only 1 or 2 replicates were performed for each experiment, so the extent of variation for a given set of parameters is difficult to ascertain.

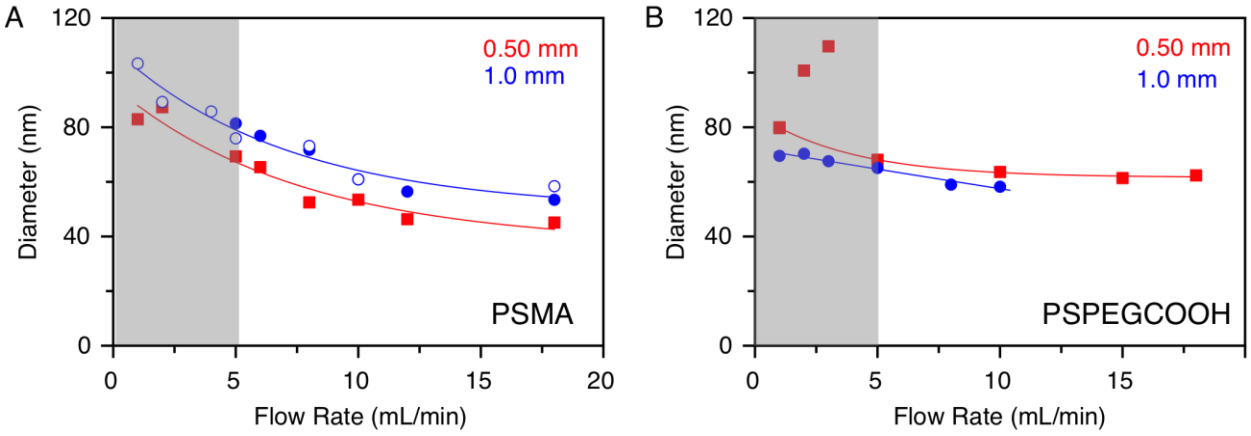

Figure 5.7 Effect of flow rate on average particle diameters obtained from the average of lognormal fitting of NTA scattering and fluorescence modes using T-mixers with IDs of 0.05 mm or 1.0 mm for **(A)** F8BT/PSMA Pdots or **(B)** F8BT/PSPEGCOOH Pdots. Hollow data points represent a replicate trial. The grey box represents the regime of poor mixing.

The relative volume of the aqueous and organic phases has also been reported to affect the particle sizes obtained by nanoprecipitation [60, 194, 210]. To this end, flow synthesis of F8BT/PSPEGCOOH Pdots was performed using asymmetric flow rates. Preliminary data are shown in Figure 5.8. The aqueous solution was pushed at a rate of 18 mL/min whereas the flow rate used for the organic solution ranged from 6–18 mL/min (*i.e.*, corresponding to equal or lower volumes of THF dispensed than water). The amount of polymer (by mass) was kept constant for each flow rate. Symmetric flow rates (*i.e.*, equal volumes of water and THF) produced particles with the largest average diameter as determined by NTA (~80 nm). Flow ratios less than unity (*i.e.*, less organic solvent) produced Pdots ranging from ~50–60 nm, with no significant variation for different flow ratios, although the exact quantitative results are expected to show some variance upon completion of additional replicates. The samples synthesized with asymmetric flow rates showed similar migration patterns in gel electrophoresis (Figure 5.8B), with significant emissive material remaining in the well and uniform streaks instead of tight bands (as is typical for Pdots in our hands). The sample synthesized at a symmetric flow rate (*i.e.*, 18 mL/min) showed distinct behaviour, migrating slightly further than the other samples and forming a bright band at the end of the streak. The bright band indicates that this sample contained a unique sub-population of particles compared to the samples synthesized at asymmetric flow rates, although the nature of this difference is unclear.

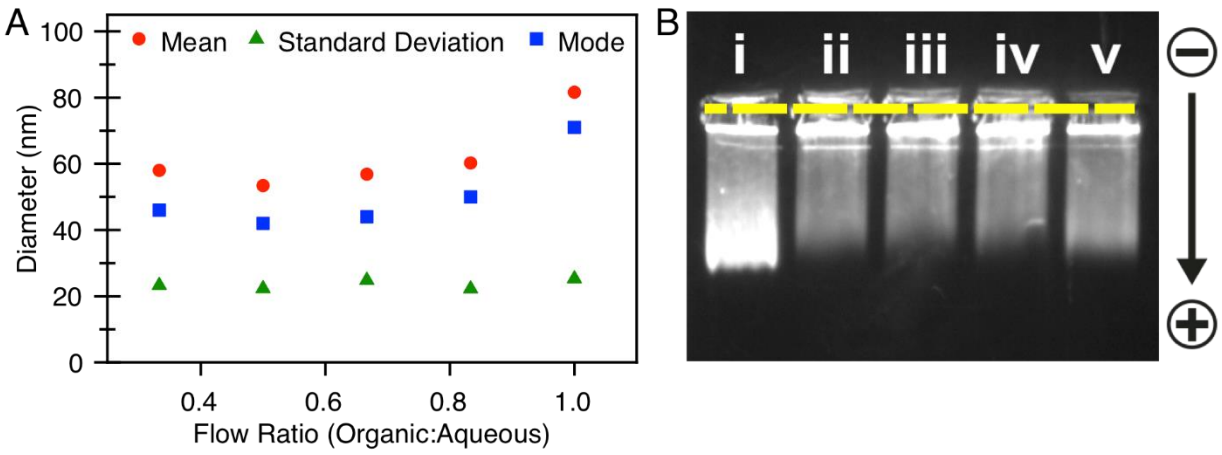

Figure 5.8 (A) Particle sizes and standard deviations (from lognormal fitting of fluorescence mode NTA data) and **(B)** fluorescence image of an agarose gel image run with F8BT/PSPEGCOOH Pdots synthesized at asymmetric flow rates (organic/aqueous). Flow ratios (organic flow rates): (i) 1 (18 mL/min), (ii) 0.83 (15 mL/min), (iii) 0.67 (12 mL/min), (iv) 0.5 (9 mL/min), (v) 0.33 (6 mL/min).

The natures of the organic and aqueous phases were also varied, using F8BT/PSMA as a model system. Using a precursor solution containing a water-miscible cosolvent (ethanol) and a water-immiscible solvent (chloroform) did not result in the formation of Pdots. The SPs used are all soluble in chloroform. It was hypothesized that upon particle formation, Pdots would partition into the aqueous phase even in the presence of a good solvent. However, the use of chloroform as a co-solvent at a small fraction (10%) caused the solubilization of the free polymers in the distinct organic phase and no Pdots were formed in the aqueous phase. Ethanol as a cosolvent resulted in the formation of large aggregates and the deposition of SP on the walls of the reaction vessel. Changing the character of the aqueous phase either by using neutral buffer (25 mM HEPES, pH 7.4) or sodium chloride solutions of low ionic strength (10–50 mM) also resulted in the formation of precipitates and the deposition of material on the walls of the reaction vessel. The presence of inorganic or organic salts appeared to preclude the formation of Pdots, likely due to the increased

destabilization of the SP at increased ionic strengths. Changes to the pH or ionic strength of the solution may also change the solubility of the amphiphilic species, making it less available to stabilize the Pdots.

The output of syringe pump flow synthesis experiments was typically collected in its entirety and not fractionated. However, this output included a *dead volume* corresponding to the volume expelled from the start of flow to the point where the pumps reached equilibrium flow conditions (neglecting any deviations from steady state after equilibrium was established). Pdots formed in the dead volume may have been smaller or larger than those produced under equilibrium conditions due to inconsistent flow, and, when the dead volume was collected, they would have contributed to the obtained size distribution. To test the extent of this contribution, the output solution was collected manually as ~1.5 mL fractions and each fraction analyzed by NTA (Figure 5.9A). The dead volume was estimated by the volume of the tubing and mixer element and was estimated to be much less than 1 mL. The first fraction, which contained any contribution from the dead volume, displayed higher mean and mode particle sizes compared to the other fractions assumed to be collected after the pumps had reached equilibrium. From fraction 3 onwards, obtained particle diameters were consistent, save for fraction 6. The first fraction displayed distinct behaviour in gel electrophoresis (Figure 5.9B). Fractions 2–7 displayed uniform anodic streaking with most emissive material remaining in the wells. Fraction 1 displayed a bright band originating from the well but extending into the gel, followed by uniform streaking although with less migration than most of the other fractions, indicating a unique population of particles existed in the first fraction.

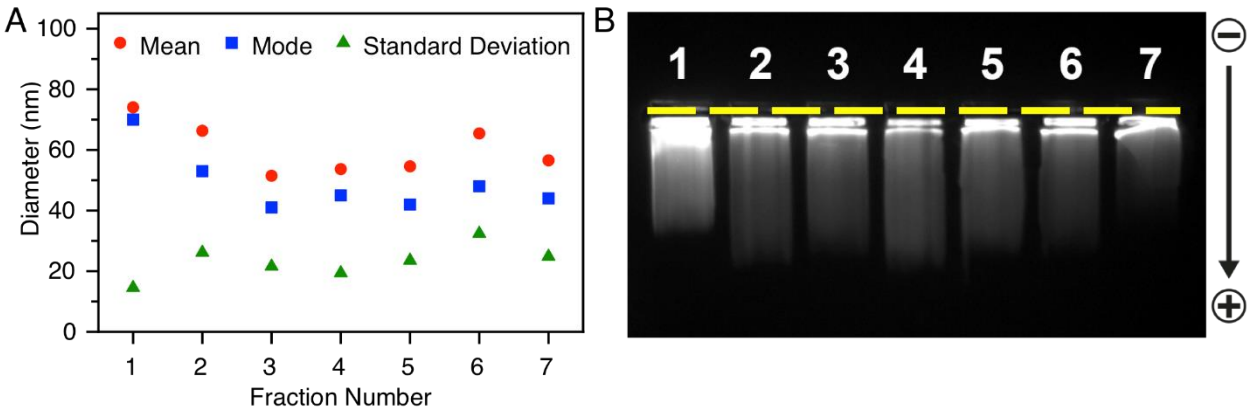

Figure 5.9 (A) NTA mean/mode diameters and standard deviations (from lognormal fitting of scattering mode data) for multiple fractions collected for a single synthesis (manual collection of ~1.5 mL fractions). (B) Fluorescence image of fractions 1-7 run on an agarose gel.

The above flow synthesis experiments were performed on a 10 mL scale, comparable to typical volumes used for manual injection. The ideal synthesis method should be scalable to both higher and lower volumes to suit the needs of particular experiments. For example, low volumes are preferred for conserving materials when testing new formulations. To this end, the syringe pump setup was used to formulate F8BT/PSMA Pdots on a 1 mL scale, using 1 mL syringes to deliver 500 µL of the organic and aqueous precursor solutions using variable F8BT concentrations at a flow rate of 2.5 mL/min (Figure 5.10). Similar trends were observed as with the 10 mL formulations, where the mean particle diameter decreased with increasing F8BT concentration, and quickly reached a plateau above 10 µg/mL. A limit diameter of ~80 nm was observed, about 20 nm greater than the limit size observed at the 10 mL scale. The nature of this effect is currently unknown and should be evaluated further. Pdots made with higher precursor concentrations were seen to be more reproducible (*i.e.*, less variation in mean diameters). These trends were mirrored in the gel electrophoresis data (Figure 5.10B), where larger particles exhibited less anionic

migration and an increased amount of fluorescent material remaining in the well. All samples exhibited streaking which was likely due to the size distributions of the particles. The relative fluorescence intensity of the bands corresponds to the amount of fluorescent material used in synthesis.

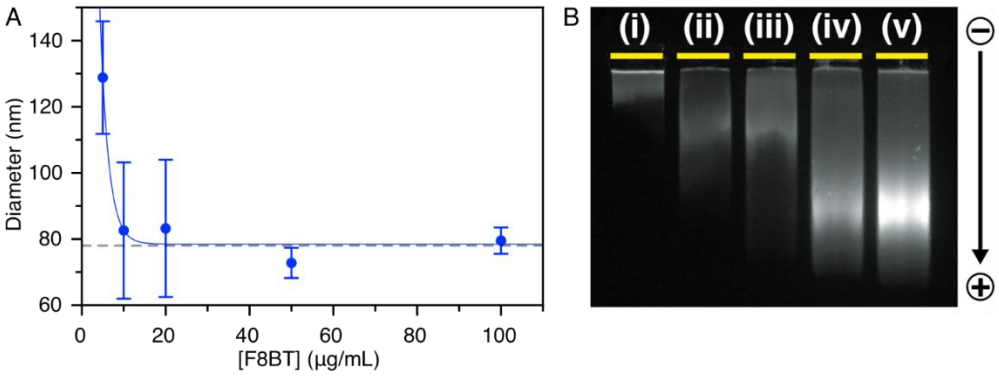

Figure 5.10 (A) Mean particle diameters (average of lognormal fitted fluorescence and scattering mode NTA data) for F8BT/PSMA Pdots synthesized by flow synthesis on a 1 mL scale using different precursor concentrations of F8BT. The limit size (78 nm) is indicated by the dashed line. **(B)** Gel electrophoresis of Pdots synthesized using (i) 5 µg/mL, (ii) 10 µg/mL, (iii) 20 µg/mL, (iv) 50 µg/mL, (v) 100 µg/mL precursor concentrations of F8BT. The dashed yellow line indicates the location of the wells.

5.2.3 Encapsulation of Rhodamine 640 by flow synthesis

Pdots have a soft, disordered core capable of acting as a host for other hydrophobic materials. When a hydrophobic fluorophore having suitable spectral overlap is doped into the Pdot core, highly efficient energy transfer resulting in acceptor emission occurs due to the small donor-acceptor distance. Dye-doping has been demonstrated as a valuable strategy for tuning Pdot emission (*e.g.*, narrowing and red-shifting the emission peak) and for the design of ratiometric fluorescence sensors when the dye is responsive to an analyte [63, 75].

Flow synthesis was used to non-specifically dope F8BT/PSMA Pdots with Rh640, a dye having suitable spectral overlap to act as an energy acceptor in an energy transfer configuration. In the case of successful encapsulation of the dye, efficient energy-transfer sensitized dye emission occurred due to the suitable spectral overlap and short donor-acceptor distance. Encapsulation was achieved by adding Rh640 to the precursor solution used in nanoprecipitation at concentrations of 34, 340, and 3400 nM. Due to the hydrophobic nature of the dye, Rh640 would either embed itself in the Pdot core or non-specifically adsorb onto the particle surface or within the amphiphilic shell layer. After synthesis and solvent removal, excess dye was removed by spin filtration. Final concentrations of the dye in solution were not be determinable due to variations in volume during the solvent removal and purification steps.

The absorption, emission, and excitation spectra for the three dye concentrations tested are shown in Figure 5.11. The absorption spectra show intense peaks at ~460 nm and ~325 nm corresponding to the first two electronic transitions of F8BT, respectively. For the 340 nM and 3400 nM samples, a small peak occurs at ~574 nm, corresponding to the absorbance band of Rh640. As evidenced in the emission spectra, Rh640 is present in the 34 nM sample, although at such a low concentration that its absorbance was not detected. Fluorescence signals arising from energy transfer sensitized dye emission occurred for all three samples. Although direct excitation of Rh640 may contribute to the observed emission intensity, the summation of this contribution and the expected contribution from Pdot emission at 598 nm does not account for the observed signal, indicating that energy transfer to Rh640 occurred. Both dye and Pdot emission were significantly quenched

in the 340 nM and 3400 nM samples, possibly because of energy transfer from the Pdot to non-emissive dye aggregates that formed at high concentrations. Non-emissive H-aggregates of dyes have blue-shifted absorbance bands, so any absorbance signal from a fraction of dyes in the aggregated form would have been obscured by the strong absorption peak of the Pdots. If some fraction of Rh640 molecules were not part of aggregates, then they would have produced the expected emission signature. Strong Pdot emission was observed for the 34 nM sample, suggesting that non-emissive Rh640 aggregates formed to a much lesser degree at this low concentration. The excitation spectra, recorded using an emission wavelength of 640 nm, mirror the trends in intensity observed in the emission spectrum, namely that the 34 nM sample had significantly higher emission than the 340 nM and 3400 nM samples, as was observed in the emission spectra. Sufficient concentrations of Rh640 remained in the 34 and 3400 nM samples that a distinct Rh640 peak was observed at 572 nm in the excitation spectra.

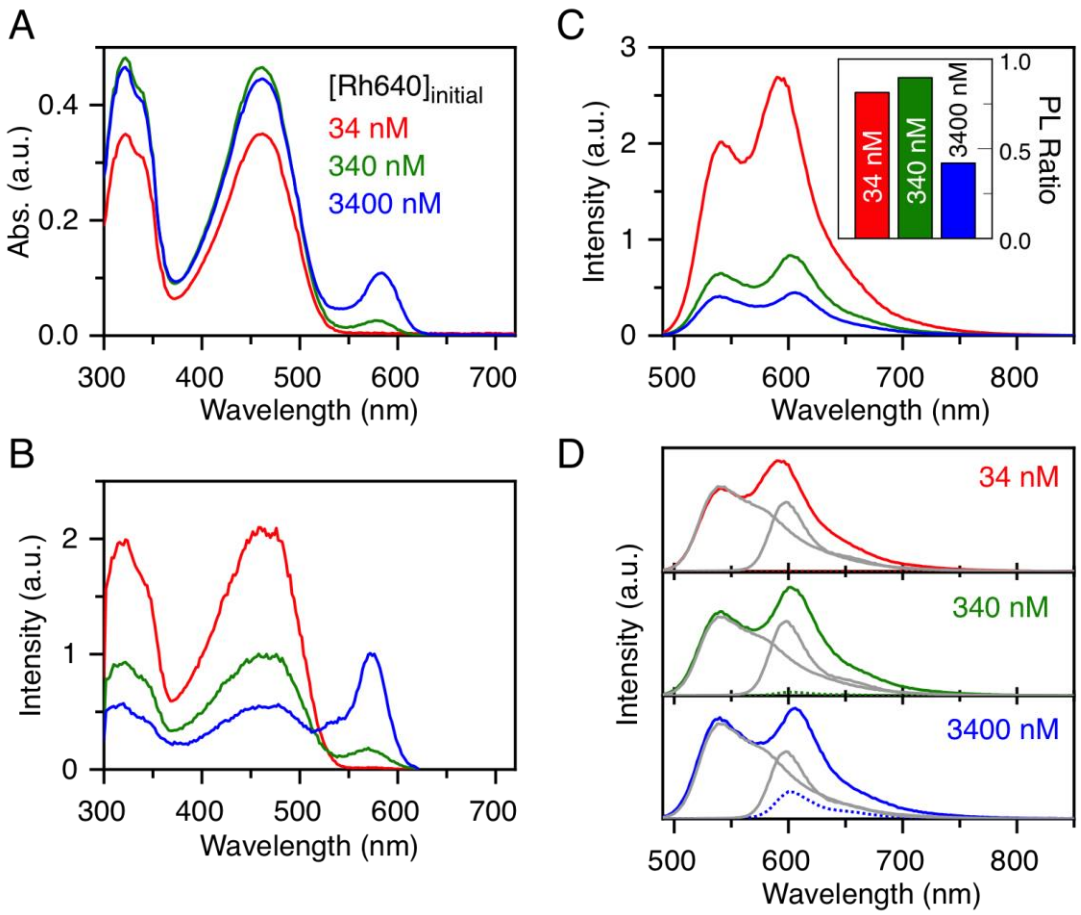

Figure 5.11 (A) Absorption, **(B)** excitation ($\lambda_{em.}$ = 640 nm), and **(C)** emission ($\lambda_{ex.}$ = 460 nm) spectra of Pdots doped with Rh640 at an initial concentration of 34 nM, 340 nM, and 3400 nM. Final dye concentrations were not determinable. The inset in panel C shows the PL ratios tabulated from the deconvolved data shown in panel D. **(D)** Deconvoluted contributions of the Pdot and Rh640 (grey) to the overall fluorescence intensity for the data in panel B. The dotted line represents the theoretical maximum contribution to the signal from the direct excitation of Rh640, estimated from the ratio of maximum absorbance and maximum emission intensity for a standard solution of Rh640 measured under the same conditions as the sample, and neglecting the possible formation of non-emissive aggregates.

5.2.4 Scope of polymer materials

Flow synthesis was used to probe the particle-forming capabilities of various combinations of SP and AP. Flow synthesis is semi-automated and was therefore thought to control for variations in particle formation arising from experimental variation. In addition to F8BT, the SPs used were

CNMEHPPV, MEHPPV, PFVA, and PFMEHPPV, having emission colours ranging from green to red. These SPs contain either the fluorene monomer or the phenylene vinylene monomer and exhibit extended π-conjugation throughout their backbones, rendering them hydrophobic and suitable for Pdot synthesis by nanoprecipitation. The structures of the polymers tested are shown in Figure 5.12A. Selected physical and optical properties of these polymers are listed in Table 5.1.

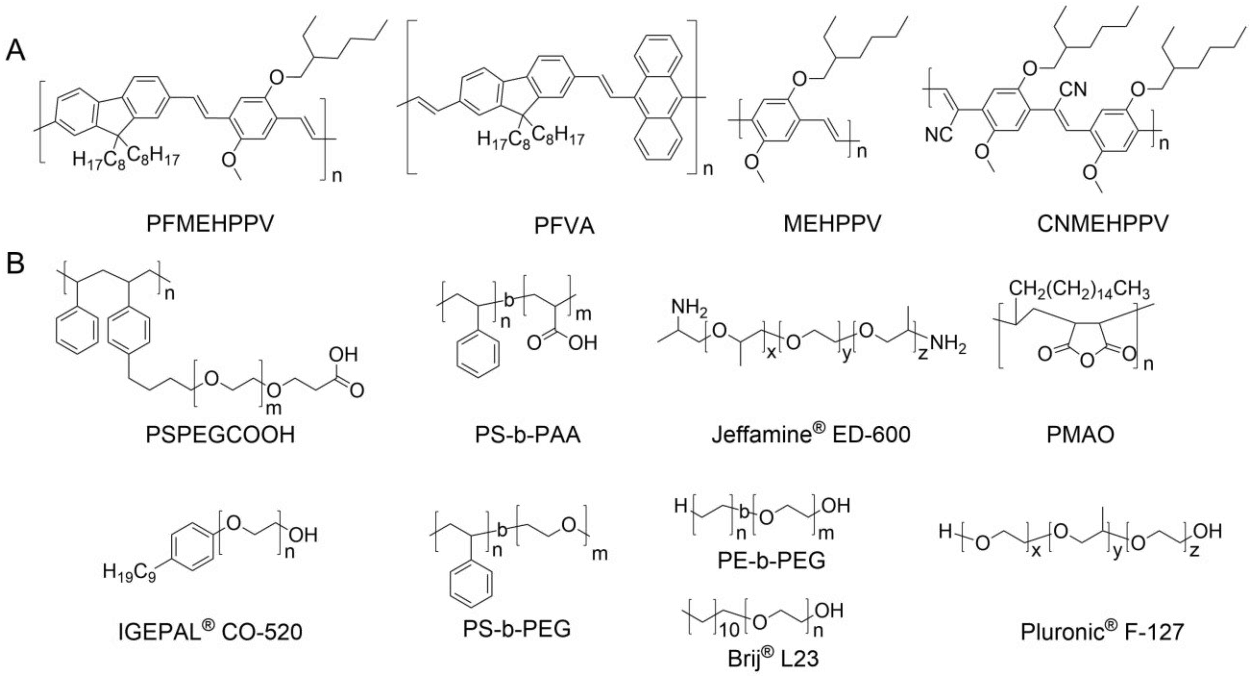

Figure 5.12 Structures of **(A)** semiconducting polymers and **(B)** amphiphilic polymers evaluated for Pdot synthesis.

Table 5.1. Selected properties of the semiconducting polymers used in this study

Polymer	$\lambda_{max,Abs.}$ (nm)[a]	$\lambda_{max,Em.}$ (nm)[b]	Em. colour[c]	M_w[d]	M_n[e]	PDI[f]	Contour Length (nm)[g]
PFMEHPPV	481	504	Green	178000		3.0	393
F8BT	453	540	Green-yellow		≤25000	≤3.00	49
PFVA	443	552	Yellow	19000		3.2	49
CNMEHPPV	453	552	Yellow-orange	350000		13.9	668
MEHPPV	502	555	Red-orange	>100 000			188

[a] Wavelength of maximum absorption in THF, [b] Wavelength of maximum emission in THF, [c] Emission colour in THF visible by eye, [d] Molecular weight provided by manufacturer, [e] Molecular number provided by manufacturer, [f] Polydispersity index (M_w/M_n) provided by manufacturer. [g] Estimated contour length based on manufacturer's M_w or M_n.

In addition to PSMA, nine APs were selected for testing with flow synthesis, the structures of which are shown in Figure 5.12B. Selected properties of these APs are listed in Table 5.2. The APs were selected to test the effects of multiple variables including molecular weight, monomer arrangement, charge, identity of hydrophobic and hydrophilic segments, and the ratio of hydrophobic to hydrophilic monomers in the polymer.

Selected combinations of SPs and APs were used for flow synthesis. Upon evaporation of THF, the resulting solutions were characterized by NTA and DLS (Table 5.3). Representative scattering and fluorescence mode size distributions for Pdots made with PSMA are shown in Figure 5.13. Although flow synthesis typically produced clear (*i.e.*, not turbid) solutions with bright fluorescence under longwave UV excitation, only some combinations of materials gave unambiguous evidence for nanoparticle formation via physical characterization.

Table 5.2. Selected properties of amphiphilic polymers

Polymer	M_w[a]	M_n[b]	Polymer type[c]	PDI[d]	Hydrophilic moiety[e]	Hydrophobic moiety[f]
PS-PEG-COOH		36 500	Graft	1.3	PEG-carboxylate (charged)	Phenyl
PS-b-PAA		5.2-b-4.0[g]	Block	1.15	Carboxylate (charged)	Phenyl
PSMA		1700	Random		Carboxylate (charged)[h]	Phenyl
PMAO		30000-50000	Alternating		Carboxylate (charged)[h]	Alkyl
Jeffamine ED-600	600		Block		PEG (neutral)	Alkyl
IGEPAL CO-520		441	Block		PEG (neutral)	Alkyl
PS-b-PEG		6.1-b-46.9[i]	Block	1.08	PEG (neutral)	Phenyl
PE-b-PEG		920	Block		PEG (neutral)	Alkyl
Brij L23	1198		Block		PEG (neutral)	Alkyl
Pluronic F-127	12 600		Block		PEG (neutral)	Alkyl

[a] Molecular weight, [b] Molecular number, [c] Arrangement of monomers in polymer [d] Polydispersity index (M_w/M_n), [e] Nature of hydrophilic polymer segment, [f] Nature of hydrophobic polymer segment, [g] M_n of PS block and PAA block, [h] Anhydride hydrolyzes in water to form 2 carboxylate groups, [i] M_n of PS block and PEG block

Table 5.3. Selected physical properties of Pdots of varying composition synthesized by the syringe pump method. Values are represented as the mean and standard deviation of three replicate batches. Materials with good agreement between all modes of characterization are labeled green. Materials with good agreement between characterization methods after the rejection of unreliable data are labeled blue. Data rejected as unreliable are marked with an asterisk (*). Data that were not recorded are marked with a dash (-). Physical characterization data for all materials tested is shown in Appendix A.1.

Semiconducting Polymer	Amphiphilic Polymer	D_{NTA} (nm)[a]		D_{DLS} (nm)[d]
		Scattering[b]	Fluorescence[c]	
F8BT	PSMA	59 ± 7	58 ± 6	53 ± 9
F8BT	PMAO	63 ± 20	31 ± 5	-
F8BT	PS-b-PEG	74 ± 2	79 ± 1	-
F8BT	PE-b-PEG	94 ± 8	99 ± 8	-
CNMEHPPV	PSMA	54 ± 1	39 ± 7	48 ± 3
CNMEHPPV	PMAO	67 ± 14	50 ± 10	35 ± 3
CNMEHPPV	PS-b-PAA	66 ± 11	24 ± 3	45 ±10
CNMEHPPV	PE-b-PEG	84 ± 4	86 ± 4	84 ± 6
CNMEHPPV	PSPEGCOOH	75 ± 5	80 ± 8	72 ± 4
CNMEHPPV	PS-b-PEG	103 ± 2	112 ± 3	105 ± 1
CNMEHPPV	None	97 ± 11	74 ± 56	100 ± 18
CNMEHPPV	Pluronic F127	99 ± 22	110 ± 35	93 ± 9
CNMEHPPV	Brij L23	80 ± 4	90 ± 3	78 ± 2
MEHPPV	PSMA	66 ± 5	*	31 ± 3
MEHPPV	PMAO	90 ± 16	*	34 ± 14
MEHPPV	PE-b-PEG	100 ± 3	*	99 ± 6
MEHPPV	PSPEGCOOH	82 ± 2	77 ± 15	70 ± 2
MEHPPV	PS-b-PEG	105 ± 3	153 ± 22	114 ± 55
MEHPPV	None	121 ± 4	*	120 ± 5
MEHPPV	Pluronic F127	105 ± 9	130 ± 27	115 ± 16
MEHPPV	IGEPAL	113 ± 18	87 ± 35	111 ± 26
PFVA	PMAO	102 ± 9	*	41 ± 3
PFVA	PS-b-PAA	114 ± 6	*	36 ± 8
PFVA	PE-b-PEG	81 ± 2	*	72 ± 3
PFVA	None	85 ± 2	*	74 ± 6
PFVA	PSPEGCOOH	93 ± 25	*	55 ± 4
PFVA	PS-b-PEG	87 ± 11	*	86 ± 2

[a] Mean diameter from raw NTA data (*i.e.,* no fitting applied), [b] Mean diameter from scattering mode NTA measurements (no filter), [c] Mean diameter from fluorescence mode NTA measurements (500 nm LP filter) [d] Mean diameter from intensity weighted DLS measurements (lognormal fitted)

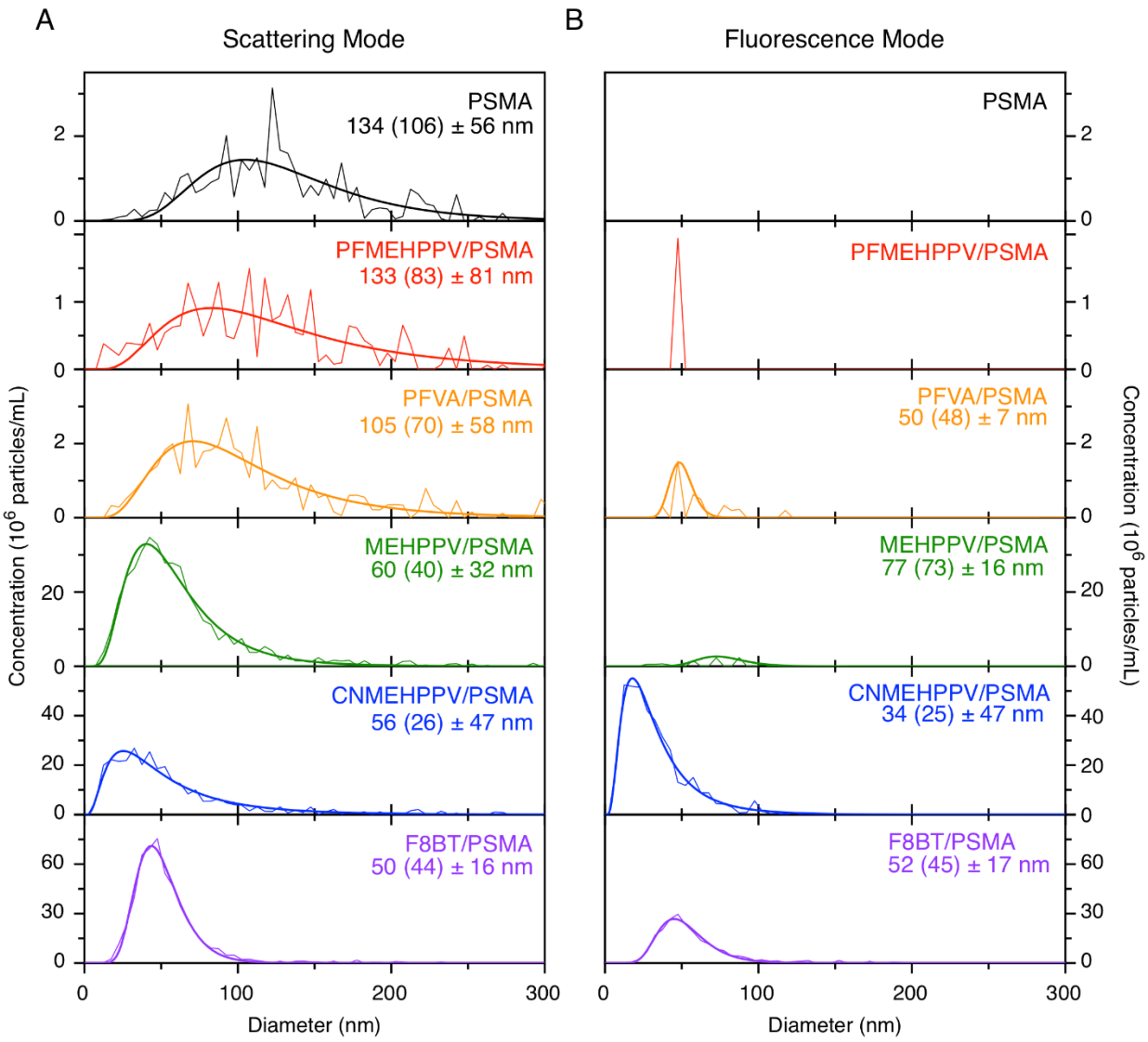

Figure 5.13 NTA size distributions from **(A)** scattering mode and **(B)** fluorescence mode for PSMA only nanoparticles and Pdots of SPs with PSMA. Particle sizes are indicated as the mean (mode) ± one standard deviation of the lognormal distribution. Note that the vertical axis scale changes between materials. Pdots composed of F8BT, CNMEHPPV and MEHPPV generally had sufficiently high particle counts in fluorescence mode to indicate successful Pdot formation.

Good agreement (± 15 nm) between scattering mode NTA, fluorescence mode NTA, and DLS was considered an indication of successful Pdot formation. However, only 10 out of the 41

combinations tested had good agreement between all characterization methods (green rows in Table 5.3), and these had either F8BT, CNMEHPPV, or MEHPPV as the SP. Nevertheless, disagreement between the three methods was not sufficient to rule out successful Pdot formation. Discrepancies between NTA and DLS analysis, or between scattering and fluorescence modes of NTA, may have arisen from the inherent limitations associated with NTA measurements. Such limitations included the possible exclusion of small (< 20 nm) or dim (weakly scattering or not brightly emissive) particles, or difficulties detecting particles with non-ideal optical properties (*i.e.*, inefficient scattering/excitation at 488 nm or dim emission between 500–600 nm). As a result, low particle counts were obtained in fluorescence mode for MEHPPV, PFVA, and PFMEHPPV (Figure 5.13). Some samples were also observed to rapidly photobleach under video acquisition conditions (Figure A.1 in Appendix A). We therefore established a number of statistical criteria for rejecting NTA datasets as unreliable based on the measured particle concentrations, number of valid tracks, or the ratio of valid tracks to total tracks (see Appendix A.2). Rejecting unreliable NTA data resulted in agreement between NTA and DLS data for five additional combinations of materials (blue rows in Table 5.3), indicating particle formation.

Agreement between NTA and DLS data is not strictly sufficient to unambiguously support particle formation. Ideally, further confirmation would be provided by an imaging technique such as TEM or AFM. Only one combination of materials synthesized by flow was characterized by TEM (F8BT/PSMA, Figure 5.3A), but gave identical particle morphologies and sizes to Pdots of identical composition synthesized by manual injection. Previously, TEM images were obtained for Pdots composed of F8BT and CNMEHPPV with PSMA and PSPEGCOOH as the amphiphiles

synthesized by manual injection, showing quasi-spherical particle morphologies and sub-100 nm particle diameters (data not shown). The reliable synthesis of these particles by manual injection indicates that formation of particles of the same composition by flow is probable.

Ideally, co-precipitation of the SP and the AP forms a putative core/shell (or core/corona) structure where the AP is wrapped around the hydrophobic SP core. Some APs may not associate efficiently with the SPs, precluding the formation of this structure. Gel electrophoresis was used to indirectly test the association between the two species (Figure 5.14). Pdots have non-ideal behaviour in gel electrophoresis (formation of uneven streaks, low resolution), but characterization by capillary electrophoresis was unsuccessful as Pdots did not elute from the capillary, likely due to non-specific binding to the silica capillary. If the intended Pdot structure was formed with an anionic amphiphile, the resulting particles should be negatively charged and migrate towards the anode. Pdots made with PSMA (vii) or PSPEGCOOH (vi) reliably showed anodic migration, providing evidence for particle formation, whereas Pdots made with PS-b-PAA (iv) and PMAO (v) remained in the well, likely indicative of the formation of large aggregates or separate populations of structures containing only SP or AP (the APs are non-emissive and would not appear in the gel image). Conversely, Pdots synthesized with a neutral, PEGylated amphiphile should not have migrated towards the anode and should have remained in the well or shown slight migration towards the cathode from electroendosmosis. This result held true for PS-b-PEG materials (iii), but PE-b-PEG materials (ii) showed significant anodic migration in all cases. This result was unusual, as these materials were expected to be neutral in charge but showed more migration than particles made with SP only (*i.e.*, no AP), which are thought to obtain a negative surface charge

by oxidation of the functional groups along the SP backbone [62]. The origin of this effect is unknown, but may arise from undetermined chemical changes to the structures of the AP or SP.

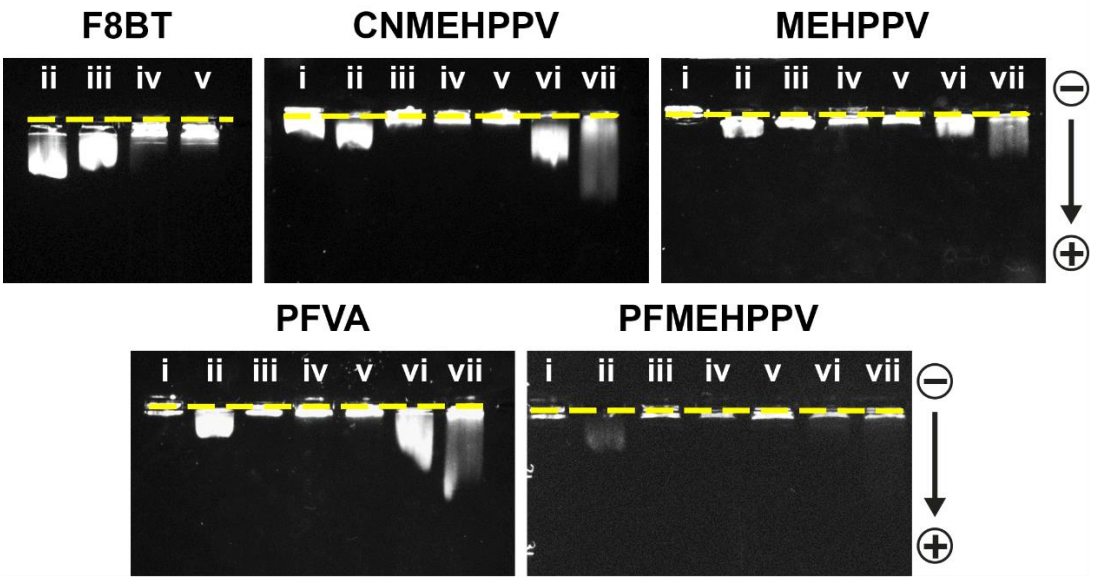

Figure 5.14 Agarose gels of nominal F8BT, CNMEHPPV, MEHPPV, PFVA and PFMEHPPV Pdots synthesized with (i) no amphiphile, (ii) PE-b-PEG, (iii) PS-b-PEG, (iv) PS-b-PAA, (v) PMAO, (vi) PSPEGCOOH and (vii) PSMA. The location of the wells is indicated by the dashed yellow line.

If the APs did not efficiently associate with the SPs, a distinct population of amphiphile-only structures may have formed but would not have been observed by fluorescence methods. Flow synthesis was used to prepare amphiphile-only particles by nanoprecipitation, and the solutions were then characterized by NTA (Table 5.4). The resulting nanoparticles were large (> 100 nm) in diameter with broad size distributions and low as-synthesized particle concentrations. NTA size distributions for nanoparticles of PSMA with and without SP are shown in Figure 5.13. For Pdots with sufficiently high particle counts (*i.e.*, MEHPPV, CNMEHPPV, F8BT), the obtained size

distributions are distinct from those of the PSMA only particles. Additionally, these Pdots gave high particle counts in fluorescence mode, indicating that most particles formed contained SP. PFMEHPPV and PFVA Pdots are not well-suited for NTA analysis and had low particle counts in both scattering and fluorescence methods. It is probable that some fraction of good Pdots were formed due to the non-zero particle counts in fluorescence mode, although difficult to quantify due to differences in sensitivity between scattering and fluorescence mode for each material.

Table 5.4. Average particle diameter for amphiphile-only nanoparticles determined by NTA from 3 replicate batches (scattering mode)

Amphiphile	Average diameter (nm)	Average standard deviation (nm)	Stock concentration (pM)
PSMA	138 ± 7	62 ± 10	56 ± 2
PSPEGCOOH	145 ± 9	81 ±12	140 ± 20
PMAO	146 ± 23	60 ± 6	50 ± 20
PS-b-PAA	149 ± 17	96 ± 31	29 ± 2
PS-b-PEG	140 ± 15	63 ± 14	140 ± 30
PE-b-PEG	159 ± 5	64 ± 10	60 ± 20

Selected combinations of SP and AP were used for Pdot synthesis by manual injection to test if the results obtained by flow synthesis (*i.e.*, whether a given combination produced Pdots) could be replicated manually. MEHPPV/PSPEGCOOH was selected as it reliably produced particles by flow. F8BT/PE-b-PEG was selected as it gave evidence for particle formation via physical characterization but demonstrated unexpected behaviour in gel electrophoresis and emission measurements. PFVA/PMAO was selected as a combination that was not expected to form particles based on the results from flow synthesis.

Physical characterization results for the Pdots synthesized by manual injection are shown in Table 5.5 and optical properties are shown in Table 5.6. None of the combinations of materials tested showed good agreement between NTA and DLS, likely due to the bias of DLS towards larger particle sizes (*i.e.*, aggregates). There was also significant variation in particle diameter between the three replicate batches for DLS, likely owing to the poor reproducibility of manual injection. However, all three materials showed anodic migration in gel electrophoresis (Figure 5.15), indicating that some proportion of good particles were formed. All materials tested had similar optical properties (peak shapes and spectral positions) to corresponding materials synthesized by flow, save for F8BT/PE-b-PEG whose absorption band showed a 10 nm red-shift (attributed to the formation of large aggregates and visible turbidity for the manual injection samples) and whose emission band did not display a second peak that was observed for samples of the same composition synthesized by flow synthesis (*vide infra*).

Table 5.5. Average particle diameters for Pdots composed of various materials synthesized by manual injection. Values are presented as the mean ± one standard deviation of three replicates batches. Asterisks (*) denote unreliable datasets (see Appendix A.2).

Semiconducting Polymer	Amphiphilic Polymer	D_{NTA} (nm)[a]		D_{DLS} (nm)[d]
		Scattering[b]	Fluorescence[c]	
F8BT	PE-b-PEG	98 ± 5	163 ± 45	240 ± 20
MEHPPV	PSPEGCOOH	86 ± 13	*	150 ± 31
PFVA	PMAO	85 ± 3	*	230 ± 22

[a] Mean diameter from raw NTA data (i.e. no fitting applied), [b] Mean diameter from scattering mode NTA measurements (no filter), [c] Mean diameter from fluorescence mode NTA measurements (500 nm LP filter) [d] Mean diameter from intensity weighted DLS measurements (lognormal fitted)

Table 5.6. Optical properties of Pdots of varying composition synthesized by the manual injection method. Values are presented as the mean ± one standard deviation of three replicate batches.

Semiconducting Polymer	Amphiphilic Polymer	$\lambda_{max,Abs.}$ (nm)[a]	$\lambda_{max,Em.}$ (nm)[b]
F8BT	PE-b-PEG	479 ± 5	539
MEHPPV	PSPEGCOOH	503	591
PFVA	PMAO	440	577

[a] Wavelength of maximum absorption for the lowest energy peak, [b] Wavelength of maximum emission (All wavelength values are ±3 nm or less unless otherwise noted).

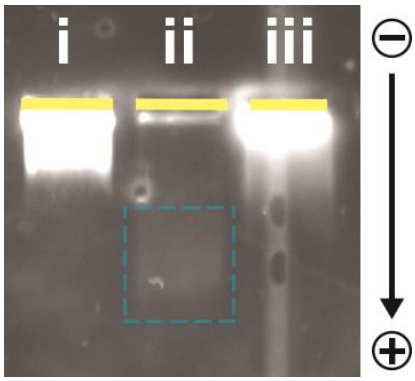

Figure 5.15 Gel electrophoresis for (i) F8BT/PE-b-PEG, (ii) MEHPPV/PSPEGCOOH and (iii) PFVA/PMAO Pdots synthesized by manual injection. The dashed yellow line indicates the location of the wells. The dashed blue box indicates the location of the band for MEHPPV/PSPEGCOOH Pdots, which were not brightly emissive under the conditions of image acquisition.

Pdots from flow synthesis were also characterized optically (Table 5.7). Representative absorbance, emission, and excitation spectra for CNMEHPPV, MEHPPV, PFVA, and PFMEHPPV Pdots are shown in Figure 5.16. For a given SP, the spectral positions of the absorbance and emission peaks were fairly consistent (*i.e.*, < 10 nm shift) across batches synthesized with different APs. The emission peak shapes were also largely unchanged for a given SP across different APs. Differences in peak shape were quantified by χ^2, Eqn. 5.1, where I is the

normalized emission intensity at wavelength λ, *S* refers to the sample under comparison, and *ref.* refers to the reference material. SP/PSMA Pdots were used as the reference material and emission peaks were aligned to their wavelength of maximum emission for the calculation of χ^2.

$$\chi^2 = \sum \frac{(I_S(\lambda) - I_{ref.}(\lambda))^2}{I_{ref.}(\lambda)} \tag{5.1}$$

χ2 values less than or equal to 1 indicated little change in peak shapes (green rows in Table 5.7). Several combinations (F8BT with PS-b-PAA and PMAO; PFMEHPPV with Brij L23 and Jeffamine ED-600) exhibited χ^2 values between 1–10, which corresponded to increased intensity in the shoulder region at wavelengths above the emission maximum. F8BT/PE-b-PEG peak had a χ^2 value of ~21, corresponding to the appearance of a new emission peak that may arise from increased intensity in the shoulder region (red row in Table 5.7). Across three replicates, the relative intensity of the second peak compared to the original peak varied slightly. The cause of this peak is unknown; a corresponding peak did not appear when the same combination of materials was used for Pdot synthesis by manual injection. This peak may have arisen from changes in chain packing or local environment of the chromophores, or may be from an unidentified contaminant whose absorption signature is masked by strong absorption from the Pdot. Emission spectra for F8BT Pdots synthesized with PSMA (reference material), PS-b-PEG, PE-b-PEG (increased shoulder intensity), PS-b-PAA (increased shoulder intensity), and PE-b-PEG (new emission peak) are shown in Figure 5.17A. The peak shapes from the absorption and excitation spectra (Figure 5.17B) were identical for F8BT/PSMA and F8BT/PE-b-PEG Pdots, although the absorption peak for F8BT/PE-b-PEG was red-shifted by ~2 nm.

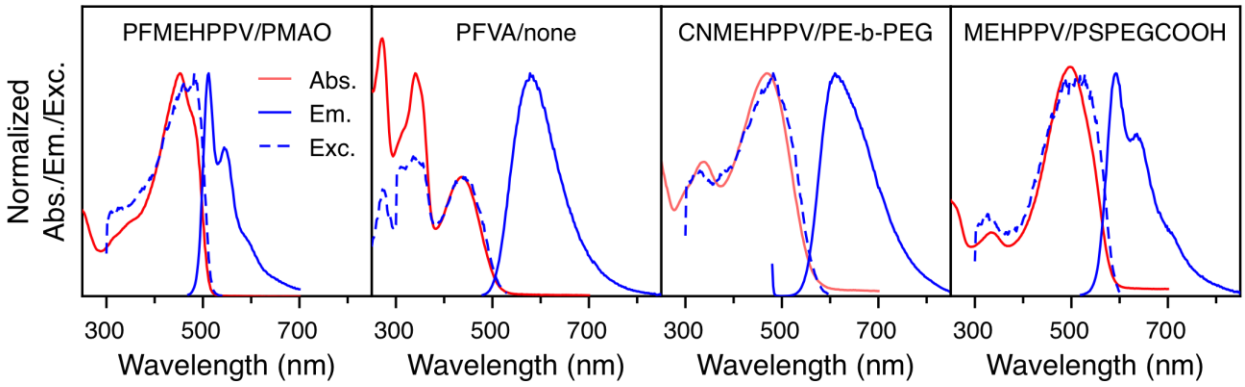

Figure 5.16 Normalized absorption, emission and excitation spectra for Pdots composed of the indicated semiconducting polymers and amphiphiles.

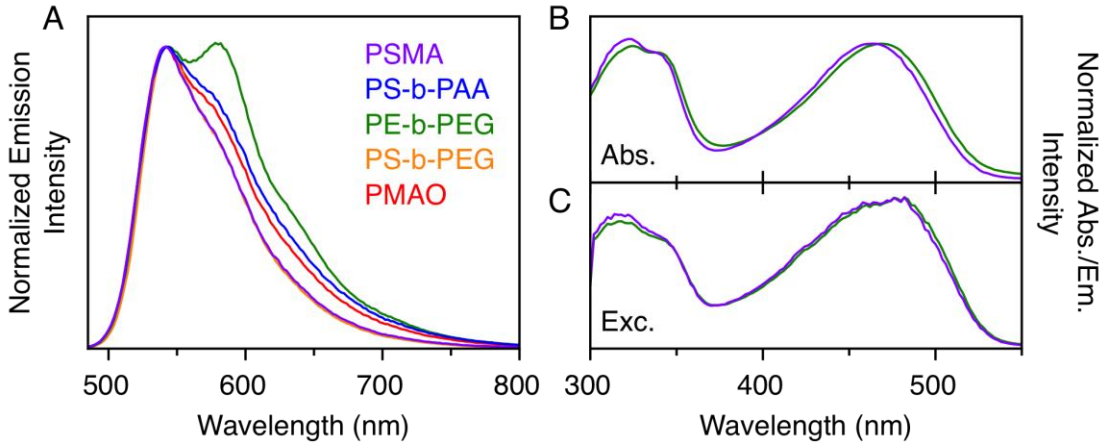

Figure 5.17 (A) Aligned and normalized emission spectra for Pdots synthesized with F8BT and the indicated amphiphile ($\lambda_{ex.}$ = 460 nm). The spectrum for F8BT/PS-b-PEG aligns with and is obscured by the spectrum for F8BT/PSMA. **(B)** Absorption and **(C)** excitation spectra ($\lambda_{em.}$ = 600 nm) for F8BT/PSMA Pdots and F8BT/PE-b-PEG Pdots synthesized by syringe pump flow synthesis.

Table 5.7. Optical properties of Pdots of varying composition synthesized by the syringe pump method, for the same samples shown in Table 5.3. Values are represented as the mean and standard deviation of three replicates batches. Optical characterization data for all materials tested is shown in Appendix A.1. Pdots synthesized with PSMA were used as the reference material for the determination of χ^2 and therefore do not have an associated χ^2 value. Materials with little change in peak shape compared to the Pdot with PSMA are labeled green. F8BT/PE-b-PEG, labeled red, displayed a new emission peak above the emission maximum of F8BT/PSMA Pdots.

Semiconducting Polymer	Amphiphilic Polymer	$\lambda_{max,Abs.}$ (nm)[a]	$\lambda_{max,Em.}$ (nm)[b]	χ^2 [c]
F8BT	PSMA	464	541	-
F8BT	PE-b-PEG	469	543	21 ± 8
F8BT	PS-b-PEG	465	541	0.11 ± 0.03
CNMEHPPV	PSMA	471	616	-
CNMEHPPV	PS-b-PAA	475	619	0.12 ± 0.05
CNMEHPPV	PE-b-PEG	468	611	0.16 ± 0.05
CNMEHPPV	PS-b-PEG	470	610	0.27 ± 0.07
CNMEHPPV	PMAO	470	615	0.4 ± 0.4
CNMEHPPV	PSPEGCOOH	471	616	0.4 ± 0.3
CNMEHPPV	Brij L23	469	614	0.05 ± 0.02
CNMEHPPV	Pluronic F127	467	611	0.2 ± 0.1
CNMEHPPV	none	468	610	0.3 ± 0.1
MEHPPV	PSMA	497	592	-
MEHPPV	PE-b-PEG	501	593	0.08 ± 0.04
MEHPPV	PS-b-PEG	500	593	0.2 ± 0.1
MEHPPV	PMAO	500	592	0.14 ± 0.05
MEHPPV	PSPEGCOOH	498	592	0.18 ± 0.03
MEHPPV	IGEPAL	501	591	0.25 ± 0.04
MEHPPV	Pluronic F127	499	592	0.3 ± 0.2
MEHPPV	none	501	591	0.4 ± 0.2
PFVA	PSMA	432	577	-
PFVA	PS-b-PAA	438	583	0.2 ± 0.2
PFVA	PE-b-PEG	439	582	0.08 ± 0.03
PFVA	PS-b-PEG	439	579	0.3 ± 0.3
PFVA	PMAO	436	578	0.3 ± 0.2
PFVA	PSPEGCOOH	436	580	0.2 ± 0.1
PFVA	none	437	579	0.4 ± 0.2

[a] Wavelength of maximum absorption for the lowest energy peak, [b] Wavelength of maximum emission (all wavelength values are ±3 nm or less) [c] χ^2 of emission peak against peak shape of SP/PSMA Pdots (± represents the standard deviation for 3 replicates).

For comparison, χ^2 was also calculated for SP/PSMA Pdots using the unaggregated SP in THF as a reference (Table 5.8). The absorption and emission spectra of the Pdots are red-shifted compared to the unaggregated SP in THF (but spectra were aligned to their emission maxima for the determination of χ^2). Except for F8BT, the χ^2 values were significantly larger when comparing the unaggregated SP to the Pdots than comparing the Pdots of varying composition. The emission peak shapes for F8BT and PFVA were similar in the unaggregated and Pdot forms. PFMEHPPV and MEHPPV showed increased intensity in the red-shoulder region in Pdot form, and CNMEHPPV showed significant peak broadening after aggregation into Pdot structures.

Table 5.8. Selected optical properties for unaggregated SPs in THF.

Semiconducting Polymer	$\lambda_{max,Abs.}$ (nm)[a]	$\lambda_{max,Em.}$ (nm)[b]	χ^2 [c]
F8BT	453	536	4.6
CNMEHPPV	453	552	80
MEHPPV	502	552	96
PFVA	443	550	0.99
PFMEHPPV	481	500	36

[a] Wavelength of maximum absorption for the lowest energy peak
[b] Wavelength of maximum emission
[c] χ^2 of emission peak of SP/PSMA Pdots against peak shape of unaggregated SP in THF

5.2.5 Scale up

The commercial production of Pdots will require the development of large-scale synthetic methods capable of reliably and reproducibly delivering litres of materials, ideally in an automated or semi-automated format. Synthesis by manual injection is inherently limited in scale to volumes that can

be handled by an individual. Although some scalability is achievable using the syringe pump set up, for the hardware used here, the maximum compatible syringe volume is 60 mL owing to the pump fittings and the power of the pump motor.

With large scale synthesis in mind, programmable continuous flow pumps were used to manufacture Pdots on a large scale (up to 100 mL for proof-of-concept). This system used the same components (tubing and mixer elements) as the syringe pump system, other than the pumps themselves. The continuous flow pumps may be operated at flow rates of up to 5 mL/min, in contrast to the maximum flow rate of the syringe pumps (dependent upon the syringe volumes; 18 mL/min for the 10 mL scale).

We first undertook systematic studies of flow rate and precursor concentration to optimize conditions for scale up. F8BT/PSMA Pdots were synthesized using Y-mixers and PTFE tubing of varying ID. The precise IDs of the mixing elements were unknown, but the mixers were of similar dimensions to the T-mixers used previously (~0.2–1 mm ID), and were categorized as ‘small’, ‘medium’, or ‘large’. Synthesis was performed on a 6 mL scale with manual fraction collection of ~1.5 mL fractions. The first fraction was discarded to account for the time needed for the pumps to reach steady state flow. Figure 5.18 shows the NTA-derived average sizes for the synthesized Pdots. As with the syringe pump system, some size tuning was achieved between ~30–100 nm depending upon the mixer and tubing IDs and flow rate. Using narrow tubing lead to over-pressurization of the pumps and synthesis could not be performed above 3 mL/min for 0.50 mm ID tubing or 1 mL/min for 0.025 mm ID tubing when paired with the ‘small’ Y-mixer.

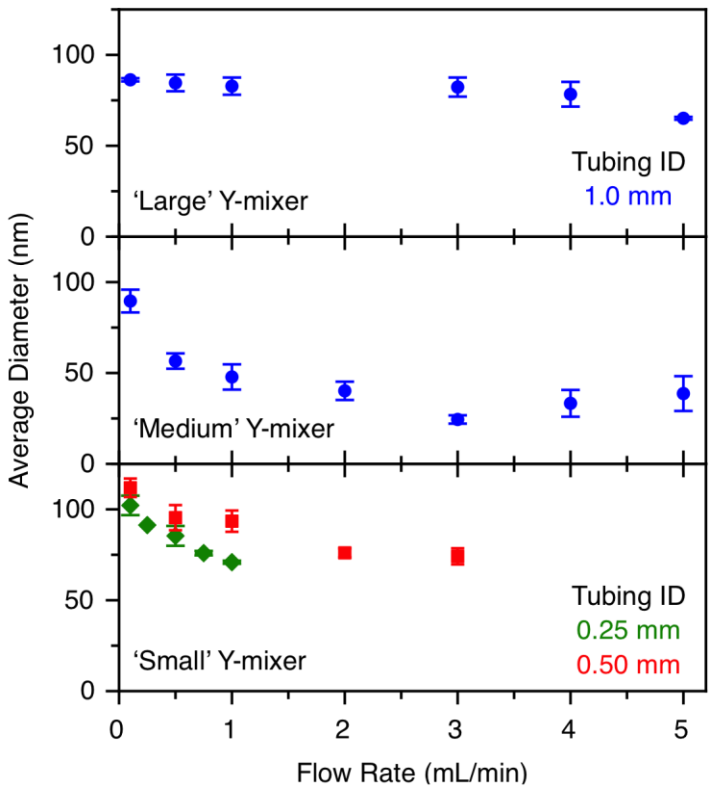

Figure 5.18 Average diameters obtained varying flow rate and tubing ID (indicated in figure) using continuous flow pumps for 'large' Y-mixer (top), 'medium' Y-mixer (middle) and 'small' Y-mixer (bottom). Sizes were determined from lognormal fitting of fluorescence mode NTA data. Tubing IDs are indicated in the figure. The true IDs of the mixer elements are unknown. Error bars represent the standard deviation of fractions 2-4 for a single run.

Optimization experiments were also performed using T-mixers of differing ID. For these and subsequent experiments, the continuous flow pump system was paired with a liquid handler to enable automated fraction collection. Some control over average particle diameters was achieved by varying flow rate and precursor concentration. Precursor concentrations of 0.02 mg/mL F8BT were used for flow synthesis at varying flow rates using T-mixers of differing internal diameters (Figure 5.19A). Partitioning and the occurrence of Schlieren lines were observed for flow rates below 1 mL/min, implying incomplete mixing in the mixer element as was observed for low flow

rates with the syringe pump hardware. For all mixers, some decrease in particle size was observed for increasing flow rates ranging from *ca*. 50–130 nm, similar to the trends observed using Y-mixers (Figure 5.18). Pdots synthesized with varying concentrations of F8BT displayed little change in average diameter except at low (10^{-4} mg/mL) F8BT concentrations, where both the average size and standard deviation were increased compared to the other samples. The formation of uniform Pdots was likely disfavoured at low concentrations, where instead large aggregates may have formed more readily to stabilize individual polymer chains in solution, increasing the observed average diameter.

Scale up experiments were performed using two combinations of SP and AP: F8BT/PSMA and CNMEHPPV/PS-b-PEG. F8BT and CNMEHPPV were chosen because, of the SPs available, they were the most amenable to NTA analysis. PSMA and PS-b-PEG were chosen to compare a random polymer to a block polymer and a charged amphiphile to a neutral PEG amphiphile. Scale up was performed using the 0.20 mm diameter T-mixer and 0.25 mm ID tubing. The pumps were operated continuously at a flow rate of 5 mL/min, collecting 1.1 mL fractions to a final volume of 100 mL.

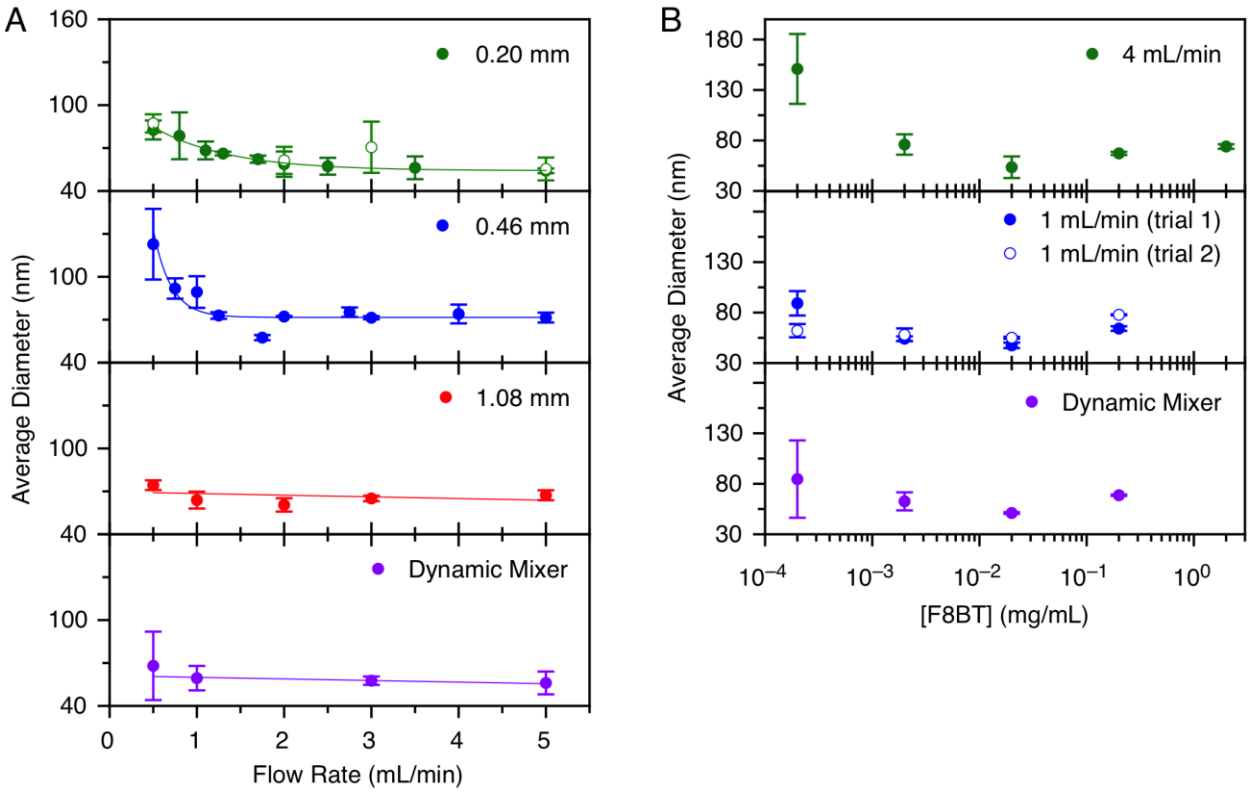

Figure 5.19 Optimization of continuous flow pump synthesis of F8BT/PSMA Pdots. **(A)** Average diameter determined by fluorescence mode NTA as a function of flow rate for a 0.20 mm ID t-mixer, 0.46 mm ID t-mixer, 1.08 mm ID t-mixer and a dynamic mixer. Hollow data points represent a replicate synthesis performed using 0.002 mg/mL F8BT. **(B)** Average diameter determined by fluorescence mode NTA as a function of F8BT concentration at flow rates of 4 mL/min, 1 mL/min using a 0.20 mm ID t-mixer and using a dynamic mixer at a flow rate of 4 mL/min. Hollow data points represent a replicate synthesis utilizing the same conditions. Error bars represent the standard deviation of three replicate batches.

Three replicates were run for each combination of polymers, and the NTA sizing results are shown in Figure 5.20. For F8BT/PSMA, the average particle diameter was relatively consistent (~45 nm) across three replicates. At longer times, more spread was oberved in the data, indicating decreased reproducibility. Between 10–70 mL the first trial produced larger than average diameters. At 100 mL, there was significant disparity between the three replicates. For CNMEHPPV/PS-b-PEG, the average diameters obtained for trial 1 were signifcantly larger than those obtained for trials 2

and 3, which agreed well. Further experiments are required to determine if this variability arose from the combination of polymers used, the continouous flow system itself, or if this dataset may be treated as an outlier. The average diameter tabulated from 3 trials was fairly consistent throughout the synthesis, but with large variability attributed to trial 1. Discounting trial 1, the average diameters determined from trials 2 and 3 only showed a slight increase from ~80 nm to ~90 nm, although further replicates are required to determine if this is a replicable trend or a consequence of the limited resolution of NTA. Both combinations of polymers exhibited comparable or smaller average diameters compared to the same materials synthesized by syringe pump (~50–60 nm for F8BT/PSMA and ~100–110 nm for CNMEHPPV/PS-b-PEG).

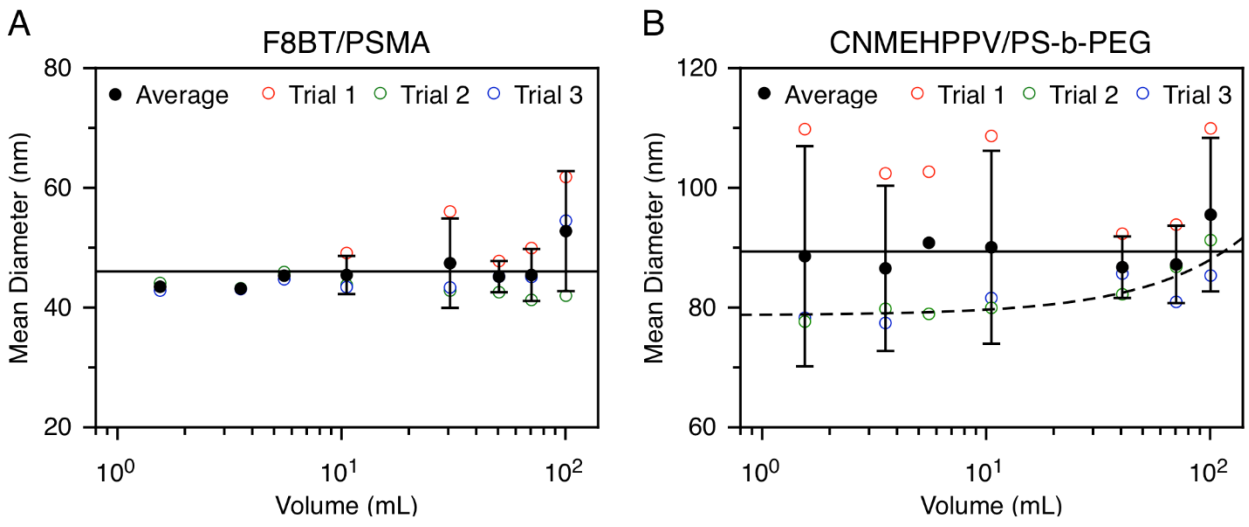

Figure 5.20 Average particle diameters (lognormal fitted) as a function of synthesis volume for **(A)** F8BT/PSMA Pdots (fluorescence mode) and **(B)** CNMEHPPV/PS-b-PEG Pdots (scattering mode). The solid line represents the line of best fit for trials 1-3 and the dashed line represents the line of best fit for trials 2 and 3 only. The linear function is distorted by the logarithmic-scale horizontal axis.

Due to the large number of aliquots produced for the continuous flow pump experiments, it was not feasible to fully remove the organic solvent from each aliquot before analysis. For consistency, no solvent removal was performed before NTA analysis. A possible source of disparity between aliquots was the variable amount of time each aliquot spent in an environment of higher organic character (lower polarity). As synthesis was performed at a much faster rate than analysis, aliquots eluted at later time points spent more time in the organic/aqueous solution before analysis was performed. It is possible that this delay had an unknown effect on particle sizes (*e.g.*, longer effective mixing time of the two solvents, slow evaporation of THF in ambient conditions). Full chain collapse and particle formation likely does not occur until most of the organic solvent has been removed from solution, so it is possible that nanoparticles were not truly formed until the aliquots were diluted in water for NTA analysis, where the dilution step is a poorly controlled process (*i.e.*, possibility of different mixing environments for each aliquot). The continuous flow pumps heat up over the course of the run (~20 min), which may also change the dynamics of particle formation within the system (*e.g.*, increased volatilization of THF and increased pressure within the tubing and mixing element or effects on thermodynamics of particle formation).

5.3 Discussion

The production of Pdots by flow synthesis will require additional optimization beyond the proof-of-concept demonstrated here. Trends in size and reproducibility were observed to hold for individual experiments, but there was considerable variation between experiments performed using different stock solutions, particularly for stock solutions prepared at different times. Although all stock solutions were prepared in THF containing a stabilizer (butylated hydroxytoluene, BHT) to prevent the formation of peroxides, one hypothesis is that, over time,

reactive peroxides formed and began to chemically degrade the polymers. Changes in the chemical structure of the polymers may change the hydrophobic character or polarity of that species, changing the way the polymer chains collapse into particles during nanoprecipitation and ultimately changing the particle size obtained. Despite being hydrophobic, many SPs form well-dispersed nanoparticles without an amphiphile, which is thought to occur due to the formation of polar species via oxidation of the polymer backbone that act to stabilize particles in water [62]. Oxidation of the polymer simply by introduction to water suggests that other physicochemical changes can occur easily in other circumstances as well. The time scale of these hypothesized chemical changes is not apparent, and it may be difficult to observe these changes by NMR or mass spectrometry due to the low concentrations of the stock solutions, the polydispersity of the polymers, and the likelihood that only a small number of constituent monomers are modified along the polymer backbone. One possible solution is to make fresh stock solutions for each synthesis, however, this approach is not practical due to the small amount of material needed (~μg) and the desire to keep concentrations constant for a particular set of experiments.

The ideal synthetic method allows for the fine-tuning of particle size by simple manipulation of one of the formulation parameters. We observed some control of size at low flow rates and low concentrations with both the syringe pump and continuous flow pump systems, but in all cases reached an apparent plateau over much of the range of accessible parameter values. This result implies that mixing and by extension particle formation achieve maximum efficiency above certain thresholds.

The effect of flow rate on size in Figure 5.7 and Figure 5.19 suggests the existence of multiple regimes of mixing efficiency depending on the dimensions of the mixing element. At sufficiently high flow rates, highly efficient (more turbulent) mixing occurs and achieves a maximum mixing efficiency. Within this regime, the obtained particle size is unchanged (*i.e.*, the rate of chain aggregation is slower than the rate of mixing). At sufficiently low flow rates, mixing occurs with lower efficiency (*i.e.*, more laminar flow) and particle size is predominantly controlled by the polymer concentration. Between these extremes, the extent of turbulent mixing is determined by the flow rate and the particle size should depend on both the flow rate and the polymer concentration.

The trends in precursor concentration and particle size in Figure 5.6 and Figure 5.19 suggest that particle nucleation and growth are favoured in different concentration regimes. The hydrophobic SP is soluble in THF, but becomes supersaturated in the homogeneous, fully mixed solution of THF and water. As a consequence of this supersaturation, a large number of small particle nuclei are formed at high precursor concentrations. Particle growth occurs by particle-particle collisions [210], although if smaller particles are stabilized (*e.g.*, by the presence of an amphiphile at the particle surface), these collisions may not lead to the aggregation of two particles. At low precursor concentrations the hydrophobic polymers experience less supersaturation and there is less driving force for particle nucleation; instead particle growth dominates, resulting in the formation of larger particles and aggregates. At intermediate concentrations, both mixing rates and dilution rates are expected to determine the balance between nucleation and growth (*i.e.*, rate of change of the local concentrations of the solubilized polymers). With further optimization of the system, better control

over obtained particle sizes should be achievable by changes in flow rate and precursor concentration.

For most configurations, a minimum limit size of 50–60 nm was obtained by both the syringe pump and continuous flow pump systems for F8BT Pdots with various amphiphiles. The minimum limit size for other SPs with various APs was larger, ranging from *ca.* 70–90 nm depending on the specific polymers used. This limit size was likely controlled by the backbone rigidity of the SP and its contour length (Table 5.1). Smaller particle diameters were usually obtained for F8BT Pdots than CNMEHPPV or MEHPPV (*i.e.*, the other SPs suited to NTA analysis), possibly because its contour length was an order of magnitude less than those polymers. Ideally, flow synthesis would be able to make particles ranging from 10 nm to over 100 nm with any SP and AP materials. Beyond the proof-of-concept demonstrated here, additional optimization and characterization of the system is required to achieve this goal.

In syringe pump flow synthesis, beyond the waste solution collected during the priming step, the final Pdot solution was not fractionated. The dead volume, or the volume outputted between the initiation of flow and the establishment of (assumed) equilibrium flow conditions, was collected along with the final Pdot solution. Inefficient or inconsistent mixing associated with the dead volume may be a significant contribution to the observed distribution of particle sizes for a given sample. This effect was avoided with the continuous flow pumps, as a liquid handler was used to automate fraction collection. The first ~ 1 mL of Pdot solution was discarded and fractions could be collected at any point along the experimental run, eliminating inconsistencies associated with the dead volume.

Due to challenges with NTA characterization and the non-ideal migration patterns of Pdots in gel electrophoresis, it is somewhat ambiguous which combinations of SPs and APs form good Pdots. Of the anionic APs, only PSMA and PSPEGCOOH showed good size agreement across SPs (for those that are amenable to analysis by NTA) and showed the expected migration pattern in gel electrophoresis, indicating particle formation. Of the neutral APs, PS-b-PEG and PE-b-PEG yielded good size agreement with multiple SPs. PS-b-PEG showed the expected gel migration pattern (*i.e.*, no migration due to lack of charge), but PE-b-PEG unexpectedly showed anodic migration despite the nominal lack of charge. PE-b-PEG likely formed Pdot structures with the SPs that were stabilized due to unknown chemical changes to either the AP or SP polymer structures that introduced charge. An unknown contaminant introduced with the PE-b-PEG may also have introduced charge to the Pdot surface or caused unknown chemical changes to the polymers. The other amphiphiles did not give sufficient evidence for particle formation, although further analysis by TEM or AFM is required to determine if Pdots were truly formed with these materials.

Although our flow-based manufacturing system shows improvements over manual injection in terms of reproducibility and scalability, it is important to also consider the cost and complexity of these methods. The ubiquity of the manual injection method is partially driven by its low cost and accessibility. This method requires only common laboratory equipment (*e.g.*, ultrasonicator) and is easy to perform. Syringe pump flow synthesis is intermediate in complexity, requiring a double syringe pump (or two connected syringe pumps if asymmetric flow rates are to be used). Beyond the start-up costs associated with purchasing pumps, relatively inexpensive hardware (mixers,

PTFE tubing) must also be purchased. Upon installation of this hardware, operation of the syringe pump set up is straightforward. The continuous flow pump method presents additional cost and complexity. Its operation requires trained personnel (although automation is a possible future direction), but it allows for production at scales that are not possible with the syringe pump or manual injection methods.

The rate limiting step for the downstream use of Pdots, regardless of their synthetic method, is solvent removal and concentration. Solvent is typically removed under vacuum or under nitrogen flow. Most of the flow synthesis experiments here used symmetric flow rates and therefore equal volumes of organic solvent and water. Although THF is a volatile solvent, its removal is time and energy intensive. For industrial scale applications, limiting the amount of organic solvent used would simplify post-synthetic processing and limit energy consumption. However, this approach requires the use of asymmetric flow rates, where the organic precursor solution is pumped at a slower rate than the aqueous solution. Changes in the relative flow rate would change the dynamics of mixing and would likely require further optimization. The relative volume of organic and aqueous solutions has been reported to affect the particle size obtained in manual injection [60], and may be used analogously to tune particle size by flow synthesis.

5.4 Conclusions

We have developed a flow-based method for manufacturing Pdots on both small (1–10 mL) and large (100 mL) scales. Flow synthesis offers several key advantages over traditional manual injection synthesis, including improved reproducibility and some tuning of particle sizes. Particle size may be tuned somewhat by changes in the flow rate or precursor polymer concentration. Flow

synthesis was used to encapsulate a fluorescent dye within the Pdot matrix, demonstrated by the occurrence of energy transfer-sensitized dye emission. Flow synthesis was further used to systematically determine the nanoparticle forming behaviours of a variety of semiconducting and amphiphilic polymers, and several materials with good potential for forming Pdots were identified. Although we have demonstrated proof-of-concept, additional optimization of both the syringe pump and continuous flow methods is required to achieve fine-tuning of particle size and still greater reproducibility. A greater understanding of the fluid dynamics within the mixer elements, attainable through computational fluid dynamics modelling, will enable better control of mixing efficiency and therefore particle size.

5.5 Experimental Methods

5.5.1 Materials

Polymer stock solutions were made using THF [ACS reagent ≥ 99.0% with 250 ppm BHT as an inhibitor from Sigma Aldrich (Oakville, ON, CA) or OmniSolv HPLC grade BHT stabilized (250 ppm) from Millipore (Billerica, MA, USA)]. Stock solutions were diluted in purified THF (from a MB-SPS 5/7 solvent purification system, MBRAUN, Stratham, NH, USA). Rhodamine 640 (Rh640) was from Exciton (Lockbourne, OH).

5.5.2 Pdot synthesis by manual injection

Manual injection was carried out as described in Section 3.3, excepting that equal volumes of organic precursor and water (5 mL) were used to match the conditions of symmetric flow rates on the syringe pump setup. Precursor concentrations were varied as described in the results and discussion, but a 5:1 mass ratio of the SP and AP was maintained for all experiments.

5.5.3 Flow synthesis of Pdots with syringe pumps

Flow synthesis was performed using two connected programmable Legato 110 Dual Rate System syringe pumps (KD Scientific, Holliston, MA). Precursor solutions containing a semiconducting polymer, amphiphilic polymer, or both were prepared in THF and loaded into a 10 mL glass-walled syringe (Trajan Scientific Americas Inc., Austin, TX, USA) or a 1 mL polypropylene syringe (VWR, Mississauga, ON, CA) at a volume at least 20% greater than the injection volume. Polypropylene syringes used for organic solutions were discarded after a single use. A second identical syringe was loaded with water at a volume at least 20% greater than the injection volume. The syringes were loaded into separate (but digitally connected) syringe pumps and connected to polytetrafluoroethylene (PTFE) tubing of variable internal diameter (1.0 mm for most experiments). The PTFE tubing was connected to the inlets of a mixer (internal diameters ~0.2–1.1 mm) whose outlet was connected to a short piece of PTFE tubing. The tubing was primed by manually flowing solution from both syringes simultaneously until solution emerged from the outlet tubing and this solution was discarded. The pumps were started simultaneously and were programmed to deliver a specified volume (usually 5 or 0.5 mL) at a specified flow rate. Pdot solutions in THF/water were collected in a glass vial and partially dried under rotary evaporation to remove THF and concentrate the solution.

5.5.4 Encapsulation of Rh640 by flow synthesis

Rh640 was dissolved in THF and the desired amount was added to the precursor organic solution containing the SP and AP. Syringe pump flow synthesis was performed as described above. After

solvent removal and concentration, excess dye was removed by washing 500 µL aliquots of dye-loaded Pdots three times with water using a spin filter (MWCO 100 kDa).

5.5.5 Flow synthesis of Pdots with continuous flow pumps

Flow synthesis was performed using two continuous flow pumps (M6 pump heads and M50 pump motors, VICI Valco Canada, Brockville, ON). The hardware was operated using custom software. Inlet PTFE tubing was placed either in the precursor solution or in water and the pumps operated continuously, flowing the solutions through a static mixer of fixed geometry or a dynamic mixer at a programmed flow rate. The outlet solution was collected as fractions (1.0 mL for optimization, 1.1 mL for scale up) by a liquid handler (N9, North Robotics, Victoria, BC, Canada). The first ~1 mL generated was discarded to allow the pumps to reach equilibrium flow conditions.

Chapter 6: Investigation of the energy transfer mechanism between semiconducting Polymer Dots and organic dyes

This chapter is based on a manuscript currently in preparation, co-written by Kelsi Lix and Russ Algar. KL designed and performed all experiments, and analyzed the data with assistance from RA. KL performed the DFT simulations. Saeid Kamal assisted with fluorescence lifetime and transient absorption measurements. Valerie Chiykowski, Yang Cao, and Dan Bizzotto assisted with cyclic voltammetry measurements.

6.1 Introduction

Semiconducting polymer dots (Pdots) are an emerging type of luminescent nanoparticle that are rapidly gaining popularity for applications in bioimaging because of their exceptional brightness, good photostability, and low cytotoxicity [26, 109, 118]. Pdots are conjugated polymer nanoparticles with > 50% mass or volume fractions of semiconducting polymer, a hydrophobic core, and, in some definitions, a size < 30 nm [26]. Examples of applications of Pdots include but are not limited to cellular labelling [24, 59, 212], *in vivo* imaging [124, 139, 186, 213-214], and drug delivery [96, 215]. Other popular luminescent nanoparticle materials, such as semiconductor quantum dots and lanthanide-based upconverting nanoparticles, have been used not only for bioimaging but also for energy transfer (ET)-based bioanalysis [17, 216]. There is similar and growing interest in using Pdots as energy donors; however, compared to materials such as quantum dots, the ET-applications of Pdots are far less numerous and the process much less characterized.

To date, the interest in ET with Pdot materials has been principally motivated by either tuning the emission properties of Pdots or coupling the brightness of Pdots to functional dyes. For tuning emission properties, many types of energy donors and acceptors have been paired with Pdots, including multiple semiconducting polymers within one particle [113, 217], quantum dots [151], silver [218] and gold nanoparticles [69, 219-220], and luminescent lanthanide complexes [33, 71, 83]. Donor and acceptor groups have also been incorporated into the semiconducting polymer backbone [93]. For coupling brightness to functional dyes, Pdots have been paired with analyte-sensitive fluorescent dyes for sensing applications [31, 221-225] and with sensitizers for photodynamic therapy [188, 226-230]. Many dyes are hydrophobic and easily doped into the hydrophobic core of the Pdot during synthesis [63, 68, 108, 231-233]. This approach has the advantage of minimizing the donor-acceptor distance and maximizing ET efficiency. Ionic or dissolved gas analytes are also able to access at least some of the Pdot-hosted dyes to enable chemical sensing. There are comparatively few examples of Pdot-acceptor systems where the acceptor dye is conjugated to the nanoparticle surface [119, 156-157]. This configuration is most relevant for biosensing applications because biorecognition-induced changes in ET are more likely to occur at the nanoparticle surface, particularly for biomacromolecular analytes, such as proteins, enzymes, and nucleic acids, which will not partition into the hydrophobic core of a Pdot.

Although many ET-based applications have been reported for Pdots, detailed photophysical characterizations of the ET process have been comparatively scarce. A typical assumption is that ET occurs through FRET [69, 217-218, 227-228, 231, 234], where studies on semiconducting polymer nanoparticles with blends of semiconducting polymers [113, 159] and doped dyes [76]

support this assumption, albeit that one study has suggested photoinduced electron transfer (PET) concurrent with FRET [119].

Here, we report a systematic study of ET processes for multiple configurations where a Pdot was paired as a donor with an organic dye as an energy acceptor. These configurations are summarized in Figure 6.1 and included partitioning of a hydrophobic dye onto the Pdot core, covalent conjugation of a hydrophilic dye to the Pdot surface, either directly or through biomacromolecules on the Pdot surface. These configurations differ from a previous study by Wu *et al.* [76] in that the dyes are introduced post-synthesis of the Pdots, in the use of hydrophilic dyes and biomacromolecular bridges, in the evaluation of multiple dyes from both the cyanine and rhodamine dye families, and in the scope of characterization methods. ET was evaluated through measurements of fluorescence intensity, fluorescence lifetime, and transient absorption, supported by nanoparticle tracking analysis, electrochemical measurements of HOMO/LUMO levels and density functional theory (DFT) modeling. The cumulative results are discussed in the contexts of the theoretical frameworks for FRET, Dexter ET, and PET, with consideration of Pdot size, polydispersity, and morphology. Although FRET is the most probable dominant mechanism of ET, FRET alone is not sufficient to describe the observed qualitative and quantitative trends in ET efficiency. Dexter ET and PET likely occur concurrently, particularly in systems where an appreciable proportion of the acceptors are in near-proximity to F8BT.

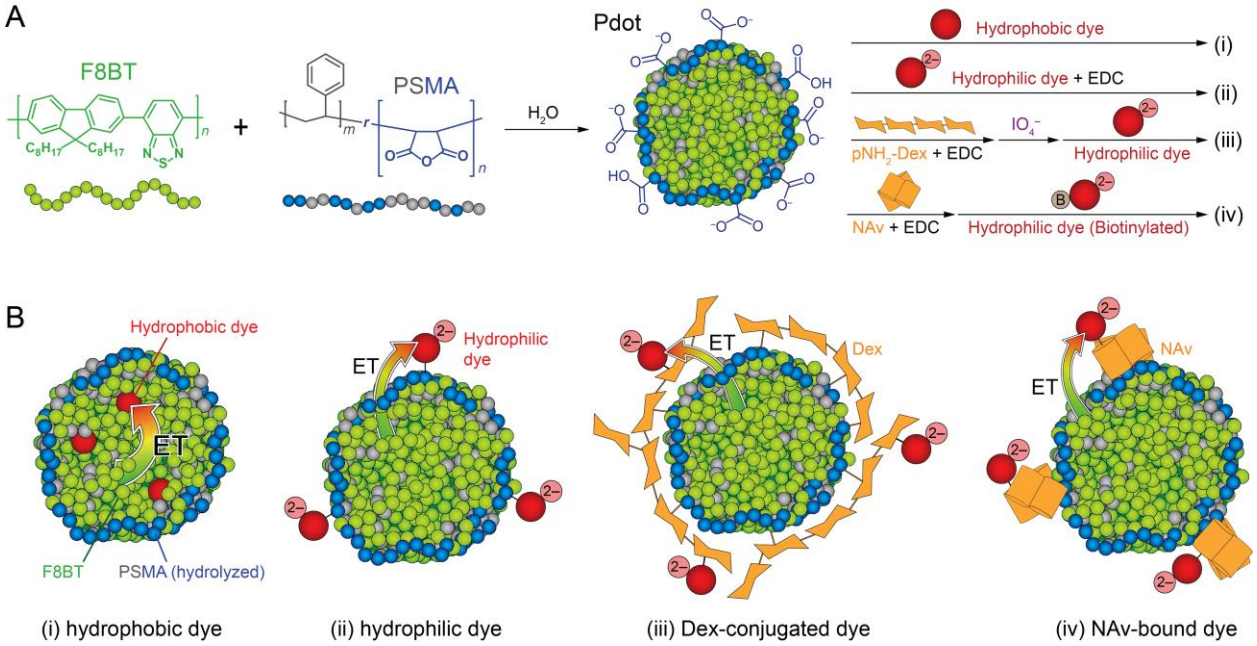

Figure 6.1 ET configurations with Pdots and dyes. **(A)** Nanoprecipitation of F8BT and PSMA to form Pdot donors (with hydrolyzed PSMA) and post-synthetic modifications to introduce dye acceptors: (i) hydrophobic dye via partitioning/adsorption; (ii) hydrophilic dye via carbodiimide (EDC) coupling to the PSMA; (iii) hydrophilic dye via hydrazone conjugation to a partially oxidized dextran (Dex) coating on the Pdot; and (iv) biotinylated hydrophilic dye via binding to NeutrAvidin (NAv) that is conjugated to the PSMA via EDC. **(B)** Cartoon representations (not to scale) of the ET configurations (i)-(iv). For clarity, the carboxyl(ate) groups have been omitted in panel B and only three dyes and three dextran or NAv molecules are shown.

6.2 Results

6.2.1 Pdot synthesis and characterization

Pdots were synthesized with F8BT as the semiconducting polymer and PSMA as the amphiphilic copolymer. The PSMA is a random copolymer of styrene and maleic anhydride monomers, the latter of which hydrolyze in water to carboxyl(ate) groups. F8BT is the source of fluorescence in Pdots and has broad emission with a peak at ~540 nm. Selected optical properties of F8BT/PSMA Pdots, the nominal acceptor dyes, and their pairing are listed in Table 6.1.

Table 6.1. Selected optical properties of F8BT/PSMA Pdots and organic dye acceptors.

	$\Phi_{measured}$[a]	ε (10^3 M^{-1} cm^{-1})[b]	λ abs. (nm)[c]	λ em. (nm)[d]	J_{FRET} (10^{-10} cm^6 mol^{-1})[e]	R_0 (nm)[f]	J_{Dexter} (10^{-4} cm)[g]
Pdot	0.35 ± 0.24 [i]	2 200 000	464	542	--	--	--
Cy5	0.20 ± 0.03	250	646	662	9.0	4.6	1.3
sCy5	0.29 ± 0.03	271	646	662	6.9	5.4	1.2
Cy5.5	0.31 ± 0.03	209	684	710	4.3	4.2	0.68
sCy5.5	0.19 ± 0.03	195	675	694	3.9	5.0	0.78
Cy7	0.22 ± 0.03	199	750	773	2.4	3.9	0.33
sCy7	0.08 ± 0.01	240	750	773	2.2	4.8	0.29
Rh590	1.00 ± 0.05	115	528	556	2.5	4.6	1.6
Rh610	0.94 ± 0.05	106	554	578	3.9	4.9	2.6
Rh640	1.01 ± 0.05	95	576	598	4.8	4.0	2.6

[a] Quantum yield. Values were determined in water (Pdot, sCyX) or dichloromethane (CyX, RhX). [b] Molar extinction coefficient. Pdot value determined via UV-Vis and NTA concentration measurements. Values for dyes were provided by the manufacturer for species in water (CyX and sCyX) or EtOH (Rh590), or taken from ref. [235] for dyes in EtOH (Rh610 and Rh640). [c] Spectral position of the absorbance maximum. [d] Spectral position of the fluorescence emission maximum. [e] Value of the FRET spectral overlap integral. [f] Calculated Förster distance, using the Φ value for the Pdot batch used for the ET titration and assuming an orientation factor of $\kappa^2 = 0.476$ and a refractive index of 1.75 (F8BT) for CyX and RhX or assuming an orientation factor of $\kappa^2 = 2/3$ and a refractive index of 1.4 (buffer) for sCyX. *Vide infra* for the rationale for using these values. [g] Value of the Dexter spectral overlap integral. [i] Standard deviation across five batches of Pdots.

Representative TEM images of a batch of Pdots are shown in Figure 6.2A. The Pdots were approximately spherical in shape with an average (dehydrated) diameter of 36 ± 14 nm. NTA measurements indicated average hydrodynamic diameters of 55 ± 35 nm (mode 33 nm; scattering) and 46 ± 33 nm (mode 25 nm; fluorescence), respectively, and DLS measurements indicated average hydrodynamic diameters of 23 ± 11 (mode 16 nm; number-weighted) and 77 ± 38 nm (mode 53 nm; intensity-weighted). Size histograms for all three methods are shown in Figure 6.2B. Fluorescence-tracking NTA was expected to give somewhat smaller average diameters than

scattering-tracking because of the exclusion of contributions from any non-fluorescent particulate impurities. The intensity-weighted DLS diameter was expected to be larger because of the greater sensitivity of this method to larger particles. NTA sizing data for all batches of Pdots used in this study can be found in Table C.1 and Table C.2 (Appendix C). Excluding one outlier batch, the average Pdot diameter across our experiments was 59 ± 7 nm (mode 38 ± 5 nm). We refer to these nanoparticles as Pdots because of the large mass fraction of semiconducting polymer, even though the average diameters are greater than the 30 nm threshold that has been suggested in some definitions [26].

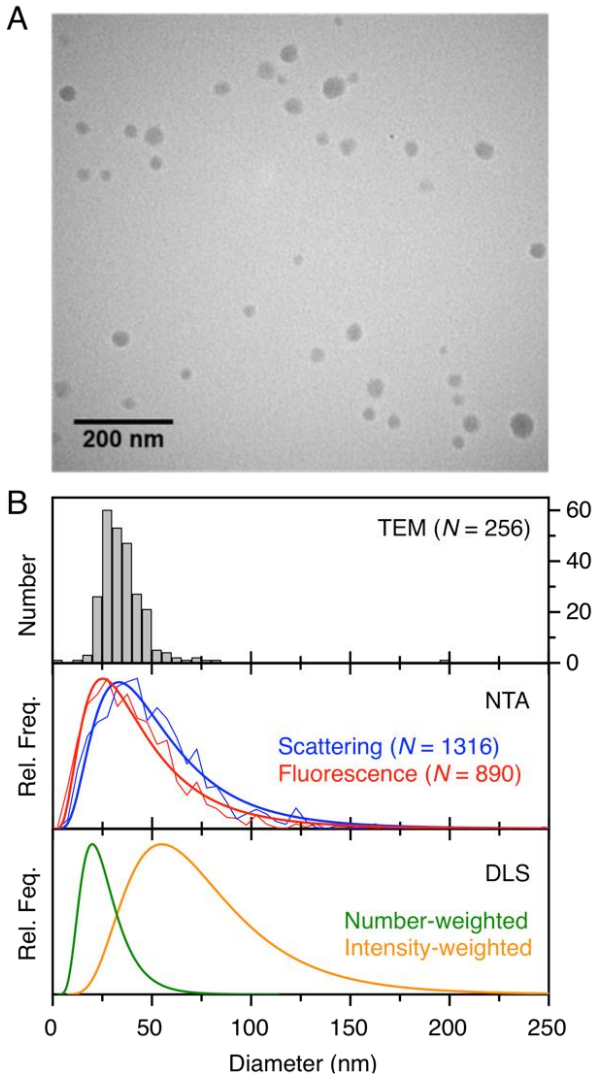

Figure 6.2 Representative physical characterization of F8BT Pdots: **(A)** representative TEM image; **(B)** Pdot size distributions from (top) TEM analysis (*N* = 256), (middle) NTA analysis (raw data and lognormal fit curves, *N* = 1316 ± 160 for scattering and *N* = 890 ± 40 for fluorescence), and (bottom) DLS analysis (lognormal data).

6.2.2 Donor-acceptor pairs and conjugates

F8BT Pdots were selected as donors because of their prior use and characterization for bioimaging [24, 236-238], their prior use in a previous ET study [76], and because their green-yellow fluorescence emission is suitable for pairing with many acceptor dye candidates. The number of

acceptor dye candidates and the ability to resolve ET-sensitized acceptor emission would be less with a Pdot material that had longer-wavelength fluorescence. Selected acceptor dyes were from the cyanine dye family (Cy5, Cy.5.5, and Cy7) and from the rhodamine dye family (Rh590, Rh610, Rh640) with the idea that a series of dyes would be useful for evaluating the trend in ET efficiency as a function of the spectral overlap integrals (relevant to FRET and Dexter ET) and the alignment of the highest occupied (HOMO) and lowest unoccupied (LUMO) molecular orbitals (relevant to PET).

Figure 6.3A shows that the absorbance spectra of all the CyX dyes had significant spectral overlap with the emission spectrum of the F8BT Pdots, and that the CyX dye emission peaks were resolved from the emission of the Pdots. These dyes also had large molar absorption coefficients (Table 6.1) and were minimally excited at the optimum Pdot excitation band (*ca.* 450–475 nm). Both non-sulfonated and sulfonated cyanine dyes were used for experiments. The non-sulfonated CyX dyes had octanol-water partition coefficients of $K_{ow} \geq 50$ (significant hydrophobicity) and spontaneously and rapidly associated with the Pdot. In contrast, the sulfonated sCyX dyes had $K_{ow} \leq 0.01$ (significant hydrophilicity) and minimal non-specific interactions with Pdots, as determined from the absence of ET-sensitized dye emission after separation of Pdots from unbound dye (data not shown). Measured K_{ow} values are given in Table 6.2. To obtain ET-sensitized dye emission, it was necessary to covalently conjugate sCyX to the Pdot surface using carbodiimide chemistry.

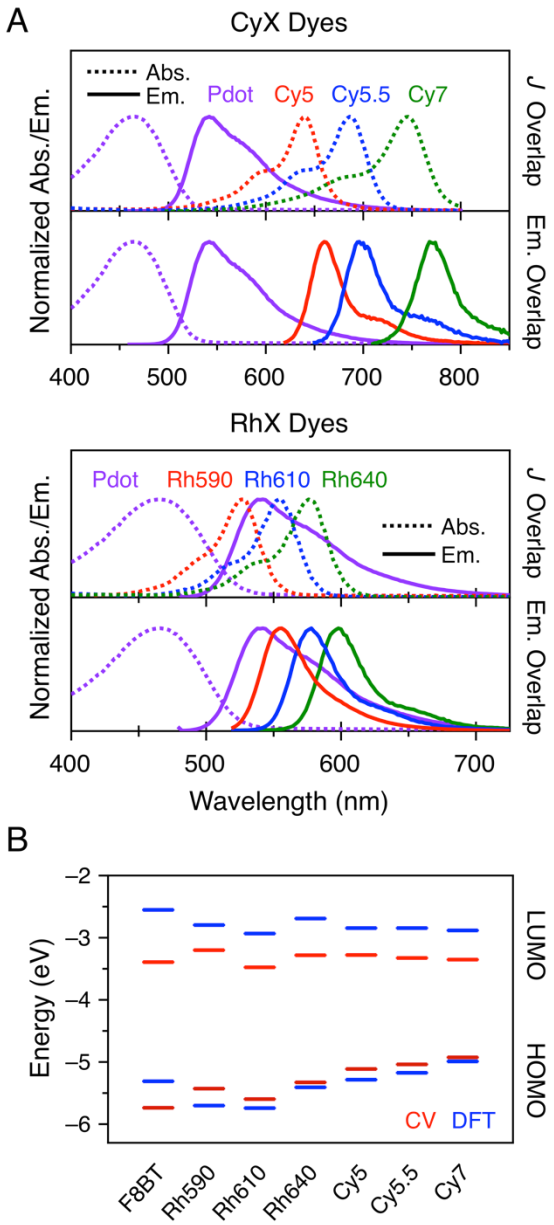

Figure 6.3 (A) Absorption (Abs.) and fluorescence emission (Em.) spectra for the F8BT Pdots and CyX and RhX dyes, grouped to qualitatively illustrate the spectral overlap (*J*) relevant to ET (top) and the overlap of the different emission signals (bottom). The spectra for the sCyX dyes were not significantly different than the spectra for the CyX dyes. **(B)** HOMO and LUMO levels of F8BT polymer, RhX, and CyX estimated by CV (red) and DFT calculations (blue). CV measurements were performed in DCM (F8BT), MeCN (RhX), and EtOH/MeCN (CyX).

Table 6.2. K_{ow} values for cyanine and rhodamine dyes.

Dye	K_{ow}
Cy5	120
Cy5.5	50
Cy7	77
sCy5	~0
sCy5.5	0.0010
sCy7	0.0033
Rh590	15
Rh610	34
Rh640	290

The RhX dyes were hydrophobic with $K_{ow} \geq 15$. The Rh590 and Rh640 associated with the Pdots spontaneously, but Rh610 but did not, as reported elsewhere [31]. Figure 6.3A shows the trend in the absorbance/emission spectral overlap between the RhX dyes and Pdots, and shows that the emission of the rhodamine dyes was much more difficult to resolve from the emission of the F8BT Pdots than the CyX dyes. Formal linear decomposition (*cf.* a simple crosstalk correction) of the spectra was required (Figure 6.4). Hydrophilic derivatives of the selected rhodamine dyes were not commercially available and therefore not tested.

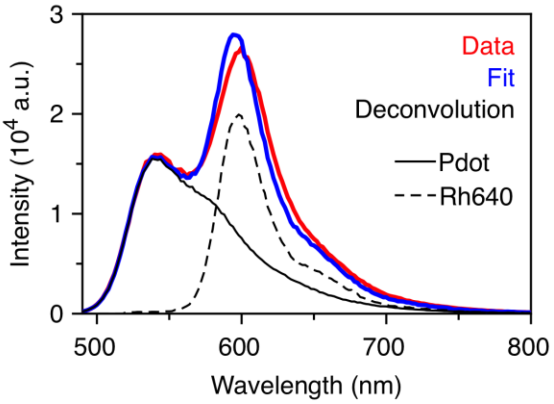

Figure 6.4 Example of unmixing of an emission spectrum from a sample with a Rh640 added to F8BT Pdots. This sample had ~93 dyes per Pdot.

Figure 6.3B plots the HOMO and LUMO energies estimated by cyclic voltammetry (CV) and calculated by density functional theory (DFT). Corresponding CV data are shown in Figure 6.5 and the HOMO and LUMO energies determined by DFT using various solvents are shown in Table 6.3. Although the DFT results were offset from the CV results, the trends are largely the same between the dyes. The primary qualitative discrepancy between the DFT and CV data were the alignments (higher or lower) of the F8BT energy levels relative to the dyes. The DFT results suggested that the dye LUMO levels were lower in energy than the F8BT LUMO, and that the relative alignment of the HOMO levels was dye-dependent. The CV data suggested that the dye LUMO levels are similar to that of the F8BT, and that the dye HOMO levels were higher in energy than the F8BT HOMO level.

Table 6.3. HOMO/LUMO energies from DFT calculations in different solvents.

Solvent	ε[a]	Orbital	Orbital Energy (eV)						
			F8BT	Cy5	Cy5.5	Cy7	Rh590	Rh610	Rh640
H_2O	78.3553	HOMO	-5.3	-5.2	-5.1	-5.0	-5.7	-5.7	-5.4
		LUMO	-2.6	-2.8	-2.8	-2.8	-2.8	-2.9	-2.7
MeCN	35.688	HOMO	-	-5.3	-5.2	-5.0	-5.7	-5.7	-5.4
		LUMO	-	-2.8	-2.8	-2.9	-2.8	-2.9	-2.7
DCM	8.93	HOMO	-5.3	-	-	-	-	-	-
		LUMO	-2.6	-	-	-	-	-	-
Ben	2.2706	HOMO	-5.2	-6.2	-6.0	-5.9	-6.7	-6.7	-6.3
		LUMO	-2.5	-3.8	-3.8	-3.8	-3.7	-3.9	-3.6

[a] Dielectric constant used in Gaussian calculations

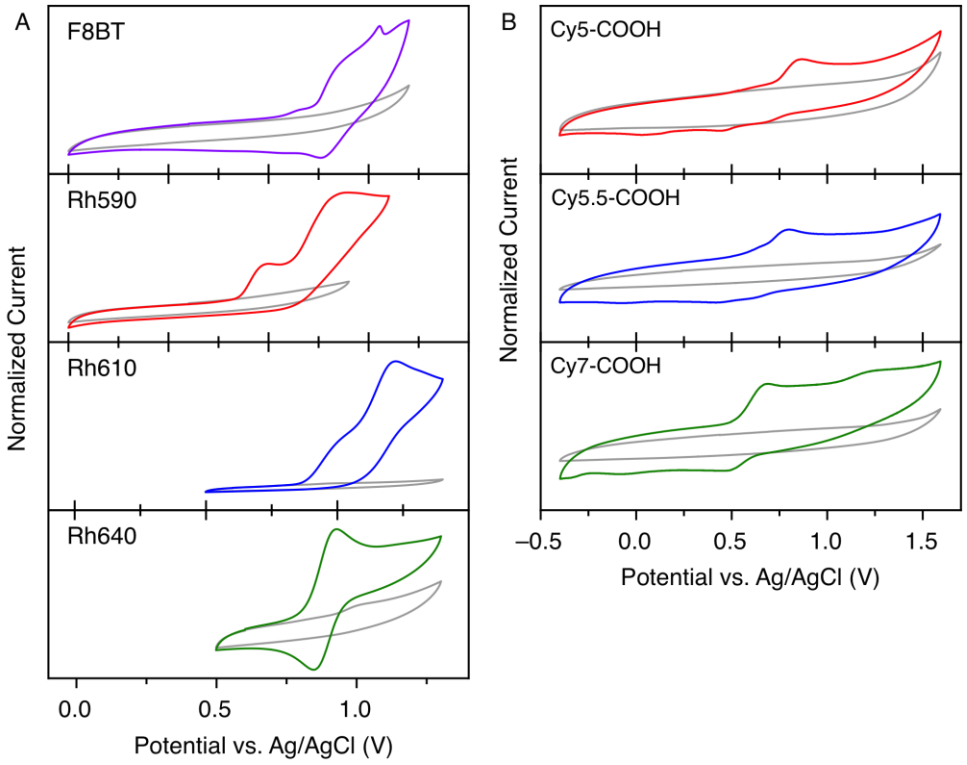

Figure 6.5 (A) Cyclic voltammograms of unaggregated F8BT polymer (solution phase, scan rate = 0.15 V/s) in DCM, and Rh590 (scan rate = 0.1 V/s), Rh610 (scan rate = 0.1 V/s) and R640 (in MeCN, scan rate = 0.05 V/s). **(B)** Cyclic voltammograms of CyX-COOH in EtOH/MeCN (scan rate = 0.1 V/S). The background scans are shown in grey. The position of the oxidative and reductive peaks shifted by ~0.1 V when the scan rates were varied from 0.05 V/s to 1 V/s.

6.2.3 Spectrofluorimetric measurements

ET in the various Pdot-dye configurations (see Figure 6.1B) was first measured spectrofluorimetrically with an increasing number of dye molecules per Pdot. For analysis, we accounted for variations in quantum yield and particle diameter by plotting the apparent ET efficiency (measured via quenching of the Pdot emission) versus the term $N\Phi_D r_{avg}^{-6}$, where N is the estimated average number of dyes per Pdot, Φ_D is the quantum yield of the specific batch of Pdot donor, and r_{avg} is the average particle radius for the specific batch of Pdots, which is proportional to the average donor-acceptor distance. This strategy normalizes for the effects of batch-to-batch variation in these parameters as per Eqn. 6.1, where r is the average donor-acceptor separation, R_0 is the Förster distance, $L = Cn^{-4}\kappa^2 J_{\mathrm{FRET}}$, C is a constant, n is the refractive index of the medium, and κ is the orientation factor. The average donor-acceptor separation, r, is assumed to be equal to θr_{avg}^{-6}, where θ is a proportionality constant equal to ¾ for a perfectly spherical particle [239]. Note that Eqn. 6.1 treats the Pdot as a single emitter, which is an assumption that is discussed later.

$$E = \frac{NR_0^6}{r^6 + NR_0^6} = \frac{L\theta^{-6}N\Phi_D r_{avg}^{-6}}{1 + L\theta^{-6}N\Phi_D r_{avg}^{-6}} \tag{6.1}$$

Figure 6.6A and C show representative emission data, and the corresponding absorbance and excitation data for panel A are shown in Figure 6.7 and Figure 6.8. Figure 6.6B and D plot the ET efficiency, measured via quenching of the Pdot emission intensity, as a function of the ensemble average number of dyes per Pdot, the donor quantum yield, and the average particle radius to normalize for differences in those parameters between batches of Pdots. The ensemble ET

efficiency generally increased as the number of acceptor dyes per Pdot increased, regardless of whether the dye was CyX, sCyX, Rh590, or Rh640. In each case, ET was indicated by both quenching of the Pdot and observation of ET-sensitized dye emission. Emission intensity from direct excitation of the acceptor dyes was negligible. The Pdot-Rh610 combination showed minimal quenching of the Pdot and minimal ET-sensitized dye emission, presumably as a consequence of the low number of dyes per Pdot. Upon inspection, the trends in the ET efficiencies between the CyX and sCyX dyes did not match expectations based on the spectral overlap integrals and Förster distances in Table 6.1. The ET rates per acceptor, treating the Pdot as a single emitter, are shown in Table 6.4.

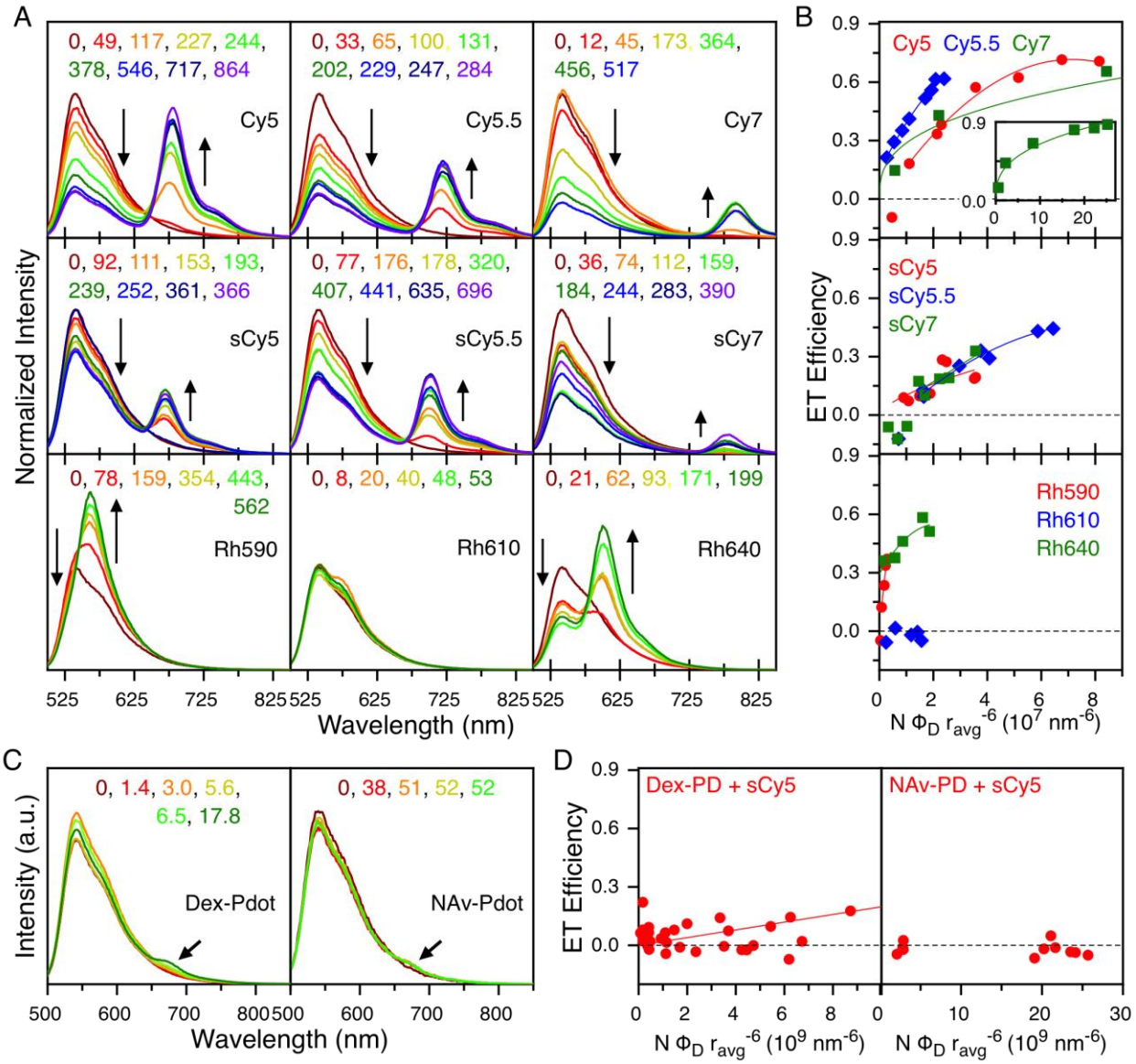

Figure 6.6 (A) Representative emission spectra for titrations of Pdots with CyX (top row), sCyX (middle row), and RhX (bottom row). The colors indicate the average number of dye molecules per Pdot (*N*). **(B)** Plots of ET efficiency versus $N\Phi_D r_{avg}^{-6}$ for the configurations in panel A. **(C)** Representative emission spectra for titrations of dextran (Dex)-Pdots and NeutrAvidin (NAv)-Pdots with sCy5. The arrows point to small shoulders from ET-sensitized sCy5 emission. **(D)** Plots of ET efficiency versus $N\Phi_D r_{avg}^{-6}$ for the configurations in panel C.

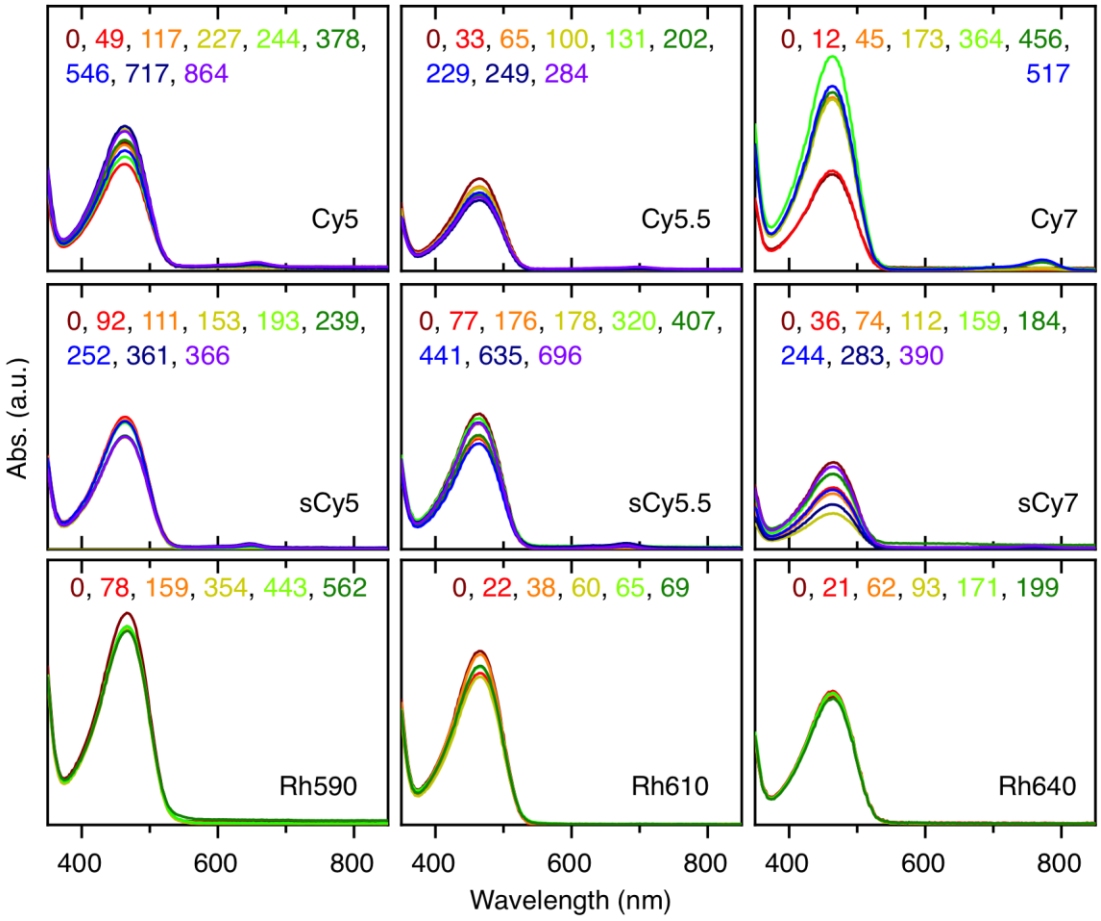

Figure 6.7 Raw absorption spectra for the FRET titrations in Figure 6.6A, Figure 6.9A and Figure 6.10A. The colors indicate the average number of dye molecules per Pdot (*N*).

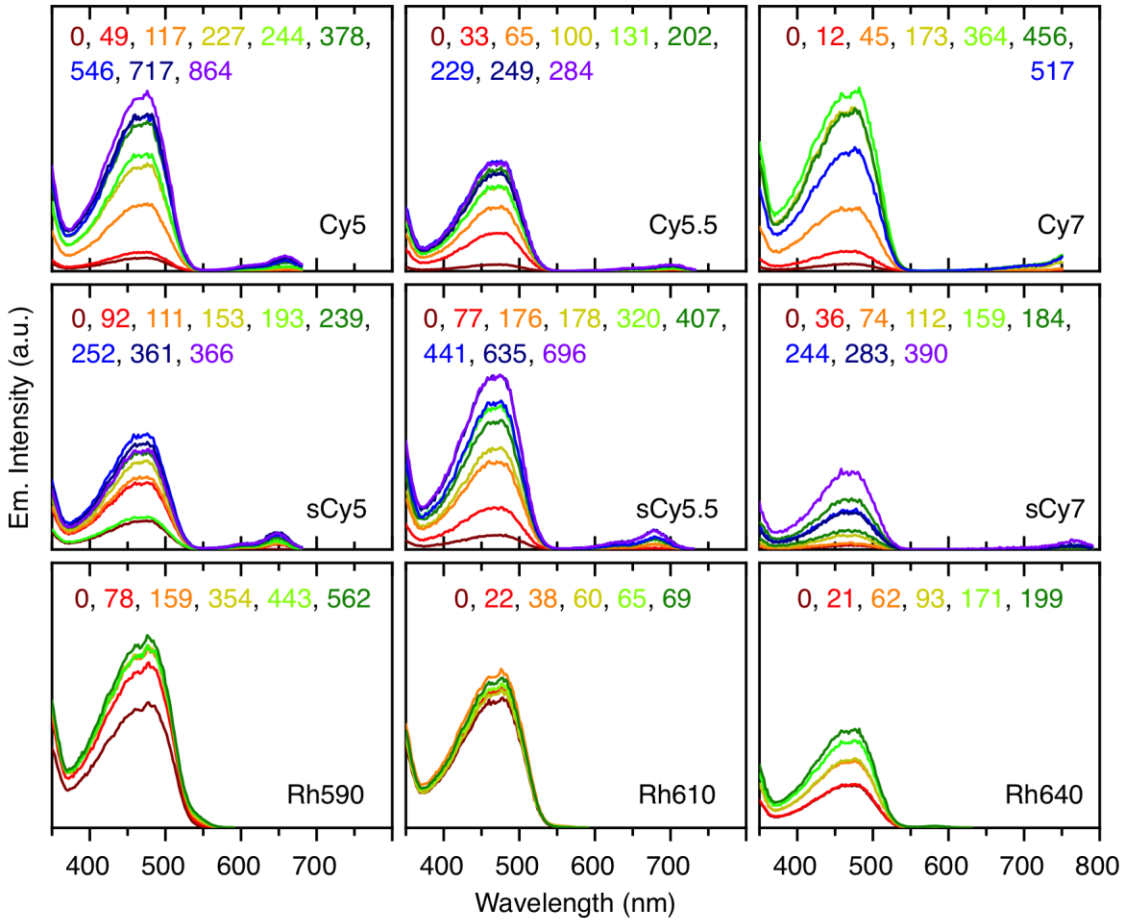

Figure 6.8 Raw excitation spectra for ET titration samples in Figure 6.6A, Figure 6.9A and Figure 6.10A. The colors indicate the average number of dye molecules per Pdot (*N*).

Table 6.4. Energy transfer rates (k_{ET}) for Pdot-dye pairs determined by steady state intensity measurements and fluorescence lifetime measurements.

Dye	k_{ET} (steady state emission, 10^5 s^{-1})	k_{ET} (fluorescence lifetime, 10^5 s^{-1})
Cy5	35.2	17.8
Cy5.5	96.2	40.7
Cy7	171.0	12.3
sCy5	12.2	3.5
sCy5.5	15.0	3.1
sCy7	14.7	6.4
Rh640	185.7	37.9

If the Pdot is assumed to represent a single emitter, then the ET rates per acceptor dye (determined from intensity-derived efficiencies) were $3.5 \times 10^6\ s^{-1}$, $9.6 \times 10^6\ s^{-1}$ and $17 \times 10^6\ s^{-1}$ for hydrophobic Cy5, Cy5.5, and Cy7, respectively. Note that these values do not account for batch-to-batch variations in particle size or quantum yield. This trend was opposite that expected based on the estimated spectral overlap integrals and Förster distances in Table 6.1. The ET rate per acceptor dye for Rh640 was $19 \times 10^6\ s^{-1}$. The ET rates for Rh590 and Rh610 could not be determined because of the extensive overlap of their emission spectra with the F8BT emission spectrum precluding useful lifetime measurements. For the three sCyX dyes, the ET rates per acceptor did not significantly differ between dyes and were $1.2 \times 10^6\ s^{-1}$, $1.5 \times 10^6\ s^{-1}$ and $1.5 \times 10^6\ s^{-1}$ for sCy5, sCy5.5 and sCy7 respectively. The higher rate of ET with CyX versus sCyX was assumed to be from closer proximity between F8BT and dye for the former (partitioned into or adsorbed onto the Pdot) versus the latter (conjugated to the Pdot surface via the amphiphilic polymer).

The effect of proximity was further studied by coating the Pdot surface with dextran (Dex) or NeutrAvidin (NAv). Conjugation of a hydrophilic dye to these materials was expected to increase the average distance between the Pdot and dye and minimize (if not prevent) direct contact between the F8BT and dye. The dextran was selectively conjugated with dye through oxidation with periodate and reaction with sCy5-hydrazide; the NeutrAvidin was selectively conjugated with sCy5-biotin. Figure 6.6D shows that a relatively low average number of sCy5 per Pdot were conjugated over multiple titrations, resulting in low ET efficiencies. Consistent with qualitative expectations, conjugation of dye to dextran resulted in higher ET efficiencies than conjugation to

NeutrAvidin, where the ET efficiency with dextran was, on average, similar to that measured for an equal number of directly conjugated sCy5.

6.2.4 Fluorescence lifetime measurements

To complement the spectrofluorimetric measurements, fluorescence lifetime measurements were also made with the CyX, sCyX, and Rh640 paired with the Pdots. Note that the samples measured were the same ones used for spectrofluorimetric measurements (Figure 6.6A). Figure 6.9A shows representative decay curves for Pdots paired with CyX and sCyX acceptors, and Figure 6.10 shows analogous data for Rh640. (The emission overlap between the F8BT Pdot and Rh590 and Rh610 precluded useful lifetime measurements.) The derived amplitude-weighted lifetimes for all samples are given in Table B.1–Table B.3 (see Appendix B). Overall, the average Pdot fluorescence lifetime decreased with an increasing number of acceptor dyes per Pdot, and apparent ET efficiencies were calculated from the decrease in the amplitude-weighted average lifetime. (Alternate approaches to fitting of the lifetime data are discussed in Appendix B.3.) Analogous to the spectrofluorimetric data, ET was more efficient with the CyX dyes than the sCyX dyes; however, there was poor correspondence between the ET efficiencies measured from intensity data and lifetime data, with the lifetime-derived efficiencies consistently lower than the intensity-derived values. The lifetime-derived trends in relative ET efficiency across the CyX and sCyX dyes were also somewhat inconsistent with the corresponding intensity-derived trends, and with expectations based on spectral overlap integrals and Förster distances.

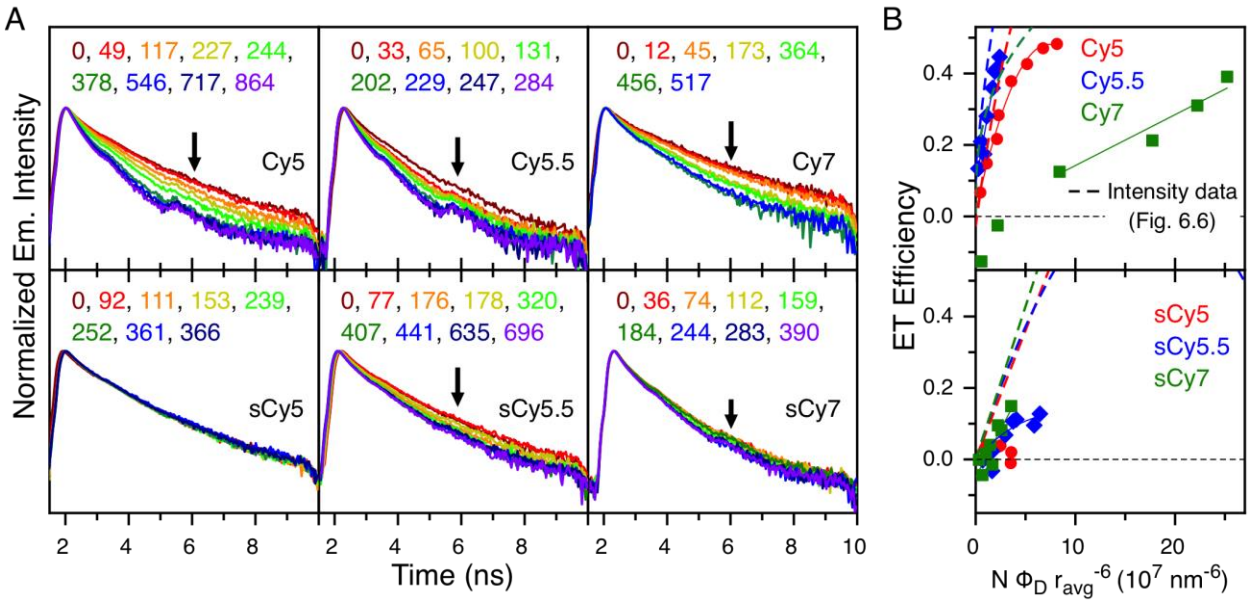

Figure 6.9 (A) Representative fluorescence decay curves and ET efficiencies for titrations of Pdots with CyX (top) and sCyX (bottom). The colors indicate the average number of dye molecules per Pdot (*N*). **(B)** Plots of ET efficiency versus the number of dyes per Pdot for the systems in panel A**.**

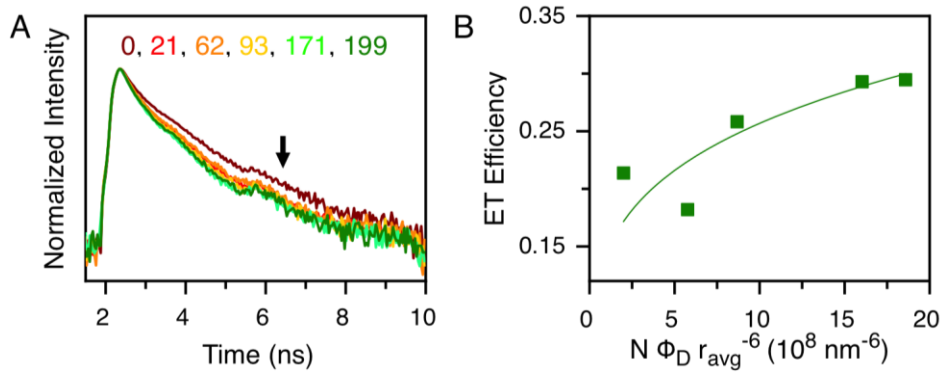

Figure 6.10 (A) Lifetime decay curves and **(B)** ET efficiencies measured for Rh640 mixed with F8BT Pdots. The colors indicate the average number of dye molecules per Pdot (*N*).

6.2.5 Nanoparticle tracking analysis measurements

ET in the Pdot-Cy5 configuration was also investigated using NTA with the sequential use of two different emission filters to measure Pdot and Cy5 emission (approximately) separately. This approach was quasi-single-particle characterization because the individual particles measured were different between the two filter channels, such that information was still only inferred about the ensemble. NTA data and corresponding emission spectra are shown in Figure 6.11. Detailed results are summarized in Table 6.5; however, the main results were that the particles had approximately the same size in both channels, and that the concentration of particles measured in the Cy5 filter channel were approximately one third the concentration measured in the Pdot filter channel. The latter was similar to the discrepancies between Pdot-only concentrations derived from scatter-mode and fluorescence-mode NTA. Note that it was challenging to optimize this experiment to achieve negligible signal for Pdot-only samples and adequate signal for Pdot-Cy5 samples in the nominal Cy5 channel. As discussed later, this challenge impacted our interpretation of the data.

Table 6.5. ET efficiencies and particle counts for NTA measurements

No. Dyes/Pdot	ET Efficiency	Particle Counts		Mean (Mode) Diameter (nm)	
		Pdot Channel (500 nm filter)	Cy5 Channel (650 nm filter)	Pdot Channel	Cy5 Channel
0	--	3064 ± 132	6 ± 4	37 (32) ± 11	42 (43) ± 7
306	0.28	3579 ± 55	1112 ± 50	34 (30) ± 11	37 (29) ± 15
831	0.42	3202 ± 168	1233 ± 100	37 (32) ± 11	42 (31) ± 19

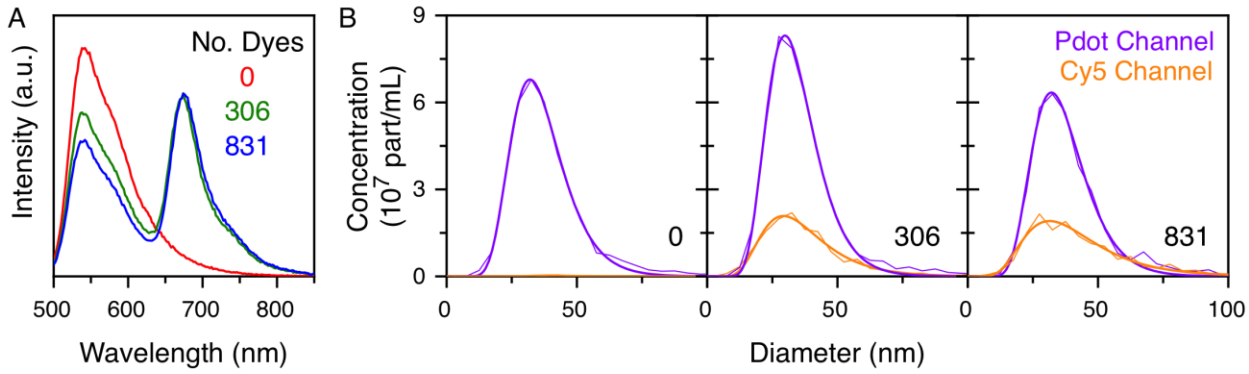

Figure 6.11 (A) Emission spectra and **(B)** NTA size distributions for measurement of FRET by NTA. The number of dyes per Pdot (*N*) is indicated in each panel.

6.2.6 Transient absorption measurements

The Pdot-Cy5 configuration was also studied by ultrafast transient absorption spectroscopy. Figure 6.12A shows that a sample of only Pdots (no Cy5 acceptor) exhibited the expected bleach and recovery of the ground state population at ~470 nm. The bleach peak gradually red shifted over delay times up to 100 ps (Figure 6.12C). The positive features above 500 nm likely arose from a combination of stimulated emission and excited state absorption. At short delay times (< 100 ps), a trough appeared between 525–650 nm, which corresponded to the wavelength range of the emission spectrum of F8BT Pdots and was therefore likely from stimulated emission. However, this process was in competition with excited state absorption at 550 nm (*e.g.*, polaron absorption), resulting in an overall feature that was positive and decayed towards zero at long delay times. Analogous measurements on a sample with Cy5 partitioned into the Pdot (14 dyes per Pdot corresponding to an ET efficiency of 0.30) yielded nearly indistinguishable results. Figure 6.12B shows that the ground state bleach feature (~470 nm) for the Pdot alone had an amplitude-weighted average lifetime of ~800 ps, which decreased to ~740 ps with the Cy5 present. Likewise, the

positive feature at ~525 nm decayed back to baseline with an average lifetime of 490 ps for the Pdot alone and ~320 ps with the Cy5 present. The off-peak wavelength 475 nm was used for kinetic analysis to avoid interference from the Raman peak of water at ~460 nm at short delay times.

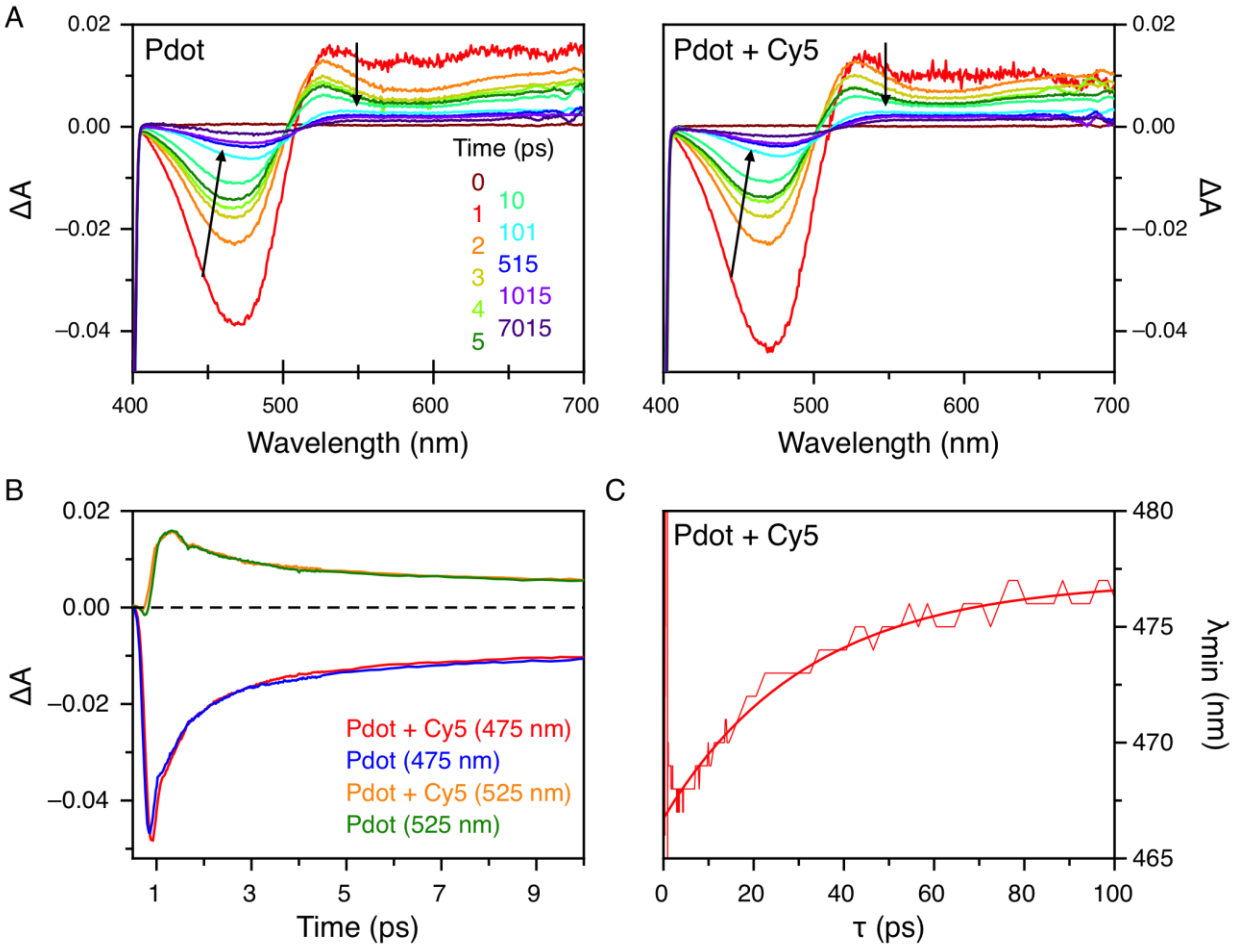

Figure 6.12 (A) Transient absorption spectra of Pdots (left) and Pdots with partitioned Cy5 dye (right). **(B)** Kinetic traces over the first 10 ps for the spectral features at 475 nm and 525 nm. **(C)** Wavelength of minimum ΔA for the ground state bleach peak (~470 nm) in panel A as a function of delay time (τ) indicating the red shift of the peak over time.

6.3 Discussion

6.3.1 Number of dyes per Pdot

A challenge in this study was the much larger extinction coefficient of the Pdot (~10^9 M^{-1} cm^{-1}) versus the dyes (~10^5 M^{-1} cm^{-1}). Even with an estimated hundreds of dyes per Pdot, the contribution of the Pdot to overall extinction spectrum was two orders of magnitude larger than the contribution from an acceptor dye. Thus, for picomolar sample concentrations of Pdots, the absorbance from the dyes was less than 0.01 and therefore not reliable for quantitation. Instead, we estimated the number dyes per Pdot using a fluorescence-based method (see Section 6.5.10), which is less ideal than an absorbance-based method. Nevertheless, repeated measurements of the same sample using this method suggested a precision better than 10%. Systematic control over the number of dyes per Pdot was also difficult to exercise because neither the partitioning of the hydrophobic dyes nor carbodiimide coupling of the hydrophilic dyes was 100% efficient.

Another source of uncertainty was the molar absorption coefficient of the Pdots. These values are not widely reported in the literature, and our determination relied on accurate measurements of particle concentrations via NTA. On average, the concentration of Pdots measured in fluorescence mode was about half the concentration measured in scattering mode, but was frequently as low as one third and sometimes equal (within ~10%). Scattering mode has a higher detection efficiency for the Pdots than fluorescence mode because smaller Pdots are less bright and track less reliably; however, fluorescence mode is more specific to Pdots. From these results, we estimate that the average concentration from the two NTA measurement modes is within ± 30–50% of the real concentration. Accordingly, the uncertainty in the number of dyes per Pdot was also ± 30–50%. Regardless of this uncertainty, the Pdots had, in principle, sufficient surface area to accommodate

between 1000–3000 dyes per particle (assuming a 4 nm^2 footprint for the dyes). By volume, the Pdots would, in principle, accommodate an even larger number of dyes per particle.

6.3.2 Particle size and polydispersity

In the absence of efficient energy migration within the Pdot (*vide infra*), the observed ensemble efficiency of ET as a function of the average number of dyes per Pdot will depend not only on the donor-acceptor distance, spectral overlap integrals (for FRET and Dexter ET), and frontier orbital alignment (for PET) but also on the size of the Pdots. Larger and more polydisperse Pdots should yield lower ensemble ET efficiencies due to the increased average donor-acceptor distance. Qualitatively, this consideration can account for the data where Cy7 quenched its Pdot by roughly the same extent as Cy5 despite its smaller spectral overlap integral, owing to the smaller average diameter of the Pdot batch used for that ET titration (41 nm for Cy7 *vs.* 51 nm for Cy5). Likewise, the low efficiencies for Rh590 compared to Rh640 can be rationalized versus the abnormally large batch of Pdots used with these materials (average Pdot diameter ~100 nm versus 40–60 nm when paired with other dyes). This interpretation assumes that the exciton is confined to its initial position within the Pdot, and neglects the possibility of energy migration between the numerous distinct chromophores within the Pdot core. In reality, exciton migration occurs with a finite efficiency and may decrease the magnitude to which Pdot size determines ET efficiency. However, a decrease of ET efficiency with increasing Pdot size is still expected in the presence of energy migration, even if the magnitude of change is decreased.

6.3.3 Pdot structure and location of acceptors

Figure 6.13 shows a highly idealized cross-sectional model for the Pdot-Cy5 ET systems examined in this study. For simplicity, a well-defined spherical core/shell structure is assumed. The core of a Pdot is an aggregate of multiple semiconducting polymer chains. We estimate between 1200–3500 F8BT chains for Pdots with diameters between 50–70 nm, based on the NTA Pdot concentrations, molecular weight of F8BT and assuming all polymer chains are incorporated into Pdots during synthesis. The hydrolyzed-PSMA amphiphilic polymer molecules are nominally a shell around a core of F8BT semiconducting polymer. We estimate a 1–2 nm thickness for such a shell by assuming that the volume fraction of each polymer in the Pdot was directly proportional to the mass fraction during synthesis, and by assuming a clean separation between semiconducting polymer and amphiphilic polymer in a spherical morphology. This value is consistent with the widthwise dimension of the polymer chain. For the real Pdots, the degree to which the F8BT and PSMA intermixed, and the uniformity of the putative PSMA coating around the F8BT, were both unknown and likely not as well-defined as the model in Figure 6.13. Some studies suggest that the semiconducting polymer chains within a Pdot exist primarily in a disordered glassy phase [110]. In this case, partitioned hydrophobic dyes may be better described as adsorbed onto the surface of semiconducting polymer core rather than embedded within it, as the dyes may not be able to partition significantly into the glassy core structure.

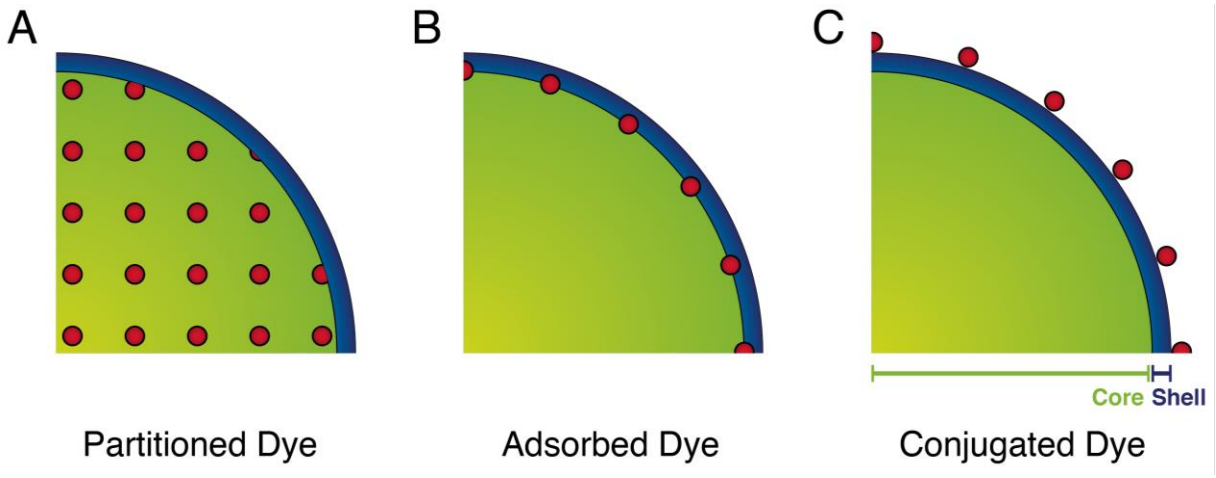

Figure 6.13 Idealized model of Pdot structure. The core (green) is composed of hydrophobic F8BT chains and the shell (blue) is composed of hydrolyzed PSMA. Dye molecules are shown as red circles. Model for Pdots with **(A)** non-specifically partitioned hydrophobic dye, **(B)** non-specifically adsorbed hydrophobic dye and **(C)** specifically conjugated hydrophilic dye.

6.3.4 Energy Migration

Energy migration is known to occur within SPs by exciton migration. Exciton diffusion has the potential to funnel energy from the center of the semiconducting polymer core of a Pdot out to dyes near its periphery, such as in the case of adsorbed hydrophobic dye or conjugated hydrophilic dye. The progressive red shift in the F8BT bleach peak in the TA data (Figure 6.12C) suggests that some energy migration occurs within the Pdots. Assuming the measured absorbance spectrum corresponds to the superposition of contributions from chromophores of varying effective conjugation lengths, rapid exciton migration to lower energy states (*i.e.*, those with red-shifted absorption) populates their excited states and prevents them from absorbing the probe pulse, resulting in a red shift of the bleach peak. Inter-chain ET via FRET dominates in disordered systems such as nanoparticles, and is inclusive of ET from one chromophore to a distant (*i.e.*, non-adjacent) chromophore in the same chain, such as when a chain folds back on itself. This energy migration first occurs downhill from shorter conjugated polymer segments to longer ones, then

subsequently via thermally activated hopping between segments of similar conjugation length [64]. Energy transfer to an exogenous acceptor would then occur from one of these lower energy states.

The exciton diffusion length for F8BT has been reported to be 8–12 nm in thin films [240-241] and 12 nm in nanoparticles [242]. An average radius for all the Pdots used in this study is *ca.* 30 nm (± 15 nm average standard deviation for each batch size distribution). The Förster distances in Table 6.1 are *ca.* 4–6 nm, such that 3 nm is a reasonable estimate of a general $0.5R_0$ distance. An excitation near the centre of a Pdot would therefore need to migrate approximately 5 diffusion lengths to reach an F8BT chromophore that had near-unity probability of transferring to an acceptor at the surface of the Pdot, assuming exciton migration follows a random walk. Given that exciton diffusion length is a function of the exciton lifetime, the probability of diffusing this distance is approximately 2% (versus 37% for one diffusion length). Consequently, energy migration from the centre of the Pdot core to adsorbed or conjugated dye is expected to be relatively infrequent. Thusly, for the subsequent analyses, Pdots are treated as a single emitter where excitation places the exciton, on average, at a distance of three quarters of the particle radius from acceptors at the surface. Given the short Pdot lifetimes and the low photon flux associated with the excitation sources used, it is unlikely that multiple excitons existed simultaneously within a single particle, and they can therefore be treated as single emitters.

6.3.5 Likely mechanism(s) of ET and quenching

Our data clearly show that the F8BT Pdots engaged in ET as donors with the CyX, sCyX, Rh590, and Rh640 dyes, which showed sensitized emission as acceptors. The dye-induced decrease in the

Pdot excited state lifetime, measured from fluorescence decays and TA, indicated a dynamic quenching mechanism, at least in part. The most likely candidate ET mechanisms are therefore FRET, Dexter ET, and photoinduced electron transfer (PET), as illustrated in Figure 6.14. As the observed emission was a linear combination of the donor F8BT and acceptor dye emission, we ruled out significant exciplex formation. The discrepancy between quenching efficiencies derived from fluorescence intensity and lifetime data either suggests an additional static quenching mechanism, or that a sub-population of the F8BT is dynamically quenched with very high efficiencies (approaching 100%) and does not contribute to the measured lifetimes. The overwhelming absorbance contribution from the overall Pdot precluded observation of changes in absorbance spectra that would have been diagnostic for formation of non-fluorescent ground-state complex between dye and an F8BT monomer as a static quenching mechanism, so this possibility cannot be ruled out on this basis. With respect to ET by one or more of these mechanisms, several observations need to be reconciled: the quenching efficiency versus the number dyes per Pdot; the discrepancy between quenching efficiencies from lifetime and intensity data; and the discrepancy between the trend in quenching efficiencies and quantitative trend in spectral overlap. These points are addressed in the subsequent sub-sections.

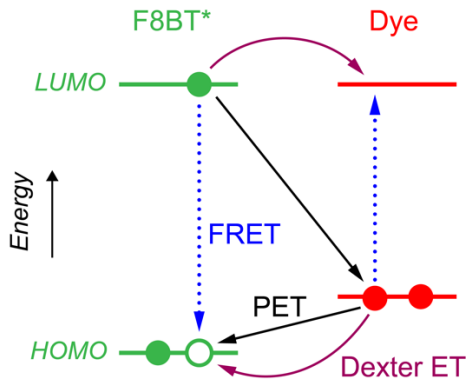

Figure 6.14 Simple mechanistic models for FRET, Dexter ET, and PET between an excited-state F8BT Pdot and a dye acceptor.

It is also useful to refer back to the NTA results in the context of dynamic quenching. The particle concentrations determined in the Cy5 channel were lower than in the F8BT channel, but not by ratios that were inconsistent with differences in concentrations measured for Pdot-only samples via the scattering (higher concentration) and fluorescence (lower concentration) modes of NTA. We thus attribute the result to different tracking sensitivities for the F8BT and Cy5 channels rather than a significant sub-population of Pdots that does not engage in ET. Our subsequent analyses and discussion therefore assume that all particles in the ensemble are quenched by ET.

6.3.5.1 Consideration of FRET

As an ET mechanism, FRET is consistent with the qualitative spectral overlap between the F8BT Pdot and dyes, dynamic quenching of Pdot fluorescence, and sensitization of dye emission, but is not consistent with the discrepancy between lifetime and intensity data and the trends in quenching efficiency versus spectral overlap.

An assumption of the orientation factor is frequently made in the calculation of Förster distances. The assumption that $\kappa^2 = 0.667$ is widely used and corresponds to dynamic random orientations of both donor and acceptor. This assumption is questionable for the F8BT because of its sub-nanosecond excited state lifetime and its dense packing within the Pdot, and similarly questionable for adsorbed or partitioned hydrophobic dye. An alternative assumption is static random orientations of donor and acceptor, for which $\kappa^2 = 0.476$ has been proposed [64]. This assumption leads to a mere 6% change in the Förster distance. For conjugated hydrophilic dye, which more plausibly dynamically samples random orientations, the value of κ^2 will be intermediate to these two values, although $\kappa^2 = 0.667$ was used to determine the Förster distances for the hydrophilic dyes in Table 6.1. None of these three cases may be a perfect match to the real system, but it is unlikely that the real Förster distances differ significantly from those listed in Table 6.1, which should be adequate for analysis.

6.3.5.1.1 Fractions of F8BT within $0.5R_0$ and beyond $2R_0$

For an isolated donor-acceptor pair, a separation distance $\leq 0.5R_0$ results in a FRET efficiency > 98%. Such high FRET efficiencies would decrease the lifetime of an F8BT donor to a value too short to reliably measure and nearly completely quench its emission intensity. The range of this near-unity FRET efficiency is extended when an F8BT donor is able to interact with multiple acceptors, which becomes more likely with more dyes per Pdot.

For the case of partitioned hydrophobic dye in Figure 6.13A, between 0.3–0.8% of the F8BT core volume is within $0.5R_0$ (~2-3 nm) of an individual dye molecule. To roughly estimate the interactions of an F8BT donor with multiple dye acceptors, we assume that the dye embeds within

the Pdot core in a lattice-like arrangement and take a hypothetical F8BT donor at the center of a unit cell. From this model, and accounting for the polydispersity of the Pdots, the upper limits of the average number of dyes per Pdot to obtain complete quenching via FRET are between 550–1700. For the cases of adsorbed hydrophobic dye and conjugated hydrophilic dye, the core volumes within $0.5R_0$ of the hypothetical dye interfaces are 25–40% and 15–25%, respectively. To roughly estimate the interactions of an F8BT donor with multiple dye acceptors, we assumed a grid pattern of surface dyes with a hypothetical F8BT donor at the centre but $0.5R_0$ below the surface. When accounting for the polydispersity of the Pdots, this simple model estimates between 600–1200 adsorbed hydrophobic dyes and 750–1750 conjugated hydrophilic dyes per Pdot (on average) for complete quenching of the $0.5R_0$-deep surface layer of F8BT via FRET. All ranges of dyes per Pdot represent uncertainty in the precise Pdot size distributions, batch-to-batch variation in the Pdot sizes, and also expected differences between the different dyes and Förster distances.

At the other extreme, separation greater than $2R_0$ for an isolated donor-acceptor pair results in a FRET efficiency < 2%, which is negligible within the precision of the experiments. For adsorbed hydrophobic dye and conjugated hydrophilic dye, any volume fraction of the F8BT core beyond $2R_0$ from these interfaces would, to a first approximation (and neglecting energy migration), not engage in FRET and therefore not have its intensity quenched and contribute a native F8BT fluorescence lifetime. Approximately 10–20% and 15–25% of the core volume is beyond a $2R_0$-deep surface layer for hydrophobic adsorbed dye and conjugated hydrophilic dye, respectively. Considering that a putative F8BT donor would only need to interact with ≥ 7 dyes for the FRET efficiency at $2R_0$ to reach ≥ 10%, the volume fraction of Pdot that is beyond the range for FRET

should become quite small as the number dyes per Pdot becomes sufficient to fully quench the $0.5R_0$-deep layer of F8BT.

The above analysis suggests that the intensity-based quenching efficiency reflects both short-range, near-unity FRET efficiencies within *ca.* $0.5R_0$, as well as long-range, non-unity FRET efficiencies beyond $0.5R_0$, whereas the lifetime-based quenching efficiency only reflects the long-range FRET. This hypothesis qualitatively accounts for the discrepancies in ET efficiencies between intensity and lifetime data.

6.3.5.2 Consideration of Dexter ET

As an electron exchange mechanism of ET that occurs at van der Waals contact distances (< 1 nm), only the surface-adjacent F8BT would engage in Dexter ET for the case of adsorbed hydrophobic dye or, to a presumably much lesser extent, for the case of conjugated hydrophilic dye. For partitioned hydrophobic dye, only dye-adjacent F8BT would be expected to engage in Dexter ET. Thus, compared to FRET, Dexter ET as the predominant ET mechanism is much more dependent on efficient energy migration within the F8BT or large numbers of dye per Pdot to obtain high quenching efficiencies.

If Dexter ET is treated as having ~100% efficiency at < 1 nm and ~0% efficiency at > 1 nm, then the cases of adsorbed hydrophobic dye and conjugated hydrophilic dye should exhibit little or no ET-sensitized dye emission in absence of efficient energy migration. Likewise, hydrophobic partitioned dye would require an average of thousands of dyes per Pdot for efficient quenching.

Any volume fractions of F8BT quenched would, however, decrease the measured fluorescence intensity without a resolvable change in the measured lifetime.

Other than the above, Dexter ET would yield qualitatively similar results to FRET, with lower efficiencies observed per dye with larger and more polydisperse Pdots, and expectation of a similar trend with the Pdot-dye spectral overlaps.

6.3.5.3 Consideration of PET

An important distinction between PET and both FRET and Dexter ET is that PET is not expected to sensitize dye emission, but will still quench the F8BT emission intensity and shorten its lifetime. PET depends upon the redox potentials of the donor and acceptor species (*i.e.*, frontier orbital alignment), but does not depend on spectral overlap unlike FRET and Dexter ET. If PET, like Dexter ET, is also assumed to operate with ~100% efficiency at < 1 nm and ~0% efficiency at > 1 nm, it would be heavily dependent on energy migration for achieving high quenching efficiencies, and would quench the measured fluorescence intensity without a resolvable change in the measured lifetime.

Overall, the alignment of the HOMO and LUMO levels in Figure 6.3B suggest a greater tendency toward reductive PET than oxidative PET. In reductive PET, an electron moves from the HOMO of the dye into the HOMO of the Pdot after the Pdot is photoexcited. The alignments in Figure 6.3B also suggest that the CyX dyes should engage in PET more efficiently than the RhX dyes, and that, within the CyX dye family, the expected trend in PET rate should be opposite the expected trend in FRET rate.

There are several caveats for the interpretation of Figure 6.3B. The CV data for F8BT is on free polymer in a good solvent, and assumes a single representative HOMO energy for the whole polymer chain. Within the Pdot, the F8BT chains are likely to be more disordered with shorter average conjugation lengths, such that additional states are anticipated at energies slightly higher than in Figure 6.3B. Intra- or interchain interactions when the polymers aggregate into nanoparticles may also change the orbital energies. The CVs were recorded in solvents of different polarities across the classes of material (*i.e.,* DCM for F8BT, acetonitrile for RhX, and ethanol/acetonitrile for CyX), that are not necessarily reflective of the local environments of the chromophores in the Pdot system (*i.e.,* higher polarity when in contact with water, lower polarity inside the Pdot core).

6.3.5.4 Relative contributions of ET mechanisms

Qualitatively, the observed ET efficiency decreased for increased donor-acceptor distances (*i.e.,* the hydrophilic, surface-conjugated dyes displayed lower apparent ET efficiencies than the partitioned/adsorbed hydrophobic dyes). However, this trend is expected for all of the ET mechanisms considered, albeit with different quantitative dependencies. Due to the increased donor-acceptor distance for the hydrophilic dyes (both surface-conjugated and conjugated via NeutrAvidin and dextran), ET likely occurs most often by FRET in these configurations. (Albeit with small probability, direct contact between the surface-conjugated dyes and the F8BT core may occur, enabling Dexter ET and PET.)

For the hydrophobic dyes, the model presented in Figure 6.13B, where the dye is adsorbed onto the surface of the hydrophobic F8BT core, likely best reflects the real system, with the caveat that in reality, the core/shell structure is probably poorly defined and unevenly mixed. The reported disordered, glassy phase conformation of the constituent polymer chains likely prevents the dyes, which are added post-synthetically, from fully partitioning into the core. In this model, the qualitative discrepancies between the intensity- and lifetime-derived efficiencies can be rationalized by invoking FRET as the dominant ET mechanism, and considering three regimes of quenching: $\leq 0.5R_0$, where quenching occurs with near 100% efficiency; $\geq 2R_0$, where quenching is negligible; and between $0.5R_0$–$2R_0$, where the ET efficiency depends on the donor-acceptor distance and the number of acceptors accessible to a single donor. Discrepancies between intensity- and lifetime-derived data may also arise from static quenching, which we were unable to rule out based on our data. Treatment of the experimental data using the FRET framework and considering the donor quantum yield and particle size did not yield qualitative agreement between the observed ET efficiency, the spectral overlap, and the Förster distance for a given set of dyes. For dyes of similar average donor-acceptor distance, the ET efficiency is expected to decrease with the extent of spectral overlap (*e.g.*, (s)Cy5 > (s)Cy5.5 > (s)Cy7), which was not observed for the CyX and sCyX dyes. Owing to the difficulties associated with the Rh610 titration, caution should be taken interpreting trends from the RhX data.

Dexter ET and PET are short range interactions compared to FRET, and require donor-acceptor separations of ≤ 1 nm. Although PET may contribute to the observed ET, we rule it out as the dominant contribution because it is not expected to sensitize acceptor emission, yet CyX, sCyX, Rh590, and Rh640 displayed intense ET-sensitized emission (the low intensity from Rh610 is

attributed to the lower number of dyes doped into the Pdot). There was also no spectral evidence for the formation of non-emissive ground state complexes that could be formed by PET, although any such signal would likely be obscured by the strong contribution from the Pdot. While Dexter ET is expected to sensitize acceptor emission, its short range of action means that highly efficient quenching, as was observed for Pdots with CyX, sCyX, Rh590 and Rh640, would require either substantial energy migration through the Pdot or a large number of dyes per Pdot. For these reasons, Dexter ET is likely not a dominant mechanism of ET in the systems studied here. For acceptors within close proximity to F8BT chromophores, both PET and Dexter ET are possible and likely occur, albeit to a much lesser extent than FRET. The non-zero contributions from these mechanisms are expected to contribute to the deviations from the trends expected for ET purely by FRET.

6.4 Conclusions

The nature of energy transfer in Pdot-dye systems was studied using steady-state and time-resolved spectroscopy. F8BT/PSMA Pdots were used as donors and paired with several families of dye acceptors (CyX, sCyX, and RhX) in a number of configurations, intended to test the dependency of ET on the extent of spectral overlap and the donor-acceptor distance. Energy transfer was seen to occur to all the selected acceptors, albeit with varying efficiency. The Pdot fluorescence lifetime generally decreased with an increasing number of acceptors per particle, indicating a dynamic quenching mechanism, at least in part. ET was therefore analyzed using the framework of FRET, Dexter ET, and PET.

Of these three mechanisms, FRET is most likely the dominant mechanism of ET, and it can be used to qualitatively rationalize the observed trends in donor-acceptor distance and the apparent discrepancies between intensity- and lifetime-derived ET efficiencies. However, quantitative analysis of the experimental data using the framework of FRET, considering the batch-to-batch variation in particle size and donor quantum yield, did not yield the expected trends. Dexter ET and PET have different quantitative dependencies on the spectral overlap and frontier orbital alignment, respectively. If these mechanisms occur concurrently with FRET, divergence from the expected trends in ET efficiency is anticipated. The efficiency of ET to adsorbed or surface-conjugated dyes by any mechanism may also be affected by energy migration, which was largely neglected in our analysis.

Several key limitations in the experimental precision may also have been partially (or wholly) responsible for the discrepancies, namely the limited accuracy of both particle sizes and concentrations determined by NTA, the use of a fluorescence method rather than an absorbance method to estimate the number of dyes per particle, and the use of amplitude-weighted average fluorescence lifetimes to determine ET efficiencies. Although we consider our estimations of the number of dyes per particle to be accurate within 30–50% of the real value, this variation could be significant enough to change the observed trends. The tabulated ET efficiencies for the sCyX dyes were similar, such that even a small (*i.e.*, factor of 2) variation in the average number of dyes per particle could shift the observed trend to better reflect the differences in spectral overlap with F8BT.

Although we accounted for batch-to-batch variation in quantum yield and average donor-acceptor distance, other aspects of batch-to-batch variation may also affect ET. Pdots of different sizes will have a different proportion of the F8BT molecules at or near the particle surface, and these molecules are more prone to oxidation, which may introduce additional trap states at the surface or within a depth of a few nanometres. The extent and effect of trap states is non-trivial to determine experimentally, especially for a polydisperse ensemble, and are expected to vary batch-to-batch. For adsorbed and surface-conjugated dyes, energy migration towards the surface is likely important for efficient ET, and a high density of surface or near-surface trap states, where the exciton decays thermally, may prevent ET. Quantitative modelling is a possible strategy to account for the heterogeneity of the system, including effects of size polydispersity, exciton migration and trapping, and the arrangement and number of dyes per Pdot. Monte Carlo simulations can be used to model energy migration with a model Pdot, considering the idealized configurations shown in Figure 6.13. Unlike the experimental results presented in this chapter, simulations are not limited to ensemble averages. Comparison between simulation and experimental results may elucidate which ET mechanisms occur in the real Pdot system.

6.5 Experimental methods and data analysis

6.5.1 Materials

Dextran (M_r ~6000) was from Sigma-Aldrich (Oakville, ON, Canada). Cy5-hydrazide, Cy5.5-NHS ester, Cy7-hydrazide, sulfoCy5-NHS ester, sulfoCy5.5-NHS ester, sulfoCy7-NHS ester, Cy5-COOH, Cy5.5-COOH and Cy7-COOH were from Lumiprobe (Hallandale Beach, FL). These dyes are abbreviated as CyX or sCyX. The sCyX dyes were converted to hydrazide dyes by reaction with adipic acid dihydrazide, (see Section 6.5.3). Rhodamine 590, Rhodamine 610, and

Rhodamine 640 (RhX) were from Exciton (Lockbourne, OH). NeutrAvidin was from Thermo Fisher Scientific (Rockford, IL). Tetrahydrofuran (THF) was OmniSolv HPLC grade BHT stabilized (250 ppm) from Millipore (Billerica, MA, USA).

6.5.2 Determination of octanol-water partition coefficients

The hydrophobicity and hydrophilicity of the dyes was quantified by their octanol-water partition coefficient (K_{ow}), as per Eqn. 6.2, where C denotes the concentration of the dye in octanol (O) or water (W). The concentration in each phase was determined by UV-visible spectrophotometry.

$$K_{ow} = \frac{C_O}{C_W} \tag{6.2}$$

6.5.3 Hydrazide-functionalized dye synthesis

Adipic acid dihydrazide (4.6 mg, 26 μmol) was dissolved in 100 μL of HEPES buffer (25 mM, pH 7.3). sCyX-NHS ester (1.0 mg) was dissolved in 50 μL DMSO and a 2 μL aliquot was added to the adipic acid dihydrazide solution. The solution was vortexed and left to react in the dark at room temperature for 4 h. The dye was purified by silica column chromatography (sCy5-hydrazide and sCy5.5-hydrazide; solvent mixture: 7:2:1 ethyl ether:methanol:water) or by C18 Sep-Pak cartridge (Waters Corp., Mississauga, ON, Canada; sCy7-hydrazide; solvent mixture 9:1 acetonitrile:water). TLC (7/2/1 ethyl ether/methanol/water) was used to confirm a successful reaction. The product was dried by vacuum centrifugation or rotary evaporation.

6.5.4 Addition of dye acceptors

Doping of hydrophobic dyes was performed as follows: HEPES buffer (3 μL; 1.0 M, pH 7.3) was added to a solution of Pdots (100 μL) followed by the desired amount of hydrazide-CyX or RhX. Several solutions of varying dye concentration were prepared and the solutions brought to equal volume by the addition of water. The solutions were mixed for 1 h at room temperature or overnight at 4 °C in the dark. Pdot-dye conjugates were purified from excess dye by spin filtration (100 kDa MW cutoff) and washed with 25 mM HEPES buffer (pH 7.3).

sCyX-Pdot conjugates were prepared as follows: HEPES buffer (3 μL; 1.0 M, pH 7.3) was added to a solution of Pdots (100 μL). The solution was briefly mixed and the desired amount of hydrazide-sCyX was added. Freshly prepared 1-ethyl-3-(3-dimethylaminopropyl)-carbodiimide solution (EDC; 3 μL, 10 mg/mL in water) was added. Several solutions of varying dye concentration were prepared by the same procedure and the solutions brought to equal volume by the addition of water. The solutions were mixed for 4 h at room temperature or overnight at 4 °C in the dark and purified as above prior to fluorescence measurements.

6.5.5 Amine-modified dextran synthesis, conjugation, and ET titration

Dextran (MW ~6 kDa, 1.99 g, 332 μmol) was dissolved in 15 mL of water and was partially oxidized by reaction with sodium (meta)periodate (0.72 g, 3.37 mmol) overnight at 4 °C. The product was purified by dialysis against water for 72 h or by precipitation with ethanol, then dried by vacuum or lyophilization.

Oxidized dextran (1.58 g) was dissolved in 30 mL of water and hexamethylene diamine was added (9.93 g). The reaction was stirred at room temperature for 2 h, followed by the addition of sodium cyanoborohydride (0.44 g). The reaction was stirred overnight at room temperature, and the product purified analogously to the oxidized dextran.

Amine-modified dextran (10.9 mg) was dissolved in 1 mL aqueous Pdot solution and 20 µL of HEPES buffer (1.0 M, pH 7.3) was added. EDC (1-ethyl-3-(3 dimethylaminopropyl) carbodiimide hydrochloride, 20 µL, 10 mg/mL) was added and the reaction mixed at room temperature in the dark for 4 h. The dextran-conjugated Pdots were purified by spin filtration (100 kDa MW cutoff) and washed with 25 mM HEPES buffer (pH 7.3).

Sodium (meta)periodate (1000–5000-fold molar excess versus dextran-Pdots) was added to between 100–800 µL of dextran-Pdot solution (257 pM–2.5 nM) and the solution was mixed for 1 h in the dark. The product was purified by spin filtration. sCy5-hydrazide was added (between 0–40 000-fold molar excess versus oxidized dextran-Pdots) and the solution was mixed overnight. Excess dye was removed by spin filtration (MWCO 100 kDa) prior to fluorescence measurements.

6.5.6 Synthesis of biotinylated sCy5

Sulfo-Cy5-biotin was prepared using a modified procedure from Gruber *et al.* [243]. A stock solution of sCy5-NHS ester (25.7 mM) was prepared in anhydrous DMSO. An aliquot (3.9 µL) of the stock solution was further diluted into 50 µL of anhydrous DMF. Next, *N,N,N′,N′*-Tetramethyl-*O*-(*N*-succinimidyl)uronium hexafluorophosphate (HMTU, 40 µL, 10 mM) and 1.1 µL of DIPEA (5% v/v in anhydrous DMF) were added. The reaction was rotary mixed in the dark for 30 min,

then added to 0.5 mg of (+)-Biotinamidohexanoic acid hydrazide. One drop of neat DIPEA was added. The reaction mixture was briefly vortexed and then left to react on a rotary mixer for 2 h in the dark. The product was purified by a C18 Sep-Pak cartridge, eluting sequentially with ~5 mL of 0%, 5%, 10% and 20% v/v acetonitrile in water. Successful reaction was verified by TLC (7/3/0.4 $CHCl_3$, MeOH, AcOH).

6.5.7 NeutrAvidin conjugation and ET titration.

PEG-3350 (50 µL, 5% w/v) and borate buffer (50 µL, 800 mM, pH 8.5) were added to 964 µL of Pdots (~360 pM) and the solution vortexed. NeutrAvidin (50 µL, 3.5 µM) was added and the solution mixed by pipette. EDC (10 µL, 10 mM in borate buffer, pH 8.5) was added. The reaction mixture was placed on a rotary mixer in the dark for 1 h and purified by spin filtration (MWCO 100 kDa). Next, sCy5-biotin was added, and the solutions placed on a rotating sample mixer in the dark for 1.5 h. Excess dye was removed by spin filtration (MWCO 100 kDa) prior to fluorescence measurements.

6.5.8 Transient absorption measurements

Transient absorption measurements were performed using a Newport transient absorption spectrometer (Newport Corp., Irvine, CA). Pump and probe pulses were from a femtosecond Ti-Sapphire amplifier with output at 800 nm, a pulse duration of ~130 fs, and a repetition rate of 1 kHz. Samples were pumped at 400 nm and the probe pulse was broadband white light with a spectral range from 350 to 750 nm. Spectra were recorded with an Oriel MS260 spectrograph (Newport Corp.) and CCD camera.

6.5.9 Electrochemistry

Cyclic voltammograms (CVs) of F8BT (as polymer dissolved in solution) and the RhX dyes were recorded at room temperature using a CHI660D potentiostat (CH Instruments, Austin, TX) with a platinum wire counter electrode, Ag/AgCl reference electrode, and a platinum working electrode. Electrolyte solutions were ~0.1 M *n*-NBu_4BF_4 in dichloromethane (for F8BT) or acetonitrile (for RhX). CVs were recorded at scan rates of 50 mV/s (Rh640), 100 mV/s (Rh610 and Rh590), and 150 mV/s (F8BT).

CVs of CyX-COOH were recorded at room temperature using a PGStat30 potentiostat (Metrohm Autolab, Utrecht, Netherlands) and a screen-printed electrode set (PCR-P01, Biodevice Technology, Japan) that included a carbon working electrode, carbon counter electrode, and an Ag/AgCl reference electrode. CyX dyes and *n*-NBu_4BF_4 were dissolved in acetonitrile and diluted in ethanol for measurements to prevent degradation of the electrode. CVs were recorded at scan rates ranging from 100 mV/s to 1.00 V/s.

6.5.10 Post-purification determination of the number of dyes per Pdot

The concentration of (s)CyX or RhX dyes remaining in solution after purification was estimated by Eqn. 6.3, where *C* is the concentration of the dye, and *I* is the maximum intensity of the dye from the excitation spectrum. Dye concentrations could not be determined by absorption measurements because of the low concentrations and relatively low absorption coefficients of the dyes (~10^5 M^{-1} cm^{-1}) compared to the Pdots (~10^9 M^{-1} cm^{-1}). The excitation spectra were used instead of the emission spectra because the dye and Pdot signals were better resolved. The parameters for the excitation spectra measurements are in Table 6.6.

$$C_{purified} = \frac{C_{unpurified} I_{purified}}{I_{unpurified}} \tag{6.3}$$

Table 6.6. Excitation spectra measurement parameters for the determination of dye concentrations.

Dye	Exc. scan range (nm)	Em. Wavelength (nm)
(s)Cy5	300–680	700
(s)Cy5.5	300–730	750
Cy7	300–750	773
sCy7	300–790	810
Rh640	300–630	650
Rh610	300–590	610
Rh590	350–590	610

The concentration of Pdots was determined by NTA. The average number of organic dye acceptors per Pdot was taken as the ratio of the concentration of the dye to the concentration of the Pdot.

6.5.11 Determination of spectral overlap integrals

Values for FRET spectral overlap, *J*, were determined by Eqn. 6.4, where $F(\lambda)$ is the emission spectrum of the donor (Pdot), $\varepsilon(\lambda)$ is the wavelength-dependent molar extinction coefficient of the acceptor (dye), and λ is the wavelength [162].

$$J = \frac{\int F(\lambda)\varepsilon(\lambda)\lambda^4 d\lambda}{\int F(\lambda) d\lambda} \tag{6.4}$$

Values for the Dexter spectral overlap, *J'*, were determined by Eqn. 6.5 where $\bar{\nu}$ is the energy in terms of wavenumber [115].

$$J' = \frac{\int F(\bar{\nu})\varepsilon(\bar{\nu})d\bar{\nu}}{\int F(\bar{\nu})d\bar{\nu}\int \varepsilon d\bar{\nu}} \tag{6.5}$$

6.5.12 Calculation of ET efficiencies

ET efficiencies, *E*, were derived from changes in the fluorescence intensity (*F*) or average fluorescence lifetime (τ) of the donor species between the presence (F_{DA} or τ_{DA}) and absence ($F_{D,cor}$ or τ_D) of the acceptor species according to Eqns. 6.6–6.8.

$$E = 1 - \frac{F_{DA}}{F_{D,cor}} \tag{6.6}$$

$$E = 1 - \frac{\langle \tau \rangle_{DA}}{\langle \tau \rangle_{D}} \tag{6.7}$$

$$\langle \tau \rangle = \frac{A_1\tau_1 + A_2\tau_2}{A_1 + A_2} \tag{6.8}$$

For Eqns. 6.6–6.8, emission intensity was measured at ~540 nm for all Pdot-dye pairs because the CyX dyes had negligible emission at this wavelength. Given the overlap between the emission spectra of the Pdot and the rhodamine dyes, the values of F_D and F_{DA} for the rhodamine dyes were determined via mathematical unmixing of the two spectral contributions (*vide infra*). Eqn. 6.6 also uses a corrected emission intensity for the donor alone. The reason is that the concentrations of the Pdot-dye samples were different from samples of the Pdot alone because of changes in volume and potential loss during purification (*e.g.*, via spin filtration). Consequently, an accurate donor-only reference intensity cannot be measured directly. The unquenched emission intensity from the

Pdot was assumed to be proportional to its concentration, and the concentration was assumed to be proportional to the Pdot absorbance. Therefore, the ratio of the fluorescence intensity and absorbance of the Pdot-only sample was used to estimate the theoretical unquenched fluorescence intensity of the Pdot samples with dye acceptors based on their measured absorbances. This approach assumes that the properties of the Pdot (*e.g.*, quantum yield, particle size distribution) remain constant between the quenched and unquenched samples. The value of $F_{\mathrm{D,cor}}$ was estimated by Eqn. 6.9, where A_D is the absorbance of the Pdot-only sample, A_{DA} is the absorbance of the Pdot-dye sample after purification, and F_{D} is the measured PL emission intensity for Pdot alone. Absorbances were recorded at 460 nm, which was the absorption maximum of the Pdot and a wavelength where the CyX and RhX dyes had minimal absorbance. We attribute the calculation of some slightly negative ET efficiencies to errors associated with the estimation of $F_{D\,cor.}$

$$F_{D,cor} = \frac{F_D A_{DA}}{A_D} \tag{6.9}$$

For Eqns. 6.7–6.8, ET efficiencies were determined from the amplitude weighted average fluorescence lifetime of the donor species in the presence and absence of the acceptor species, $\langle\tau\rangle_{DA}$ and $\langle\tau\rangle_D$, respectively. Data was collected in the wavelength channel corresponding to 540 ± 6.25 nm. Fluorescence decay curves were fit with a biexponential function, and amplitude-weighted average lifetimes, $\langle\tau\rangle$, were calculated using Eqn. 6.8, where A_1, A_2 and τ_1, τ_2 are the amplitude and lifetime components of the decay, respectively. The choice to use a biexponential decay model is discussed in Appendix B.3.

6.5.13 Calculation of ET rates

Energy transfer rates, k_{ET}, were determined by Eqns. 6.10 and 6.11, where E is ET efficiency, N is the number of acceptors per Pdot, k_0 is the radiative rate of the Pdot in the absence of acceptors and τ_D is the fluorescence lifetime of the Pdot in the absence of acceptors. ET efficiency data was fitted with Eqn. 6.10 to determine the value of the parameter b. k_{ET} was then determined using Eqn. 6.11.

$$E = \frac{Nb}{1+Nb} \tag{6.10}$$

$$b = \frac{k_{ET}}{k_0} = k_{ET}\tau_D \tag{6.11}$$

6.5.14 Spectral unmixing of Pdot-RhX emission data

Given the high extent of overlap between the emission spectra of Pdots and the RhX dyes, mathematical deconvolution was necessary to determine their respective emission intensities. The parameters a and b in Eqn. 6.12 were solved to minimize the sum of the squared residuals (SSR) between a linear combination of the emission spectra of the Pdot and the RhX dye ($F_{Pdot}(\lambda)$ and $F_{RhX}(\lambda)$) and a RhX-Pdot sample ($F_{data}(\lambda)$). The deconvolution is represented graphically in Figure 6.4.

$$SSR = \sum \left(aF(\lambda)_{Pdot} + bF(\lambda)_{RhX} - F(\lambda)_{data} \right)^2 \tag{6.12}$$

6.5.15 Estimation of HOMO/LUMO levels by cyclic voltammetry

The HOMO energy level was determined from the half-peak potential of the oxidative (positive) scan. This value was either taken as the average of the peak potentials from the forward and reverse

scans, or as the forward scan peak potential minus 29.6 mV, assuming the peak corresponds to a one electron redox process. Peak potentials were tabulated relative to ferrocene (4.4 eV) as a standard. The optical bandgap was taken as the absorption onset, which was determined by fitting red edge of the absorption band with a linear function. The LUMO energy level was determined by the sum of the HOMO energy level and the band gap energy.

6.5.16 DFT simulations

Ground state geometry optimization and frequency calculations were performed using Gaussian 16 [244]. F8BT was modelled as a tetrameric oligomer where the alkyl side chains were substituted by methyl groups to reduce computational time. It has been previously shown that this substitution does not significantly affect the equilibrium geometry or molecular orbital distribution of the molecule [245]. Calculations were performed using the B3LYP functional and the 6-31G(d) basis set. The input geometries, optimized geometries and calculated HOMOs and LUMOs are shown in Figure 6.15.

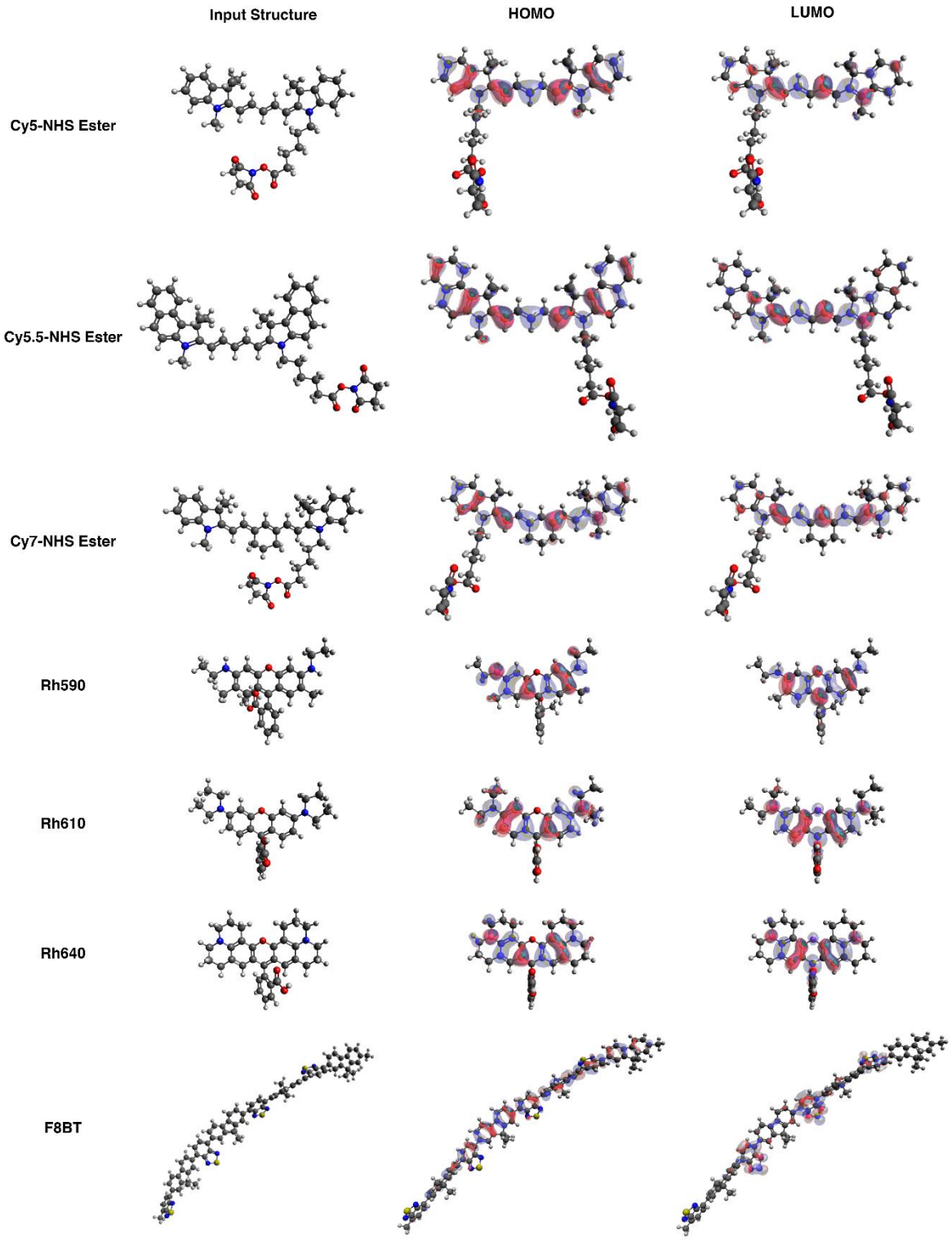

Figure 6.15 Input structures, output structures, and HOMO and LUMOs of CyX, RhX, and simplified F8BT.

Chapter 7: Dextran-functionalization of semiconducting polymer dots and conjugation with tetrameric antibody complexes for bioanalysis and imaging

This chapter is based on a published manuscript, written by Kelsi Lix with editing from Russ Algar and minor contributions from co-authors. KL performed all experiments and data analysis with the following exceptions: AFM images were provided by Ethan Sauvé, cell labelling and imaging experiments were performed by Michael Tran who analyzed the data with KL, NMR analysis was performed by Kelly Rees, and immunoassay development and data analysis were performed by Melissa Massey.

7.1 Introduction

Pdots continue to gain popularity as a fluorescent probe for a variety of applications in bioanalysis and imaging, where their extremely high per-particle brightness, good photostability, and low cytotoxicity are highly advantageous [26, 109, 118]. These materials have been defined as a subclass of conjugated polymer nanoparticles having high (> 50%) mass or volume concentrations of semiconducting polymer, hydrophobic cores, and small diameters [118]. Pdots have been used for cellular labelling [59, 78, 93] and *in vivo* imaging [139, 187], chemical and biochemical sensing [31, 77, 157], and photodynamic therapy [49, 246]. However, many Pdot materials suffer from non-trivial limitations that must be addressed before they can reach their full potential in bioanalysis and imaging.

Pdots are generally held together by relatively weak, entropically-driven hydrophobic interactions [26, 59], leading to modest particle stability. Like other nanoparticles, Pdots may also suffer from

poor colloidal stability and fouling depending on their surface chemistry and environment. For example, Pdots with anionic surface chemistry are colloidally destabilized at low pH and at high ionic strength and are prone to non-specific binding with proteins and on some surfaces [27, 59]. Another limitation of Pdots, which is common for emerging nanoparticle materials, is that relatively few surface chemistries and bioconjugate chemistries have been reported. The most commonly used chemistry to date is carbodiimide-mediated conjugation at surface carboxyl groups, which itself suffers from several limitations, including but not limited to poor control and reproducibility with respect to the number and orientation of biomolecules per Pdot [154]. A strategy for addressing these limitations is modification of the Pdot surface with a coating material that has robust aqueous solubility, minimal non-specific interactions with biomolecules, and supports well-controlled bioconjugate chemistry. For Pdots, amphiphiles functionalized with PEG have come the closest to this ideal, albeit still often used with carbodiimide chemistry for bioconjugation [28, 86, 89].

Dextrans are a class of homopolysaccharides of glucose (glucans) whose major chains are composed of consecutive α(1,6)-linkages. The structure of dextran is shown in Figure 7.1. Dextrans typically possess a small number (3–50% of total glycosidic bonds) of side chains stemming from α(1,3)-linkages, or, less frequently, α(1,4)- or α(1,2) branched linkages. The exact structure of dextran depends upon which bacterial strain was used for its synthesis. Dextrans are synthesized by dextransucrase enzymes (of the glycoside-hydrolase class) in *Leuconostoc*, *Streptococcus* and *Lactobacillus* species using sucrose as a starting material [247]. Dextrans and dextran derivatives have found much commercial use. Clinically, dextran of moderate molecular weight (40–100 kDa) is used as a therapeutic agent for restoring blood volume due to its ability to

retain water and provide colloid osmotic pressure to pull fluid from the interstitial space into plasma. Iron-dextran complexes have been used to alleviate iron deficiency and as a magnetic resonance imaging contrast agent [248]. Cross-linked dextran, known commercially as Sephadex (separation Pharmacia dextran), is used as a medium for size exclusion chromatography [247]. Dextran is readily chemically modifiable and its properties can be tuned depending upon the nature of these modifications [249].

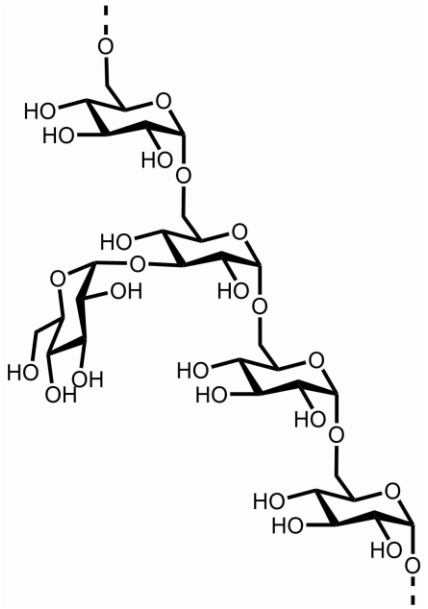

Figure 7.1 Structure of dextran showing the α(1,6)-linked glucopyranose backbone and a branch originating from the 3-position.

Dextran is advantageous as a surface coating material because it is strongly hydrophilic, chemically modifiable, biocompatible, stable in acidic and basic conditions, and commercially available in a range of molecular weights [250]. Dextran-coated magnetic iron oxide nanoparticles have been used in a number of biomedical imaging techniques, including magnetic resonance, and, when paired with an appropriate label, optical imaging, photodynamic therapy, and positron

emission tomography [251]. For *in vivo* applications, dextran has been shown to prevent particle degradation and prolong circulation half-life [252]. Beyond iron oxide nanoparticles, dextran has been used as a surface coating for inorganic composite nanoparticles [253], silicon nanoparticles [252], and non-conjugated polymer nanoparticles [254].

This chapter presents the development of dextran-functionalized Pdots (Dex-Pdots). Dextran was modified to have multiple pendant amine groups per chain, supporting conjugation to a carboxylated Pdot at multiple surface sites, putatively crosslinking the Pdot to itself. Dextran functionalization improved the colloidal stability of Pdots over ranges of pH and ionic strength. Moreover, specific labeling of biological targets with Dex-Pdots was achieved using a bifunctional tetrameric antibody complex (TAC) with an anti-dextran antibody and an anti-target antibody [255-256]. TACs have been used in the selection and isolation of cells [257-262], but have not been widely used for fluorescence labelling. These complexes are advantageous in that antibody conjugation is achieved spontaneously, without covalent crosslinking, and with optimal orientation of the anti-target antibody for binding. Using TAC-conjugated Dex-Pdots, we demonstrated a proof-of-concept fluorescence-linked immunosorbent assay (FLISA) for human erythropoietin (EPO) and selective labeling of human epidermal growth factor receptor 2 (HER2) antigens on the surface of SK-BR3 breast cancer cells, where the dextran functionalization reduced non-specific binding and the TAC increased specific labeling. Dextran functionalization is thus a promising strategy for improving the stability of Pdots, enabling new methodologies for their bioconjugation, and enhancing their performance in bioanalysis and imaging.

7.2 Results

7.2.1 Pdot materials

Pdots were synthesized via the nanoprecipitation method using F8BT as the semiconducting polymer and PSMA as the amphiphilic copolymer, as illustrated in Figure 7.2A. The hydrophobic semiconducting polymer and the hydrophobic styrene monomers of PSMA are thought to co-condense into the Pdot core in water, where the maleic anhydride monomers hydrolyze into hydrophilic carboxyl(ate) groups at or near the particle surface to form a shell-like layer around the hydrophobic core. The anionic carboxylate groups confer pH-dependent colloidal stability to the Pdots and are also reactive groups for bioconjugation. The optical properties of a Pdot are largely determined by the identity of the semiconducting polymer that it comprises. The green-yellow emitting F8BT semiconducting polymer was primarily used in this study. Orange-emitting CNMEHPPV/PSMA Pdots were additionally used for cell immunolabeling. The absorbance, excitation, and emission spectra of F8BT/PSMA and CNMEHPPV/PSMA Pdots are shown in Figure 7.3.

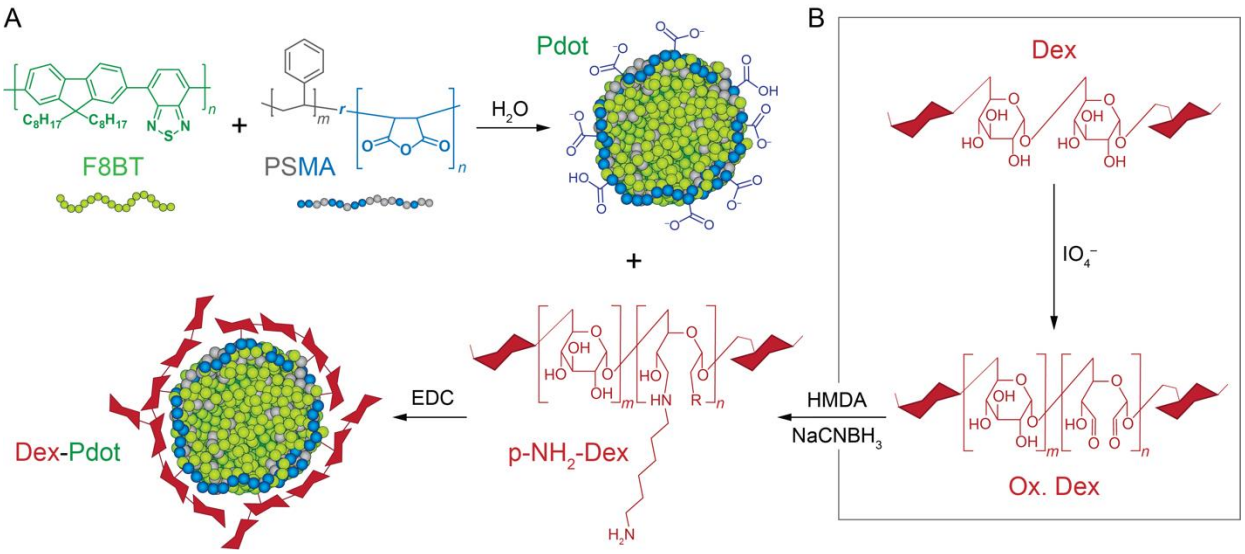

Figure 7.2 (A) Preparation of F8BT/PSMA Pdots by nanoprecipitation and functionalization with amine-modified dextran (p-NH_2-Dex) via carbodiimide (EDC) activation. **(B)** Preparation of amine-modified dextran through an oxidized dextran (Ox. Dex) intermediate and hexamethylenediamine (HMDA). The R group on p-NH_2-Dex may be another HMDA modification, an unreacted aldehyde (or the corresponding hydrate), or have cyclized with the secondary amine of the shown HMDA modification.

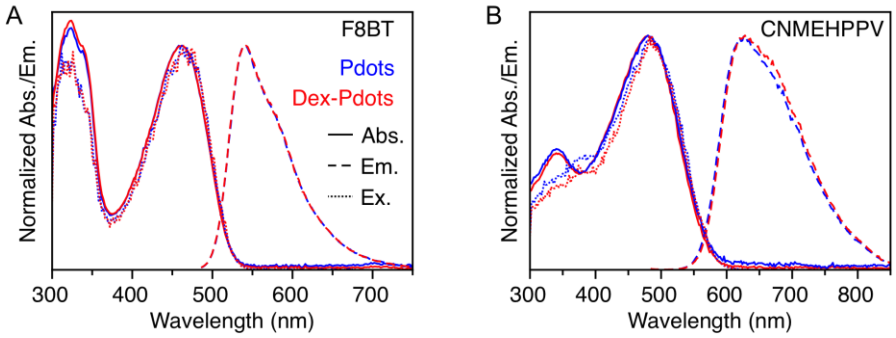

Figure 7.3 Normalized absorbance and fluorescence emission and excitation spectra for **(A)** F8BT and **(B)** CNMEHPPV Pdots and the corresponding Dex-Pdots. Dextran functionalization did not significantly change the spectral profiles.

7.2.2 Dextran functionalization

Dextran modified with pendant amine groups (p-NH_2-Dex) was synthesized by the partial oxidation of dextran (~6 kDa) with periodate followed by reductive amination with

hexamethylenediamine (HMDA), as illustrated in Figure 7.2B. The modified dextran was characterized by IR and NMR spectroscopy (Figure 7.4 and Figure 7.5), which did not unambiguously indicate the formation of the partially oxidized or aminated dextran products. We attributed this result to a small number of modifications versus the number of unmodified glucose units. Functional tests were therefore important for confirming modification of the dextran and subsequent functionalization of the Pdots.

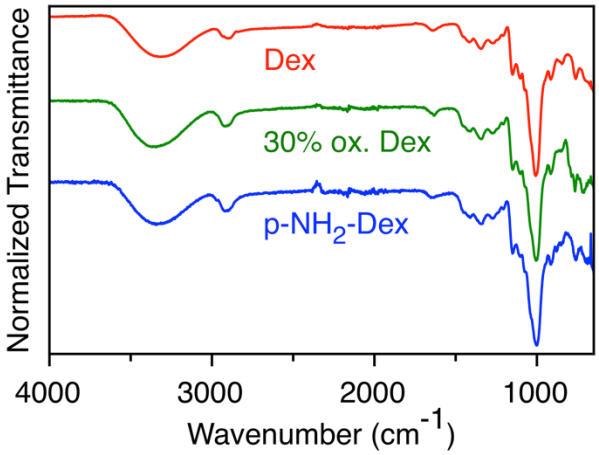

Figure 7.4 ATR-FTIR spectra of dextran (red), 30% oxidized dextran (green) ,and p-NH_2-Dex (blue). The spectra are offset from one another for clarity.

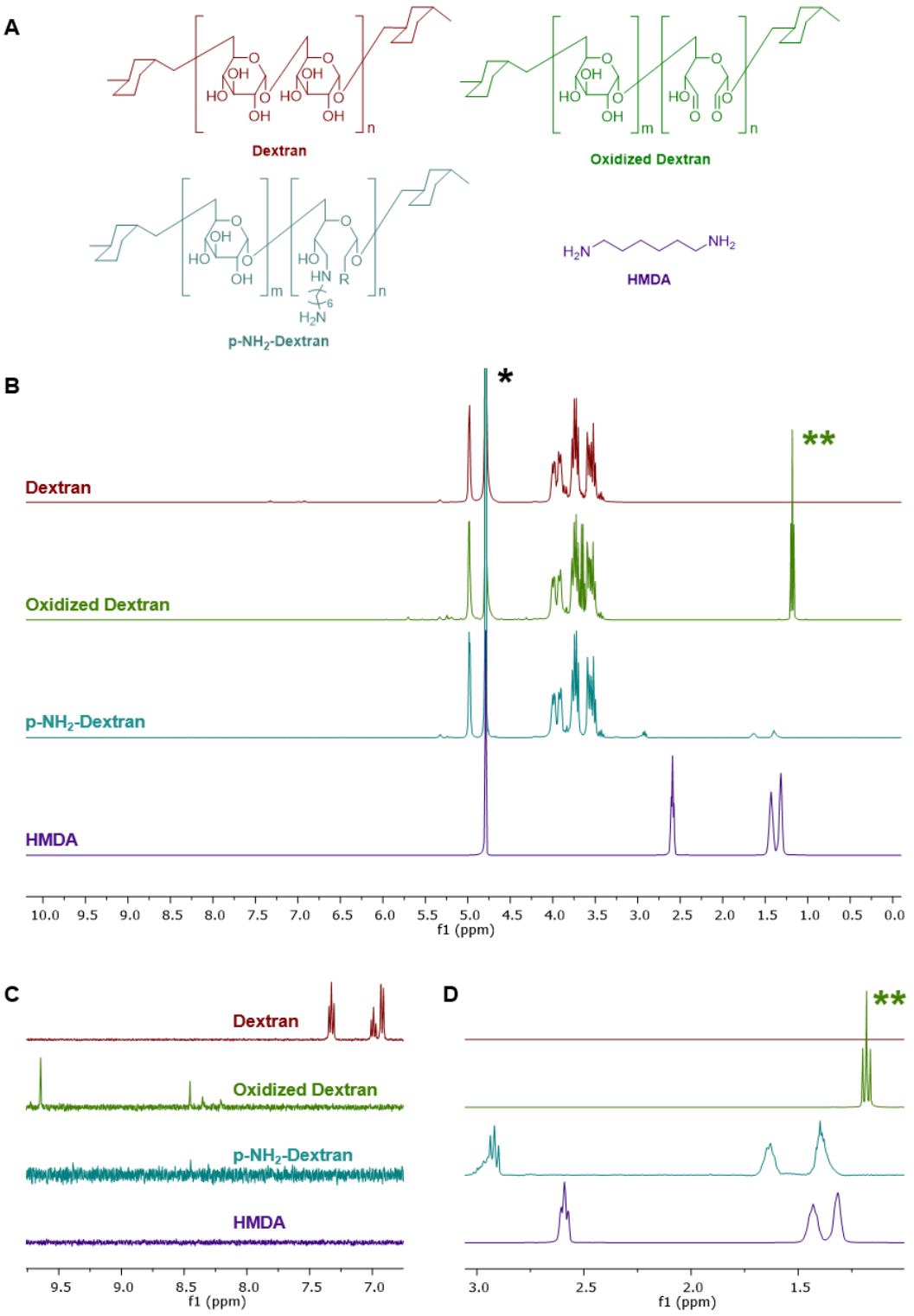

Figure 7.5 NMR characterization. **(A)** Molecular structures. ^{1}H NMR spectra of dextran (red), 30% oxidized dextran (green), p-NH_2-Dex (blue), and hexamethylenediamine (purple): **(B)** full spectra; **(C)** zoom on 6.75–9.75 ppm; **(D)** zoom on 1–3 ppm. The asterisks, * and **, denote solvent peaks for water and ethanol, respectively.

p-NH_2-Dex was conjugated to the Pdot surface by carbodiimide-mediated crosslinking between the amine groups along the dextran chain and surface carboxyl groups on the Pdot (Figure 7.2A). The presence of dextran on the Pdot surface was confirmed by the addition of Concanavalin A (ConA), a homotetrameric lectin that binds to internal glucosyl groups. ConA has four binding sites and may thus bind to multiple Pdots, causing aggregation. As shown in Figure 7.6, Pdots remained stable in colloidal suspension whereas Dex-Pdots aggregated in the presence of ConA, confirming the presence of dextran on the Pdot surface.

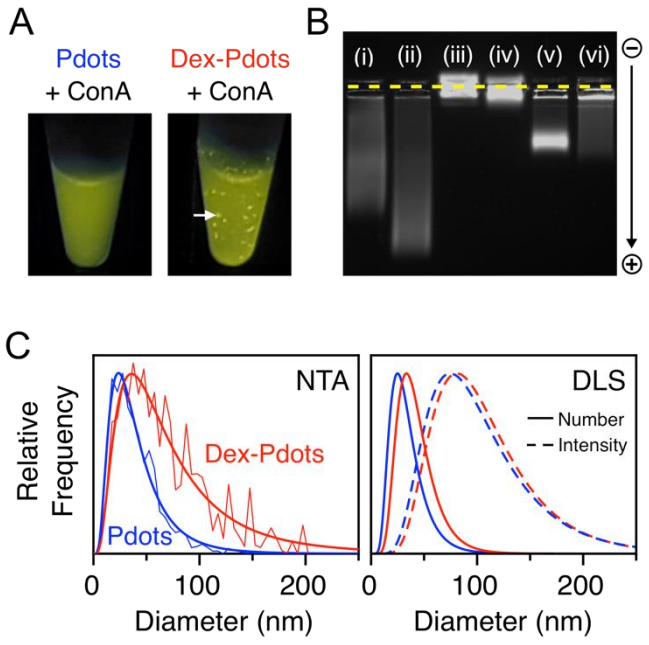

Figure 7.6 (A) Photographs of the fluorescence from Pdot and Dex-Pdot solutions 90 min after mixing with ConA. The photographs were taken under long-wave UV illumination (~365 nm). The arrow highlights one of the macroscopic aggregates. **(B)** Fluorescence image of an agarose gel (0.5% w/v) loaded with samples of (i) Pdots, (ii) Pdots + EDC, (iii) Pdots + p-NH_2-Dex + EDC, (iv) Pdots + p-NH_2-Dex without EDC, (v) Pdots + oxidized p-Dex + EDC, and (vi) Pdots + unmodified dextran + EDC. The location of the wells is shown as the dashed yellow line. Case (iii) is the formal preparation of Dex-Pdots. **(C)** Particle sizing: (Left) normalized fluorescence-mode NTA-derived size distribution and lognormal fit curves for Pdots (N = 1358 particles) and the corresponding Dex-Pdots (N = 968); (Right) DLS-derived size distributions for Pdots and the corresponding Dex-Pdots. Both intensity-weighted and number-weighted distributions are shown.

An additional test for dextran functionalization of the Pdots was a colorimetric assay with anthrone, which gave a positive result after purification to remove unconjugated dextran (Figure 7.7). The concentration of dextran in three replicate ~1 nM samples of Dex-Pdots was estimated via an assay with anthrone. Concentrated sulfuric acid dehydrates dextran to form a furfural product which condenses with anthrone to form a blue-green coloured complex whose concentration may be determined spectrophotometrically. A calibration curve was prepared using standard solutions of p-NH_2-Dex. The average number of p-NH_2-Dex per Pdot was estimated to be 5700, or 0.53 dextran chains per nm^2 assuming perfectly spherical nanoparticles and estimated average surface area of 10 800 nm^2 (accounting for the lognormal particle size distribution measured by NTA). This density of dextran per Pdot seems higher than plausible for purely covalent conjugation, where between 200–5000 dextran chains per Pdot would be expected for complete monolayer coverage, assuming dextran maintains a linear, extended conformation and a footprint of 45 nm^2 for dextran conjugated to the surface along its length and a footprint of 2 nm^2 for end-conjugated dextran. One consideration is that the NTA-derived Pdot concentration has a minimum uncertainty of at least ± 20%, although this uncertainty is likely not sufficient to account for the apparent density of dextran. Other considerations are that the anthrone assay is not quantitative in our hands, or that the dextran coating around the Pdots comprised both covalently bound dextran chains and non-covalently bound dextran chains. The latter were presumably strongly hydrogen bonded to covalently bound dextran chains. Alternatively, the result may be indication of multilayer formation (*cf.* monolayer), or some combination of all of these possibilities. Dextran has been known to form hydrogels at high concentrations in water [263], and the local concentration at the Pdot interface will be high. Large amounts of unconjugated dextran

as an outcome of inefficient purification were ruled because of the success of the TAC and ConA binding, which would be inhibited by a large excess of free dextran.

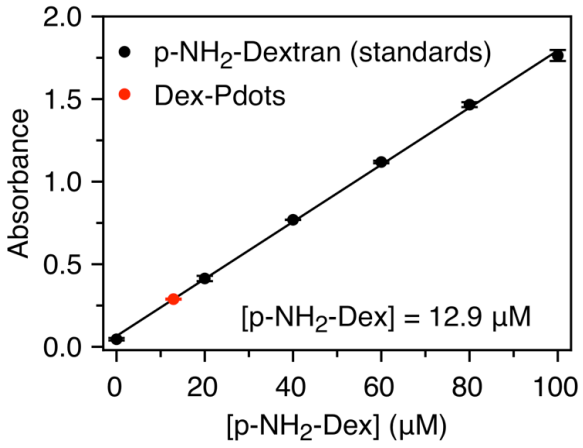

Figure 7.7 Calibration curve for the quantitation of dextran on Pdots via an anthrone-based colorimetric assay. Error bars (which fall within the diameter of the plotted data points) represent the standard deviation of three replicate measurements.

7.2.3 Solution-phase characterization

The functionalization of carboxylated Pdots with amine-modified dextran via carbodiimide chemistry was expected to decrease the anionic surface charge. Zeta potential measurements were done on a representative Pdot sample, where the zeta potential increased from –55 ± 3 mV to –8 ± 1 mV after dextran functionalization. Relative changes in size and surface charge were also assessed by gel electrophoresis, as shown in Figure 7.6B. The anionic Pdots migrated towards the anode as a streak, likely reflecting their size polydispersity. With the addition of EDC but not amine-modified dextran, the Pdots migrated slightly further as a streak. In contrast, the addition of both amine-modified dextran and EDC resulted in a dramatic decrease in mobility, with the Pdots

remaining near the sample well with slight cathodic mobility. The loss of anodic mobility was expected with the small increase in particle size and, more importantly, the decrease in zeta potential. The slight cathodic mobility likely arose from electroendosmosis within the gel. A similar migration pattern was observed when the amine-modified dextran was added to the Pdots without EDC, although distinguishable from the case with EDC. We hypothesize that electrostatic interactions between dextran-associated aminium groups and Pdot-associated carboxylate groups, and possibly the hydrophobic character of the HMDA side chains, contributed to this non-covalent interaction, which was confirmed by a ConA aggregation test (Figure 7.8). Pdots mixed with oxidized dextran and native dextran also showed migration that was altered versus Pdots alone and distinct from all other cases. Lane (v) shows that mixing Pdots with oxidized dextran resulted in a comparatively narrow band with anionic mobility, albeit less than the starting Pdot. Lane (vi) shows that mixing Pdots with native dextran resulted in some streaking, where the leading edge had a mobility similar to lane (v). More material was left at the edge of the well in lane (vi) versus lane (v). ConA aggregation tests, shown in Figure 7.8, confirmed that the dextran or modified dextrans in (iv), (v), and (vi) were associated with the Pdots. The significant retention of anionic mobility for sample (v) suggested that the carboxylate groups of the PSMA amphiphile were retained, which led us to hypothesize that an undetermined reaction occurred between the aldehyde groups of the oxidized dextran and the semiconducting polymer. The streaking for sample (vi), as well as the more limited aggregation with ConA when compared to samples (iv) and (v), suggests a weak interaction between native dextran and the Pdots, likely from some surfactant-like properties of the dextran.

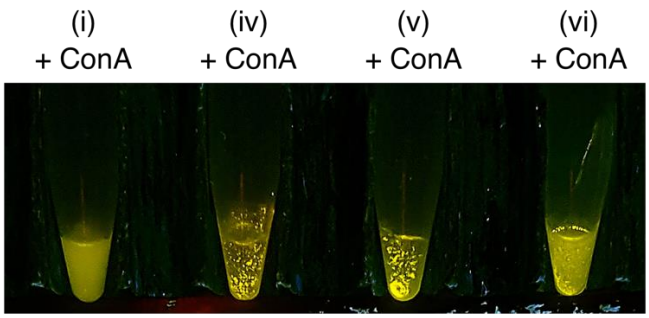

Figure 7.8 Photographs of the fluorescence from samples corresponding to (i), (iv), (v) and (vi) in Figure 7.6B taken 60 min after mixing with ConA. The illumination was long-wave UV (~365 nm).

The hydrodynamic sizes and concentrations of Pdots and Dex-Pdots in solution were determined by nanoparticle tracking analysis (NTA). For the representative sample data in Figure 7.6C, the starting Pdots had an average particle diameter of 51 (39) ± 23 nm compared to 59 (44) ± 28 nm for Dex-Pdots (written as mean (mode) ± 1 standard deviation of a lognormal distribution). For measurement of the same batch by number-weighted dynamic light scattering (DLS), the starting Pdots were measured as 33 (24) ± 16 nm in diameter whereas the Dex-Pdots had an average diameter of 40 (31) ± 18 nm. For intensity-weighted DLS, the corresponding diameters were 104 (74) ± 52 nm for Pdots and 107 (81) ± 49 nm for Dex-Pdots. Relative to NTA and number-weighted DLS measurements, larger sizes were expected from intensity-weighted DLS measurements because of its bias toward larger particles.

More generally, there was considerable batch-to-batch variation from both the nanoprecipitation method for Pdot preparation and from coupling dextran to the Pdot surface. Compared to Pdots, the Dex-Pdots showed increases in average diameter that ranged from 2–20 nm and 2–37 nm (as measured by scattering- and fluorescence-mode NTA, respectively) across multiple batches.

Regardless of this batch-to-batch size variation, all batches of Dex-Pdots showed the same qualitative behaviour (*e.g.*, large mobility shifts on agarose gels, aggregation with ConA).

7.2.4 Particle imaging

Dex-Pdots were further characterized by transmission electronic microscopy (TEM) and atomic force microscopy (AFM), with representative images shown in Figure 7.9. TEM images revealed that the Pdots were approximately spherical in shape and had an average dehydrated diameter of 30 ± 7 nm (± 1 standard deviation). The Dex-Pdots retained the approximately spherical morphology of the original Pdots and had an average dehydrated diameter of 33 ± 13 nm. The average diameters are statistically indistinguishable, indicating that the addition of the dextran surface coating did not significantly change the size or particle morphology of the Pdot core. This result was consistent with the expected small thickness of the dextran layer relative to the overall size of the particle, native dextran's minimal contrast in TEM, and the dehydration of the samples.

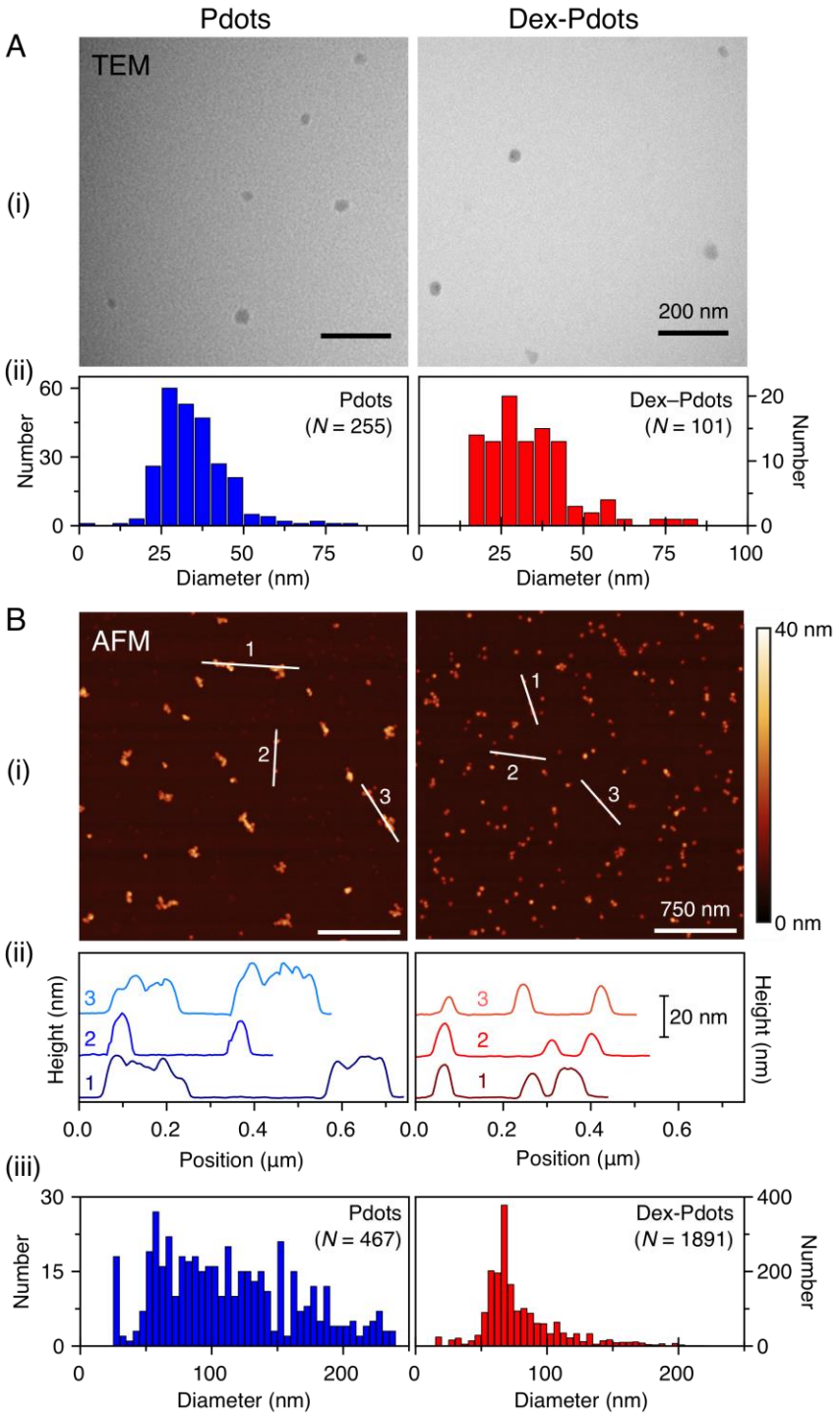

Figure 7.9 (A) TEM characterization of Pdots and Dex-Pdots: (i) TEM images; (ii) diameter histograms from TEM imaging. **(B)** AFM characterization of Pdots and Dex-Pdots: (i) topography images of the particles on mica; (ii) selected height profiles for the lines indicated in the images; and (iii) diameter histograms from AFM imaging.

AFM images of the Pdots showed large, irregularly shaped aggregates with mean diameters of 116 ± 56 nm. Although the Pdots were stable in solution, the particles aggregated together on the substrate and lost their spherical morphology upon drying. Conversely, the Dex-Pdots did not aggregate (mean diameter of 80 ± 32 nm) and retained a morphology consistent with spherical particles upon drying (notwithstanding some flattening of the particles), indicating that the dextran functionalization provided structural stability upon solvent removal. Larger diameters were expected for AFM compared to TEM because of the loss of resolution associated with the width of the AFM tip. Representative height traces for Pdots and Dex-Pdots are shown in Figure 7.9Bii, and diameter histograms are shown in Figure 7.9Biii. Height traces for the Dex-Pdots had symmetric peak shapes, consistent with individual particles, whereas traces for the Pdots had multiple overlapping peaks, indicating the presence of aggregates. The heights of the Dex-Pdot traces were also ~10 nm shorter than those for the Pdots, further supporting the aggregation hypothesis.

7.2.5 Fluorescence properties

Optically, the addition of a dextran coating did not alter the peak positions or shapes of absorbance and fluorescence excitation and emission spectra of the Pdots (Figure 7.3), nor alter the rate of photobleaching, but did decrease the quantum yield and the fluorescence lifetime (Figure 7.10). For two representative samples, upon conjugation of dextran to the Pdot surface, the quantum yield decreased by *ca.* 30–40% of its pre-dextran value (typically between 0.2–0.7) and the amplitude-weighted average fluorescence lifetime decreased by *ca.* 20–40% of its pre-dextran value (typically 500–1000 ps). The exact cause of these changes is not apparent, but presumably arose from a change in local environment next to the semiconducting polymer core after dextran

functionalization, physicochemical changes in the Pdot during the dextran functionalization reaction and purification steps, or some combination of these hypotheses.

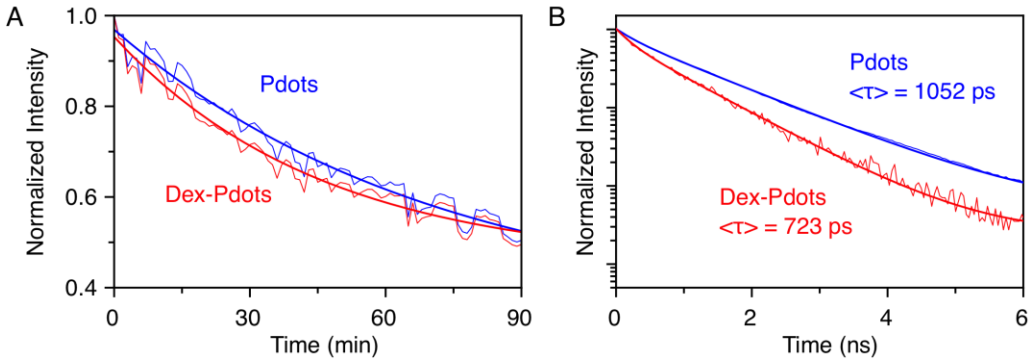

Figure 7.10 (A) Photobleaching curves for F8BT Pdots and the corresponding Dex-Pdots. **(B)** Representative fluorescence decay curves for F8BT Pdots and the corresponding Dex-Pdots. The amplitude-weighted average fluorescence lifetimes are indicated.

7.2.6 Particle stability

The stabilities of Pdots and Dex-Pdots in phosphate-citrate buffer ranging from pH 3.0 to 7.3 were measured over a period of 7 days, tracked by measuring the absorbance in solution (aggregates were centrifuged out of solution and were not measured), as shown in Figure 7.11. Photographs of the microcentrifuge tubes after dilution (0 days) and after 7 days are shown in Figure 7.12. Within minutes of mixing, the Pdots in all buffer solutions began to destabilize, as indicated by fluorescent residue on the walls of the microcentrifuge tube above the solution level and the loss of apparent fluorescence intensity. The extent of destabilization increased with decreasing pH because more of the surface carboxyl groups became protonated at lower pH, reducing the overall surface charge

and inter-particle repulsion. Conversely, Dex-Pdots were initially stable across all solutions. After 7 days, the Pdots in all buffer solutions showed increased destabilization. Although the Dex-Pdots showed some destabilization in the buffer solutions, it was significantly less than the Pdots. Interestingly, Dex-Pdots in water were less stable than the Dex-Pdots in buffer and also less stable than the Pdots in water.

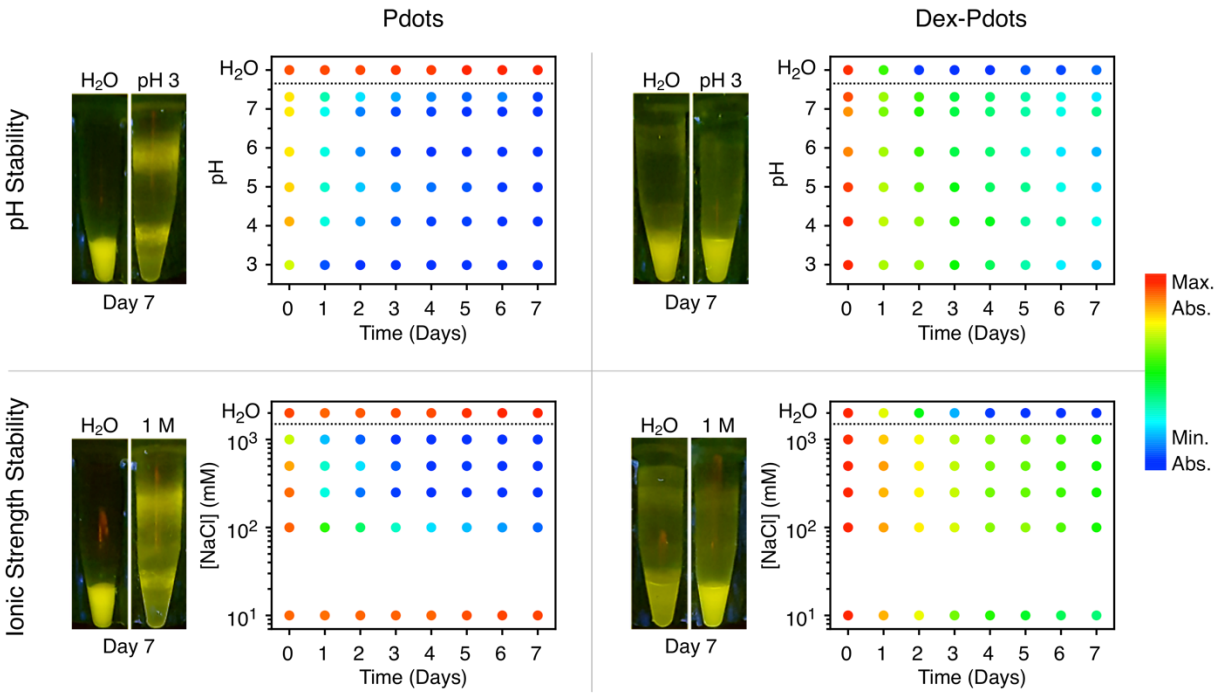

Figure 7.11 Colloidal stability tests on Pdots and Dex-Pdots dispersed in aqueous buffers at different pH and in aqueous sodium chloride solutions of different ionic strength, both at room temperature. Water is used as a reference. Photographs are of solutions with ~400 pM Pdots after 7 days in water, pH 3 phosphate-citrate buffer, and 1.0 M NaCl (aq). (The fluorescence from the Pdots appears more yellow in the photographs than it does by eye. The color balance was adjusted uniformly across all photographs to remove a false blue-light background from scattered and reflected UV light. Photographs for all solutions can be found in Figure 7.12.) Stability was tracked semi-quantitatively by monitoring the absorbance of the supernatant of each sample at daily intervals. More aggregation correlated with lower absorbance.

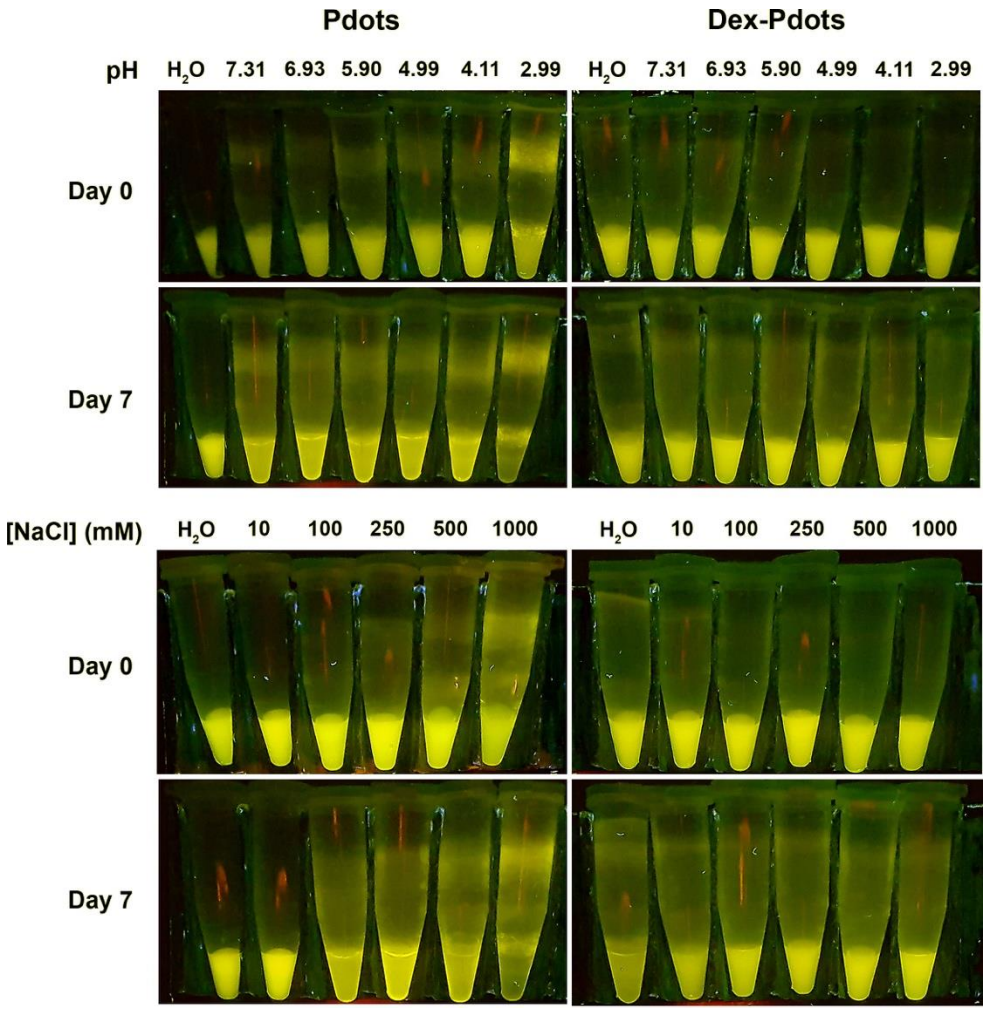

Figure 7.12 Photographs of ~400 pM Pdots and Dex-Pdots incubated at room temperature in solutions of varying pH and ionic strength under long-wave UV excitation (~365 nm). The fluorescence from the Pdots appears more yellow in the photographs than it does by eye. The color balance was adjusted uniformly across all photographs to remove a false blue-light background from scattered and reflected UV light.

Similar trends were observed for Pdots and Dex-Pdots in NaCl (aq) solutions ranging from 10–1000 mM (Figure 7.11 and Figure 7.12). Upon addition to solutions with high ionic strengths, the Pdots began to destabilize whereas Dex-Pdots were initially stable in water and across all ionic strengths. After 7 days the Pdots continued to destabilize when the ionic strength was ≥ 100 mM

but were stable in water and 10 mM NaCl (aq). Dex-Pdots showed some gradual destabilization in all conditions but their overall stability was significantly greater than the Pdots when the ionic strength was ≥ 100 mM. Dex-Pdots were less stable than the Pdots in water and 10 mM NaCl (aq). The apparent sensitivity of Dex-Pdot colloidal stability to ionic strength, both with buffer and NaCl (aq), is discussed later.

7.2.7 Immunoassay

Dex-Pdots were used as a fluorescent label in a proof-of-concept FLISA for human EPO, a glycoprotein that regulates red blood cell formation. Dex-Pdots are a potentially ideal material for such an application because of their high brightness, and because the dextran coating was expected to reduce non-specific binding. The assay was based on a commercial enzyme-linked immunosorbent assay (ELISA) kit for EPO, where Dex-Pdot-antibody conjugates were substituted for a horseradish peroxidase (HRP) conjugate and its colorimetric substrate. An anti-dextran/anti-EPO TAC complex was used to prepare the Dex-Pdot antibody conjugates. The assay is done in a 96-well plate, with the molecular binding format illustrated in Figure 7.13A.

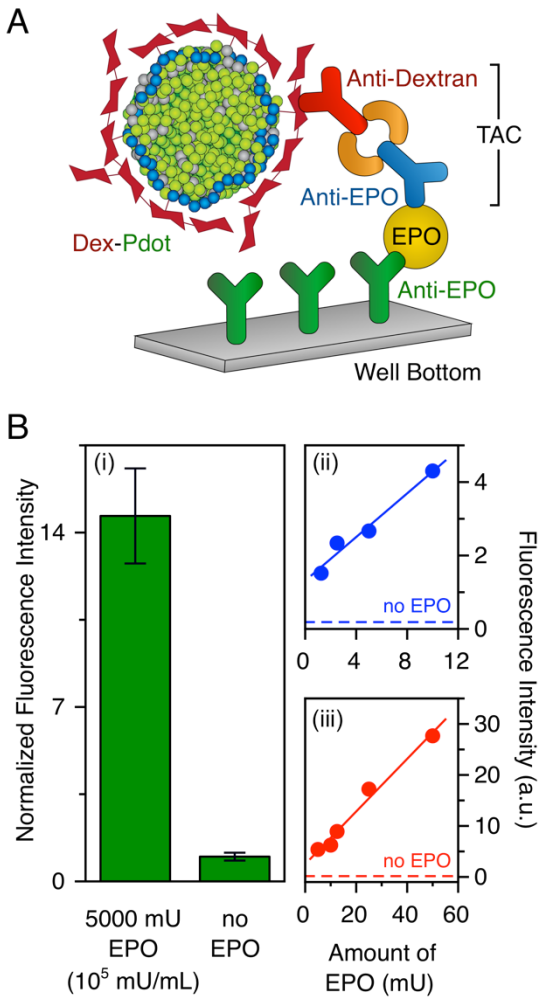

Figure 7.13 Model FLISA using Dex-Pdots conjugated with an anti-EPO TACs. **(A)** Illustration of the assay format (not drawn to scale). **(B)** Proof-of-concept assays. (i) Fluorescence signal contrast between a negative control sample (no EPO; signal normalized to unity) and 5000 mU EPO. Error bars are the standard deviation of three replicates. Calibration plots for EPO concentrations between (ii) 1.3–20 mU and (iii) 5–50 mU (see Figure 7.15 for 31–500 mU). Dashed lines represent the signal levels for negative control samples. The y-axes between (ii) and (iii) are not directly comparable.

To test the assay, calibration curves across three ranges of EPO amounts were measured: 31–500 mU, 5–50 mU, and 1.3–20 mU. For the lowest EPO concentrations in these calibrations, contrast ratios between 8:1 and 34:1 were obtained between the fluorescence signals for samples with and without EPO, indicating selective binding between the EPO and anti-EPO component of the Pdot-

conjugated TAC. Moreover, for 5000 mU of EPO, the Pdot emission was visible by eye in the well plate (Figure 7.14), highlighting the excellent brightness of the Pdots. Calibration curves for the 1.3–20 mU and 5–50 mU EPO ranges are shown in Figure 7.13B (and in Figure 7.15 for the 31–500 mU). A linear trend was observed in each case, confirming that the assay is quantitative. Relative standard deviations of the fluorescence signals were *ca.* 10–15%.

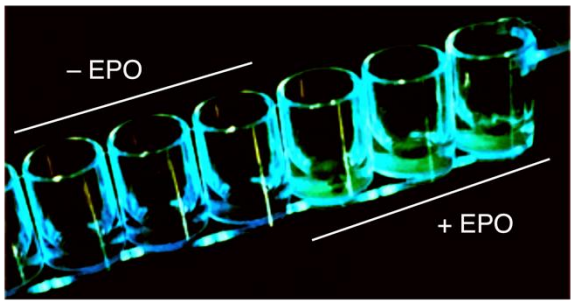

Figure 7.14 Photograph of a well-plate strip showing visible contrast in the presence (+) or absence (–) of 5000 mU EPO. The digital image has been processed (*e.g.,* contrast, brightness, color balance) to make clear the contrast seen by eye. All regions of the image were processed equivalently.

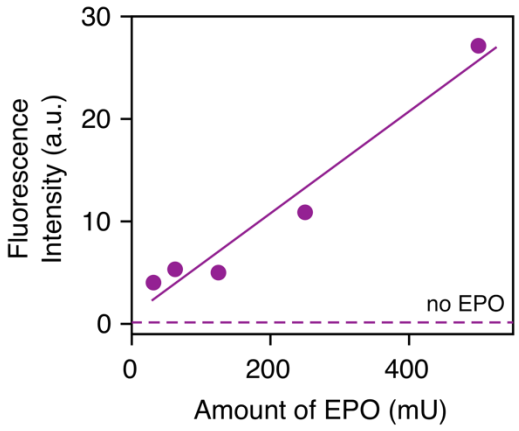

Figure 7.15 Immunoassay calibration curve for 31–500 mU EPO.

7.2.8 Cell labeling and imaging

TAC conjugates of Dex-Pdots were used to immunolabel fixed SK-BR3 cells, which overexpress the HER2 antigen. The TAC incorporated anti-dextran and anti-HER2 antibodies, as illustrated in Figure 7.16A. Representative images of cells are shown in Figure 7.16B. The cell nuclei were stained with DAPI for reference. Pdots showed significant non-specific binding to cells, with a contrast ratio of only 1.4 (± 0.2):1 for the F8BT fluorescence signal from cells exposed to Pdots with and without TAC, where the TAC was adsorbed to the Pdots. The Dex-Pdots showed brighter labeling of the cells with TAC, and a much-improved contrast ratio of 5.7 (± 0.4):1, reflective of both lower non-specific binding and higher specific binding. The latter was presumably a result of more effective conjugation of antibody. Emission spectra acquired from the image fields of view (Figure 7.17) showed the characteristic emission band of F8BT Pdots, suggesting that the Pdots were solely responsible for the measured fluorescence signal. These experiments were replicated using orange-emitting CNMEHPPV/PSMA Pdots (Figure 7.18), which yielded contrast ratios of 9.5 (± 2.2):1 for Dex-Pdots (with and without TAC) and 1.3 (± 0.5):1 for Pdots (with and without TAC), once again indicating higher specific binding and lower non-specific binding with Dex-Pdots. Figure 7.16C summarizes the contrast ratio data for both colours of Pdot and Dex-Pdot.

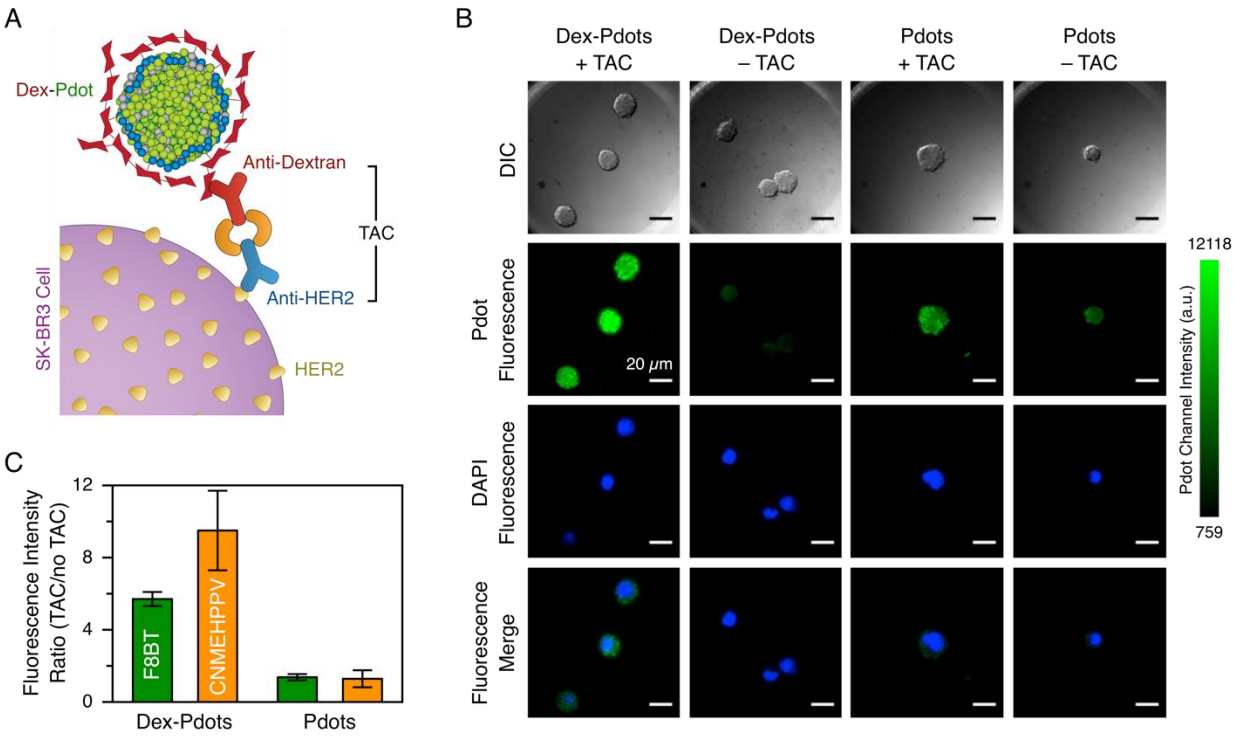

Figure 7.16 (A) Illustration of the cell immunolabeling strategy. **(B)** Differential interference contrast (DIC) and epifluorescence microscopy images of fixed SK-BR3 cells labelled with Pdots and Dex-Pdots. Scale bars = 20 µm. **(C)** Contrast ratios for fixed SK-BR3 cells labelled with Pdots and Dex-Pdots, with and without TAC, for both F8BT- and CNMEHPPV-based materials.

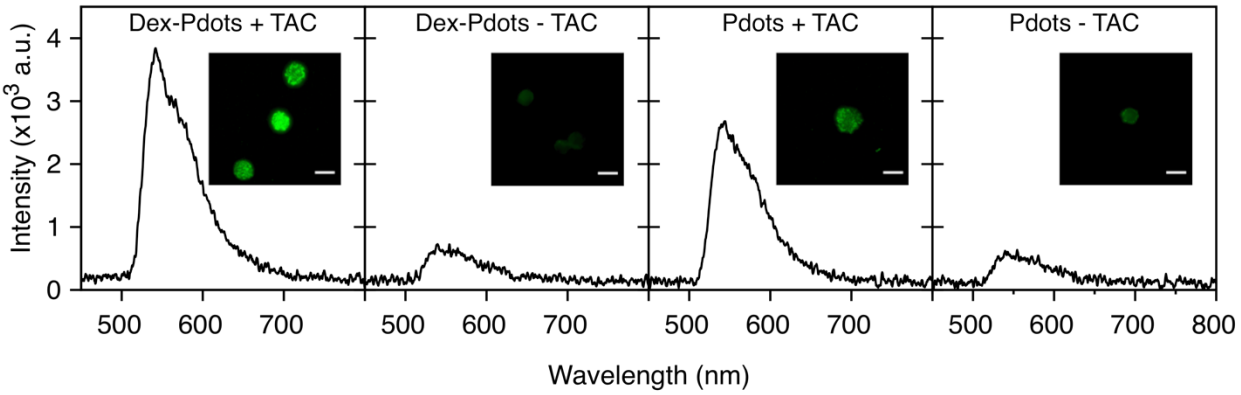

Figure 7.17 Fluorescence emission spectra recorded from the same sample regions as the fluorescence images in Figure 7.16 (reproduced as insets; scale bar = 20 µm). The spectra confirmed that Pdot fluorescence was being measured (*i.e.,* not cell autofluorescence).

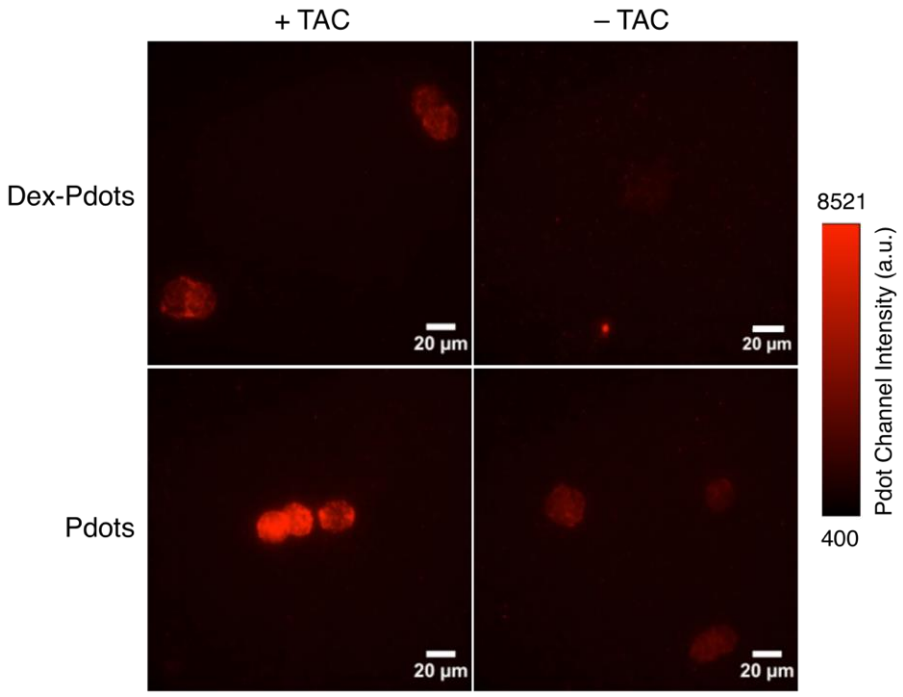

Figure 7.18 Labeling of SK-BR3 cells with Pdots and Dex-Pdots based on CNMEHPPV semiconducting polymer.

7.3 Discussion

Our results show that dextran functionalization confers several benefits to the Pdots: improved colloidal stability at physiologically relevant conditions, simple and effective non-covalent antibody conjugation, and reduced non-specific binding. It is possible that the magnitude of these benefits will increase with further optimization of the dextran functionalization process. Possibilities include, but are not necessarily limited to, the molecular weight of the dextran, the extent of oxidation by periodate, and the length of the amine terminated linker. With respect to the equivalents of amine terminated linker, we used a large excess of HMDA relative to the maximum number of aldehyde groups present after oxidation. The goal was to maximize the number of pendant primary amine groups by minimizing the probability that both ends of an HDMA molecule

coupled to the same dextran chain. Although not yet evaluated, optimization of dextran molecular weight and its extent of oxidation may be a balancing act between retaining the properties and advantages of native dextran and most effectively crosslinking an outer shell around the Pdot.

The presented strategy for dextran functionalization was not our only attempt at Dex-Pdots. Efforts to synthesize Pdots using a dextran-based amphiphile (long alkyl chains grafted analogously to HMDA) instead of PSMA were unsuccessful. Carbodiimide-mediated grafting of dextran with a HMDA modification at its reducing end (*i.e.,* a single linker at its terminus rather than multiple linkers along its length) was also attempted, but was likewise unsuccessful, causing destabilization of the Pdots in the form of aggregation and adhesion of the F8BT to the vessel walls. For both cases, we hypothesize that the very high hydrophilicity of the dextran was the cause. The driving force for dextran's full solubilization in water overcame the hydrophobic interactions that would have otherwise kept it associated with the F8BT through the PSMA, putatively resulting in F8BT-only nanoparticles without the stabilization of an amphiphile. Support for this hypothesis comes from the colloidal stability data in Figure 7.11 and Figure 7.12, where Dex-Pdots had better stability than Pdots at high ionic strength but worse stability at low ionic strength. Uncharged hydrophobic molecules, such as the styrene units of the PSMA amphiphile, tend to have better solubility in aqueous solutions of lower ionic strength. PSMA-conjugated dextran may have therefore been able to "pull" some of the PSMA from the F8BT at low ionic strength, but not at higher ionic strength. Overall, the presented strategy for dextran functionalization was likely successful because of the multiple HDMA modifications and links to the Pdot per dextran chain.

As noted earlier, use of TACs for conjugation of antibodies to Dex-Pdots is advantageous in that it is spontaneous, not subject to competing hydrolysis, and positions the anti-target antibody in a productive orientation for binding. These features are in contrast to carbodiimide-mediated conjugation of antibodies directly to the Pdots, which offers less control over the number of antibodies per particle because of competing hydrolysis, and less control over antibody orientation because of the multitude of lysine residues that may react. Similar limitations apply to conjugation of antibodies via adsorption. Although carbodiimide chemistry was used for functionalization of Pdots with dextran, the limitations of this chemistry are preferable at this step rather than antibody conjugation. The dextran is utilized in large excess and, since a majority of the glucosyl monomers are unmodified, the precise number and location of links to the Pdot is unlikely to significantly affect downstream TAC binding.

Another anticipated advantage of dextran functionalization was reduced non-specific interactions, which was borne out in the cell immunolabeling experiments in Figure 7.16 and Figure 7.18. We suggest that the reduction in non-specific interactions was not only from the inherent low-fouling character of dextran, but also from the dextran functionalization stabilizing the outer structure of the Pdot. In the AFM experiments in Figure 7.9, and in other handling of Pdot materials, we have sometimes observed what appears to be surface-induced unfolding of Pdots and adsorption of the F8BT onto that surface. The dextran-functionalization is a putative hindrance to surface stimuli that induce this behavior, but likely not fully preventative as we found in the FLISA that non-specific background signal from Dex-Pdots increased with increasing incubation time (data not shown). The assay time was limited to $\leq$ 2 h to avoid this behavior.

The FLISAs in Figure 7.13 and Figure 7.15 were intended as proof-of-concept for TAC binding. Aside from the abovementioned assay time, only the concentration of Pdots and the number of antibodies per Pdot were partially optimized for the different concentration ranges tested. Future work may benefit from additional optimization of these and other parameters (*e.g.*, Pdot size). Even with minimal optimization, the assay was able to detect physiologically relevant concentrations of EPO (normal median levels are 6–10 mU/mL [264], but can be elevated by 2–3 orders of magnitude by some pathologies). Detection was possible in 2 h (*cf.* 3 h for the commercial ELISA kit [265]) and eliminated the need for several steps and reagents associated with the ELISA protocol. The detection of as little as ~ 1 mU without amplification is a testament to the excellent brightness of the Pdots, affirming their value for bioanalysis and imaging.

7.4 Conclusions

This chapter has presented a method for functionalization of Pdots with dextran and shown that the resulting Dex-Pdots are promising materials for bioanalysis and imaging. The dextran functionalization did not substantially increase the size of the Pdots, largely retained the spectral properties and brightness of the Pdots, and also enhanced particle stability over a range of pH, at higher ionic strength, and toward surface-induced unfolding. It also reduced non-specific binding and enabled immunoconjugation via TACs, the utility of which was demonstrated through a proof-of-concept FLISA and labeling of HER2-positive SK-BR3 cells. Dextran functionalization is a promising strategy for overcoming some the current limitations of Pdots, such as modest stability, tendency toward non-specific binding, and limited bioconjugate chemistries.

7.5 Experimental methods

7.5.1 Materials

Dextran from Leuconostoc spp. (M_r ~6000 Da), sodium (meta)periodate, sodium cyanoborohydride, hexamethylenediamine (HMDA), Concanavalin A (from Canavalia ensiformis (Jack bean)) and anthrone were from Sigma-Aldrich (Oakville, ON, Canada).

7.5.1.1 Tetrameric Antibody Complex (TAC) assembly

TACs were prepared using the components from an EasySep™ Human "Do-It-Yourself" Positive Selection Kit II immunomagnetic positive selection cell isolation kit (STEMCELL Technologies, Vancouver, BC, Canada). The buffer used for TAC assembly was PBS buffer (pH 7.2, 1.54 mM KH_2PO_4, 2.71 mM Na_2HPO_4, 155 mM NaCl, Ca^{2+}/Mg^{2+} free) (GIBCO Life Technologies, supplied by ThermoFisher, Waltham, MA). The anti-target antibodies are noted under the sub-headings for their application.

7.5.1.2 Immunoassay

Fluorescence-linked immunosorbent assays (FLISAs) for the detection of human erythropoietin (EPO) were done using a 96-well microtiter EPO immunoaffinity isolation plate (coated with a high-affinity monoclonal anti-EPO antibody) and selected buffer components from a commercial EPO ELISA kit (STEMCELL Technologies). The EPO samples were prepared from lyophilized human recombinant EPO (rhEPO) (STEMCELL Technologies) by reconstituting the lyophilized protein in sterile water (5 μg/25 μL) and diluting to 1.0 mL with Buffer B from the ELISA kit (PBS buffer with additives). The TAC was prepared using a mouse monoclonal anti-EPO antibody

(EPO-16, clone 16F1H11, mouse monoclonal antibody to human erythropoietin) (STEMCELL Technologies).

7.5.1.3 Cell immunolabeling

Anti-HER2 antibody (NBP2-32863) from Novus Biologicals (Centennial, CO) was used for TAC assembly. The human breast cancer cell line SK-BR3 (HTB-30) was from ATCC (Manassas, VA).

7.5.2 Synthesis of p-NH_2-Dex

Dextran (1.98 g, ~331 µmol dextran, ~11.0 mmol glucose monomer) was dissolved in 15 mL of water and was partially oxidized by reaction with sodium (meta)periodate (0.716 g, 3.35 mmol) overnight at room temperature. The extent of oxidation was controlled stoichiometrically with the amount of periodate added and was equivalent to no more than 35% of the glucose monomers in the dextran chain. The product was purified by dialysis against water for 72 h, or by repeated precipitation with ethanol, then dried under vacuum or by lyophilization. Oxidized dextran (1.6 g, 260 µmol dextran, ~8.8 mmol glucose monomer) was dissolved in 30 mL water and a 16-fold excess of HMDA (9.93 g, 85.5 mmol) was added. The reaction was stirred at room temperature for 2 h, followed by the addition of sodium cyanoborohydride (0.44 g, 7.1 mmol). The reaction was stirred overnight at room temperature, and the product purified as above. The reaction was performed at various scales from tens of milligrams up to ~5 g of dextran, but the molar ratios of all reagents remained approximately constant. Scheme 7.1 shows the synthetic steps for the preparation of p-NH_2-Dex.

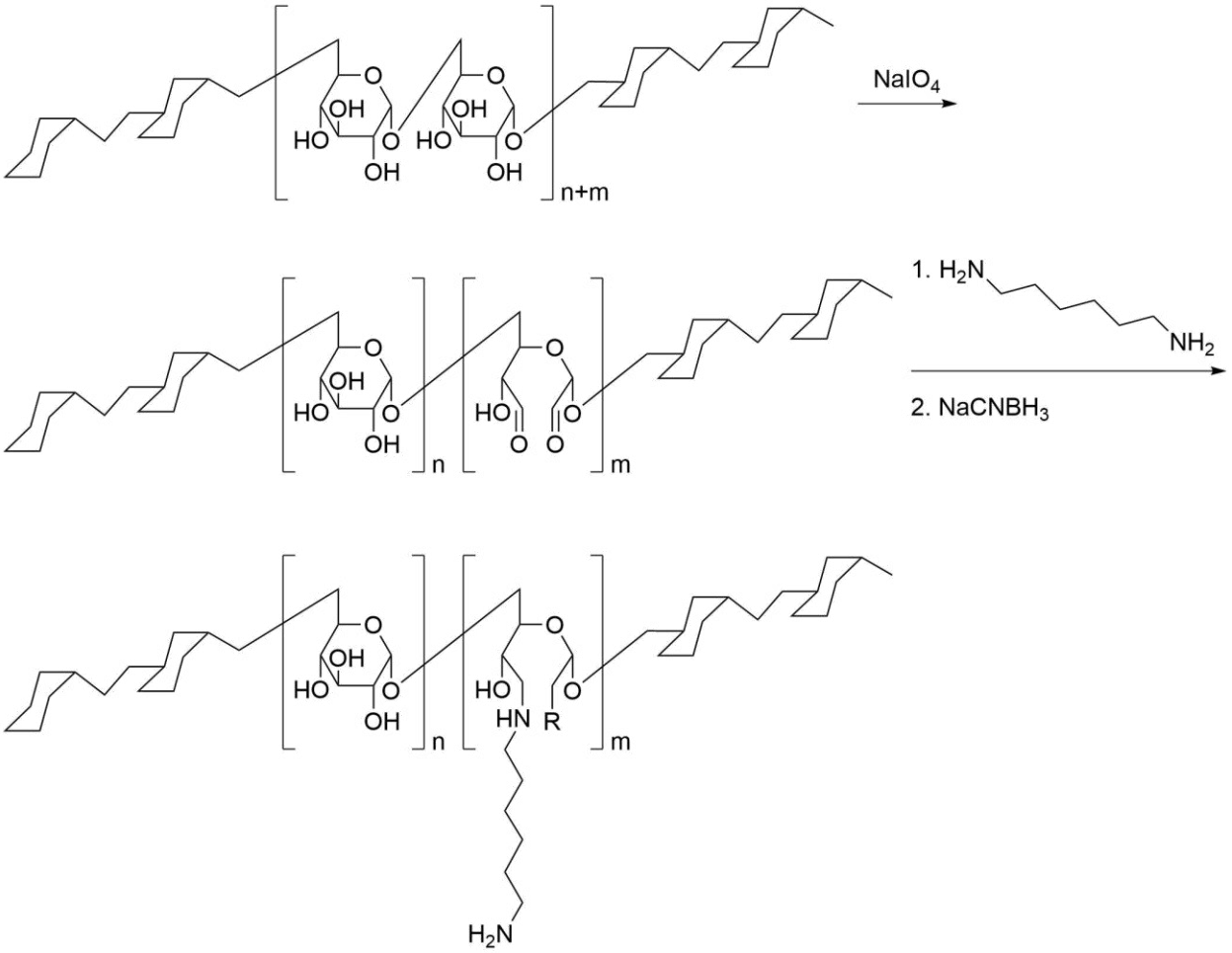

Scheme 7.1. Synthesis of p-NH_2-Dex. The R group on p-NH_2-Dex may be another hexamethylenediamine (HMDA) modification, an unreacted aldehyde (or the corresponding hydrate), or have cyclized with the secondary amine of the shown HMDA modification.

7.5.3 IR and NMR characterization of modified dextran

ATR-FTIR absorption spectra were measured with a Frontier FT-IR (Perkin Elmer, Waltham, MA). Proton NMR spectra were measured with an AV III HD 400 MHz spectrometer (Bruker, Billerica, MA). All samples were prepared in deuterium oxide. Dextran NMR samples were prepared at a concentration of ~20 mg/mL. For the dextran samples, at least 32 scans were collected with a delay time of 4 s. For HMDA, 16 scans were performed with a delay time of 1 s.

7.5.4 Functionalization of Pdots with Dextran

p-NH_2-Dex (~10 mg, 1.6 μmol) was dissolved in a 1.0 mL aqueous solution of Pdots (at the concentration from synthesis, *ca.* 0.2–0.8 nM) and 20 μL of HEPES buffer (1.0 M, pH 7.3) was added. The solution was mixed and 20 μL of freshly-prepared EDC solution (10 mg/mL in water, 1.3 μmol) was added. The solution was mixed for 4 h in the dark and purified by spin filtration (100 kDa MWCO).

7.5.5 Concanavalin A (ConA) assay

A 2.0 mg/mL solution of ConA in 25 mM HEPES buffer (pH 7.3) with 2.0 mM Ca^{2+} and 2.0 mM Mn^{2+} was prepared. HEPES buffer (2.5 μL, 1.0 M, pH 7.3) was added to 100 μL of Pdots or Dex-Pdots. ConA solution (10 μL) was added and the solutions were mixed by inversion. Solutions were incubated at room temperature for 60–90 min and were briefly centrifuged before photographs were taken.

7.5.6 Colloidal stability tests

Pdots and Dex-Pdots (75 μL, ~800 pM) were added to 75 μL of phosphate-citrate buffer (between pH 3–7) or NaCl solution (10–1000 mM in water), vortex mixed, and briefly centrifuged before UV-visible absorption measurements and photographs were taken. The solutions were then left at room temperature in the dark and absorbance measurements and photographs were taken every 24 h for 7 days under long-wave UV illumination.

7.5.7 Anthrone colourimetric assay

A concentrated solution of p-NH_2-Dex in 0.10 M NaOH (aq) was further diluted in 0.10 M NaOH to produce standard solutions with final concentrations between 0–100 μM, and the standard solutions were sonicated for 10 min. After cooling in an ice bath for 10 min, 1.0 mL of 0.75% w/w anthrone in concentrated sulfuric acid was added and the solutions were mixed by inversion. The solutions were heated in a 110 °C dry bath for 10 min and then cooled in an ice bath for 30 min. UV-visible absorption spectra were recorded immediately, using 572 nm (the absorbance maximum) as the analytical wavelength to construct a calibration curve. Dex-Pdots were concentrated to ~1 nM by spin filtration (100 kDa MWCO) and aliquots prepared by the same procedure as above. The concentration of dextran in the Dex-Pdot aliquots was determined via comparison to the calibration curve. The concentration of Dex-Pdots was then determined by nanoparticle tracking analysis. This procedure is adapted from ref. [266].

7.5.8 Immunoassay

Dex-Pdots were used as a label in a FLISA for human EPO via specific conjugation to a TAC with anti-dextran and anti-EPO.

7.5.8.1 Preparation of the Anti-EPO TAC

A stock solution of anti-EPO TAC (15 μg/mL anti-EPO) was prepared in PBS buffer according to the manufacturer's protocol supplied with the EasySep™ "Do-It-Yourself" Positive Selection Kit. Briefly, 15 μL of a 1.0 mg/mL solution of mouse anti-EPO antibody was mixed with 100 μL of Component A and 100 μL of Component B, in this order. The sample was then diluted to 1.0 mL

using PBS buffer and incubated at 37 ˚C overnight. The TAC anti-EPO complex was passively cooled to room temperature for use in experiments or stored at 4 ˚C until needed.

7.5.8.2 Preparation of the TAC-Dex-Pdot conjugates

Stock solutions of TAC-Dex-Pdot conjugates were prepared immediately before use. Solutions of TAC-Dex-Pdot conjugates were prepared in 1.7 mL microcentrifuge tubes by mixing Pdots in Buffer B (PBS-based) with TAC anti-EPO complexes in PBS buffer. The solutions stood at room temperature for 30 min before mixing with EPO standards in the 96-well EPO immunoaffinity isolation plate from the commercial ELISA kit (*vide infra*). The concentration of TAC-Dex-Pdot conjugates varied according to the concentration of EPO to be detected in order to minimize non-specific adsorption of the conjugates. Table 7.1 lists the amounts and ratios of TAC:Dex-Pdot conjugates used for the FLISAs with different EPO concentration ranges.

Table 7.1. Pdot and TAC amounts used to form Pdot-TAC conjugates.

Pdots (fmol)	TAC (fmol)	TAC:Pdot ratio	EPO (mU)	[EPO] (mU/mL)
21	300	~15:1	31–500	626-10 000
22	300	~14:1	5–50	100-1 000
6.6	50	~7.5:1	1.3–20	25-400

7.5.8.3 Immunoassay

Starting from the commercial EPO ELISA kit, the Pdot EPO FLISA was tested using 14 samples ranging from 25–100 000 mU/mL (*ca.* 310 amol–124 pmol added per well). The EPO samples for the assay were prepared by serial dilution of an EPO protein stock solution (200 μg/mL or 1 100 000 mU/mL) in Buffer B (from kit). For performing the immunoassay, 25 μL of Buffer A

(from kit) was added to each well, followed by 50 μL of EPO sample. The plate wells were covered with an adhesive cover, and the EPO samples were incubated in the wells for 30 min at room temperature. After the 30 min incubation period, Pdot-TAC conjugates were added to the wells, followed by incubation for ~1.5 h. After incubation, the wells were washed twice with 150 μL of Wash Buffer (from kit). Either full PL spectra (490–750 nm) or single-point PL intensities at 542 nm, both using an excitation wavelength of 442 nm, were measured. EPO-positive samples, EPO-negative samples, and control samples to subtract background (from the plate well) were also measured.

7.5.8.4 Data analysis

For immunoassays with tested EPO concentration ranges between 100–100 000 mU/mL, the background-subtracted Pdot emission intensity at the emission maximum (542 nm) was used as the analytical signal. For immunoassays with tested EPO concentration ranges between 25–400 mU/mL, the background-subtracted sum of PL intensities from 490–750 nm was used as the analytical signal.

7.5.9 Cell labeling and imaging

Dex-Pdots were used to fluorescently label fixed SK-BR3 cells using the methods described in the follow subsections.

7.5.9.1 Cell culture

SK-BR3 cells were cultured in a humidified incubator with 95% air/5% CO_2 at 37 °C. The culture medium was McCoy's 5A (GE Healthcare, Chicago, IL) supplemented with 10% v/v fetal bovine

serum and 1× antibiotic and antimycotic (ThermoFisher). Cells were cultured in T25 flasks and sub-cultured every 5–7 days.

7.5.9.2 Preparation of (Anti-HER2-TAC)-Dex-Pdot Conjugates

A 15 µg/mL stock solution of TAC with anti-HER2 antibody was prepared in PBS buffer by following the manufacturer's protocol for the Do-It-Yourself Positive Selection Kit II. Briefly, 15 µg of mouse anti-HER2 antibody (NBP2-32863; Novus Biologicals, Centennial, CO, USA) were mixed with 100 µL of Component A and 100 µL of Component B (from kit). The sample was incubated overnight at 37 ˚C. The TAC-anti-HER2 complex was then diluted to 1.0 mL with PBS buffer and stored at 4 ˚C until needed.

TAC-Pdot conjugates were freshly prepared prior to cell immunolabeling. The TAC-anti-HER2 complex was diluted to a final concentration of 22 nM in 1× PBS buffer. An aliquot of TAC stock (30 µL, 22 nM, 0.646 pmol, 21 equivalents) was spiked into a 100 µL solution of Dex-Pdots (0.03 pmol, 300 pM). The sample was topped up by the addition of 20 µL of 1× PBS buffer, and then incubated at room temperature for 30 min.

7.5.9.3 Imaging Fixed SK-BR3 Cells

A suspension of freshly trypsinized SK-BR3 cells (*ca*. 10^6 cells) was pelleted by centrifugation at 55 rcf for 5 min. The supernatant was removed, and the pellet resuspended in 2.0 mL of PBS buffer. A volume of 2.0 mL of 4% (w/v) paraformaldehyde in PBS was added and the sample gently mixed via pipette. The sample was incubated at room temperature for 5–10 min before

pelleting via centrifugation at 55 rcf for 5 min. The supernatant was discarded, and the pellet resuspended in 4.0 mL of PBS buffer.

A suspension (20 µL) of paraformaldehyde-fixed SK-BR3 cells in PBS was pipetted into a 1.7 mL microcentrifuge tube. The SK-BR3 cell suspension was then spiked with 5.0 µL of (anti-HER2-TAC)-Dex-Pdot conjugates (~300 pM, 15 equivalents TAC-HER2 relative to nanoparticles). The sample mixture was mixed briefly via pipette and then incubated on the benchtop for 15 min in the dark. Following incubation, the labeled cells were pelleted via centrifugation at 55 rcf and the supernatant removed by pipette. The cells were resuspended in 20 µL of fresh PBS buffer.

Samples were prepared by pipetting 7.5 µL of a suspension of labeled cells onto a microscope slide. A cover slip was applied, and the sample was inverted and imaged through the cover slip. The fluorescence filter sets used for imaging are listed in Table 7.2. The emission spectra of the cells labeled with (anti-HER2-TAC)-Dex-Pdot conjugates (F8BT) were acquired with a diode-array spectrometer (Greenwave 16 VIS-50; StellarNet, Tampa, FL) that was coupled to the trinocular head of the microscope via a fiber-optic cable.

Table 7.2. Fluorescence microscopy optics for SK-BR3 labeling.

(anti-HER2-TAC)-Dex-Pdot	Exc. Filter [a]	Em. Filter [a, b]	Dichroic Mirror [c]	Objective Lens [d]
F8BT	450/50 BP	500LP	T470	100XO (1.40 NA)
CNMEHPPV	450/50 BP	550LP	T565	60X (0.9 NA)

Notes: [a] Center wavelength/bandwidth, BP = bandpass filter. [b] LP = longpass filter. [c] T = transmission cut-on wavelength. All numbers in units of nanometers. [d] X = magnification factor, air-immersion; XO = magnification factor, oil-immersion; NA = numerical aperture.

7.5.9.4 Data Analysis

Microscope images were analyzed using ImageJ software. Contrast ratios were determined as follows: A threshold was applied to the pixel intensity to reject the background and only analyze fluorescence signal from the labelled cells. The mean pixel intensity of the labelled cells was determined for three images ($N > 10$ cells). A threshold was then applied to isolate and determine the intensity of the background. Cell and background intensities were averaged across three images, and the contrast determined as the ratio of the background-subtracted intensity of the Pdots or Dex-Pdots with (+) or without (–) TAC.

Chapter 8: Conclusions and future work

8.1 Thesis overview

This thesis has presented advances in the development, characterization and optimization of Pdots, specifically as fluorescent probes in biosensing and bioanalysis applications. In the scientific literature, proof-of-concept utilization of Pdots as a fluorescent probe has been demonstrated for a huge variety of bioanalytical applications, including *in vitro* sensing and imaging [223], *in vivo* imaging [139], chemical sensing [222], flow cytometry [68, 92, 217], multiphoton fluorescence imaging [74, 141], and super resolution microscopy [88, 136, 267]. The broad scope of these demonstrated applications highlights that Pdots are a highly promising luminescent material, owing largely to their very high brightness and good biocompatibility. However, the continued development of these applications and the advent of new applications is currently limited by several key shortcomings of the materials that have yet to be fully addressed in the literature. This thesis has identified and addressed a number of these limitations, with the aim of enabling future innovations in the bioanalytical applications of Pdots.

Pdots are commonly synthesized by nanoprecipitation, where an organic precursor solution containing hydrophobic polymers is injected by hand into an aqueous solution, and the formation of nanoscale particles is driven by the sudden loss of solubility for the polymers. This method is poorly controlled as local variations in mixing efficiency and polymer concentration (*i.e.*, extent of supersaturation) affect the driving forces for particle formation. Greater control of mixing can be achieved using a microfluidic platform, although microfluidic platforms suffer from their own drawbacks (*e.g.*, expense and difficulty of microfluidic chip production, solvent compatibility,

limitations of scale). Millifluidic platforms offer ease of production and scale up, but have not yet been utilized for Pdot synthesis. Chapter 5 presented the development of a millifluidic flow-based method for Pdot synthesis, offering improved reproducibility and scalability. Some tuning of particle size was achieved varying precursor concentration and flow rate, with minimum limit sizes depending upon the properties of the semiconducting polymer (SP) used in synthesis. Flow synthesis was used to study the particle forming capabilities of many combinations of SPs and amphiphilic polymers, and several promising materials that reliably formed Pdots were identified. We also demonstrated the potential for millifluidic flow synthesis to produce large volumes of Pdots, where continuous flow pumps produced up to 100 mL of Pdots with good reproducibility, excepting one unusual run with CNMEHPPV/PS-b-PEG Pdots and a small number of possible outliers.

There is growing interest in using Pdots as donors in energy transfer (ET)-based sensing configurations, although ET pathways involving Pdots are poorly understood. Förster resonance energy transfer (FRET) is widely considered to be the dominant ET mechanism in these systems, but there is limited evidence supporting this hypothesis. Given the unique structure of Pdots, an acceptor may be located at a number of positions relative to the nanoparticle: within the core covalently bound to the SP backbone, non-specifically doped into the particle core, adsorbed onto the particle surface, or specifically conjugated to the particle surface. As a result, there are many possible arrangements of the donor and acceptor in these systems. An additional layer of complexity arises from the multichromophoric nature of Pdots, where an individual particle can contain hundreds of chromophore units. Excitation can occur anywhere within the particle, but the resulting exciton can migrate within the Pdot, increasing its probability of encountering an

acceptor. ET-based sensors with Pdots tend to be developed and optimized empirically, not rationally as is possible with other materials (*e.g.* a QD acting as a single chromophore transferring energy to a known number of nearby acceptors specifically conjugated to its surface). Chapter 6 presented a systematic study of energy transfer in Pdot-dye systems, where the dyes were located at the Pdot core and conjugated to the amphiphilic polymer at its surface. Considering the effects of batch-to-batch variation on particle sizes and quantum yields, size polydispersity, and the possibility of energy migration within the Pdot, FRET alone was not sufficient to describe the observed trends in ET efficiency. Although FRET is most likely the main ET mechanism, especially to acceptors located at a non-trivial distance from F8BT donors, Dexter ET and PET likely have a non-zero contribution to the observed ET. Future computational modelling of the system will provide further insight into which mechanisms are active in Pdot-acceptor systems.

The structure and surface chemistry of Pdots also presents limitations to their widespread use. Being held together by weak hydrophobic interactions, Pdots suffer from poor colloidal stability and are prone to surface-induced unfolding. Their surface chemistries are dictated by the amphiphile co-precipitated with the SP during synthesis, commonly a carboxylated or PEGylated amphiphile. Little variety in Pdot surface chemistry has been reported, limiting the scope of bioconjugate chemistries that have been employed with Pdots. Carbodiimide crosslinking is frequently used but suffers from its own limitations. Other than silica, additional surface coating materials have not been widely used, but are a promising strategy for overcoming these limitations. Chapter 7 presented development of dextran-based surface coating material, shown to improve stability in physiologically relevant conditions and decrease non-specific binding. Dextran coatings provide a new, specific bioconjugation pathway via the use of tetrameric antibody

complexes (TACs), that is reagent-free and selective. Dextran-coated Pdots were used in a quantitative fluorescence linked immunosorbent assay (FLISA) for a model analyte, erythropoietin, with a physiologically relevant dynamic range and minimal non-specific binding. Dextran-Pdots were further used to specifically immunolabel breast cancer cells with TAC, showing reduced non-specific binding and excellent signal contrast compared to unmodified Pdots. Dextran-based surface materials are thus a highly promising strategy for improving Pdot stability and performance in bioanalytical applications.

8.2 Future work

Pdots offer several advantages over other fluorophores, namely their brightness and biocompatibility. The rise of Pdots is likely to mirror that of semiconductor QDs to some extent, where gradual optimization of the material properties and surface chemistries will allow for increased sophistication of downstream applications. Increased understanding of the nanoscale structure of Pdots will also aid in their continued development. Of particular interest is the development of Pdots for use in point-of-care (POC) diagnostic applications [49]. POC technologies may be enabled using consumer electronic devices as the analytical platform, such as smartphone cameras as previously demonstrated by the Algar Research Group [268-269]. To date, QDs have found extensive use in such platforms at the research stage, but POC platforms reliant on luminescent nanomaterials have not been widely deployed in a clinical setting. Owing to their high brightness, Pdots are promising materials to overcome limitations in assay sensitivity and detection limits for POC applications. Preliminary reports show that Pdots are also promising for smartphone detection but require continued development [75, 270]. The challenges of using Pdots in these applications stem from difficulties in controlling their synthesis (*e.g.*, poor reproducibility

of particle sizes, broad size distributions), poor colloidal stability (*e.g.*, surface-induced unfolding and the formation of large aggregates, especially when solutions are not refrigerated as would likely be the case in a point-of-need setting), high non-specific binding (to biomolecules and substrates), and the dearth of controllable bioconjugate chemistries available. Integration of the results presented in this thesis will allow for the development of robust Pdots that may be deployed in a variety of downstream applications, including in POC settings.

8.2.1 Flow synthesis of Pdots

Chapter 5 presented the proof-of-concept for semi-automated, millifluidic flow synthesis of Pdots, but continued development and characterization of the system is required to achieve reliable, reproducible and highly tuneable Pdots. Many aspects of this work invite continued investigation: the age and storage conditions of the polymer stock solutions in THF (Figure 5.6), the impact of asymmetric flow rates on both obtained particle sizes and mixing dynamics within the mixer element (Figure 5.8), the differences in obtained particle size for 1 mL formulations (Figure 5.10), and continued studies into the nature of mixing and particle formation in the system. The thermodynamics of interactions between polymer and solvent molecules, and the resulting conformation of polymer chains in solution can be described by Flory-Huggins theory [178]. Using this framework, the transition of the SPs used in this work from swollen coils in good solvent (*i.e.*, THF) to collapsed globules in poor solvent (*i.e.*, water), may be analyzed to better understand the nanoprecipitation process [271]. The use of asymmetric flow rates is a particularly promising strategy to control Pdot sizes, as reducing the volume of organic solvent increases the extent of supersaturation and may result in the formation of sub-50 nm particle sizes which has yet to be demonstrated using our system. More data is required to fully characterize the impacts of flow rate

and precursor concentration when considering all possible hardware configurations (*e.g.,* mixer geometry, mixer internal diameter (ID), tubing ID, pump type). Other types of flow such as segmented flow (where streams are divided by air bubbles) or other types of mixer elements (*e.g.,* more experiments with dynamic mixers, impinging jet mixers) may also be investigated, with the aim of improving mixing efficiency to produce smaller particles and to further control mixing efficiency to achieve size tuning.

The use of fluid dynamics modelling may answer some of the remaining questions about the flow synthesis system. The nature of mixing within the mixer element is currently unknown. At low flow rates, laminar flow is expected with mixing occurring only via diffusion from the interface of the two fluid streams. At high flow rates, the flow is expected to be more turbulent in character, leading to more efficient mixing and smaller Pdots. The balance between these two regimes likely depends on the flow rates used, but also on the relative viscosities of the two solvents (*i.e.,* THF and water in our system), the diameter and geometry of the mixing channel, and possibly temperature and pressure conditions, which may change over the course of the run. The nature of mixing may change drastically if asymmetric flow rates are used, affecting the outcome of synthesis. Computational modelling of the flow synthesis system with these variables in mind will lead to improved understanding of the nature of mixing, allowing for informed choice over the many variables affecting synthesis to obtain the desired outcome (*e.g.,* tuning particle size, loading cargo, *etc.*).

We have demonstrated that the doping of small molecules into the Pdot core can be achieved using flow synthesis, but the process itself was not optimized. Flow synthesis utilizing a wider range of

conditions (*e.g.*, precursor concentrations, cargo concentrations, flow rates) will allow for the determination of maximum loading efficiency. The scope of materials doped may also be expanded to include other optically active materials (*e.g.*, acceptor dyes to narrow and red-shift Pdot emission, sensitizers for photothermal or photodynamic therapy) and bioactive materials (*e.g.*, hydrophobic drug molecules). With tighter control over mixing, more efficient and more controllable doping may be possible with flow synthesis than with manual injection, for example, offering a predictable method for loading a desired number of molecules into the Pdot core.

Although we have identified some materials that reliably form Pdots, our results for other materials are somewhat ambiguous. Determination of particle morphologies by imaging techniques such as TEM and AFM will enable more robust confirmation of particle formation, especially for materials that are not amenable to NTA analysis. Advanced particle imaging techniques such as liquid-phase electron microscopy or liquid-phase atomic force microscopy can give a more robust picture of Pdot structure in their native, aqueous environment, at the cost of increased measurement complexity. Characterization of the nature of chain packing within the Pdot core and near the Pdot surface may provide additional insight into particle formation. For example, small-angle (SAXS) and wide-angle X-ray scattering (WAXS) may be used to determine nanoscopic or sub-nanoscopic level structure *in situ* (*e.g.*, crystal packing, amorphous structure), respectively, as has been demonstrated in semicrystalline polyethylene nanoparticles [272].

The scope of materials tested should also be increased to identify trends in what polymer properties lead to the formation of good Pdots (*e.g.*, contour lengths, backbone rigidity for SPs and molecular weight, relative masses of hydrophilic and hydrophobic components for APs). The unexpected

behaviour of PE-b-PEG Pdots should be further investigated, for example, by TEM or scanning electron microscopy with energy dispersive X-ray spectroscopy (SEM/EDX) to obtain spatially resolved topographical and compositional information, and fluorescence correlation spectroscopy.

Large-scale production of Pdots will require scale up beyond 100 mL, the upper limit for our demonstrated proof-of-concept. Larger scales are feasible with the continuous flow pumps as they may be operated continuously at a maximum flow rate of 5 mL/min for an arbitrary amount of time, so long as a sufficient volume of precursor solution is supplied. However, reproducible and controllable Pdot manufacturing will require smooth operation of the pumps with no changes in flow, and the heating of the pumps (and increased pressurization) over the course of the run must be controlled. These factors were not taken in to account for the 100 mL runs (requiring a 20 min run time), but will be important for production on larger scales.

Beyond improvements to the flow synthesis systems presented here, our systems present opportunities for continued engineering development. The continuous flow pump system featured automated fraction collection, but further automation may be deployed to quickly test the effects of different synthesis conditions or rapidly perform replicate experiments. Inline connection of characterization techniques (*e.g.,* dilution and delivery of aliquots to the NTA) to the flow synthesis system could enable automation of both the synthesis and characterization steps, eliminating variations arising from differences in storage time before analysis. In this way, the effects of polymer properties (molecular weight, PDI, contour length) could be rapidly surveyed. Further increasing hardware sophistication, on-the-fly mixing and dilutions of solutions or the introduction of microfluidic elements could also be incorporated, and machine learning algorithms

could be employed to develop recipes for 'made-to-order' Pdots of a desired size or colour (*e.g.*, by combining SPs or doping in dyes) without extensive experimental time or human effort.

8.2.2 Energy transfer studies

Some of the ambiguity presented in Chapter 6 may be addressed by the use of molecular modelling. Monte Carlo simulations have been used to model exciton migration in SPs [273]. Using similar methods confined to the structure of a Pdot, the balance of energy migration, the probability of energy transfer (ET) and exciton trapping, the distribution of Pdot size and the number of dyes per Pdot may be considered and compared to the empirical data. Agreements between the data and models based on a given ET mechanism may elucidate which processes dominate in the real system. Such simulations have been initiated by collaborators in the Algar Research Group.

Our ET studies also pave the way for future experimental work. The results presented in Chapter 6 were performed on ensembles of particles, and our interpretation relied on ensemble averages that may not be truly reflective of the nanoscopic system. Owing to the heterogeneity of the Pdot-dye system, single-particle energy transfer studies will likely provide valuable information about both the heterogeneity of the sample and ET dynamics in individual particles. For example, the extent of quenching for an individual Pdot may be used to estimate the number of quenchers associated, and over measurements of many particles be used to determine the distribution of quenchers per Pdot. Single-particle FRET has been used to study photobleaching and photoswitching in Pdots and SPNs [234, 274], but single particle studies of other photophysical processes in Pdots have yet to be reported. The Algar lab is currently constructing a multicolour, single-molecule fluorescence microscope system that will enable these studies in the near future.

With an understanding of ET in Pdots, more sophisticated ET pathways can be developed. For example, energy transfer cascades, where energy transfer occurs directionally from an initial donor to several subsequent acceptors, may be used to increase the Stokes shift of a Pdot [217] or, in principle, may possibly direct energy from the Pdot core to acceptors near the surface, where a biorecognition event that could modulate the fluorescence signal is most likely to occur. Concentric FRET (cFRET), which the Algar Research Group has invented and developed, is another possible FRET strategy where several unique acceptors are associated with a single donor to enable multiplexing with a single probe [275]. cFRET has been demonstrated with quantum dot (QD) donors where their well-understood photophysics and significant surface area for the conjugation of acceptors make them ideal materials for such applications. The broad emission spectrum of Pdots allows them to act as energy donors to a wide variety of potential acceptors in a cFRET configuration, and such configurations may be a promising path forward for multiplexing with Pdots.

With improved understanding of ET in Pdots, biosensors can be designed more rationally, with less reliance on empirical, ensemble-averaged results. Improved sophistication of sensor design will undoubtedly lead to improved sensor performance. The combination of bright Pdot luminescence and well-controlled ET will allow for the invention of assays with excellent analytical figures of merit that may be adapted to a POC platform.

8.2.3 Surface chemistries and bioconjugation

The dearth of reported surface and bioconjugate chemistries, and the reliance on poorly controlled carbodiimide chemistry, represent a serious limitation in the development of Pdots. We have presented one route forward, but many other surface engineering possibilities exist, including the use of silica shells and non-emissive polymer shells [34, 103-105], that retain the excellent brightness and photostability of the materials.

Nevertheless, dextran-based surface materials deserve attention owing to their numerous desirable properties. Our dextran coatings performed excellently, but optimization of the material may yield further improvements. Although we used a fairly short dextran chain (*ca.* 6 kDa), dextrans of many molecular weights are commercially available. The thickness of the surface coating (related to the molecular weight of the dextran), the extent of chemical modification (*i.e.*, the percentage of monomers oxidized and converted to primary amines), the length of the functionalized alkyl linker, the number of dextran chains per particle and the possibility of crosslinking the dextran to itself (as in the preparation of dextran hydrogels [276]) are all variables that remain to be optimized. Dextran is commonly used as a surface coating material for superparamagnetic iron oxide nanoparticles, where crosslinking of the dextran chain via a reagent such as epichlorohydrin increases the stability of the structure and prevents dissociation of the non-specifically bound dextran from the nanoparticle surface [251]. A similar crosslinking strategy may prove useful for Pdots. The nature and extent of branching off of the main chain also varies between the bacterial species used for biosynthesis, which may be an important consideration for the nominal conformation of the dextran with regards to the Pdot surface (*i.e.*, whether the chain remains close to the surface or extends radially into the bulk solution). Where immunolabeling is not possible or

desired, reactive functionalities other than amines may be installed along the dextran chain to enable other bioconjugation pathways.

We have shown that dextran-coated Pdots can be deployed in bioanalysis and bioimaging applications, albeit that our results are proof-of-concept. Owing to the flexibility of immunolabeling with TAC, the scope of analytes or labeling targets is limited only by the availability of an appropriate antibody. The high brightness of Pdots combined with the reduction of non-specific binding afforded by the dextran coating makes dextran-coated Pdots an extremely promising fluorescent label for many bioanalysis and imaging applications, and the development of assays and imaging techniques with these materials is anticipated.

8.3 Concluding remarks

This thesis has presented interdisciplinary original research spanning the fields of materials, physical and bioanalytical chemistry. Key contributions were made towards the development of Pdots in terms of their synthesis, understanding of their photophysics, and engineering their surfaces for enhanced performance in bioanalytical applications. Taken together, the results presented in this thesis can be integrated for the improved design of Pdot probes. These results have important implications in the field of bioanalysis and bioimaging, where the development of benign, stable, and ultrabright fluorescent probes will enable future innovations in fluorescence sensing and imaging. Pdots are a particularly promising fluorophore due to their extremely high brightness and their unique structure compared to other luminescent materials. This work represents the first research performed by the Algar Research Group using Pdots and provides a robust foundation for future research utilizing these materials. Although much advancement has

been made, both by the author and many other researchers globally, continued development is required before Pdots will truly rival QDs and molecular dyes in the field of bioanalysis.

References

1. Leary, J. A.; Arnold, M. A., Bioanalytical Chemistry. *Curr. Opin. Chem. Biol.* **2002,** *6,* 631-632.

2. Bowser, M. T., Introduction to New Frontiers in Bioanalytical Chemistry. *Chem. Rev.* **2013,** *113,* 2267-2268.

3. Resch-Genger, U.; Grabolle, M.; Cavaliere-Jaricot, S.; Nitschke, R.; Nann, T., Quantum Dots Versus Organic Dyes as Fluorescent Labels. *Nat. Methods* **2008,** *5,* 763-775.

4. Stepanenko, O. V.; Verkhusha, V. V.; Kuznetsova, I. M.; Uversky, V. N.; Turoverov, K. K., Fluorescent Proteins as Biomarkers and Biosensors: Throwing Color Lights on Molecular and Cellular Processes. *Curr. Protein Pept. Sci.* **2008,** *9,* 338-369.

5. Lövestam, G.; Rauscher, H.; Roebben, G.; Klüttgen, B. S.; Gibson, N.; Putaud, J.-P.; Stamm, H. *Considerations on a Definition of Nanomaterial for Regulatory Purposes*; 2010.

6. Wolfbeis, O. S., An Overview of Nanoparticles Commonly Used in Fluorescent Bioimaging. *Chem. Soc. Rev.* **2015,** *44,* 4743-4768.

7. Algar, W. R.; Susumu, K.; Delehanty, J. B.; Medintz, I. L., Semiconductor Quantum Dots in Bioanalysis: Crossing the Valley of Death. *Anal. Chem.* **2011,** *83,* 8826-8837.

8. Petryayeva, E.; Algar, W. R., Toward Point-of-Care Diagnostics with Consumer Electronic Devices: The Expanding Role of Nanoparticles. *RSC Adv.* **2015,** *5,* 22256-22282.

9. Chen, Y.; Guo, X.; Liu, W.; Zhang, L., Paper-Based Fluorometric Immunodevice with Quantum-Dot Labeled Antibodies for Simultaneous Detection of Carcinoembryonic Antigen and Prostate Specific Antigen. *Microchim. Acta* **2019,** *186,* 112.

10. Bruns, O. T.; Bischof, T. S.; Harris, D. K.; Franke, D.; Shi, Y.; Riedemann, L.; Bartelt, A.; Jaworski, F. B.; Carr, J. A.; Rowlands, C. J.; Wilson, M. W. B.; Chen, O.; Wei, H.; Hwang, G. W.; Montana, D. M.; Coropceanu, I.; Achorn, O. B.; Kloepper, J.; Heeren, J.; So, P. T. C.; Fukumura, D.; Jensen, K. F.; Jain, R. K.; Bawendi, M. G., Next-Generation in Vivo Optical Imaging with Short-Wave Infrared Quantum Dots. *Nat. Biomed. Eng.* **2017,** *1*.

11. Cayuela, A.; Soriano, M. L.; Carrillo-Carrión, C.; Valcárcel, M., Semiconductor and Carbon-Based Fluorescent Nanodots: The Need for Consistency. *Chem. Commun.* **2016,** *52,* 1311-1326.

12. Yao, B.; Huang, H.; Liu, Y.; Kang, Z., Carbon Dots: A Small Conundrum. *Trends Chem.* **2019,** *1,* 235-246.

13. Esteves da Silva, J. C. G.; Gonçalves, H. M. R., Analytical and Bioanalytical Applications of Carbon Dots. *TrAC, Trends Anal. Chem.* **2011,** *30,* 1327-1336.

14. Xia, C.; Cao, M.; Xia, J.; Zhou, G.; Jiang, D.; Zhang, D.; Wang, J.; Li, H., An Ultrafast Responsive and Sensitive Ratiometric Fluorescent pH Nanoprobe Based on Label-Free Dual-Emission Carbon Dots. *J. Mater. Chem. C* **2019,** *7,* 2563-2569.

15. Liu, H.; Sun, Y.; Li, Z.; Yang, J.; Aryee, A. A.; Qu, L.; Du, D.; Lin, Y., Lysosome-Targeted Carbon Dots for Ratiometric Imaging of Formaldehyde in Living Cells. *Nanoscale* **2019,** *11,* 8458-8463.

16. Gu, B.; Zhang, Q., Recent Advances on Functionalized Upconversion Nanoparticles for Detection of Small Molecules and Ions in Biosystems. *Adv. Sci.* **2018,** *5,* 1700609.

17. Achatz, D. E.; Ali, R.; Wolfbeis, O. S., Luminescent Chemical Sensing, Biosensing, and Screening Using Upconverting Nanoparticles. In *Luminescence Applied in Sensor Science*, Prodi, L.; Montalti, M.; Zaccheroni, N., Eds. Springer Berlin Heidelberg: Berlin, Heidelberg, 2011; pp 29-50.

18. Zhang, R.; Liang, L.; Meng, Q.; Zhao, J.; Ta, H. T.; Li, L.; Zhang, Z.; Sultanbawa, Y.; Xu, Z. P., Responsive Upconversion Nanoprobe for Background-Free Hypochlorous Acid Detection and Bioimaging. *Small* **2019,** *15,* 1803712.

19. Zhao, J.; Chu, H.; Zhao, Y.; Lu, Y.; Li, L., A NIR Light Gated DNA Nanodevice for Spatiotemporally Controlled Imaging of microRNA in Cells and Animals. *J. Am. Chem. Soc.* **2019,** *141,* 7056-7062.

20. Yan, J.; Estévez, M. C.; Smith, J. E.; Wang, K.; He, X.; Wang, L.; Tan, W., Dye-Doped Nanoparticles for Bioanalysis. *Nano Today* **2007,** *2,* 44-50.

21. Wang, C.; Otto, S.; Dorn, M.; Heinze, K.; Resch-Genger, U., Luminescent Top Nanosensors for Simultaneously Measuring Temperature, Oxygen, and pH at a Single Excitation Wavelength. *Anal. Chem.* **2019,** *91,* 2337-2344.

22. Kim, S. E.; Zhang, L.; Ma, K.; Riegman, M.; Chen, F.; Ingold, I.; Conrad, M.; Turker, M. Z.; Gao, M.; Jiang, X.; Monette, S.; Pauliah, M.; Gonen, M.; Zanzonico, P.; Quinn, T.; Wiesner, U.; Bradbury, M. S.; Overholtzer, M., Ultrasmall Nanoparticles Induce Ferroptosis in Nutrient-Deprived Cancer Cells and Suppress Tumour Growth. *Nat. Nanotechnol.* **2016,** *11,* 977-985.

23. Szymanski, C.; Wu, C.; Hooper, J.; Salazar, M. A.; Perdomo, A.; Dukes, A.; McNeill, J., Single Molecule Nanoparticles of the Conjugated Polymer MEH−PPV, Preparation and Characterization by Near-Field Scanning Optical Microscopy. J. *Phys. Chem. B* **2005,** *109,* 8543-8546.

24. Wu, C.; Bull, B.; Szymanski, C.; Christensen, K.; McNeill, J., Multicolor Conjugated Polymer Dots for Biological Fluorescence Imaging. *ACS Nano* **2008,** *2,* 2415-2423.

25. Pecher, J.; Mecking, S., Nanoparticles of Conjugated Polymers. *Chem. Rev.* **2010,** *110,* 6260-6279.

26. Wu, C.; Chiu, D. T., Highly Fluorescent Semiconducting Polymer Dots for Biology and Medicine. *Angew. Chem. Int. Ed.* **2013,** *52,* 3086-3109.

27. Zhang, X.; Yu, J.; Wu, C.; Jin, Y.; Rong, Y.; Ye, F.; Chiu, D. T., Importance of Having Low-Density Functional Groups for Generating High-Performance Semiconducting Polymer Dots. *ACS Nano* **2012,** *6,* 5429-5439.

28. Osakada, Y.; Hanson, L.; Cui, B., Diarylethene Doped Biocompatible Polymer Dots for Fluorescence Switching. *Chem. Commun.* **2012,** *48,* 3285-3287.

29. Özenler, S.; Yucel, M.; Tüncel, Ö.; Kaya, H.; Özçelik, S.; Yildiz, U. H., Single Chain Cationic Polymer Dot as a Fluorescent Probe for Cell Imaging and Selective Determination of Hepatocellular Carcinoma Cells. *Anal. Chem.* **2019,** *91,* 10357-10360.

30. Jo, S.; Kim, J.; Noh, J.; Kim, D.; Jang, G.; Lee, N.; Lee, E.; Lee, T. S., Conjugated Polymer Dots-on-Electrospun Fibers as a Fluorescent Nanofibrous Sensor for Nerve Gas Stimulant. *ACS Appl. Mater. Interfaces* **2014,** *6,* 22884-22893.

31. Ye, F.; Wu, C.; Jin, Y.; Chan, Y.-H.; Zhang, X.; Chiu, D. T., Ratiometric Temperature Sensing with Semiconducting Polymer Dots. *J. Am. Chem. Soc.* **2011,** *133,* 8146-8149.

32. Li, S.; Wang, X.; Hu, R.; Chen, H.; Li, M.; Wang, J.; Wang, Y.; Liu, L.; Lv, F.; Liang, X.-J.; Wang, S., Near-Infrared (NIR)-Absorbing Conjugated Polymer Dots as Highly Effective Photothermal Materials for in Vivo Cancer Therapy. *Chem. Mater.* **2016,** *28,* 8669-8675.

33. Li, Q.; Zhang, J.; Sun, W.; Yu, J.; Wu, C.; Qin, W.; Chiu, D. T., Europium-Complex-Grafted Polymer Dots for Amplified Quenching and Cellular Imaging Applications. *Langmuir* **2014,** *30,* 8607-8614.

34. Qiao, Z.-A.; Huo, Q.; Chi, M.; Veith, G. M.; Binder, A. J.; Dai, S., A "Ship-in-a-Bottle" Approach to Synthesis of Polymer Dots@Silica or Polymer Dots@Carbon Core-Shell Nanospheres. *Adv. Mater.* **2012,** *24,* 6017-6021.

35. Wang, S.; Liu, J.; Feng, G.; Ng, L. G.; Liu, B., NIR-II Excitable Conjugated Polymer Dots with Bright NIR-I Emission for Deep in Vivo Two-Photon Brain Imaging through Intact Skull. *Adv. Funct. Mater.* **2019,** *29,* 1808365.

36. Zhu, S.; Wang, L.; Zhou, N.; Zhao, X.; Song, Y.; Maharjan, S.; Zhang, J.; Lu, L.; Wang, H.; Yang, B., The Crosslink Enhanced Emission (CEE) in Non-Conjugated Polymer Dots: From the Photoluminescence Mechanism to the Cellular Uptake Mechanism and Internalization. *Chem. Commun.* **2014,** *50,* 13845-13848.

37. Vallan, L.; Urriolabeitia, E. P.; Benito, A. M.; Maser, W. K., A Versatile Room-Temperature Method for the Preparation of Customized Fluorescent Non-Conjugated Polymer Dots. *Polymer* **2019,** *177,* 97-101.

38. Tong, D.; Li, W.; Zhao, Y.; Zhang, L.; Zheng, J.; Cai, T.; Liu, S., Non-Conjugated Polyurethane Polymer Dots Based on Crosslink Enhanced Emission (CEE) and Application in Fe^{3+} Sensing. *RSC Adv.* **2016,** *6,* 97137-97141.

39. Liu, S. G.; Liu, T.; Li, N.; Geng, S.; Lei, J. L.; Li, N. B.; Luo, H. Q., Polyethylenimine-Derived Fluorescent Nonconjugated Polymer Dots with Reversible Dual-Signal pH Response and Logic Gate Operation. J. *Phys. Chem. C* **2017,** *121,* 6874-6883.

40. Sun, Y.; Cao, W.; Li, S.; Jin, S.; Hu, K.; Hu, L.; Huang, Y.; Gao, X.; Wu, Y.; Liang, X.-J., Ultrabright and Multicolorful Fluorescence of Amphiphilic Polyethyleneimine Polymer Dots for Efficiently Combined Imaging and Therapy. *Sci. Rep.* **2013,** *3*.

41. Sun, B.; Zhao, B.; Wang, D.; Wang, Y.; Tang, Q.; Zhu, S.; Yang, B.; Sun, H., Fluorescent Non-Conjugated Polymer Dots for Targeted Cell Imaging. *Nanoscale* **2016,** *8,* 9837-9841.

42. Zhu, S.; Song, Y.; Shao, J.; Zhao, X.; Yang, B., Non-Conjugated Polymer Dots with Crosslink-Enhanced Emission in the Absence of Fluorophore Units. *Angew. Chem. Int. Ed.* **2015,** *54,* 14626-14637.

43. Chen, Y.; Zhang, Y.; Lyu, T.; Wang, Y.; Yang, X.; Wu, X., A Facile Strategy for the Synthesis of Water-Soluble Fluorescent Nonconjugated Polymer Dots and their Applications in Tetracyclines Detection. *J. Mater. Chem. C* **2019,** 9241-9247.

44. Han, L.; Liu, S. G.; Zhang, X. F.; Tao, B. X.; Li, N. B.; Luo, H. Q., A Sensitive Polymer Dots-Manganese Dioxide Fluorescent Nanosensor for "Turn-on" Detection of Glutathione in Human Serum. *Sens. Actuators, B* **2018,** *258,* 25-31.

45. Luo, D.; Liu, S. G.; Li, N. B.; Luo, H. Q., Water-Soluble Polymer Dots Formed from Polyethylenimine and Glutathione as a Fluorescent Probe for Mercury(II). *Microchim. Acta* **2018,** *185*.

46. Zhang, Y.; Chen, Y.; Li, X.; Zhang, J.; Chen, J.; Xu, B.; Fu, X.; Tian, W., Folic Acid-Functionalized AIE Pdots Based on Amphiphilic PCL-b-PEG for Targeted Cell Imaging. *Polym. Chem.* **2014,** *5,* 3824-3830.

47. Guan, X.; Lu, B.; Jin, Q.; Li, Z.; Wang, L.; Wang, K.; Lai, S.; Lei, Z., AIE-Active Fluorescent Nonconjugated Polymer Dots for Dual-Alternating-Color Live Cell Imaging. *Ind. Eng. Chem. Res.* **2018,** *57,* 14889-14898.

48. Wang, W.; Zhang, Y.; Liu, Y.; He, Y., Highly Selective and Sensitive Ratiometric Fluorescent Polymer Dots for Detecting Hypochlorite in 100% Aqueous Media. *Spectrochim. Acta, Part A* **2019,** *207,* 73-78.

49. Guo, L.; Ge, J.; Wang, P., Polymer Dots as Effective Phototheranostic Agents. *Photochem. Photobiol.* **2018,** *94,* 916-934.

50. Behrendt, J. M.; Esquivel Guzman, J. A.; Purdie, L.; Willcock, H.; Morrison, J. J.; Foster, A. B.; O'Reilly, R. K.; McCairn, M. C.; Turner, M. L., Scalable Synthesis of Multicolour Conjugated Polymer Nanoparticles (Direct Polymerization Method) via Suzuki-Miyaura Polymerisation in a Miniemulsion and Application in Bioimaging. *React. Funct. Polym.* **2016,** *107,* 69-77.

51. Kelly, T. L.; Wolf, M. O., Template Approaches to Conjugated Polymer Micro- and Nanoparticles. *Chem. Soc. Rev.* **2010,** *39,* 1526-1535.

52. Landfester, K., Miniemulsion Polymerization and the Structure of Polymer and Hybrid Nanoparticles. *Angew. Chem. Int. Ed.* **2009,** *48,* 4488-4507.

53. Landfester, K., The Generation of Nanoparticles in Miniemulsions. *Adv. Mater.* **2001,** *13,* 765-768.

54. Landfester, K.; Montenegro, R.; Scherf, U.; Güntner, R.; Asawapirom, U.; Patil, S.; Neher, D.; Kietzke, T., Semiconducting Polymer Nanospheres in Aqueous Dispersion Prepared by a Miniemulsion Process. *Adv. Mater.* **2002,** *14,* 651-655.

55. Kietzke, T.; Neher, D.; Landfester, K.; Montenegro, R.; Güntner, R.; Scherf, U., Novel Approaches to Polymer Blends Based on Polymer Nanoparticles. *Nat. Mater.* **2003,** *2,* 408-412.

56. Howes, P.; Thorogate, R.; Green, M.; Jickells, S.; Daniel, B., Synthesis, Characterisation and Intracellular Imaging of PEG Capped BEHP-PPV Nanospheres. *Chem. Commun.* **2009,** 2490-2492.

57. Virgili, T.; Botta, C.; Mróz, M. M.; Parrenin, L.; Brochon, C.; Cloutet, E.; Pavlopoulou, E.; Hadziioannou, G.; Geoghegan, M., Size-Dependent Photophysical Behavior of Low Bandgap Semiconducting Polymer Particles. *Front. Chem.* **2019,** *7*.

58. Kurokawa, N.; Yoshikawa, H.; Hirota, N.; Hyodo, K.; Masuhara, H., Size-Dependent Spectroscopic Properties and Thermochromic Behavior in Poly(Substituted Thiophene) Nanoparticles. *ChemPhysChem* **2004,** *5,* 1609-1615.

59. Wu, C.; Schneider, T.; Zeigler, M.; Yu, J.; Schiro, P. G.; Burnham, D. R.; McNeill, J. D.; Chiu, D. T., Bioconjugation of Ultrabright Semiconducting Polymer Dots for Specific Cellular Targeting. *J. Am. Chem. Soc.* **2010,** *132,* 15410-15417.

60. Andronico, L. A.; Chen, L.; Mirasoli, M.; Guardigli, M.; Quintavalla, A.; Lombardo, M.; Trombini, C.; Chiu, D. T.; Roda, A., Thermochemiluminescent Semiconducting Polymer Dots as Sensitive Nanoprobes for Reagentless Immunoassay. *Nanoscale* **2018,** *10,* 14012-14021.

61. Sun, K.; Chen, H.; Wang, L.; Yin, S.; Wang, H.; Xu, G.; Chen, D.; Zhang, X.; Wu, C.; Qin, W., Size-Dependent Property and Cell Labeling of Semiconducting Polymer Dots. *ACS Appl. Mater. Interfaces* **2014,** *6,* 10802-10812.

62. Clafton, S. N.; Beattie, D. A.; Mierczynska-Vasilev, A.; Acres, R. G.; Morgan, A. C.; Kee, T. W., Chemical Defects in the Highly Fluorescent Conjugated Polymer Dots. *Langmuir* **2010,** *26,* 17785-17789.

63. Jin, Y.; Ye, F.; Zeigler, M.; Wu, C.; Chiu, D. T., Near-Infrared Fluorescent Dye-Doped Semiconducting Polymer Dots. *ACS Nano* **2011,** *5,* 1468-1475.

64. Mikhnenko, O. V.; Blom, P. W. M.; Nguyen, T.-Q., Exciton Diffusion in Organic Semiconductors. *Energy Environ. Sci.* **2015,** *8,* 1867-1888.

65. Kularatne, R. S.; Magurudeniya, H. D.; Sista, P.; Biewer, M. C.; Stefan, M. C., Donor–Acceptor Semiconducting Polymers for Organic Solar Cells. *J. Polym. Sci., Part A: Polym. Chem.* **2013,** *51,* 743-768.

66. Grey, J. K.; Kim, D. Y.; Norris, B. C.; Miller, W. L.; Barbara, P. F., Size-Dependent Spectroscopic Properties of Conjugated Polymer Nanoparticles. *J. Phys. Chem. B* **2006,** *110,* 25568-25572.

67. Green, M.; Howes, P.; Berry, C.; Argyros, O.; Thanou, M., Simple Conjugated Polymer Nanoparticles as Biological Labels. *Proc. R. Soc. A* **2009,** *465,* 2751-2759.

68. Kuo, C.-T.; Thompson, A. M.; Gallina, M. E.; Ye, F.; Johnson, E. S.; Sun, W.; Zhao, M.; Yu, J.; Wu, I. C.; Fujimoto, B.; DuFort, C. C.; Carlson, M. A.; Hingorani, S. R.; Paguirigan, A. L.; Radich, J. P.; Chiu, D. T., Optical Painting and Fluorescence Activated Sorting of Single Adherent Cells Labelled with Photoswitchable Pdots. *Nat. Commun.* **2016,** *7*.

69. Lin, Z.; Zhang, G.; Yang, W.; Qiu, B.; Chen, G., Cea Fluorescence Biosensor Based on the FRET between Polymer Dots and Au Nanoparticles. *Chem. Commun.* **2012,** *48,* 9918-9920.

70. Yang, W.; Zhang, G.; Weng, W.; Qiu, B.; Guo, L.; Lin, Z.; Chen, G., Signal on Fluorescence Biosensor for MMP-2 Based on FRETt between Semiconducting Polymer Dots and a Metal Organic Framework. *RSC Adv.* **2014,** *4,* 58852-58857.

71. Li, Q.; Sun, K.; Chang, K.; Yu, J.; Chiu, D. T.; Wu, C.; Qin, W., Ratiometric Luminescent Detection of Bacterial Spores with Terbium Chelated Semiconducting Polymer Dots. *Anal. Chem.* **2013,** *85,* 9087-9091.

72. Kuo, C.-T.; Wu, I. C.; Chen, L.; Yu, J.; Wu, L.; Chiu, D. T., Improving the Photostability of Semiconducting Polymer Dots Using Buffers. *Anal. Chem.* **2018,** *90,* 11785-11790.

73. Li, S.; Chen, J.; Chen, G.; Li, Q.; Sun, K.; Yuan, Z.; Qin, W.; Xu, H.; Wu, C., Semiconductor Polymer Dots Induce Proliferation in Human Gastric Mucosal and Adenocarcinoma Cells. *Macromol. Biosci.* **2015,** *15,* 318-327.

74. Wu, C.; Szymanski, C.; Cain, Z.; McNeill, J., Conjugated Polymer Dots for Multiphoton Fluorescence Imaging. *J. Am. Chem. Soc.* **2007,** *129,* 12904-12905.

75. Sun, K.; Yang, Y.; Zhou, H.; Yin, S.; Qin, W.; Yu, J.; Chiu, D. T.; Yuan, Z.; Zhang, X.; Wu, C., Ultrabright Polymer-Dot Transducer Enabled Wireless Glucose Monitoring via a Smartphone. *ACS Nano* **2018,** *12,* 5176-5184.

76. Wu, C.; Zheng, Y.; Szymanski, C.; McNeill, J., Energy Transfer in a Nanoscale Multichromophoric System: Fluorescent Dye-Doped Conjugated Polymer Nanoparticles. *J. Phys. Chem. C* **2008,** *112,* 1772-1781.

77. Chan, Y.-H.; Jin, Y.; Wu, C.; Chiu, D. T., Copper(II) and Iron(II) Ion Sensing with Semiconducting Polymer Dots. *Chem. Commun.* **2011,** *47,* 2820-2822.

78. Wu, C.; Jin, Y.; Schneider, T.; Burnham, D. R.; Smith, P. B.; Chiu, D. T., Ultrabright and Bioorthogonal Labeling of Cellular Targets Using Semiconducting Polymer Dots and Click Chemistry. *Angew. Chem. Int. Ed.* **2010,** *49,* 9436-9440.

79. Li, Y.; Zhang, N.; Zhao, W.-W.; Jiang, D.-C.; Xu, J.-J.; Chen, H.-Y., Polymer Dots for Photoelectrochemical Bioanalysis. *Anal. Chem.* **2017,** *89,* 4945-4950.

80. Wang, N.; Feng, Y.; Wang, Y.; Ju, H.; Yan, F., Electrochemiluminescent Imaging for Multi-Immunoassay Sensitized by Dual DNA Amplification of Polymer Dot Signal. *Anal. Chem.* **2018,** *90,* 7708-7714.

81. Luo, J.; Li, Q.; Chen, s.; Yuan, R., A Coreactant-Free Dual Amplified Electrochemiluminescent (ECL) Biosensor Based on Conjugated Polymer Dots for the Ultrasensitive Detection of microRNA. *ACS Appl. Mater. Interfaces* **2019,** *11,* 27363-27370.

82. Fernando, L. P.; Kandel, P. K.; Yu, J.; McNeill, J.; Ackroyd, P. C.; Christensen, K. A., Mechanism of Cellular Uptake of Highly Fluorescent Conjugated Polymer Nanoparticles. *Biomacromolecules* **2010,** *11,* 2675-2682.

83. Sun, W.; Yu, J.; Deng, R.; Rong, Y.; Fujimoto, B.; Wu, C.; Zhang, H.; Chiu, D. T., Semiconducting Polymer Dots Doped with Europium Complexes Showing Ultranarrow Emission and Long Luminescence Lifetime for Time-Gated Cellular Imaging. *Angew. Chem. Int. Ed.* **2013,** *52,* 11294-11297.

84. Chen, H.; Zhang, J.; Chang, K.; Men, X.; Fang, X.; Zhou, L.; Li, D.; Gao, D.; Yin, S.; Zhang, X.; Yuan, Z.; Wu, C., Highly Absorbing Multispectral Near-Infrared Polymer Nanoparticles from One Conjugated Backbone for Photoacoustic Imaging and Photothermal Therapy. *Biomaterials* **2017,** *144,* 42-52.

85. Zhang, M.; Liu, J.; Wang, G., Highly Biocompatible Nanoparticles of Au@ Fluorescent Polymers as Novel Contrast Agent for in Vivo Bimodality NIR Fluorescence/CT Imaging. *Contrast Media Mol. Imaging* **2019,** *2019*.

86. Chen, D.; Wu, I. C.; Liu, Z.; Tang, Y.; Chen, H.; Yu, J.; Wu, C.; Chiu, D. T., Semiconducting Polymer Dots with Bright Narrow-Band Emission at 800 nm for Biological Applications. *Chem. Sci.* **2017,** *8,* 3390-3398.

87. Liu, R.; Cui, Q.; Yang, Y.; Peng, R.; Li, L., Preparation of Conjugated Polymer Nanoparticles with White Emission and their Application for Cell Imaging. *J. Photochem. Photobiol., A* **2018,** *355*, 389-397.

88. Sun, Z.; Liu, Z.; Chen, H.; Li, R.; Sun, Y.; Chen, D.; Xu, G.; Liu, L.; Wu, C., Semiconducting Polymer Dots with Modulated Photoblinking for High-Order Super-Resolution Optical Fluctuation Imaging. *Adv. Opt. Mater.* **2019,** *7*, 1900007.

89. Zhang, Y.; Yu, J.; Gallina, M. E.; Sun, W.; Rong, Y.; Chiu, D. T., Highly Luminescent, Fluorinated Semiconducting Polymer Dots for Cellular Imaging and Analysis. *Chem. Commun.* **2013,** *49*, 8256-8258.

90. Wu, L.; Wu, I. C.; DuFort, C. C.; Carlson, M. A.; Wu, X.; Chen, L.; Kuo, C.-T.; Qin, Y.; Yu, J.; Hingorani, S. R.; Chiu, D. T., Photostable Ratiometric Pdot Probe for in Vitro and in Vivo Imaging of Hypochlorous Acid. *J. Am. Chem. Soc.* **2017,** *139*, 6911-6918.

91. Liao, F.; Song, X.; Yang, S.; Hu, C.; He, L.; Yan, S.; Ding, G., Photoinduced Electron Transfer of Poly(O-Phenylenediamine)–Rhodamine B Copolymer Dots: Application in Ultrasensitive Detection of Nitrite in Vivo. *J. Mater. Chem. A* **2015,** *3*, 7568-7574.

92. Wu, X.; DeGottardi, Q.; Wu, I.-C.; Yu, J.; Wu, L.; Ye, F.; Kuo, C.-T.; Kwok, W. W.; Chiu, D. T., Lanthanide-Coordinated Semiconducting Polymer Dots Used for Flow Cytometry and Mass Cytometry. *Angew. Chem. Int. Ed.* **2017,** *56*, 14908-14912.

93. Rong, Y.; Wu, C.; Yu, J.; Zhang, X.; Ye, F.; Zeigler, M.; Gallina, M. E.; Wu, I. C.; Zhang, Y.; Chan, Y.-H.; Sun, W.; Uvdal, K.; Chiu, D. T., Multicolor Fluorescent Semiconducting Polymer Dots with Narrow Emissions and High Brightness. *ACS Nano* **2013,** *7*, 376-384.

94. Chan, Y.-H.; Gallina, M. E.; Zhang, X.; Wu, I. C.; Jin, Y.; Sun, W.; Chiu, D. T., Reversible Photoswitching of Spiropyran-Conjugated Semiconducting Polymer Dots. *Anal. Chem.* **2012,** *84*, 9431-9438.

95. Li, J.; Cui, D.; Huang, J.; He, S.; Yang, Z.; Zhang, Y.; Luo, Y.; Pu, K., Organic Semiconducting Pro-Nanostimulants for Near-Infrared Photoactivatable Cancer Immunotherapy. *Angew. Chem. Int. Ed.* **2019,** *58*, 2680–12687.

96. Jiang, Y.; Cui, D.; Fang, Y.; Zhen, X.; Upputuri, P. K.; Pramanik, M.; Ding, D.; Pu, K., Amphiphilic Semiconducting Polymer as Multifunctional Nanocarrier for Fluorescence/Photoacoustic Imaging Guided Chemo-Photothermal Therapy. *Biomaterials* **2017,** *145*, 168-177.

97. Petkau, K.; Kaeser, A.; Fischer, I.; Brunsveld, L.; Schenning, A. P. H. J., Pre- and Postfunctionalized Self-Assembled π-Conjugated Fluorescent Organic Nanoparticles for Dual Targeting. *J. Am. Chem. Soc.* **2011,** *133*, 17063-17071.

98. Gezici, O.; Durmaz, I.; Bilget Guven, E.; Unal, O.; Ozgun, A.; Cetin-Atalay, R.; Tuncel, D., Dual Functionality of Conjugated Polymer Nanoparticles as an Anticancer Drug Carrier and a Fluorescent Probe for Cell Imaging. *RSC Adv.* **2014,** *4,* 1302-1309.

99. Chen, H.; Fang, X.; Jin, Y.; Hu, X.; Yin, M.; Men, X.; Chen, N.; Fan, C.; Chiu, D. T.; Wan, Y.; Wu, C., Semiconducting Polymer Nanocavities: Porogenic Synthesis, Tunable Host–Guest Interactions, and Enhanced Drug/siRNA Delivery. *Small* **2018,** *14,* 1800239.

100. Miao, Q.; Xie, C.; Zhen, X.; Lyu, Y.; Duan, H.; Liu, X.; Jokerst, J. V.; Pu, K., Molecular Afterglow Imaging with Bright, Biodegradable Polymer Nanoparticles. *Nat. Biotechnol.* **2017,** *35,* 1102.

101. Urbano, L.; Clifton, L. A.; Ku, H. K.; Kendall-Troughton, H.; Vandera, K.-K. A.; Matarèse, B. F. E.; Abelha, T. F.; Li, P.; Desai, T. A.; Dreiss, C. A.; Barker, R. D.; Green, M. A.; Dailey, L. A.; Harvey, R. D., Influence of Surfactant Structure on Photoluminescent π-Conjugated Polymer Nanoparticles: Interfacial Properties and Protein Binding. *Langmuir* **2018,** *34,* 6125-6137.

102. Wu, C.; Szymanski, C.; McNeill, J., Preparation and Encapsulation of Highly Fluorescent Conjugated Polymer Nanoparticles. *Langmuir* **2006,** *22,* 2956-2960.

103. Zhen, X.; Feng, X.; Xie, C.; Zheng, Y.; Pu, K., Surface Engineering of Semiconducting Polymer Nanoparticles for Amplified Photoacoustic Imaging. *Biomaterials* **2017,** *127,* 97-106.

104. Zhu, H.; Fang, Y.; Zhen, X.; Wei, N.; Gao, Y.; Luo, K. Q.; Xu, C.; Duan, H.; Ding, D.; Chen, P.; Pu, K., Multilayered Semiconducting Polymer Nanoparticles with Enhanced NIR Fluorescence for Molecular Imaging in Cells, Zebrafish and Mice. *Chem. Sci.* **2016,** *7,* 5118-5125.

105. Geng, J.; Liu, J.; Liang, J.; Shi, H.; Liu, B., A General Approach to Prepare Conjugated Polymer Dot Embedded Silica Nanoparticles with a SiO_2@CP@SiO_2 Structure for Targeted HER2-Positive Cellular Imaging. *Nanoscale* **2013,** *5,* 8593-8601.

106. Shanks, H. R.; Zhu, M.; Milani, A. H.; Turton, J.; Haigh, S.; Hodson, N. W.; Adlam, D.; Hoyland, J.; Freemont, T.; Saunders, B. R., Core–Shell–Shell Cytocompatible Polymer Dot-Based Particles with Near-Infrared Emission and Enhanced Dispersion Stability. *Chem. Commun.* **2018,** *54,* 9364-9367.

107. Guo, Y.; Cao, F.; Li, Y.; Xiong, L., Facilely Synthesized pH-Responsive Fluorescent Polymer Dots Entrapping Doped and Coupled Doxorubicin for Nucleus-Targeted Chemotherapy. *J. Mater. Chem. B* **2017,** *5,* 2921-2930.

108. Wu, C.; Bull, B.; Christensen, K.; McNeill, J., Ratiometric Single-Nanoparticle Oxygen Sensors for Biological Imaging. *Angew. Chem. Int. Ed.* **2009,** *48,* 2741-2745.

109. Massey, M.; Wu, M.; Conroy, E. M.; Algar, W. R., Mind Your P's and Q's: The Coming of Age of Semiconducting Polymer Dots and Semiconductor Quantum Dots in Biological Applications. *Curr. Opin. Biotechnol.* **2015,** *34,* 30-40.

110. Wu, C.; McNeill, J., Swelling-Controlled Polymer Phase and Fluorescence Properties of Polyfluorene Nanoparticles. *Langmuir* **2008,** *24,* 5855-5861.

111. Ye, F.; Wu, C.; Sun, W.; Yu, J.; Zhang, X.; Rong, Y.; Zhang, Y.; Wu, I. C.; Chan, Y.-H.; Chiu, D. T., Semiconducting Polymer Dots with Monofunctional Groups. *Chem. Commun.* **2014,** *50,* 5604-5607.

112. Ye, F.; Sun, W.; Zhang, Y.; Wu, C.; Zhang, X.; Yu, J.; Rong, Y.; Zhang, M.; Chiu, D. T., Single-Chain Semiconducting Polymer Dots. *Langmuir* **2015,** *31,* 499-505.

113. Wu, C.; Peng, H.; Jiang, Y.; McNeill, J., Energy Transfer Mediated Fluorescence from Blended Conjugated Polymer Nanoparticles. *J. Phys. Chem. B* **2006,** *110,* 14148-14154.

114. Bravo-Anaya, L. M.; Gómez, G. L.; Figueroa-Ochoa, E.; Ramos, F. C.; Armando Soltero Martínez, J. F.; Rharbi, Y., Exchange Dynamics between Amphiphilic Block Copolymers and Lipidic Membranes through Hydrophobic Pyrene Probe Transfer. *RSC Adv.* **2018,** *8,* 39444-39454.

115. Valeur, B.; Berberan-Santos, M. N., *Molecular Fluorescence.* Wiley-VCH: Weinheim, 2013.

116. Sun, J.; Mei, H.; Wang, S.; Gao, F., Two-Photon Semiconducting Polymer Dots with Dual-Emission for Ratiometric Fluorescent Sensing and Bioimaging of Tyrosinase Activity. *Anal. Chem.* **2016,** *88,* 7372-7377.

117. Alifu, N.; Sun, Z.; Zebibula, A.; Zhu, Z.; Zhao, X.; Wu, C.; Wang, Y.; Qian, J., Deep-Red Polymer Dots with Bright Two-Photon Fluorescence and High Biocompatibility for in Vivo Mouse Brain Imaging. *Opt. Commun.* **2017,** *399,* 120-126.

118. Yu, J.; Rong, Y.; Kuo, C.-T.; Zhou, X.-H.; Chiu, D. T., Recent Advances in the Development of Highly Luminescent Semiconducting Polymer Dots and Nanoparticles for Biological Imaging and Medicine. *Anal. Chem.* **2017,** *89,* 42-56.

119. Das, S.; Jana, B.; Debnath, T.; Ghoshal, A.; Das, A. K.; Patra, A., Strategy toward Designing Semiconducting Polymer Nanoparticle–Multichomophoric Dye Assembly. *J. Phys. Chem. C* **2017,** *121,* 4050-4059.

120. Kumar, A.; Dey, A.; Dhir, A.; Kabra, D., Quantitative Estimation of Exciton Quenching Strength at Interface of Charge Injection Layers and Organic Semiconductor. *Org. Electron.* **2017,** *42,* 28-33.

121. Zhang, L. Q.; Wang, Y. H.; Sui, N.; Kang, Z. H.; Huang, T. H.; Ma, Y. G.; Zhang, H. Z., Theoretical and Experimental Study of Photophysical Characteristics between Poly(9,9-

Dioctylfluorene) and Poly(9,9-Dioctylfluorene-Cobenzothiadiazole). *Chin. J. Chem. Phys.* **2013,** *26,* 387-392.

122. Tilley, A. J.; Danczak, S. M.; Browne, C.; Young, T.; Tan, T.; Ghiggino, K. P.; Smith, T. A.; White, J., Synthesis and Fluorescence Characterization of MEHPPV Oligomers. *J. Org. Chem.* **2011,** *76,* 3372-3380.

123. Kim, J.; Lee, T. S., Emission Tuning with Size-Controllable Polymer Dots from a Single Conjugated Polymer. *Small* **2018,** *14,* 1702758.

124. Wu, C.; Hansen, S. J.; Hou, Q.; Yu, J.; Zeigler, M.; Jin, Y.; Burnham, D. R.; McNeill, J. D.; Olson, J. M.; Chiu, D. T., Design of Highly Emissive Polymer Dot Bioconjugates for in Vivo Tumor Targeting. *Angew. Chem. Int. Ed.* **2011,** *50,* 3430-3434.

125. Yao, J.; Larson, D. R.; Vishwasrao, H. D.; Zipfel, W. R.; Webb, W. W., Blinking and Nonradiant Dark Fraction of Water-Soluble Quantum Dots in Aqueous Solution. *PNAS* **2005,** *102,* 14284-14289.

126. Naahidi, S.; Jafari, M.; Edalat, F.; Raymond, K.; Khademhosseini, A.; Chen, P., Biocompatibility of Engineered Nanoparticles for Drug Delivery. *J. Controlled Release* **2013,** *166,* 182-194.

127. Williams, D. F., *The Williams Dictionary of Biomaterials*. Liverpool University Press: Liverpool UK, 1999.

128. Ye, F.; White, C. C.; Jin, Y.; Hu, X.; Hayden, S.; Zhang, X.; Gao, X.; Kavanagh, T. J.; Chiu, D. T., Toxicity and Oxidative Stress Induced by Semiconducting Polymer Dots in RAW264.7 Mouse Macrophages. *Nanoscale* **2015,** *7,* 10085-10093.

129. Han, Y.; Li, X.; Chen, H.; Hu, X.; Luo, Y.; Wang, T.; Wang, Z.; Li, Q.; Fan, C.; Shi, J.; Wang, L.; Zhao, Y.; Wu, C.; Chen, N., Real-Time Imaging of Endocytosis and Intracellular Trafficking of Semiconducting Polymer Dots. *ACS Appl. Mater. Interfaces* **2017,** *9,* 21200-21208.

130. Lyu, Y.; Zeng, J.; Jiang, Y.; Zhen, X.; Wang, T.; Qiu, S.; Lou, X.; Gao, M.; Pu, K., Enhancing Both Biodegradability and Efficacy of Semiconducting Polymer Nanoparticles for Photoacoustic Imaging and Photothermal Therapy. *ACS Nano* **2018,** *12,* 1801-1810.

131. Jiang, Y.; Upputuri, P. K.; Xie, C.; Zeng, Z.; Sharma, A.; Zhen, X.; Li, J.; Huang, J.; Pramanik, M.; Pu, K., Metabolizable Semiconducting Polymer Nanoparticles for Second Near-Infrared Photoacoustic Imaging. *Adv. Mater.* **2019,** *31,* 1808166.

132. Fang, C.-C.; Chou, C.-C.; Yang, Y.-Q.; Wei-Kai, T.; Wang, Y.-T.; Chan, Y.-H., Multiplexed Detection of Tumor Markers with Multicolor Polymer Dot-Based Immunochromatography Test Strip. *Anal. Chem.* **2018,** *90,* 2134-2140.

133. Luo, J.-H.; Cheng, D.; Li, P.-X.; Yao, Y.; Chen, S.-H.; Yuan, R.; Xu, W.-J., An Electrochemiluminescent Sensor Based on Functionalized Conjugated Polymer Dots for the Ultrasensitive Detection of Cu^{2+}. *Chem. Commun.* **2018,** *54,* 2777-2780.

134. Shi, C. Y.; Deng, N.; Liang, J. J.; Zhou, K. N.; Fu, Q. Q.; Tang, Y., A Fluorescent Polymer Dots Positive Readout Fluorescent Quenching Lateral Flow Sensor for Ractopamine Rapid Detection. *Anal. Chim. Acta* **2015,** *854,* 202-208.

135. Fang, X.; Ju, B.; Liu, Z.; Wang, F.; Xi, G.; Sun, Z.; Chen, H.; Sui, C.; Wang, M.; Wu, C., Compact Conjugated Polymer Dots with Covalently Incorporated Metalloporphyrins for Hypoxia Bioimaging. *ChemBioChem* **2019,** *20,* 521-525.

136. Chen, X.; Liu, Z.; Li, R.; Shan, C.; Zeng, Z.; Xue, B.; Yuan, W.; Mo, C.; Xi, P.; Wu, C.; Sun, Y., Multicolor Super-Resolution Fluorescence Microscopy with Blue and Carmine Small Photoblinking Polymer Dots. *ACS Nano* **2017,** *11,* 8084-8091.

137. Wang, C.-Z.; Chen, J.-L.; Tang, Y.; Zang, Y.; Chen, G.-R.; James, T. D.; Li, J.; Wu, C.; He, X.-P., Supramolecular Polymer Dot Ensemble for Ratiometric Detection of Lectins and Targeted Delivery of Imaging Agents. *ACS Appl. Mater. Interfaces* **2017,** *9,* 3272-3276.

138. Yu, J.; Wu, C.; Sahu, S. P.; Fernando, L. P.; Szymanski, C.; McNeill, J., Nanoscale 3D Tracking with Conjugated Polymer Nanoparticles. *J. Am. Chem. Soc.* **2009,** *131,* 18410-18414.

139. Xiong, L.; Shuhendler, A. J.; Rao, J., Self-Luminescing BRET-FRET Near-Infrared Dots for in Vivo Lymph-Node Mapping and Tumour Imaging. *Nat. Commun.* **2012,** *3,* 1193.

140. Liu, Y.; Liu, J.; Chen, D.; Wang, X.; Liu, Z.; Liu, H.; Jiang, L.; Wu, C.; Zou, Y., Quinoxaline-Based Semiconducting Polymer Dots for in Vivo NIR-II Fluorescence Imaging. *Macromolecules* **2019,** *52,* 5735-5740.

141. Hassan, A. M.; Wu, X.; Jarrett, J. W.; Xu, S.; Yu, J.; Miller, D. R.; Perillo, E. P.; Liu, Y.-L.; Chiu, D. T.; Yeh, H.-C.; Dunn, A. K., Polymer Dots Enable Deep in Vivo Multiphoton Fluorescence Imaging of Microvasculature. *Biomed. Opt. Express* **2019,** *10,* 584-599.

142. Pu, K.; Shuhendler, A. J.; Jokerst, J. V.; Mei, J.; Gambhir, S. S.; Bao, Z.; Rao, J., Semiconducting Polymer Nanoparticles as Photoacoustic Molecular Imaging Probes in Living Mice. *Nat. Nanotechnol.* **2014,** *9,* 233.

143. Qin, X.; Chen, H.; Yang, H.; Wu, H.; Zhao, X.; Wang, H.; Chour, T.; Neofytou, E.; Ding, D.; Daldrup-Link, H.; Heilshorn, S. C.; Li, K.; Wu, J. C., Photoacoustic Imaging of Embryonic Stem Cell-Derived Cardiomyocytes in Living Hearts with Ultrasensitive Semiconducting Polymer Nanoparticles. *Adv. Funct. Mater.* **2018,** *28,* 1704939.

144. Shi, H.; Ma, X.; Zhao, Q.; Liu, B.; Qu, Q.; An, Z.; Zhao, Y.; Huang, W., Ultrasmall Phosphorescent Polymer Dots for Ratiometric Oxygen Sensing and Photodynamic Cancer Therapy. *Adv. Funct. Mater.* **2014,** *24,* 4823-4830.

145. Geng, J.; Sun, C.; Liu, J.; Liao, L.-D.; Yuan, Y.; Thakor, N.; Wang, J.; Liu, B., Biocompatible Conjugated Polymer Nanoparticles for Efficient Photothermal Tumor Therapy. *Small* **2015,** *11,* 1603-1610.

146. Chang, K.; Gao, D.; Qi, Q.; Liu, Y.; Yuan, Z., Engineering Biocompatible Benzodithiophene-Based Polymer Dots with Tunable Absorptions as High-Efficiency Theranostic Agents for Multiscale Photoacoustic Imaging-Guided Photothermal Therapy. *Biomater. Sci.* **2019,** *7,* 1486-1492.

147. Li, J.; Jiang, R.; Wang, Q.; Li, X.; Hu, X.; Yuan, Y.; Lu, X.; Wang, W.; Huang, W.; Fan, Q., Semiconducting Polymer Nanotheranostics for NIR-II/Photoacoustic Imaging-Guided Photothermal Initiated Nitric Oxide/Photothermal Therapy. *Biomaterials* **2019,** *217,* 119304.

148. Sun, W.; Hayden, S.; Jin, Y.; Rong, Y.; Yu, J.; Ye, F.; Chan, Y.-H.; Zeigler, M.; Wu, C.; Chiu, D. T., A Versatile Method for Generating Semiconducting Polymer Dot Nanocomposites. *Nanoscale* **2012,** *4,* 7246-7249.

149. You, P.-Y.; Li, F.-C.; Liu, M.-H.; Chan, Y.-H., Colorimetric and Fluorescent Dual-Mode Immunoassay Based on Plasmon-Enhanced Fluorescence of Polymer Dots for Detection of PSA in Whole Blood. *ACS Appl. Mater. Interfaces* **2019,** *11,* 9841-9849.

150. Song, G.; Zheng, X.; Wang, Y.; Xia, X.; Chu, S.; Rao, J., A Magneto-Optical Nanoplatform for Multimodality Imaging of Tumors in Mice. *ACS Nano* **2019,** *13,* 7750-7758.

151. Chan, Y.-H.; Ye, F.; Gallina, M. E.; Zhang, X.; Jin, Y.; Wu, I. C.; Chiu, D. T., Hybrid Semiconducting Polymer Dot–Quantum Dot with Narrow-Band Emission, Near-Infrared Fluorescence, and High Brightness. *J. Am. Chem. Soc.* **2012,** *134,* 7309-7312.

152. Ma, M.; Lei, M.; Tan, X.; Tan, F.; Li, N., Theranostic Liposomes Containing Conjugated Polymer Dots and Doxorubicin for Bio-Imaging and Targeted Therapeutic Delivery. *RSC Adv.* **2016,** *6,* 1945-1957.

153. Cai, Z.; Da, Z.; Lin, X.; Chen, Y.; Wu, M.; Wei, Z.; Zhang, Z.; Liu, X.; Yao, C., Glutathione Responsive Micelles Incorporated with Semiconducting Polymer Dots and Doxorubicin for Cancer Photothermal-Chemotherapy. *Nanotechnology* **2017,** *28,* 425102.

154. Hermanson, G. T., *Bioconjugate Techniques*. Academic Press: 2013.

155. Chang, K.; Liu, Z.; Fang, X.; Chen, H.; Men, X.; Yuan, Y.; Sun, K.; Zhang, X.; Yuan, Z.; Wu, C., Enhanced Phototherapy by Nanoparticle-Enzyme via Generation and Photolysis of Hydrogen Peroxide. *Nano Lett.* **2017,** *17,* 4323-4329.

156. Sun, J.; Ling, P.; Gao, F., A Mitochondria-Targeted Ratiometric Biosensor for pH Monitoring and Imaging in Living Cells with Congo-Red-Functionalized Dual-Emission Semiconducting Polymer Dots. *Anal. Chem.* **2017,** *89,* 11703-11710.

157. Chan, Y.-H.; Wu, C.; Ye, F.; Jin, Y.; Smith, P. B.; Chiu, D. T., Development of Ultrabright Semiconducting Polymer Dots for Ratiometric pH Sensing. *Anal. Chem.* **2011,** *83,* 1448-1455.

158. Zhang, Y.; Ye, F.; Sun, W.; Yu, J.; Wu, I. C.; Rong, Y.; Zhang, Y.; Chiu, D. T., Light-Induced Crosslinkable Semiconducting Polymer Dots. *Chem. Sci.* **2015,** *6,* 2102-2109.

159. Wang, L.; Wu, C.-F.; Wang, H.-Y.; Wang, Y.-F.; Chen, Q.-D.; Han, W.; Qin, W.-P.; McNeill, J.; Sun, H.-B., Internal Structure-Mediated Ultrafast Energy Transfer in Self-Assembled Polymer-Blend Dots. *Nanoscale* **2013,** *5,* 7265-7270.

160. Broekaert, J. A., Inductively Coupled Plasma Spectrometry. In *Handbook of Spectroscopy*, Gauglitz, G.; Moore, D. S., Eds. 2014; pp 583-646.

161. Sauer, M.; Hofkens, J.; Enderlein, J., Basic Principles of Fluorescence Spectroscopy. In *Handbook of Fluorescence Spectroscopy and Imaging*, Sauer, M.; Hofkens, J.; Enderlein, J., Eds. 2011; pp 1-30.

162. Lakowicz, J. R., *Principles of Fluorescence Spectroscopy*. 3rd ed.; Springer Science + Business Media, LLC: New York, NY, 2006.

163. Diaspro, A.; Chirico, G.; Usai, C.; Ramoino, P.; Dobrucki, J., Photobleaching. In *Handbook of Biological Confocal Microscopy*, Pawley, J. B., Ed. Springer US: Boston, MA, 2006; pp 690-702.

164. Berera, R.; van Grondelle, R.; Kennis, J. T. M., Ultrafast Transient Absorption Spectroscopy: Principles and Application to Photosynthetic Systems. *Photosynth. Res.* **2009,** *101,* 105-118.

165. Waters, J. C., Accuracy and Precision in Quantitative Fluorescence Microscopy. *J. Cell Bio.* **2009,** *185,* 1135-1148.

166. Chou, K. F.; Dennis, A. M., Förster Resonance Energy Transfer between Quantum Dot Donors and Quantum Dot Acceptors. *Sensors* **2015,** *15,* 13288-13325.

167. Hwang, I.; Scholes, G. D., Electronic Energy Transfer and Quantum-Coherence in π-Conjugated Polymers. *Chem. Mater.* **2011,** *23,* 610-620.

168. Doose, S.; Neuweiler, H.; Sauer, M., Fluorescence Quenching by Photoinduced Electron Transfer: A Reporter for Conformational Dynamics of Macromolecules. *ChemPhysChem* **2009,** *10,* 1389-1398.

169. Atkins, P., *Physical Chemistry*. 6th ed.; Oxford University Press: Oxford, UK;, 1998.

170. Filipe, V.; Hawe, A.; Jiskoot, W., Critical Evaluation of Nanoparticle Tracking Analysis (NTA) by Nanosight for the Measurement of Nanoparticles and Protein Aggregates. *Pharm. Res.* **2010,** *27,* 796-810.

171. *Enhancing NTA Accuracy and Repeatability with Flow Mode Measurements*; TN160808; Malvern Instruments Limited: 2017.

172. Gerritzen, M. J. H.; Martens, D. E.; Wijffels, R. H.; Stork, M., High Throughput Nanoparticle Tracking Analysis for Monitoring Outer Membrane Vesicle Production. *J. Extracellular Vesicles* **2017,** *6*, 1333883.

173. Pecora, R., Dynamic Light Scattering Measurement of Nanometer Particles in Liquids. *J. Nanopart. Res.* **2000,** *2*, 123-131.

174. Hassan, P. A.; Rana, S.; Verma, G., Making Sense of Brownian Motion: Colloid Characterization by Dynamic Light Scattering. *Langmuir* **2015,** *31*, 3-12.

175. Stetefeld, J.; McKenna, S. A.; Patel, T. R., Dynamic Light Scattering: A Practical Guide and Applications in Biomedical Sciences. *Biophys. Rev.* **2016,** *8*, 409-427.

176. Haugstad, G., *Atomic Force Microscopy : Understanding Basic Modes and Advanced Applications*. John Wiley & Sons, Incorporated: Somerset, USA, 2012.

177. Hölscher, H., AFM, Tapping Mode. In *Encyclopedia of Nanotechnology*, Bhushan, B., Ed. Springer Netherlands: Dordrecht, 2012; pp 99-99.

178. Hunter, R. J., *Foundations of Colloid Science*. Oxford University Press: New York, 1992; Vol. I.

179. Clogston, J. D.; Patri, A. K., Zeta Potential Measurement. In *Characterization of Nanoparticles Intended for Drug Delivery*, McNeil, S. E., Ed. Humana Press: Totowa, NJ, 2011; pp 63-70.

180. Sun, W.; Ye, F.; Gallina, M. E.; Yu, J.; Wu, C.; Chiu, D. T., Lyophilization of Semiconducting Polymer Dot Bioconjugates. *Anal. Chem.* **2013,** *85*, 4316-4320.

181. Singh, L.; Samra, K. S.; Singh, R., Optical and Structural Modifications in Heavy Ion Irradiated Polystyrene. *J. Macromol. Sci., Part B* **2007,** *46*, 749-759.

182. Traiphol, R.; Sanguansat, P.; Srikhirin, T.; Kerdcharoen, T.; Osotchan, T., Spectroscopic Study of Photophysical Change in Collapsed Coils of Conjugated Polymers: Effects of Solvent and Temperature. *Macromolecules* **2006,** *39*, 1165-1172.

183. Xu, Z.; Tsai, H.; Wang, H.-L.; Cotlet, M., Solvent Polarity Effect on Chain Conformation, Film Morphology, and Optical Properties of a Water-Soluble Conjugated Polymer. *J. Phys. Chem. B* **2010,** *114*, 11746-11752.

184. Gooding, A. K.; Gómez, D. E.; Mulvaney, P., The Effects of Electron and Hole Injection on the Photoluminescence of CdSe/CdS/ZnS Nanocrystal Monolayers. *ACS Nano* **2008,** *2*, 669-676.

185. Chan, Y.-H.; Wu, P.-J., Semiconducting Polymer Nanoparticles as Fluorescent Probes for Biological Imaging and Sensing. *Part. Part. Syst. Char.* **2015,** *32,* 11-28.

186. Liu, H.-Y.; Wu, P.-J.; Kuo, S.-Y.; Chen, C.-P.; Chang, E.-H.; Wu, C.-Y.; Chan, Y.-H., Quinoxaline-Based Polymer Dots with Ultrabright Red to Near-Infrared Fluorescence for in Vivo Biological Imaging. *J. Am. Chem. Soc.* **2015,** *137,* 10420-10429.

187. Li, J.; Rao, J.; Pu, K., Recent Progress on Semiconducting Polymer Nanoparticles for Molecular Imaging and Cancer Phototherapy. *Biomaterials* **2018,** *155,* 217-235.

188. Tang, Y.; Chen, H.; Chang, K.; Liu, Z.; Wang, Y.; Qu, S.; Xu, H.; Wu, C., Photo-Cross-Linkable Polymer Dots with Stable Sensitizer Loading and Amplified Singlet Oxygen Generation for Photodynamic Therapy. *ACS Appl. Mater. Interfaces* **2017,** *9,* 3419-3431.

189. Salazar-Alvarez, G.; Muhammed, M.; Zagorodni, A. A., Novel Flow Injection Synthesis of Iron Oxide Nanoparticles with Narrow Size Distribution. *Chem. Eng. Sci.* **2006,** *61,* 4625-4633.

190. Lobry, E.; Jasinski, F.; Penconi, M.; Chemtob, A.; Croutxé-Barghorn, C.; Oliveros, E.; Braun, A. M.; Criqui, A., Continuous-Flow Synthesis of Polymer Nanoparticles in a Microreactor Via Miniemulsion Photopolymerization. *RSC Adv.* **2014,** *4,* 43756-43759.

191. Visaveliya, N.; Hoffmann, C.; Groß, A.; Täuscher, E.; Ritter, U.; Koehler, J. M., Micro-Flow Assisted Synthesis of Fluorescent Polymer Nanoparticles with Tuned Size and Surface Properties. *Nanotechnol. Rev.* **2016,** *5,* 259-272.

192. Visaveliya, N.; Knauer, A.; Köhler, J. M., Application of Polyionic Macromolecules in Micro Flow Syntheses of Nanoparticles. *Macromol. Chem. Phys.* **2017,** *218,* 1600371.

193. Park, J. I.; Saffari, A.; Kumar, S.; Günther, A.; Kumacheva, E., Microfluidic Synthesis of Polymer and Inorganic Particulate Materials. *Annu. Rev. Mater. Res.* **2010,** *40,* 415-443.

194. Karnik, R.; Gu, F.; Basto, P.; Cannizzaro, C.; Dean, L.; Kyei-Manu, W.; Langer, R.; Farokhzad, O. C., Microfluidic Platform for Controlled Synthesis of Polymeric Nanoparticles. *Nano Lett.* **2008,** *8,* 2906-2912.

195. Valencia, P. M.; Farokhzad, O. C.; Karnik, R.; Langer, R., Microfluidic Technologies for Accelerating the Clinical Translation of Nanoparticles. *Nat. Nanotechnol.* **2012,** *7,* 623.

196. Weibel, D. B.; Whitesides, G. M., Applications of Microfluidics in Chemical Biology. *Curr. Opin. Chem. Biol.* **2006,** *10,* 584-591.

197. Singh, R.; Veeramani, K.; Bajpai, R.; Kumar, A., High-Throughput Template-Free Continuous Flow Synthesis of Polyaniline Nanofibers. *Ind. Eng. Chem. Res.* **2019,** *58,* 5864-5872.

198. Couto, R.; Chambon, S.; Aymonier, C.; Mignard, E.; Pavageau, B.; Erriguible, A.; Marre, S., Microfluidic Supercritical Antisolvent Continuous Processing and Direct Spray-Coating of Poly(3-Hexylthiophene) Nanoparticles for OFET Devices. *Chem. Commun.* **2015,** *51*, 1008-1011.

199. Abelha, T. F.; Phillips, T. W.; Bannock, J. H.; Nightingale, A. M.; Dreiss, C. A.; Kemal, E.; Urbano, L.; deMello, J. C.; Green, M.; Dailey, L. A., Bright Conjugated Polymer Nanoparticles Containing a Biodegradable Shell Produced at High Yields and with Tuneable Optical Properties by a Scalable Microfluidic Device. *Nanoscale* **2017,** *9*, 2009-2019.

200. Guo, B.; Chen, J.; Chen, N.; Middha, E.; Xu, S.; Pan, Y.; Wu, M.; Li, K.; Liu, C.; Liu, B., High-Resolution 3D NIR-II Photoacoustic Imaging of Cerebral and Tumor Vasculatures Using Conjugated Polymer Nanoparticles as Contrast Agent. *Adv. Mater.* **2019,** *31*, 1808355.

201. Wang, Z.; Guo, B.; Middha, E.; Huang, Z.; Hu, Q.; Fu, Z.; Liu, B., Microfluidics-Prepared Uniform Conjugated Polymer Nanoparticles for Photo-Triggered Immune Microenvironment Modulation and Cancer Therapy. *ACS Appl. Mater. Interfaces* **2019,** *11*, 11167-11176.

202. Lohse Samuel, E., Size and Shape Control of Metal Nanoparticles in Millifluidic Reactors. *Phys. Sci. Rev.* **2018,** *3*.

203. Roberts, E. J.; Habas, S. E.; Wang, L.; Ruddy, D. A.; White, E. A.; Baddour, F. G.; Griffin, M. B.; Schaidle, J. A.; Malmstadt, N.; Brutchey, R. L., High-Throughput Continuous Flow Synthesis of Nickel Nanoparticles for the Catalytic Hydrodeoxygenation of Guaiacol. *ACS Sustainable Chem. Eng.* **2017,** *5*, 632-639.

204. Lohse, S. E.; Eller, J. R.; Sivapalan, S. T.; Plews, M. R.; Murphy, C. J., A Simple Millifluidic Benchtop Reactor System for the High-Throughput Synthesis and Functionalization of Gold Nanoparticles with Different Sizes and Shapes. *ACS Nano* **2013,** *7*, 4135-4150.

205. Vikram, A.; Kumar, V.; Ramesh, U.; Balakrishnan, K.; Oh, N.; Deshpande, K.; Ewers, T.; Trefonas, P.; Shim, M.; Kenis, P. J. A., A Millifluidic Reactor System for Multistep Continuous Synthesis of InP/ZnSeS Nanoparticles. *ChemNanoMat* **2018,** *4*, 943-953.

206. Hong, L.; Cheung, T.-L.; Rao, N.; Ouyang, Q.; Wang, Y.; Zeng, S.; Yang, C.; Cuong, D.; Chong, P. H. J.; Liu, L.; Law, W.-C.; Yong, K.-T., Millifluidic Synthesis of Cadmium Sulfide Nanoparticles and Their Application in Bioimaging. *RSC Adv.* **2017,** *7*, 36819-36832.

207. Tran, T.-T.; Nguyen, M.-H.; Tan, Y. Z.; Chew, J. W.; Khan, S. A.; Hadinoto, K., Millifluidic Synthesis of Amorphous Drug-Polysaccharide Nanoparticle Complex with Tunable Size Intended for Supersaturating Drug Delivery Applications. *Eur. J. Pharm. Biopharm.* **2017,** *112*, 196-203.

208. Dong, B.; Hadinoto, K., Direct Comparison between Millifluidic and Bulk-Mixing Platform in the Synthesis of Amorphous Drug-Polysaccharide Nanoparticle Complex. *Int. J. Pharm.* **2017,** *523,* 42-51.

209. Libi, S.; Calenic, B.; Astete Carlos, E.; Kumar, C.; Sabliov Cristina, M., Investigation on Hemolytic Effect of Poly(Lactic Co-Glycolic) Acid Nanoparticles Synthesized Using Continuous Flow and Batch Processes. In *Nanotechnol. Rev.*, 2017; Vol. 6, p 209.

210. Lepeltier, E.; Bourgaux, C.; Couvreur, P., Nanoprecipitation and the "Ouzo Effect": Application to Drug Delivery Devices. *Adv. Drug Delivery Rev.* **2014,** *71,* 86-97.

211. Chorny, M.; Fishbein, I.; Danenberg, H. D.; Golomb, G., Lipophilic Drug Loaded Nanospheres Prepared by Nanoprecipitation: Effect of Formulation Variables on Size, Drug Recovery and Release Kinetics. *J. Controlled Release* **2002,** *83,* 389-400.

212. Ye, F.; Wu, C.; Jin, Y.; Wang, M.; Chan, Y.-H.; Yu, J.; Sun, W.; Hayden, S.; Chiu, D. T., A Compact and Highly Fluorescent Orange-Emitting Polymer Dot for Specific Subcellular Imaging. *Chem. Commun.* **2012,** *48,* 1778-1780.

213. Kim, S.; Lim, C.-K.; Na, J.; Lee, Y.-D.; Kim, K.; Choi, K.; Leary, J. F.; Kwon, I. C., Conjugated Polymer Nanoparticles for Biomedical in Vivo Imaging. *Chem. Commun.* **2010,** *46,* 1617-1619.

214. Pu, K.; Shuhendler, A. J.; Valta, M. P.; Cui, L.; Saar, M.; Peehl, D. M.; Rao, J., Phosphorylcholine-Coated Semiconducting Polymer Nanoparticles as Rapid and Efficient Labeling Agents for in Vivo Cell Tracking. *Adv. Healthcare Mater.* **2014,** *3,* 1292-1298.

215. Feng, X.; Lv, F.; Liu, L.; Tang, H.; Xing, C.; Yang, Q.; Wang, S., Conjugated Polymer Nanoparticles for Drug Delivery and Imaging. *ACS Appl. Mater. Interfaces* **2010,** *2,* 2429-2435.

216. Hildebrandt, N.; Spillmann, C. M.; Algar, W. R.; Pons, T.; Stewart, M. H.; Oh, E.; Susumu, K.; Díaz, S. A.; Delehanty, J. B.; Medintz, I. L., Energy Transfer with Semiconductor Quantum Dot Bioconjugates: A Versatile Platform for Biosensing, Energy Harvesting, and Other Developing Applications. *Chem. Rev.* **2017,** *117,* 536-711.

217. Zhang, X.; Yu, J.; Rong, Y.; Ye, F.; Chiu, D. T.; Uvdal, K., High-Intensity Near-IR Fluorescence in Semiconducting Polymer Dots Achieved by Cascade FRET Strategy. *Chem. Sci.* **2013,** *4,* 2143-2151.

218. Nasirian, V.; Chabok, A.; Barati, A.; Rafienia, M.; Arabi, M. S.; Shamsipur, M., Ultrasensitive Aflatoxin B1 Assay Based on FRET from Aptamer Labelled Fluorescent Polymer Dots to Silver Nanoparticles Labeled with Complementary DNA. *Microchim. Acta* **2017,** *184,* 4655-4662.

219. Bhattacharyya, S.; Patra, A., Photoluminescence Quenching of Semiconducting Polymer Nanoparticles in Presence of Au Nanoparticles. *Bull. Mater. Sci.* **2012,** *35,* 719-725.

220. Shi, X.-M.; Mei, L.-P.; Wang, Q.; Zhao, W.-W.; Xu, J.-J.; Chen, H.-Y., Energy Transfer between Semiconducting Polymer Dots and Gold Nanoparticles in a Photoelectrochemical System: A Case Application for Cathodic Bioanalysis. *Anal. Chem.* **2018,** *90,* 4277-4281.

221. Huang, Y.-C.; Chen, C.-P.; Wu, P.-J.; Kuo, S.-Y.; Chan, Y.-H., Coumarin Dye-Embedded Semiconducting Polymer Dots for Ratiometric Sensing of Fluoride Ions in Aqueous Solution and Bio-Imaging in Cells. *J. Mater. Chem. B* **2014,** *2,* 6188-6191.

222. Childress, E. S.; Roberts, C. A.; Sherwood, D. Y.; LeGuyader, C. L. M.; Harbron, E. J., Ratiometric Fluorescence Detection of Mercury Ions in Water by Conjugated Polymer Nanoparticles. *Anal. Chem.* **2012,** *84,* 1235-1239.

223. Kuo, S.-Y.; Li, H.-H.; Wu, P.-J.; Chen, C.-P.; Huang, Y.-C.; Chan, Y.-H., Dual Colorimetric and Fluorescent Sensor Based on Semiconducting Polymer Dots for Ratiometric Detection of Lead Ions in Living Cells. *Anal. Chem.* **2015,** *87,* 4765-4771.

224. Hou, W.; Yuan, Y.; Sun, Z.; Guo, S.; Dong, H.; Wu, C., Ratiometric Fluorescent Detection of Intracellular Singlet Oxygen by Semiconducting Polymer Dots. *Anal. Chem.* **2018,** *90,* 14629-14634.

225. Shuhendler, A. J.; Pu, K.; Cui, L.; Uetrecht, J. P.; Rao, J., Real-Time Imaging of Oxidative and Nitrosative Stress in the Liver of Live Animals for Drug-Toxicity Testing. *Nat. Biotechnol.* **2014,** *32,* 373-380.

226. Grimland, J. L.; Wu, C.; Ramoutar, R. R.; Brumaghim, J. L.; McNeill, J., Photosensitizer-Doped Conjugated Polymer Nanoparticles with High Cross-Sections for One- and Two-Photon Excitation. *Nanoscale* **2011,** *3,* 1451-1455.

227. Haimov, E.; Weitman, H.; Ickowicz, D.; Malik, Z.; Ehrenberg, B., Pdots Nanoparticles Load Photosensitizers and Enhance Efficiently Their Photodynamic Effect by FRET. *RSC Adv.* **2015,** *5,* 18482-18491.

228. Haupt, S.; Lazar, I.; Weitman, H.; Senge, M. O.; Ehrenberg, B., Pdots, a New Type of Nanoparticle, Bind to mTHPC via Their Lipid Modified Surface and Exhibit Very High FRET Efficiency between the Core and the Sensitizer. *PCCP* **2015,** *17,* 11412-11422.

229. Li, S.; Chang, K.; Sun, K.; Tang, Y.; Cui, N.; Wang, Y.; Qin, W.; Xu, H.; Wu, C., Amplified Singlet Oxygen Generation in Semiconductor Polymer Dots for Photodynamic Cancer Therapy. *ACS Appl. Mater. Interfaces* **2016,** *8,* 3624-3634.

230. Wang, X.-H.; Peng, H.-S.; Yang, W.; Ren, Z.-D.; Liu, X.-M.; Liu, Y.-A., Indocyanine Green-Platinum Porphyrins Integrated Conjugated Polymer Hybrid Nanoparticles for Near-Infrared-Triggered Photothermal and Two-Photon Photodynamic Therapy. *J. Mater. Chem. B* **2017,** *5,* 1856-1862.

231. Kim, Y. K.; Lee, J. E.; Ryplida, B.; Choi, C. A.; Mazrad, Z. A. I.; Lee, G.; Lee, S.; In, I.; Jeong, J. H.; Park, S. Y., Redox-Responsive FRET-Based Polymer Dot with BODIPY for

Fluorescence Imaging-Guided Chemotherapy of Tumor. *Eur. J. Pharm. Biopharm.* **2018,** *132,* 200-210.

232. Palner, M.; Pu, K.; Shao, S.; Rao, J., Semiconducting Polymer Nanoparticles with Persistent Near-Infrared Luminescence for in Vivo Optical Imaging. *Angew. Chem. Int. Ed.* **2015,** *54,* 11477-11480.

233. Xie, C.; Zhen, X.; Miao, Q.; Lyu, Y.; Pu, K., Self-Assembled Semiconducting Polymer Nanoparticles for Ultrasensitive Near-Infrared Afterglow Imaging of Metastatic Tumors. *Adv. Mater.* **2018,** *30,* 1801331.

234. Sun, Z.; Liu, S.; Liu, Z.; Qin, W.; Chen, D.; Xu, G.; Wu, C., FRET Acceptor Suppressed Single-Particle Photobleaching in Semiconductor Polymer Dots. *Opt. Lett.* **2016,** *41,* 2370-2373.

235. Taniguchi, M.; Lindsey, J. S., Database of Absorption and Fluorescence Spectra of >300 Common Compounds for Use in PhotochemCAD. *Photochem. Photobiol.* **2018,** *94,* 290-327.

236. Wan, Y.; Zheng, L.; Sun, Y.; Zhang, D., Multifunctional Semiconducting Polymer Dots for Imaging, Detection, and Photo-Killing of Bacteria. *J. Mater. Chem. B* **2014,** *2,* 4818-4825.

237. Chan, Y. H.; Gallina, M. E.; Zhang, X. J.; Wu, I. C.; Jin, Y. H.; Sun, W.; Chiu, D. T., Reversible Photoswitching of Spiropyran-Conjugated Semiconducting Polymer Dots. *Anal. Chem.* **2012,** *84,* 9431-9438.

238. Cao, F. W.; Xiong, L. Q., Folic Acid Functionalized PFBT Fluorescent Polymer Dots for Tumor Imaging. *Chin. J. Chem* . **2016,** *34,* 570-575.

239. Arfken, G. B.; Weber, H. J., *Mathematical Methods for Physicists International Student Edition*. 6th ed.; Elsevier: London, UK, 2005.

240. Leow, C.; Ohnishi, T.; Matsumura, M., Diffusion Lengths of Excitons in Polymers in Relation to External Quantum Efficiency of the Photocurrent of Solar Cells. *J. Phys. Chem. C* **2014,** *118,* 71-76.

241. Mikhnenko, O. V.; Kuik, M.; Lin, J.; van der Kaap, N.; Nguyen, T.-Q.; Blom, P. W. M., Trap-Limited Exciton Diffusion in Organic Semiconductors. *Adv. Mater.* **2014,** *26,* 1912-1917.

242. Groff, L. C.; Wang, X.; McNeill, J. D., Measurement of Exciton Transport in Conjugated Polymer Nanoparticles. *J. Phys. Chem. C* **2013,** *117,* 25748-25755.

243. Gruber, H. J.; Hahn, C. D.; Kada, G.; Riener, C. K.; Harms, G. S.; Ahrer, W.; Dax, T. G.; Knaus, H.-G., Anomalous Fluorescence Enhancement of Cy3 and Cy3.5 Versus Anomalous Fluorescence Loss of Cy5 and Cy7 Upon Covalent Linking to IgG and Noncovalent Binding to Avidin. *Bioconjugate Chem.* **2000,** *11,* 696-704.

244. Frisch, M.; Trucks, G.; Schlegel, H.; Scuseria, G.; Robb, M.; Cheeseman, J.; Scalmani, G.; Barone, V.; Petersson, G.; Nakatsuji, H., Gaussian 16 Revision B. 01. 2016; Gaussian Inc. *Wallingford CT*.

245. Justino, L. L. G.; Luísa Ramos, M.; Abreu, P. E.; Charas, A.; Morgado, J.; Scherf, U.; Minaev, B. F.; Ågren, H.; Burrows, H. D., Structural and Electronic Properties of Poly(9,9-Dialkylfluorene)-Based Alternating Copolymers in Solution: An NMR Spectroscopy and Density Functional Theory Study. *J. Phys. Chem. C* **2013,** *117,* 17969-17982.

246. Meng, Z.; Hou, W.; Zhou, H.; Zhou, L.; Chen, H.; Wu, C., Therapeutic Considerations and Conjugated Polymer-Based Photosensitizers for Photodynamic Therapy. *Macromol. Rapid Commun.* **2018,** *39,* 1700614.

247. Naessens, M.; Cerdobbel, A.; Soetaert, W.; Vandamme, E. J., Leuconostoc Dextransucrase and Dextran: Production, Properties and Applications. *J. Chem. Technol. Biotechnol.* **2005,** *80,* 845-860.

248. Auerbach, M.; Witt, D.; Toler, W.; Fierstein, M.; Lerner, R. G.; Ballard, H., Clinical Use of the Total Dose Intravenous Infusion of Iron Dextran. *J. Lab. Clin. Med.* **1988,** *111,* 560-565.

249. Heinze, T.; Liebert, T.; Heublein, B.; Hornig, S., Functional Polymers Based on Dextran. In *Polysaccharides II*, Klemm, D., Ed. Springer Berlin Heidelberg: Berlin, Heidelberg, 2006; pp 199-291.

250. Moreno Raja, M.; Lim, P. Q.; Wong, Y. S.; Xiong, G. M.; Zhang, Y.; Venkatraman, S.; Huang, Y., Polymeric Nanomaterials: Methods of Preparation and Characterization. In *Nanocarriers for Drug Delivery*, Mohapatra, S. S.; Ranjan, S.; Dasgupta, N.; Mishra, R. K.; Thomas, S., Eds. Elsevier: 2019; pp 557-653.

251. Tassa, C.; Shaw, S. Y.; Weissleder, R., Dextran-Coated Iron Oxide Nanoparticles: A Versatile Platform for Targeted Molecular Imaging, Molecular Diagnostics, and Therapy. *Acc. Chem. Res.* **2011,** *44,* 842-852.

252. Park, J.-H.; Gu, L.; von Maltzahn, G.; Ruoslahti, E.; Bhatia, S. N.; Sailor, M. J., Biodegradable Luminescent Porous Silicon Nanoparticles for in Vivo Applications. *Nat. Mater.* **2009,** *8,* 331.

253. Selvan, S. T.; Tan, T. T. Y.; Yi, D. K.; Jana, N. R., Functional and Multifunctional Nanoparticles for Bioimaging and Biosensing. *Langmuir* **2010,** *26,* 11631-11641.

254. Liu, Y.; Liu, J.; Zhang, J.; Li, X.; Lin, F.; Zhou, N.; Yang, B.; Lu, L., A Brand-New Generation of Fluorescent Nano-Neural Tracers: Biotinylated Dextran Amine Conjugated Carbonized Polymer Dots. *Biomater. Sci.* **2019,** *7,* 1574-1583.

255. Wognum, A. W.; Lansdorp, P. M. Tetrameric Antibody Complexes for Blocking Non-Specific Labeling of Antigens. US 7387897 B2, 2008.

256. Wognum, A. W.; Thomas, T. E.; Lansdorp, P. M., Use of Tetrameric Antibody Complexes to Stain Cells for Flow Cytometry. *Cytometry* **1987,** *8,* 366-371.

257. Yang, L.; Lang, J. C.; Balasubramanian, P.; Jatana, K. R.; Schuller, D.; Agrawal, A.; Zborowski, M.; Chalmers, J. J., Optimization of an Enrichment Process for Circulating Tumor Cells from the Blood of Head and Neck Cancer Patients through Depletion of Normal Cells. *Biotechnol. Bioeng.* **2009,** *102,* 521-534.

258. Jatana, K. R.; Balasubramanian, P.; McMullen, K. P.; Lang, J. C.; Teknos, T. N.; Chalmers, J. J., Effect of Surgical Intervention on Circulating Tumor Cells in Patients with Squamous Cell Carcinoma of the Head and Neck Using a Negative Enrichment Technology. *Head & Neck* **2016,** *38,* 1799-1803.

259. Liebs, S.; Keilholz, U.; Kehler, I.; Schweiger, C.; Haybäck, J.; Nonnenmacher, A., Detection of Mutations in Circulating Cell-Free DNA in Relation to Disease Stage in Colorectal Cancer. *Cancer Medicine* **2019,** *8,* 3761-3769.

260. Esmaeilsabzali, H.; Beischlag, T. V.; Cox, M. E.; Dechev, N.; Parameswaran, A. M.; Park, E. J., An Integrated Microfluidic Chip for Immunomagnetic Detection and Isolation of Rare Prostate Cancer Cells from Blood. *Biomed. Microdevices* **2016,** *18.*

261. Trotta, T.; Guerra, L.; Piro, D.; d'Apolito, M.; Piccoli, C.; Porro, C.; Giardino, I.; Lepore, S.; Castellani, S.; Di Gioia, S.; Petrella, A.; Maffione, A. B.; Casavola, V.; Capitanio, N.; Conese, M., Stimulation of B2-Adrenergic Receptor Increases CFTR Function and Decreases ATP Levels in Murine Hematopoietic Stem/Progenitor Cells. *J. Cystic Fibrosis* **2015,** *14,* 26-33.

262. Juric, V.; O'Sullivan, C.; Stefanutti, E.; Kovalenko, M.; Greenstein, A.; Barry-Hamilton, V.; Mikaelian, I.; Degenhardt, J.; Yue, P.; Smith, V.; Mikels-Vigdal, A., MMP-9 Inhibition Promotes Anti-Tumor Immunity through Disruption of Biochemical and Physical Barriers to T-Cell Trafficking to Tumors. *PLOS ONE* **2018,** *13,* e0207255.

263. Stenekes, R. J. H.; Talsma, H.; Hennink, W. E., Formation of Dextran Hydrogels by Crystallization. *Biomaterials* **2001,** *22,* 1891-1898.

264. Grote Beverborg, N.; Verweij, N.; Klip, I. T.; van der Wal, H. H.; Voors, A. A.; van Veldhuisen, D. J.; Gansevoort, R. T.; Bakker, S. J. L.; van der Harst, P.; van der Meer, P., Erythropoietin in the General Population: Reference Ranges and Clinical, Biochemical and Genetic Correlates. *PLOS ONE* **2015,** *10,* e0125215.

265. Wognum, A.; Lam, V.; Goudsmit, R.; Krystal, G., A Specific in Vitro Bioassay for Measuring Erythropoietin Levels in Human Serum and Plasma. *Blood* **1990,** *76,* 1323-1329.

266. Bertholon, I.; Lesieur, S.; Labarre, D.; Besnard, M.; Vauthier, C., Characterization of Dextran−Poly(Isobutylcyanoacrylate) Copolymers Obtained by Redox Radical and Anionic Emulsion Polymerization. *Macromolecules* **2006,** *39,* 3559-3567.

267. Liu, Z.; Liu, J.; Sun, Z.; Zhang, Z.; Yuan, Y.; Fang, X.; Wang, F.; Qin, W.; Wu, C., Cooperative Blinking from Dye Ensemble Activated by Energy Transfer for Super-Resolution Cellular Imaging. *Anal. Chem.* **2019,** *91,* 4179-4185.

268. Petryayeva, E.; Algar, W. R., Multiplexed Homogeneous Assays of Proteolytic Activity Using a Smartphone and Quantum Dots. *Anal. Chem.* **2014,** *86,* 3195-3202.

269. Petryayeva, E.; Algar, W. R., Single-Step Bioassays in Serum and Whole Blood with a Smartphone, Quantum Dots and Paper-in-Pdms Chips. *Analyst* **2015,** *140,* 4037-4045.

270. Gupta, R.; Peveler, W. J.; Lix, K.; Algar, W. R., Comparison of Semiconducting Polymer Dots and Semiconductor Quantum Dots for Smartphone-Based Fluorescence Assays. *Anal. Chem.* **2019,** *91,* 10955-10960.

271. Pappu, R. V.; Wang, X.; Vitalis, A.; Crick, S. L., A Polymer Physics Perspective on Driving Forces and Mechanisms for Protein Aggregation. *Arch. Biochem. Biophys.* **2008,** *469,* 132-141.

272. Brunel, F.; Billuart, G.; Dugas, P. Y.; Lansalot, M.; Bourgeat-Lami, E.; Monteil, V., Crystallization of Nanodomains in Polyethylene Latexes. *Macromolecules* **2017,** *50,* 9742-9749.

273. Groves, C.; Greenham, N. C., Monte Carlo Simulations of Organic Photovoltaics. In *Multiscale Modelling of Organic and Hybrid Photovoltaics*, Beljonne, D.; Cornil, J., Eds. Springer Berlin Heidelberg: Berlin, Heidelberg, 2014; pp 257-278.

274. Davis, C. M.; Childress, E. S.; Harbron, E. J., Ensemble and Single-Particle Fluorescence Photomodulation in Diarylethene-Doped Conjugated Polymer Nanoparticles. *J. Phys. Chem. C* **2011,** *115,* 19065-19073.

275. Tsai, H.-Y.; Kim, H.; Massey, M.; Krause, K. D.; Algar, W. R., Concentric FRET: A Review of the Emerging Concept, Theory, and Applications. *Method. Appl. Fluoresc.* **2019,** *7,* 042001.

276. Denizli, B. K.; Can, H. K.; Rzaev, Z. M. O.; Guner, A., Preparation Conditions and Swelling Equilibria of Dextran Hydrogels Prepared by Some Crosslinking Agents. *Polymer* **2004,** *45,* 6431-6435.

277. Lee, K. C. B.; Siegel, J.; Webb, S. E. D.; Lévêque-Fort, S.; Cole, M. J.; Jones, R.; Dowling, K.; Lever, M. J.; French, P. M. W., Application of the Stretched Exponential Function to Fluorescence Lifetime Imaging. *Biophys. J.* **2001,** *81,* 1265-1274.

Appendices

Appendix A Characterization data and criteria for data rejection for Chapter 4

A.1 Additional characterization data

Some Pdots were seen to visibly photobleach under the acquisition conditions of the NTA. Figure A.1 shows the total intensity per frame for PFMEHPPV/PSMA Pdots, measured in scattering mode, where infusion of the syringe pump was stopped immediately before video acquisition. Ignoring diffusion of the particles out of or into the frame, the same population of particles was continuously illuminated and measured for the duration of the 30 s video.

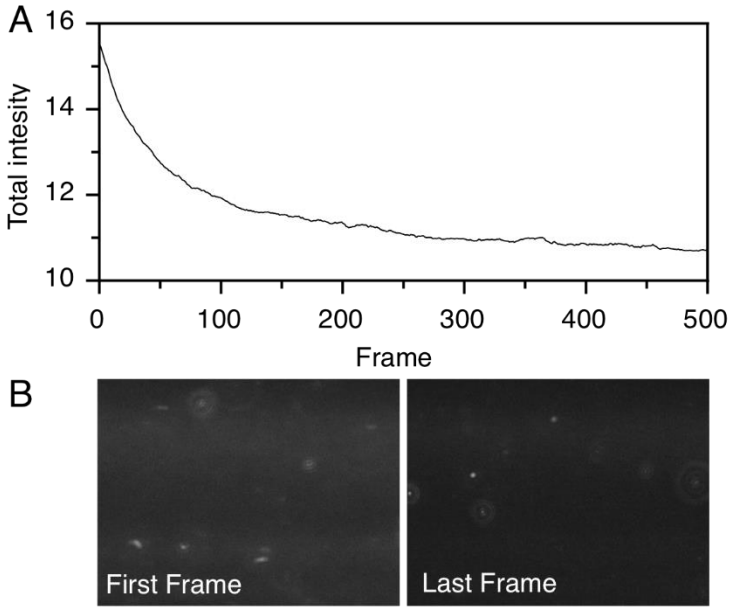

Figure A.1 Photobleaching of PFMEHPPV/PSMA Pdots during NTA video acquisition. Sample was infused for ~10 s at 1000 a.u. and the syringe pump stopped immediately before video acquisition. **(A)** Total intensity of the video frame as a function of frame number. **(B)** The first and last frames of a 30 s NTA video. In addition to well-resolved particles (distinct white spots), indistinct fluorescent material (*i.e.,* small particles or particles not in the focal plane) in the background contribute to the total observed fluorescence.

Table A.1. Selected physical and optical properties of Pdots of varying composition synthesized by the syringe pump method. Values are represented as the mean and standard deviation of three replicates batches. Values highlighted in yellow were deemed unreliable (*vide infra*). Values marked with a hyphen (-) were not measured.

Semiconducting Polymer	Amphiphilic Polymer	D_{NTA} (nm)[a]		D_{DLS} (nm)[d]
		Scattering[b]	Fluorescence[c]	
F8BT	PSMA	59 ± 7	58 ± 6	53 ± 9
F8BT	PMAO	63 ± 20	31 ± 5	-
F8BT	PS-b-PAA	73 ± 24	45 ± 13	-
F8BT	PS-b-PEG	74 ± 2	79 ± 1	-
F8BT	PE-b-PEG	94 ± 8	99 ± 8	-
CNMEHPPV	PSMA	54 ± 1	39 ± 7	48 ± 3
CNMEHPPV	PMAO	67 ± 14	50 ± 10	35 ± 3
CNMEHPPV	PS-b-PAA	66 ± 11	24 ± 3	45 ±10
CNMEHPPV	PE-b-PEG	84 ± 4	86 ± 4	84 ± 6
CNMEHPPV	PSPEGCOOH	75 ± 5	80 ± 8	72 ± 4
CNMEHPPV	PS-b-PEG	103 ± 2	112 ± 3	105 ± 1
CNMEHPPV	None	97 ± 11	74 ± 56	100 ± 18
CNMEHPPV	Pluronic F127	99 ± 22	110 ± 35	93 ± 9
CNMEHPPV	Brij L23	80 ± 4	90 ± 3	78 ± 2
MEHPPV	PSMA	66 ± 5	146 ± 106	31 ± 3
MEHPPV	PMAO	90 ± 16	83 ± 7	34 ± 14
MEHPPV	PS-b-PAA	102 ± 2	97 ± 32	28.3 ± 6
MEHPPV	PS-b-PEG	100 ± 3	131 ± 1	99 ± 6
MEHPPV	PSPEGCOOH	82 ± 2	77 ± 15	70 ± 2
MEHPPV	PS-b-PEG	105 ± 3	153 ± 22	114 ± 55
MEHPPV	None	121 ± 4	95 ± 39	120 ± 5
MEHPPV	Pluronic F127	105 ± 9	130 ± 27	115 ± 16
MEHPPV	IGEPAL	113 ± 18	87 ± 35	111 ± 26
PFVA	PSMA	100 ± 14	57 ± 3	45 ± 5
PFVA	PMAO	102 ± 9	25 ± 21	41 ± 3
PFVA	PS-b-PAA	114 ± 6	228 ± 281	36 ± 8
PFVA	PE-b-PEG	81 ± 2	25 ± 25	72 ± 3
PFVA	None	85 ± 2	50 ± 9	74 ± 6
PFVA	PSPEGCOOH	93 ± 25	77 ± 66	55 ± 4
PFVA	PS-b-PEG	87 ± 11	39 ± 7	86 ± 2
PFVA	IGEPAL	94 ± 9	41 ± 13	76 ± 6

Table A.1. Selected physical and optical properties of Pdots of varying composition synthesized by the syringe pump method. Values are represented as the mean and standard deviation of three replicates batches. Values highlighted in yellow were deemed unreliable (*vide infra*). Values marked with a hyphen (-) were not measured.

Semiconducting Polymer	Amphiphilic Polymer	D_{NTA} (nm)[a]		D_{DLS} (nm)[d]
		Scattering[b]	Fluorescence[c]	
PFVA	Jeffamine ED-600	88 ± 13	58 ± 19	67 ± 13
PFMEHPPV	PSMA	120 ± 4	53 ± 7	40 ± 1
PFMEHPPV	PMAO	130 ± 18	38 ± 11	39 ± 4
PFMEHPPV	PS-b-PAA	124 ± 3	43 ± 22	41 ± 4
PFMEHPPV	PE-b-PEG	86 ± 3	35 ± 3	66 ± 14
PFMEHPPV	None	97 ± 8	147 ± 68	
PFMEHPPV	PSPEGCOOH	108 ± 6	51[g]	47 ± 1
PFMEHPPV	PS-b-PEG	91 ± 6	73 ± 20	68 ± 26
PFMEHPPV	Jeffamine ED-600	87 ± 9	73 ± 15	59 ± 9
PFMEHPPV	Brij L23	97 ± 9	97[g]	79 ± 27

[a] Mean diameter from raw NTA data (*i.e.,*no fitting applied), [b] Mean diameter from scattering mode NTA measurements (no filter), [c] Mean diameter from fluorescence mode NTA measurements (500 nm LP filter) [d] Mean diameter from intensity weighted DLS measurements (lognormal fitted) [e] Wavelength of maximum absorption for the S_0-S_1 peak, [f] Wavelength of maximum emission, [g] Only one replicate batch recorded

Table A.2. Optical properties of Pdots of varying composition synthesized by the syringe pump method Values are represented as the mean and standard deviation of three replicates batches. Pdots synthesized with PSMA were used as the reference material for the determination of χ^2 and therefore do not have an associated χ^2 value. Materials with little change in peak shape compared to the Pdot with PSMA are labeled green. Materials exhibiting increased intensity in the red shoulder regions are labeled blue. F8BT/PE-b-PEG, labeled red, displayed a new emission peak above the emission maximum of F8BT/PSMA Pdots.

Semiconducting Polymer	Amphiphilic Polymer	$\lambda_{max,Abs.}$ (nm)[a]	$\lambda_{max,Em.}$ (nm)[b]	χ^2 [c]
F8BT	PSMA	464	541	-
F8BT	PS-b-PAA	461	543	5.3 ± 0.9
F8BT	PE-b-PEG	469	543	21 ± 8
F8BT	PS-b-PEG	465	541	0.11 ± 0.03
F8BT	PMAO	464	543	5 ± 2
CNMEHPPV	PSMA	471	616	-
CNMEHPPV	PS-b-PAA	475	619	0.12 ± 0.05
CNMEHPPV	PE-b-PEG	468	611	0.16 ± 0.05
CNMEHPPV	PS-b-PEG	470	610	0.27 ± 0.07
CNMEHPPV	PMAO	470	615	0.4 ± 0.4
CNMEHPPV	PSPEGCOOH	471	616	0.4 ± 0.3
CNMEHPPV	Brij L23	469	614	0.05 ± 0.02
CNMEHPPV	Pluronic F127	467	611	0.2 ± 0.1
CNMEHPPV	none	468	610	0.3 ± 0.1
MEHPPV	PSMA	497	592	-
MEHPPV	PS-b-PAA	498	592	0.14 ± 0.03
MEHPPV	PE-b-PEG	501	593	0.08 ± 0.04
MEHPPV	PS-b-PEG	500	593	0.2 ± 0.1
MEHPPV	PMAO	500	592	0.14 ± 0.05
MEHPPV	PSPEGCOOH	498	592	0.18 ± 0.03
MEHPPV	IGEPAL	501	591	0.25 ± 0.04
MEHPPV	Pluronic F127	499	592	0.3 ± 0.2
MEHPPV	none	501	591	0.4 ± 0.2
PFVA	PSMA	432	577	-
PFVA	PS-b-PAA	438	583	0.2 ± 0.2
PFVA	PE-b-PEG	439	582	0.08 ± 0.03
PFVA	PS-b-PEG	439	579	0.3 ± 0.3
PFVA	PMAO	436	578	0.3 ± 0.2
PFVA	PSPEGCOOH	436	580	0.2 ± 0.1
PFVA	IGEPAL	440	579	0.5 ± 0.3
PFVA	Jeffamine ED-600	424	569	1.0 ± 0.3

Table A.2. Optical properties of Pdots of varying composition synthesized by the syringe pump method Values are represented as the mean and standard deviation of three replicates batches. Pdots synthesized with PSMA were used as the reference material for the determination of χ^2 and therefore do not have an associated χ^2 value. Materials with little change in peak shape compared to the Pdot with PSMA are labeled green. Materials exhibiting increased intensity in the red shoulder regions are labeled blue. F8BT/PE-b-PEG, labeled red, displayed a new emission peak above the emission maximum of F8BT/PSMA Pdots.

Semiconducting Polymer	Amphiphilic Polymer	$\lambda_{max,Abs.}$ (nm)[a]	$\lambda_{max,Em.}$ (nm)[b]	χ^2 [c]
PFVA	none	437	579	0.4 ± 0.2
PFMEHPPV	PSMA	452	511	-
PFMEHPPV	PS-b-PAA	451	510	0.9 ± 0.8
PFMEHPPV	PE-b-PEG	455	512	0.2 ± 0.1
PFMEHPPV	PS-b-PEG	453	512	0.05 ± 0.03
PFMEHPPV	PMAO	453	512	0.3 ± 0.2
PFMEHPPV	PSPEGCOOH	452	512	0.12 ± 0.05
PFMEHPPV	Brij L23	450	510	2.3 ± 0.6
PFMEHPPV	Jeffamine ED-600	451	511	3 ± 1
PFMEHPPV	none	454	512	0.04 ± 0.01

[a] Wavelength of maximum absorption for the lowest energy peak, [b] Wavelength of maximum emission (All wavelength values are ± 3 nm or less) [c] χ^2 of emission peak against peak shape of SP/PSMA Pdots (± represents the standard deviation for 3 replicates).

Table A.3. NTA data for Pdots synthesized by flow synthesis.

Semiconducting Polymer	Amphiphile	NTA Mode	Mean Diameter (nm)	Concentration (10^9 particles/mL)	Total Tracks	Valid Tracks	Track Ratio	Concentration Ratio
CNMEHPPV	PS-b-PAA	Scattering	74	140	6471	1040	0.16	2.30
		Fluorescence	21	322	4162	904	0.22	
CNMEHPPV	PS-b-PEG	Scattering	101	185	4899	1792	0.37	0.56
		Fluorescence	110	104	2538	736	0.29	
CNMEHPPV	PSMA	Scattering	54	310	10305	1921	0.19	1.28
		Fluorescence	33	396	7339	1423	0.19	
CNMEHPPV	Pluronic F127	Scattering	124	261	8074	2667	0.33	0.61
		Fluorescence	148	159	3901	1233	0.32	
CNMEHPPV	PE-b-PEG	Scattering	89	300	8133	3289	0.40	0.52
		Fluorescence	88	157	4125	1357	0.33	
CNMEHPPV	PSPEGCOOH	Scattering	73	337	10209	3599	0.35	0.54
		Fluorescence	74	182	5476	1639	0.30	
CNMEHPPV	Brij L23	Scattering	82	365	10791	4007	0.37	0.51
		Fluorescence	88	185	5097	1591	0.31	
CNMEHPPV	none	Scattering	85	361	10073	4053	0.40	0.52
		Fluorescence	92	186	4846	1715	0.35	
F8BT	PS-b-PAA	Scattering	66	46.6	2355	509	0.22	2.90
		Fluorescence	40	135	3361	559	0.17	
F8BT	PMAO	Scattering	65	190	9481	1344	0.14	1.67
		Fluorescence	42	317	5877	878	0.15	
F8BT	PE-b-PEG	Scattering	103	163	5139	1686	0.33	0.71
		Fluorescence	108	115	2747	1045	0.38	
F8BT	PS-b-PEG	Scattering	72	348	12400	4459	0.36	0.63
		Fluorescence	79	219	5862	2113	0.36	
MEHPPV	PS-b-PAA	Scattering	103	35.0	2192	281	0.13	0.18
		Fluorescence	129	6.28	57	13	0.23	

Table A.3. NTA data for Pdots synthesized by flow synthesis.

Semiconducting Polymer	Amphiphile	NTA Mode	Mean Diameter (nm)	Concentration (10^9 particles/mL)	Total Tracks	Valid Tracks	Track Ratio	Concentration Ratio
MEHPPV	PSMA	Scattering	63	133	5624	1148	0.20	0.03
		Fluorescence	268	3.47	130	20	0.15	
MEHPPV	PMAO	Scattering	71	168	6159	1344	0.22	0.03
		Fluorescence	86	4.56	129	10	0.08	
MEHPPV	none	Scattering	116	142	3665	1348	0.37	0.04
		Fluorescence	135	5.13	124	18	0.15	
MEHPPV	PS-b-PEG	Scattering	108	196	7006	2174	0.31	0.09
		Fluorescence	139	17.5	469	83	0.18	
MEHPPV	PE-b-PEG	Scattering	97	210	6206	2256	0.36	0.10
		Fluorescence	132	20.0	483	68	0.14	
MEHPPV	IGEPAL CO-520	Scattering	92	264	7373	2701	0.37	0.28
		Fluorescence	44	74.0	1379	97	0.07	
MEHPPV	PSPEGCOOH	Scattering	81	305	7731	2762	0.36	0.12
		Fluorescence	62	36.2	878	46	0.05	
MEHPPV	Pluronic F127	Scattering	101	234	7548	2730	0.36	0.11
		Fluorescence	118	26.8	662	115	0.17	
PFMEHPPV	PMAO	Scattering	110	19.8	748	193	0.26	0.37
		Fluorescence	50	7.26	297	2	0.01	
PFMEHPPV	PSMA	Scattering	119	24.6	887	256	0.29	0.08
		Fluorescence	48	1.94	305	1	0.00	
PFMEHPPV	PS-b-PAA	Scattering	123	30.7	969	262	0.27	0.19
		Fluorescence	33	5.93	306	4	0.01	
PFMEHPPV	PSPEGCOOH	Scattering	112	34.7	1261	411	0.33	0.07
		Fluorescence	31	2.27	1321	3	0.00	
PFMEHPPV	Jeffamine ED-600	Scattering	94	80.8	3704	798	0.22	0.01
		Fluorescence	89	0.869	28	4	0.14	

Table A.3. NTA data for Pdots synthesized by flow synthesis.

Semiconducting Polymer	Amphiphile	NTA Mode	Mean Diameter (nm)	Concentration (10^9 particles/mL)	Total Tracks	Valid Tracks	Track Ratio	Concentration Ratio
PFMEHPPV	PS-b-PEG	Scattering	91	109	4202	1020	0.24	0.06
		Fluorescence	94	6.38	261	6	0.02	
PFMEHPPV	none	Scattering	106	114	4593	1130	0.25	0.03
		Fluorescence	195	3.27	203	7	0.03	
PFMEHPPV	PE-b-PEG	Scattering	89	137	5638	1194	0.21	0.05
		Fluorescence	33	6.85	461	4	0.01	
PFMEHPPV	Brij L23	Scattering	91	139	4470	1308	0.29	0.04
		Fluorescence	97	6.08	117	14	0.12	
PFVA	PSMA	Scattering	109	43.6	2428	480	0.20	0.09
		Fluorescence	61	3.90	42	9	0.21	
PFVA	PS-b-PAA	Scattering	109	48.2	2002	564	0.28	0.07
		Fluorescence	57	3.16	62	12	0.19	
PFVA	PMAO	Scattering	94	74.9	4858	760	0.16	1.07
		Fluorescence	37	80.0	2851	2	0.00	
PFVA	PSPEGCOOH	Scattering	122	91.4	3292	841	0.26	0.03
		Fluorescence	153	2.77	190	5	0.03	
PFVA	Jeffamine ED-600	Scattering	103	136	3568	1041	0.29	0.00
		Fluorescence	62	0.566	8	2	0.25	
PFVA	None	Scattering	87	163	5530	1607	0.29	0.06
		Fluorescence	58	10.5	232	8	0.03	
PFVA	IGEPAL CO-520	Scattering	87	287	8822	2955	0.33	0.06
		Fluorescence	35	16.3	178	5	0.03	
PFVA	PS-b-PEG	Scattering	92	315	9461	3496	0.37	0.07
		Fluorescence	45	23.0	375	15	0.04	
PFVA	PE-b-PEG	Scattering	79	364	10337	3640	0.35	0.00
		Fluorescence	-	0	0	0	-	

A.2 Data analysis

Sizing data for CNMEHPPV/PS-b-PEG, CNMEHPPV/PSMA, CNMEHPPV/Pluronic F127, CNMEHPPV/PE-b-PEG, CNMEHPPV/Brij L23, F8BT/PS-b-PAA and F8BT/PE-b-PEG Pdots gave good agreement between scattering- and fluorescence-mode NTA and DLS. The average number of valid tracks (scattering and fluorescence modes), ratio of valid tracks to total tracks (track ratio) and concentration ratio between fluorescence and scattering modes were calculated for these Pdots. A cut-off value was defined as the average value minus one (concentration) or two (number of tracks, track ratio) standard deviations of these values. Any value below these cut-offs was deemed unreliable and the corresponding scattering or fluorescence mode NTA data not used for analysis.

Table A.4. Determination of cut-off values for the rejection of NTA datasets.

Value	Average	Standard Deviation	Cut-off Value
Number of valid tracks (scattering)	2267	1155	0
Track ratio (scattering)	0.315	0.0821	0.150
Number of valid tracks (fluorescence)	1135	376	383
Track ratio (fluorescence)	0.284	0.077	0.131
Concentration ratio	1.01	0.873	0.138

Appendix B Fitting of fluorescence lifetime data for energy transfer titrations

B.1 Derived amplitude-weighted lifetimes for all samples measured in Chapter 6

Table B.1. Amplitude-weighted average fluorescence lifetimes for CyX dye titrations.

Cy5			Cy5.5			Cy7		
Φ_D[a]	n[b]	τ[c] (ps)	Φ_D[a]	n[b]	τ[c] (ps)	Φ_D[a]	n[b]	τ[c] (ps)
	0	748		0	590		0	774
	49	698		33	511		12	872
	117	637		65	467		45	794
	227	586		100	488	0.36	173	678
0.24	244	536	0.34	131	425		364	610
	378	465		202	378		456	534
	546	429		229	351		517	472
	717	396		247	347			
	864	387		284	327			

[a] Quantum yield of donor
[b] Average number of dyes per Pdot
[c] Amplitude-weighted fluorescence lifetime of donor

Table B.2. Amplitude-weighted average fluorescence lifetimes for sCyX dye titrations.

sCy5			sCy5.5			sCy7		
Φ_D[a]	n[b]	τ[c] (ps)	Φ_D[a]	n[b]	τ[c] (ps)	Φ_D[a]	n[b]	τ[c] (ps)
	0	742		0	671		0	533
	92	720		77	672		36	534
	111	713		178	693		74	557
	153	713		176	656		184	541
0.25	239	715	0.24	320	625	0.37	112	524
	252	713		441	596		159	512
	366	727		407	600		244	482
	361	749		696	585		283	490
				635	607		390	454

[a] Quantum yield of donor
[b] Average number of dyes per Pdot
[c] Amplitude-weighted fluorescence lifetime of donor

Table B.3. Amplitude-weighted average fluorescence lifetimes for the Rh640 titration.

Φ_D[a]	n[b]	τ[c] (ps)
0.23	0	480
	21	377
	62	393
	93	356
	199	338
	171	339

[a] Quantum yield of donor
[b] Average number of dyes per Pdot
[c] Amplitude-weighted fluorescence lifetime of donor

B.2 Instrument Response Function

Figure B.2 shows the instrument response function for the TCSPC module used for fluorescence lifetime measurements, recorded from the second harmonic response of urea (λ_{exc} = 948 nm).

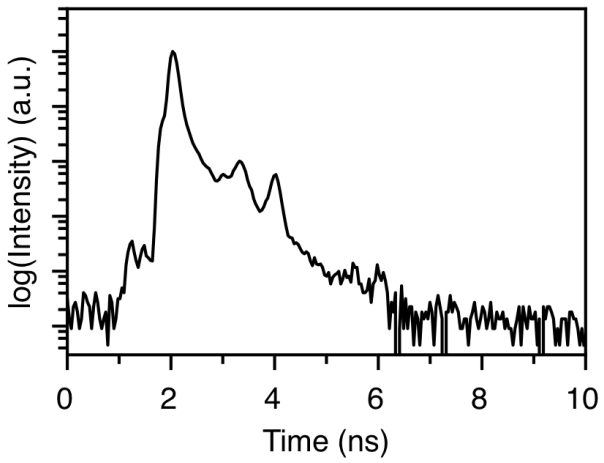

Figure B.2 Instrument response function for the TCSPC module used for lifetime measurements, derived from the second harmonic response of urea (λ_{exc} = 948 nm).

B.3 Rationales for lifetime fitting

A biexponential decay function, Eqn. B.1, was used to fit and analyze the Pdot lifetime data (*i.e.*, fluorescence decay curves) because it resulted in satisfactory empirical fits across all datasets. In Eqn. B.1, A_n and τ_n are the amplitude and lifetime parameters of the decay respectively, and C is a constant determined by fitting.

$$F(t) = A_1 e^{-\frac{t}{\tau_1}} + A_2 e^{-\frac{t}{\tau_2}} + C \tag{B.1}$$

Fitting was also attempted using a constrained triexponential decay curve, Eqn. B.2. The fluorescence decay of the Pdot in the absence of dye was fitted using a biexponential decay function, yielding parameters $A_{1,0}$, $A_{2,0}$, τ_1 and τ_2 (the amplitude and lifetime components of the decay, respectively). The fluorescence decays of the Pdot in the presence of dye were fit with a triexponential function, Eqn. B.2, where τ_1, τ_2, and the ratio of A_1 to A_2 were fixed to the values obtained from fitting the lifetime of the Pdot alone. This strategy was intended to account for any contributions from F8BT molecules or Pdots that did not participate in ET to a dye acceptor. Fitting parameters corresponding to the third exponential term, A_3 and τ_3, were allowed to vary to account for a fraction of F8BT molecules that did participate in ET. This constrained triexponential fitting did not yield satisfactory fits across all datasets. Considering tetraexponential fitting with analogous constraints, our assessment was that there were too many degrees of freedom for meaningful fitting.

$$F(t) = \left(\frac{A_{1,0}}{A_{2,0}} \right) A_2 e^{-\frac{t}{\tau_1}} + A_2 e^{-\frac{t}{\tau_2}} + A_3 e^{-\frac{t}{\tau_3}} + C \quad \text{(B.2)}$$

Further complications in the fitting of fluorescence lifetime curves potentially arise from the complex structure of the Pdots. Chromophores may exist in different local environments (*e.g.*, within the hydrophobic core, adjacent to amphiphilic polymer, or exposed to water molecules on the Pdot surface). The fluorescence decay of fluorophores in heterogeneous environments is sometimes best represented by a continuous distribution of lifetimes, rather than the sum of discrete exponential terms. The stretched exponential function, Eqn. B.3, describes a continuous distribution of contributions to the observed lifetime decay, where h ($\geq$1) is the heterogeneity parameter of the sample (h = 1 indicates a homogenous sample) [277].

$$F(t) = A_1 e^{-\left(\frac{t}{\tau_{str1}}\right)^{\frac{1}{h_1}}} + A_2 e^{-\left(\frac{t}{\tau_{str2}}\right)^{\frac{1}{h_2}}} + C \quad \text{(B.3)}$$

$$F(t) = A_1 e^{-\left(\frac{t}{\tau_{str1}}\right)^{\frac{1}{h_1}}} + C \quad \text{(B.4)}$$

Fitting was therefore also attempted using the stretched exponential function. The fluorescence decay of the Pdot alone was fitted using a stretched monoexponential function, Eqn. B.4. The decay curves for the Pdots in the presence of dyes (*i.e.*, Pdots participating in ET) were fit with a stretched biexponential function, Eqn. B.3, where the parameters A_1, τ_{str1} and h_1 were fixed and set equal to the parameters obtained from fitting the Pdot alone with a stretched monoexponential function. Fixing these parameters accounts for the fraction of F8BT molecules that are not participating in ET. We first set $h_2 = h_1$ because the distribution of lifetimes arising from the Pdot

should be consistent in the presence of a quencher. This method did not yield satisfactory fits across all datasets.

Stretched exponential fitting was also attempted by applying global fitting for h_2 across all quenched datasets (*i.e.*, specifying one value for h_2 across all quenched datasets), and by allowing h_2 to vary for each individual dataset. Neither method resulted in satisfactory fits across all datasets.

B.4 Examples of fitting for lifetime decay curves

Figure B.4 shows examples of the lifetime decay curves for the unquenched (N = 0) and quenched (N = 864) samples from the Cy5 ET titration (Figure 6.9A). For data analysis, all decay curves were fit with a biexponential function, Eqn. B.1, as this function yielded satisfactory fits across all datasets. Fitting quenched datasets with a constrained triexponential function, Eqn. B.2, did not yield improved fits (*i.e.*, lower χ^2 values) compared to the biexponential function. Fitting was also attempted using stretched exponential (Eqn B.4) and stretched biexponential functions (Eqn. B.3), which did not yield satisfactory fits for the unquenched or quenched decay curves. Regardless of the fit functions used, the observed trends (*i.e.*, decreased Pdot lifetime with increased average number of dyes per Pdot) are not expected to change.

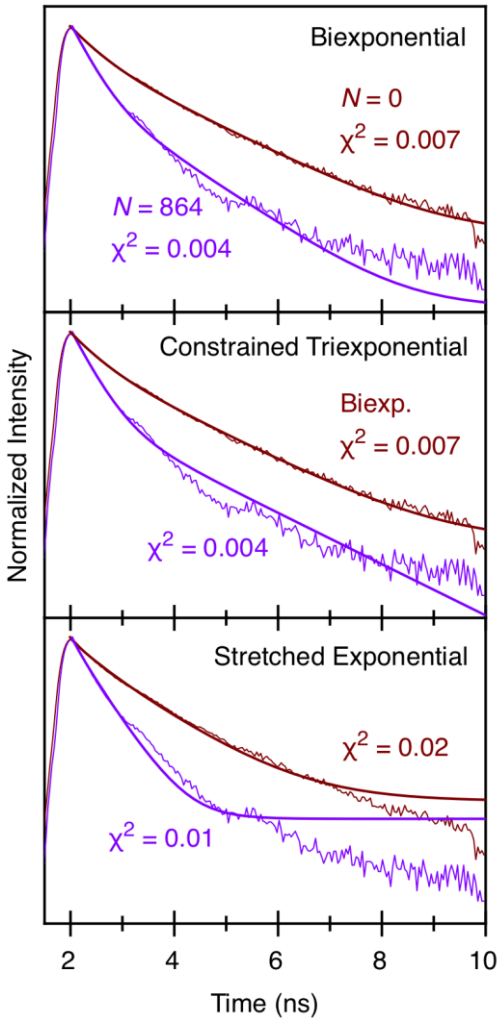

Figure B.4 Examples of exponential functions used to fit lifetime decay data. The raw data shown here is for the Cy5 ET titration (corresponding to Figure 6.9A). The red curve is the unquenched Pdot (N = 0), and the purple curve is the quenched Pdot with N = 864 dyes per Pdot. Top: Biexponential fit curves (Eqn. B.1) used for analysis. Middle: Unquenched data fit with a biexponential curve to fix $A_{1,0}$, $A_{2,0}$, τ_1 and τ_2, and quenched data fit with a constrained triexponential function (Eqn. B.2). Bottom: Unquenched and quenched data fit with single stretched exponential functions (Eqn. B.4). Fitting did not converge for the stretched biexponential function. The χ^2 values, indicating the goodness of the fits, are shown in the figure.

Appendix C NTA data for Pdots used in energy transfer studies

Table C.1. Pdot size distribution parameters measured by NTA. All dimensions are in nm.

		Scattering Mode NTA				Fluorescence Mode NTA			
Figure	Dye	Mean[a]	Mode[a]	SD[a]	*N*[b]	Mean[a]	Mode[a]	SD[a]	*N*[b]
6.6A, 6.9A	Cy5, sCy5, sCy5.5[c]	68	38	59	1839	53	34	23	484
6.6A, 6.9A	Cy5.5, sCy7[c]	63	42	45	2334	63	37	39	994
6.6A, 6.9A	Cy7	50	29	39	1984	45	32	25	1142
6.6A	Rh590	106	63	59	4373	103	76	53	2285
6.6A	Rh610	60	43	41	3149	66	46	57	1738
6.6A,6.10A	Rh640	53	41	28	4069	57	43	42	2048
6.6C	sCy5 (NAv)	58	29	40	1547	45	25	25	1442
6.6C	sCy5 (Dex, trial 1)	70	53	55	513	76	43	32	94
6.6C	sCy5 (Dex, trials 2-3)[c]	65	47	42	1458	74	67	26	234
6.6C	sCy5 (Dex, trials 4-5)[c]	77	69	34	3679	83	77	32	868
6.6C	sCy5 (Dex, trial 6)	66	52	32	3453	73	76	33	536
6.6C	sCy5 (Dex, trial 7)	48	53	39	587	118	112	55	45

[a] Raw mean, mode and standard deviation of NTA data in nm, [b] Number of particles tracked, [c] Same batch of Pdots used for multiple ET titrations

Table C.2. Lognormal fit parameters for the NTA histogram data. Mean, standard deviation (SD) and mode are in units of nm.

Figure	Dye	NTA	xc	w	A ($x10^{-8}$)	Mean	SD	Mode
6.6A, 6.9A	Cy5, sCy5, sCy5.5[a]	Scatter.	44.7	0.396	7.82	48	20	38
		Fluor.	47.2	0.470	3.17	53	26	38
6.6A, 6.9A	Cy5.5, sCy7[a]	Scatter.	44.7	0.374	11.46	48	19	39
		Fluor.	53.3	0.523	3.78	61	34	40
6.6A, 6.9A	Cy7	Scatter.	35.5	0.385	9.23	38	15	31
		Fluor.	38.8	0.491	3.40	44	23	31
6.6A	Rh590	Scatter.	89.0	0.474	23.61	100	50	71
		Fluor.	91.3	0.480	18.69	102	52	73
6.6A	Rh610	Scatter.	46.9	0.357	15.31	50	18	41
		Fluor.	47.2	0.427	10.53	52	23	39
6.6A,6.10A	Rh640	Scatter.	45.3	0.389	20.57	49	20	38
		Fluor.	47.4	0.407	13.30	52	22	40
6.6C	sCy5 (NAv)	Scatter.	46.2	0.606	10.17	56	37	32
		Fluor.	39.7	0.581	11.56	47	30	28
6.6C	sCy5 (Dex, trial 1)	Scatter.	56.1	0.321	1.86	59	19	51
		Fluor.	70.0	0.415	0.68	76	33	59
6.6C	sCy5 (Dex, trials 2-3)	Scatter.	56.5	0.406	7.79	61	26	48
		Fluor.	70.6	0.327	2.06	74	25	64
6.6C	sCy5 (Dex, trials 4-5)	Scatter.	71.5	0.320	16.30	75	25	65
		Fluor.	80.9	0.360	5.60	86	32	71
6.6C	sCy5 (Dex, trial 6)	Scatter.	58.0	0.331	14.90	61	21	52
		Fluor.	69.3	0.426	2.74	76	34	59
6.6C	sCy5 (Dex, trial 7)	Scatter.	51.9	1.244	8.83	113	217	11
		Fluor.	103.6	0.426	0.24	113	51	88

[a] Same batch of Pdots used for multiple ET titrations.